BIO-INSPIRED NANOMATERIALS IN SURFACE ENGINEERING AND BIOAPPLICATIONS

EDITED BY: Zhong Feng Gao, Guoqing Wang, Ruixue Duan and Houjuan Zhu
PUBLISHED IN: Frontiers in Chemistry

frontiers Research Topics

ISSN 1664-8714
ISBN 978-2-88974-704-7
DOI 10.3389/978-2-88974-704-7

About Frontiers

Frontiers is more than just an open-access publisher of scholarly articles: it is a pioneering approach to the world of academia, radically improving the way scholarly research is managed. The grand vision of Frontiers is a world where all people have an equal opportunity to seek, share and generate knowledge. Frontiers provides immediate and permanent online open access to all its publications, but this alone is not enough to realize our grand goals.

Frontiers Journal Series

The Frontiers Journal Series is a multi-tier and interdisciplinary set of open-access, online journals, promising a paradigm shift from the current review, selection and dissemination processes in academic publishing. All Frontiers journals are driven by researchers for researchers; therefore, they constitute a service to the scholarly community. At the same time, the Frontiers Journal Series operates on a revolutionary invention, the tiered publishing system, initially addressing specific communities of scholars, and gradually climbing up to broader public understanding, thus serving the interests of the lay society, too.

Dedication to Quality

Each Frontiers article is a landmark of the highest quality, thanks to genuinely collaborative interactions between authors and review editors, who include some of the world's best academicians. Research must be certified by peers before entering a stream of knowledge that may eventually reach the public - and shape society; therefore, Frontiers only applies the most rigorous and unbiased reviews.
Frontiers revolutionizes research publishing by freely delivering the most outstanding research, evaluated with no bias from both the academic and social point of view. By applying the most advanced information technologies, Frontiers is catapulting scholarly publishing into a new generation.

What are Frontiers Research Topics?

Frontiers Research Topics are very popular trademarks of the Frontiers Journals Series: they are collections of at least ten articles, all centered on a particular subject. With their unique mix of varied contributions from Original Research to Review Articles, Frontiers Research Topics unify the most influential researchers, the latest key findings and historical advances in a hot research area! Find out more on how to host your own Frontiers Research Topic or contribute to one as an author by contacting the Frontiers Editorial Office: frontiersin.org/about/contact

BIO-INSPIRED NANOMATERIALS IN SURFACE ENGINEERING AND BIOAPPLICATIONS

Topic Editors:
Zhong Feng Gao, Linyi University, China
Guoqing Wang, Ocean University of China, China
Ruixue Duan, Soochow University, China
Houjuan Zhu, Institute of Materials Research and Engineering (A*STAR), Singapore

Citation: Gao, Z. F., Wang, G., Duan, R., Zhu, H., eds. (2022). Bio-Inspired Nanomaterials in Surface Engineering and Bioapplications. Lausanne: Frontiers Media SA. doi: 10.3389/978-2-88974-704-7

Table of Contents

04 ***Editorial: Bio-Inspired Nanomaterials in Surface Engineering and Bioapplications***
Yun Jun Yang and Zhong Feng Gao

07 ***Near-Infrared Photoactivatable Immunomodulatory Nanoparticles for Combinational Immunotherapy of Cancer***
Ningyue Yu, Mengbin Ding and Jingchao Li

15 ***Enzyme-Loaded pH-Sensitive Photothermal Hydrogels for Mild-temperature-mediated Combinational Cancer Therapy***
Jindong Xia, Xueqin Qing, Junjian Shen, Mengbin Ding, Yue Wang, Ningyue Yu, Jingchao Li and Xiuhui Wang

25 ***pH-Responsive DNA Motif: From Rational Design to Analytical Applications***
Lin Lin Zheng, Jin Ze Li, Ying Xu Li, Jian Bang Gao, Jiang Xue Dong and Zhong Feng Gao

31 ***Injectable Hydrogel Based on Modified Gelatin and Sodium Alginate for Soft-Tissue Adhesive***
Yuhang Xing, Xueqin Qing, Hao Xia, Shiqi Hao, Haofang Zhu, Yiyan He, Hongli Mao and Zhongwei Gu

39 ***A Co-delivery System Based on a Dimeric Prodrug and Star-Shaped Polymeric Prodrug Micelles for Drug Delivery***
Man Zhou, Yan Luo, Weijia Zeng, Xiaoqing Yang, Tingting Chen, Lulu Zhang, Xiaoyan He, Xiuguang Yi, Yongxiu Li and Xiaoqing Yi

47 ***A Nanofiber Mat With Dual Bioactive Components and a Biomimetic Matrix Structure for Improving Osteogenesis Effect***
Yadi Han, Xiaofeng Shen, Sihao Chen, Xiuhui Wang, Juan Du and Tonghe Zhu

58 ***PPy@Fe_3O_4 Nanoparticles Inhibit Tumor Growth and Metastasis Through Chemodynamic and Photothermal Therapy in Non-small Cell Lung Cancer***
Danruo Fang, Hansong Jin, Xiulin Huang, Yongxin Shi, Zeyu Liu and Suqin Ben

71 ***Biomimetic Nanomaterials Triggered Ferroptosis for Cancer Theranostics***
Xinyu Zhang, Yanling Ma, Jipeng Wan, Jia Yuan, Diqing Wang, Weiyi Wang, Xiao Sun and Qingwei Meng

88 ***Surface Treatment and Bioinspired Coating for 3D-Printed Implants***
Junyi Liu, Nafisah Bte Mohd Rafiq, Lai Mun Wong and Shijie Wang

102 ***Electrochemical Biosensing Interface Based on Carbon Dots-Fe_3O_4 Nanomaterial for the Determination of* Escherichia coli *O157:H7***
Xiaofeng Lin, Yanqiu Mei, Chen He, Yan Luo, Min Yang, Ying Kuang, Xiaoming Ma, Huifang Zhang and Qitong Huang

110 ***Recent Advances in Metal/Alloy Nano Coatings for Carbon Nanotubes Based on Electroless Plating***
Lei Zhang, Yi Chao, Kenan Yang, Daodao Xue and Shisheng Zhou

frontiers in Chemistry

EDITORIAL
published: 14 March 2022
doi: 10.3389/fchem.2022.872069

Editorial: Bio-Inspired Nanomaterials in Surface Engineering and Bioapplications

Yun Jun Yang[1] *and Zhong Feng Gao*[2,3]*

[1]*Advanced Research Institute for Multidisciplinary Science, Qilu University of Technology (Shandong Academy of Sciences), Jinan, China,* [2]*Advanced Materials Institute, Qilu University of Technology (Shandong Academy of Sciences), Jinan, China,* [3]*Collaborative Innovation Center of Tumor Marker Detection Technology, Equipment and Diagnosis-Therapy Integration in Universities of Shandong, Shandong Provincial Key Laboratory of Detection Technology for Tumor Markers, College of Chemistry and Chemical Engineering, Linyi University, Linyi, China*

Keywords: biomaterial, functional nanomaterial, biomedical application, surface chemistry, nanoscience

Editorial on the Research Topic

Bio-Inspired Nanomaterials in Surface Engineering and Bioapplications

Bio-inspired nanomaterials, as a class of easy-to-use biomaterials, have emerged as versatile tools for biosensing, bioimaging, biocatalysis, antibacterial treatment, and biotherapy, and have demonstrated their usefulness in addressing a wide range of biomedical challenges (Huang et al., 2015; Madamsetty et al., 2019; Kumar et al., 2020; Lai et al., 2021). By using diverse chemical modification or biological interaction on the surface, the functional nanomaterial can be constructed to recognize the specific site in complex environments both *in vitro* and *in vivo*. While many biological systems require a highly specific lock-and-key approach for molecular interaction, surface engineering provides an alternative method to create specificity of biofunctional nanomaterials (Wu et al., 2016; Kankala et al., 2020). Attaching biological molecules, such as nucleic acids, proteins, and antibodies, at the surface of nanomaterials is a crucial condition to ensure the biosafety of nanomaterials. The primary feature of an advanced nanomaterial is that it provides low toxicity, high biocompatibility, and unique stimulus responses such as light, electricity, and magnetism, which expand its bioapplications (Reddy et al., 2012; Ge et al., 2021; Li et al., 2021).

To present state-of-the-art research in this field, we launched a Research Topic in Frontiers in Chemistry entitled "Bio-Inspired Nanomaterials in Surface Engineering and Bioapplications." This Research Topic included 11 articles, including 6 original research articles, 3 reviews, and 2 mini reviews, which covered the field of surface treatment, biosensors, tissue engineering, cancer therapy, and other bioapplications.

Several works focus on the surface engineering of nanomaterials because new surface chemistry represents a revolutionary direction in functional biomaterials and has become a topic of interest. Liu et al. reviewed the significant progress in the surface functionalities of metallic implants regarding their physical structure, chemical composition, and biological reaction by surface treatment and bioactive coating. They have presented a perspective on the current challenges and future directions for development of surface treatment on 3D-printed implants. Zhang et al. summarized the existing electroless plating methods for carbon nanotubes, and their applications including electrical, mechanical, thermal, tribological, corrosion resistance, and magnetic properties were discussed in detail. This review is critical for the future research and improvement of electroless metal/alloy nano-coating of carbon nanotubes.

Regarding the application examples, the integration of biomolecules or surface treatment can endow biosensors with high sensitivity and selectivity. Lin et al. developed a sensitive electrochemical

OPEN ACCESS

Edited and reviewed by:
Chen Zhou,
University of Central Missouri, United States

****Correspondence:***
Zhong Feng Gao
gaozhongfeng@lyu.edu.cn

Specialty section:
This article was submitted to Nanoscience, a section of the journal Frontiers in Chemistry

Received: *09 February 2022*
Accepted: *15 February 2022*
Published: *14 March 2022*

Citation:
Yang YJ and Gao ZF (2022) Editorial: Bio-Inspired Nanomaterials in Surface Engineering and Bioapplications. Front. Chem. 10:872069. doi: 10.3389/fchem.2022.872069

biosensor using carbon dots-Fe_3O_4 nanomaterial (CDs-Fe_3O_4) for *E. coli* O157:H7 detection. The functional electrochemical biosensor showed a wide detection range from 10 to 10^8 CFU/ml and a low detection limit (6.88 CFU/ml). This method has been successfully used to determine *E. coli* O157:H7 in milk and water samples. Meanwhile, a mini-review summarized the design principle and biosensing application of a pH-responsive DNA motif including triplex DNA, i-motif, and A^+-C mismatch base pair-based DNA structures (Zheng et al.). They pointed out that the modification of those DNA motifs into single-cell and modulate intercellular functions will be challenging for future studies.

In the direction of tissue engineering, Han et al. introduced a nanofiber mat with dual bioactive components and a biomimetic matrix structure to improve osteogenesis capability. By combining homogeneous blending and electrospinning technology, the nanofiber mat showed sufficient mechanical properties and a porous structure suitable for cell growth and migration, which have great potential in the application of bone repair materials. By mimicking the composition of the extracellular matrix of native tissues, Xing et al. reported an injectable hydrogel tissue adhesive with excellent biocompatibility. The measured adhesion ability was higher than that of the commercial Porcine Fibrin Sealant Kit, indicating the novel injectable hydrogel might be a promising candidate for a soft tissue adhesive.

Target-triggered nanomaterials have been considered as potential delivery systems, which could achieve the targeted delivery of antitumor drugs, reduced cytotoxicity, and enhanced therapeutic efficacy. Zhou et al. used the redox-responsive star-shaped polymeric prodrug (PSSP) and the dimeric prodrug of paclitaxel (diP) to prepare a co-delivery system (diP@PSSP) for intracellular drug release in tumor cells. The redox-responsive diP@PSSP micelles possessed high drug-loading content of paclitaxel as high as 46.9% and excellent stability. The polymeric prodrug of diP@PSSP micelles also demonstrated good biocompatibility in red blood cells and had a therapeutic effect in HeLa cells. The original research article from Fang et al. reported polypyrrole (PPy)-modified Fe_3O_4 nanoparticles (PPy@ Fe_3O_4 NPs) on inhibiting growth and metastasis of non-small cell lung cancer by a combination of photothermal therapy (PTT) and chemodynamic therapy (CDT). PPy was used as a photothermal agent to construct nanocomposites because of its high photothermal conversion efficiency and exceptional photostability. The *in vitro* and *in vivo* studies displayed that PPy@Fe_3O_4 NPs were excellent near-infrared (NIR) sensitive magnetic resonance imaging (MRI)-guided synergistic chemodynamic/photothermal cancer therapy agents, which could decrease the levels of MMP2, MMP9, and MMP13. It provides a new therapeutic strategy for non-small cell lung cancer. As another example, Xia et al. reported a glucose oxidase (GOx)-loaded hydrogel with a pH-sensitive NIR-II photothermal effect for combinational cancer therapy at mild temperature. The hydrogels were engineered *via* coordination of alginate solution containing pH-sensitive charge-transfer nanoparticles (CTNs) as the second near-infrared (NIR-II) photothermal agents and GOx. Through consuming glucose, the hydrogel mediated starvation therapy, which not only led to exhaustion of tumor cells, but also resulted in aggravated acidity in the tumor microenvironment and downregulated expression of HSP90. By integration of mild NIR-II PTT and starvation therapy, the proposed hydrogel was able to suppress the growth of subcutaneously implanted tumors and completely prevent lung metastasis in a breast cancer murine model. Yu et al. briefly introduced the rational design, construction, and working mechanisms of NIR photoactivatable agents and summarized the recent progress of NIR photoactivatable immunomodulatory nanoparticles for combinational cancer immunotherapy. They described that NIR photoactivatable immunomodulatory nanoparticles might have great potential for clinical treatment of major diseases such as cancer, infectious diseases, and autoimmunity. Zhang et al. discussed recent developments of biomimetic nanomaterials in ferroptosis-related cancer nanomedicine. Many ferroptosis-related nano-inducers have unexpected disadvantages including low circulation time, immune exposure, and ineffective tumor targeting. Biomimetic nanomaterials may be able to provide new solutions to these limitations due to their unique physicochemical properties.

Bio-inspired nanomaterials have a wide range of applications. The contributions in this Research Topic provide various kinds of nanomaterials with unique surface treatment and bioapplications including biosensor, drug delivery, cancer therapy, and tissue engineering functions. The design, fabrication, and other applications of functional nanomaterials are still the major focus in this research field. We believe this Research Topic will provide abundant technology to understand the advanced strategies of bio-inspired nanomaterials in broad applications, inspiring novel ideas for future research fields.

AUTHOR CONTRIBUTIONS

All authors listed have made a substantial, direct, and intellectual contribution to the work and approved it for publication.

ACKNOWLEDGMENTS

We very much appreciate the contributions of all authors to this Research Topic and are grateful for the time and dedication of those who contributed to the peer review process.

REFERENCES

Ge, W., Wang, L., Zhang, J., Ou, C., Si, W., Wang, W., et al. (2021). Self-Assembled Nanoparticles as Cancer Therapeutic Agents. *Adv. Mater. Inter.* 8, 2001602. doi:10.1002/admi.202001602

Huang, J., Lin, L., Sun, D., Chen, H., Yang, D., and Li, Q. (2015). Bio-inspired Synthesis of Metal Nanomaterials and Applications. *Chem. Soc. Rev.* 44, 6330–6374. doi:10.1039/C5CS00133A

Kankala, R. K., Han, Y. H., Na, J., Lee, C. H., Sun, Z., Wang, S. B., et al. (2020). Nanoarchitectured Structure and Surface Biofunctionality of Mesoporous Silica Nanoparticles. *Adv. Mater.* 32, 1907035. doi:10.1002/adma.201907035

Kumar, A., Sharma, G., Naushad, M., Al-Muhtaseb, A. a. H., García-Peñas, A., Mola, G. T., et al. (2020). Bio-inspired and Biomaterials-Based Hybrid Photocatalysts for Environmental Detoxification: A Review. *Chem. Eng. J.* 382, 122937. doi:10.1016/j.cej.2019.122937

Lai, Y., Li, F., Zou, Z., Saeed, M., Xu, Z., and Yu, H. (2021). Bio-inspired Amyloid Polypeptides: From Self-Assembly to Nanostructure Design and Biotechnological Applications. *Appl. Mater. Today* 22, 100966. doi:10.1016/j.apmt.2021.100966

Li, Y., Zheng, X., and Chu, Q. (2021). Bio-based Nanomaterials for Cancer Therapy. *Nano Today* 38, 101134. doi:10.1016/j.nantod.2021.101134

Madamsetty, V. S., Mukherjee, A., and Mukherjee, S. (2019). Recent Trends of the Bio-Inspired Nanoparticles in Cancer Theranostics. *Front. Pharmacol.* 10, 1264. doi:10.3389/fphar.2019.01264

Reddy, L. H., Arias, J. L., Nicolas, J., and Couvreur, P. (2012). Magnetic Nanoparticles: Design and Characterization, Toxicity and Biocompatibility, Pharmaceutical and Biomedical Applications. *Chem. Rev.* 112, 5818–5878. doi:10.1021/cr300068p

Wu, W., Jiang, C. Z., and Roy, V. A. L. (2016). Designed Synthesis and Surface Engineering Strategies of Magnetic Iron Oxide Nanoparticles for Biomedical Applications. *Nanoscale* 8, 19421–19474. doi:10.1039/C6NR07542H

Conflict of Interest: The authors declare that the research was conducted in the absence of any commercial or financial relationships that could be construed as a potential conflict of interest.

Publisher's Note: All claims expressed in this article are solely those of the authors and do not necessarily represent those of their affiliated organizations, or those of the publisher, the editors and the reviewers. Any product that may be evaluated in this article, or claim that may be made by its manufacturer, is not guaranteed or endorsed by the publisher.

frontiers in Chemistry

MINI REVIEW
published: 24 May 2021
doi: 10.3389/fchem.2021.701427

Near-Infrared Photoactivatable Immunomodulatory Nanoparticles for Combinational Immunotherapy of Cancer

*Ningyue Yu, Mengbin Ding and Jingchao Li**

Shanghai Engineering Research Center of Nano-Biomaterials and Regenerative Medicine, College of Chemistry, Chemical Engineering and Biotechnology, Donghua University, Shanghai, China

As a promising treatment option for cancer, immunotherapy can eliminate local and distant metastatic tumors and even prevent recurrence through boosting the body's immune system. However, immunotherapy often encounters the issues of limited therapeutic efficacy and severe immune-related adverse events in clinical practices, which should be mainly due to the non-specific accumulations of immunotherapeutic agents. Activatable immunomodulatory agents that are responsive to endogenous stimuli in tumor microenvironment can afford controlled immunotherapeutic actions, while they still face certain extent of off-target activation. Since light has the advantages of noninvasiveness, simple controllability and high spatio-temporal selectivity, therapeutic agents that can be activated by light, particularly near-infrared (NIR) light with minimal phototoxicity and strong tissue penetrating ability have been programmed for cancer treatment. In this mini review, we summarize the recent progress of NIR photoactivatable immunomodulatory nanoparticles for combinational cancer immunotherapy. The rational designs, constructions and working mechanisms of NIR photoactivatable agents are first briefly introduced. The uses of immunomodulatory nanoparticles with controlled immunotherapeutic actions upon NIR photoactivation for photothermal and photodynamic combinational immunotherapy of cancer are then summarized. A conclusion and discussion of the existing challenges and further perspectives for the development and clinical translation of NIR photoactivatable immunomodulatory nanoparticles are finally given.

Keywords: near-infrared light, nanomedicine, immunotherapy, photoactivation, phototherapy

OPEN ACCESS

Edited by:
Houjuan Zhu,
National University of Singapore, Singapore

Reviewed by:
Chen Xie,
Nanjing University of Posts and Telecommunications, China
Yu Luo,
Shanghai University of Engineering Sciences, China

****Correspondence:***
Jingchao Li
jcli@dhu.edu.cn

Specialty section:
This article was submitted to Nanoscience, a section of the journal Frontiers in Chemistry

Received: *28 April 2021*
Accepted: *12 May 2021*
Published: *24 May 2021*

Citation:
Yu N, Ding M and Li J (2021) Near-Infrared Photoactivatable Immunomodulatory Nanoparticles for Combinational Immunotherapy of Cancer. Front. Chem. 9:701427. doi: 10.3389/fchem.2021.701427

INTRODUCTION

Immunotherapy is a type of cancer treatment that uses the body's immune system to fight cancer (Del Paggio, 2018). Different from traditional treatment methods such as surgery, chemotherapy and radiotherapy that can only be effective for local tumors, immunotherapy is able to remove both local and distant metastatic tumors, and even prevent tumor recurrence (Nam et al., 2019; Li et al., 2021). Immune checkpoint blockade therapy, cancer vaccines, and adoptive T cell therapy are three key approaches for cancer immunotherapy (Pardoll, 2012; Kuai et al., 2017; Fraietta et al., 2018). With the approval of different immunotherapeutic agents by the U.S. Food and Drug Administration (FDA), a great success has been achieved for cancer immunotherapy in the clinic (Zhang and Pu,

2020). However, these agents after traditional systemic administration often have non-specific accumulations in normal tissues, resulting in limited therapeutic efficacy and severe immune-related adverse events (irAEs), such as diabetes mellitus, thyroid dysfunction, hypophysitis, myocarditis, and hypokalemia (Boutros et al., 2016; Song et al., 2018b; Chiang et al., 2018; Eun et al., 2019). Nanomedicines can modulate pharmacological profiles of immunotherapeutic agents and integrate additional therapeutic modalities to enhance the antitumor immunity, while these critical concerns of cancer immunotherapy have not been addressed because of uncontrolled release of agents from nanoparticles (Caster et al., 2019; Lim et al., 2019).

Development of smart immunotherapeutic nanoagents with controlled activation is a promising strategy to improve the efficacy and safety of cancer immunotherapy (Li and Pu, 2020; Wang et al., 2021). Activatable immunotherapeutic nanoagents may be specifically responsive to endogenous stimuli in tumor microenvironment, such as lower pH, higher glutathione concentrations, higher reactive oxygen species (ROS) levels, increased expression levels of certain enzymes, and hypoxic conditions to achieve controlled antitumor immunity (Cheng et al., 2018; Im et al., 2018; Chen et al., 2019; Peng et al., 2019; Wang et al., 2019). However, these endogenous stimuli also exist in normal tissues, which often results in off-target immune activation for such immunotherapeutic nanoagents (Tang et al., 2018).

As an external stimulation, light has the advantages of noninvasiveness, good controllability, and high spatio-temporal selectivity, and thus has been widely utilized for photoactivation of therapeutic agents (Karimi et al., 2017). The photoactivatable agents can be formed via incorporating therapeutic molecules with light-sensitive moieties, while most of them only respond to ultraviolet and visible light (100–650 nm) that shows shallow tissue-penetration depth and high phototoxicity (Gnanasammandhan et al., 2016). By contrast, near-infrared (NIR) light (650–1,700 nm) has minimal photodamage and strong penetrating capability in biological tissues, and thus has been employed to regulate the pharmacological activities of immunotherapeutic agents with the development of NIR photoactivatable immunomodulatory nanoparticles (Lin et al., 2017). Moreover, NIR light can be used for photothermal therapy (PTT) and photodynamic therapy (PDT) of tumors in the presence of photothermal agents or photosensitizers, which will contribute to enhanced antitumor immunity (Tao et al., 2014; Yang et al., 2020). Thus, NIR photoactivatable immunomodulatory nanoparticles with controlled activity and multiple therapeutic actions have been developed for combinational immunotherapy of cancer.

We herein summarize recent progress of NIR photoactivatable immunomodulatory nanoparticles for combinational immunotherapy of cancer. Design principles and construction approaches of NIR photoactivatable immunomodulatory nanoparticles and their working mechanisms to achieve regional selectivity of immune activation are briefly summarized. The feasibility of such NIR photoactivatable immunomodulatory nanoparticles for PTT/PDT combinational immunotherapy to obtain an enhanced therapeutic efficacy and biosafety is highlighted with some discussions of their potential concerns. A general conclusion and discussion of existing challenges and further perspectives in this field are then given.

DESIGN OF NEAR-INFRARED PHOTOACTIVATABLE IMMUNOMODULATORY NANOPARTICLES

NIR light can be converted into local heat and singlet oxygen ($^1O_2$) by photothermal agents and photosensitizers, respectively, which will allow for on-demand release and/or activation of therapeutic agents (Li et al., 2019a; Li et al., 2019b; Uthaman et al., 2020). In view of the two different mechanisms, immunomodulatory nanoparticles with photothermal and photodynamic activatable pharmacological actions have been designed and constructed for PTT and PDT combinational immunotherapy.

Photothermal activatable immunomodulatory nanoparticles are generally formed via integrating thermal-responsive components into nanoparticles containing immunodrugs and photothermal agents. Upon NIR laser irradiation, photothermal agents generate local heat to destroy the thermal-responsive components for controlled release of immunotherapeutic agents from nanoparticles. As such, these photothermal activatable immunomodulatory nanoparticles can afford a synergetic action of PTT and immunotherapy. The fabrications of photodynamic activatable immunomodulatory nanoparticles rely on the uses of $^1O_2$-cleavable linkers to conjugate small molecular agents with photosensitizer-based nanoparticles. During PDT processes with NIR laser irradiation, $^1O_2$ is generated by photosensitizers to initiate the cleavage of $^1O_2$-cleavable linkers to liberate caged agents for *in-situ* activation. Such controlled activation of immunotherapeutic agents in combination with PDT will potentiate antitumor immunity.

PHOTOTHERMAL ACTIVATABLE IMMUNOMODULATORY NANOPARTICLES

Due to the generation of heat during PTT, thermal-responsive phase change materials have been widely used to construct photothermal drug delivery systems to achieve on-demand release of therapeutic agents (Bordat et al., 2019). As an example, Yang's group reported a phase-transformation nanoparticle to facilitate delivery of anti-PD1 antibody (aPD1) for PTT synergized immunotherapy of melanoma (Zhang et al., 2019). They encapsulated aPD1, iron oxide and perfluoropentane (PFP) into poly(lactic-co-glycolic acid) (PLGA) shell modified with PEG and Gly-Arg-Gly-Asp-Ser (GRGDS) peptides to form phase-transformation nanoparticles (GOP@aPD1). PFP is a type of phase change material that converts from liquid to gas after the temperature increase. Due to the enhanced permeability and retention (EPR) effect and active targeting of GRGDS peptides, GOP@aPD1 showed an effective accumulation at the

melanoma sites after systemic administration. Iron oxide nanoparticles acted as a photothermal agent to generate heat under 660 nm laser irradiation, which resulted in phase-transformation of PFP to destroy nanoparticles for controlled release of aPD1. Such synergistic action of PTT and aPD1-mediated immunotherapy achieved enhanced antitumor efficacy, greatly inhibiting the growth of B16F10 tumors. In view of their high biosafety and biocompatibility, GOP@aPD1 was promising for clinical translation, while the long-term biodegradation of iron oxide should be considered.

Thermo-responsive liposomes have shown a great promise for on-demand delivery of drugs for cancer therapy (Zhen et al., 2018; Dai et al., 2019). Jin and coworkers developed a thermo-responsive liposome containing indocyanine green (ICG) as the photothermal agents and polyinosinic:polycytidylic acid (poly I:C) as the immune stimulatory molecule for photothermal-immunotherapy (Xu et al., 2019). Due to the photothermal effect of ICG, NIR laser irradiation at 808 nm increased the temperature to destroy thermo-responsive liposome to release poly I:C. The PTT effect induced cancer cell death and ablation of tumors, and the released poly I:C promoted the maturation of dendritic cells (DCs), which synergistically triggered an antigen-specific immune response to prevent lung metastasis following intravenous injection of cancer cells. Most of the agents in such photothermal activatable immunomodulatory nanoparticles have been approved by FDA, which greatly promotes their clinical uses, while the photostability of ICG should be improved.

NIR photothermal activatable immunomodulatory nanoparticles have shown great promising for cancer immunotherapy, while the tissue penetration depth of first NIR light (NIR-I) was still limited (< 1 cm) (Mura et al., 2013; Jiang et al., 2020). In contrast, the second NIR (NIR-II) light had an increased tissue penetration depth as high as 3–5 cm, which allowed the construction of NIR-II photothermal activatable immunomodulatory nanoparticles (Lyu et al., 2019). As an example, Pu's group recently constructed a semiconducting polymer nanoadjuvant ($SPN_{II}R$) with NIR-II photothermally induced on-demand release of immune adjuvants for enhanced cancer immunotherapy (Li et al., 2020a). Semiconducting polymer-based nanoparticles can be used for molecular imaging, phototherapy, and photoregulation because of their good biocompatibility and unique optical property (Jiang and Pu, 2018). Such $SPN_{II}R$ with a core-shell structure contained three main components: a semiconducting polymer nanoparticle core as the NIR-II photothermal converter, a toll-like receptor (TLR) agonist (R848) as the immunotherapeutic adjuvant, and a thermally responsive lipid shell on the nanoparticle surface. The thermally responsive lipid shell was constructed using 1,2-dipalmitoyl-sn-glycero-3-phosphocholine (DPPC), a thermal phospholipid with a phase-transition temperature of 41°C, and an amphiphilic polymer, 1,2-distearoyl-sn-glycero-3-phosphoethanolamine-poly(ethylene glycol) (DSPE-PEG), and could be melted after a photothermal effect. $SPN_{II}R$ exhibited an effective accumulation into tumors after systemic administration, which may be due to their small size and surface PEG corona. Upon NIR-II photoactivation at 1,064 nm, $SPN_{II}R$ produced heat to induce tumor cell death and immunogenic cell death (ICD). Meanwhile, the generated heat could melt thermally responsive lipid shell for controlled release of R848 to active TLR7/TLR8, thereby promoting the maturation of DCs and priming of antitumor T cells. Via the synergetic action of NIR-II PTT and immunotherapy, the growth of both primary and distant tumors and lung metastasis in a 4T1 tumor-bearing BALB/c mouse model was effectively suppressed after a single treatment. Although these promising results, the stability of $SPN_{II}R$ in biological systems should be a concern since the phospholipid could be easily oxidized and hydrolyzed. In addition, the doping of imaging probes was required to monitor the accumulation of nanoparticles into tumors so that to optimize the therapeutic window.

In addition to thermally responsive phospholipid, thermo-responsive linker has been utilized to construct NIR-II photothermal activatable drug delivery nanosystems for cancer therapy (Lei et al., 2016). In a recent study of Pu's group, the authors reported a photothermally activatable polymeric pronanoagonist (APNA) with NIR-II light regulated activity for PTT combinational immunotherapy (Jiang et al., 2021). Within APNA, a NIR-II light-absorbing semiconducting polymer served as a photothermal transducer, which was conjugated with R848 through a thermo-responsive linker (**Figure 1A**). The APNA mediated photothermal effect under 1,064 nm laser irradiation, which not only led to direct photothermal ablation of tumors and elicitation of ICD of tumor cells, but also resulted in cleavage of the thermo-responsive linker to liberate caged R848 that converted into an intact form after a subsequent hydrolysis by esterase (**Figure 1B**). The maximal activation ratio of R848 was only 8.5% if the photothermal temperature was kept at 37°C under 1,064 nm laser irradiation, which was dramatically increased to 74% when the photothermal temperature was elevated to above 45°C. Such a photo-regulated immune activation could be achieved in primary tumors of 4T1 tumor-bearing mice at a depth of 8 mm, thereby enabling complete eradication of primary tumors and efficient inhibition of both distant tumors and lung and liver metastasis without causing obvious side effects. Moreover, the relationship between intratumoral immune activation and photothermal depth was unveiled. This work indeed provided a novel approach for remote spatiotemporal controlling of immune activation. A challenge was the complicated synthesis and fabrication processes that would limit the productivity of such immunomodulatory nanoparticles for clinical uses.

PHOTODYNAMIC ACTIVATABLE IMMUNOMODULATORY NANOPARTICLES

The generation of ROS in the PDT process allowed the construction of photodynamic activatable nanoparticles for cancer therapy (Yang et al., 2016; Pei et al., 2018; Uthaman et al., 2020). For example, Yang and Song's groups reported a black phosphorus quantum dots (BPQDs)-based NIR/ROS-responsive immunoadjuvant nanoparticles for cancer photodynamic immunotherapy (Li et al., 2020b). PEG and

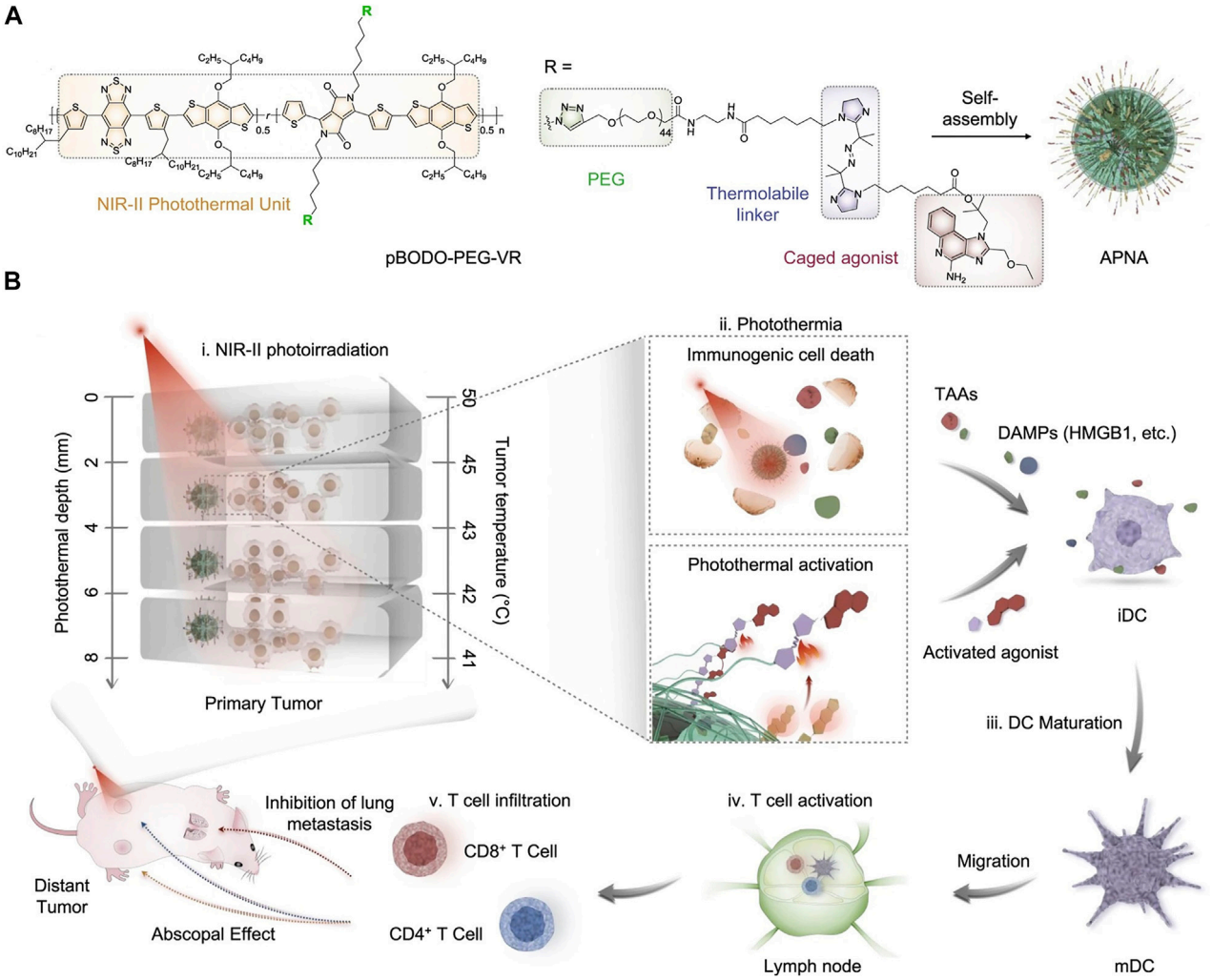

FIGURE 1 | (A) Chemical structure of NIR-II absorbing semiconducting polymer conjugated with R848 through a thermo-responsive linker and self-assembly of APNA. **(B)** Mechanism of antitumor immune response by APNA-mediated NIR-II photothermal immunotherapy. Reproduced, with permission, from Jiang et al. (2021). Copyright 2021, Nature Publishing Group.

ROS-responsive poly(propylene sulfide) (PPS) conjugated with pyrene were grafted onto BPQDs, which was used to encapsulate cytosine-phosphate-guanine oligodeoxynucleotides (CpG ODNs) as a potent adjuvant to form nanoparticles via self-assembly. As an agonist for TLR9, CpG ODNs greatly promote DC maturation, proinflammatory cytokine and chemokine secretion, leading to the activation of immunity (Scheiermann and Klinman, 2014). Upon 660 nm laser irradiation, BPQDs produced ROS to trigger the transformation of hydrophobic PPS to hydrophilic ones, which resulted in nanoparticle disassembly to release CPG ODNs in tumor microenvironment to enhance immunity and small sized BPQDs that could penetrate in deep tumors. As such, the synergistic PDT immunotherapy effectively inhibited the growth of 4T1 tumors and suppressed distant tumor growth and metastasis. In addition to antitumor effect, the on-demand dissociation of nanoparticles to release BPQDs increased tumor penetration for enhanced photoacoustic (PA) imaging, providing a stimuli-responsive nanoplatforms for cancer theranostics, which was much different from most of photoactivatable immunomodulatory nanoparticles.

Sun and coworkers recently reported a sorafenib and chlorin e6 (Ce6) co-loaded ROS-responsive nanoparticle to improve antitumor responses for PDT combinational immunotherapy (Sun et al., 2020). Sorafenib is a small molecular multi-kinase inhibitor that inhibits the functions of immunosuppressive cells in tumor microenvironment, resulting in augmented antitumor immunity via enhancing the activities of tumor-specific cytotoxic T cells (Chen et al., 2014). A ROS-responsive PEGylated hyperbranched polyphosphate containing $^1O_2$-cleavable thioketal linkers was utilized to simultaneously encapsulate Ce6 as a hydrophobic NIR photosensitizer and sorafenib, forming photodynamic activatable immunomodulatory nanoparticles. Under 660 nm laser irradiation, Ce6 generated

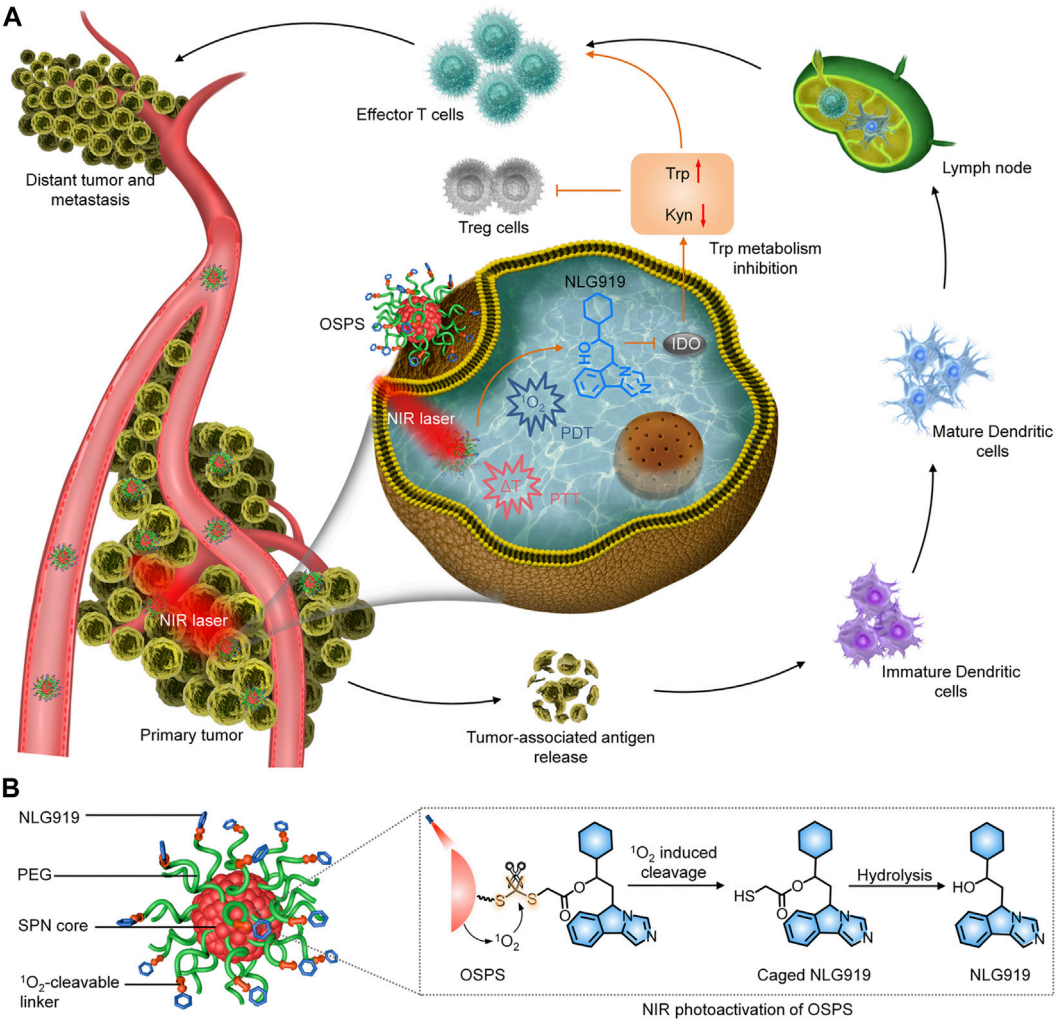

FIGURE 2 | (A) Photoactivation of OSPS for synergistic therapeutic action including phototherapy and checkpoint blockade immunotherapy. **(B)** Structure and NIR photoactivation mechanism of OSPS. Reproduced, with permission, from Li et al. (2019a). Copyright 2019, John Wiley & Sons Ltd.

$^1O_2$ to cleave the $^1O_2$-responsive linkers to destruct the nanoparticles, leading to on-demand release of sorafenib in tumor sites. After treatment in 4T1 tumor-bearing mice, the synergistical action of low-dose PDT and rapidly released sorafenib modulated the immunosuppressive tumor microenvironment to trigger a strong T cell-dependent antitumor immunity, suppressing the growth of primary and distant tumors. Although this was a promising way to achieve controlled release of drugs for amplified antitumor effects, the penetration depth of 660 nm laser was limited.

Li and coworkers developed an organic semiconducting pro-nanostimulant (OSPS) with a NIR photoactivatable immunotherapeutic action for cancer immunotherapy (**Figure 2A**) (Li et al., 2019c). OSPS was formed through conjugating a photodynamic semiconducting polymer with an indoleamine 2,3-dioxygenase (IDO) inhibitor (NLG919) via a $^1O_2$-responsive linker, followed by self-assembly. The overexpressed IDO enzyme by most cancers degraded the essential amino acid tryptophan (Trp) into kynurenine (Kyn), resulting in immunosuppressive tumor microenvironment (Feng et al., 2018). Owing to its small size and stealthy PEG surface corona, OSPS showed an effective accumulation in subcutaneous tumors after systemic administration, in which, OSPS produced heat and $^1O_2$ upon 808 nm laser irradiation for combinational PTT and PDT, and generation of tumor-associated antigens (TAAs). Meanwhile, the produced $^1O_2$ specifically triggered the cleavage of $^1O_2$-responsive linkers to release caged NLG919, which would undergo a rapid hydrolysis to generate active NLG919 (**Figure 2B**). Such a remote photoactivation of immunostimulants contributed to modulation of immunosuppressive tumor microenvironment, which in combination with OSPS-mediated phototherapy triggered a strong antitumor immune response. In a 4T1 tumor-bearing mouse model, a single treatment of OSPS could effectively inhibited the growth of both primary and distant tumors and prevented lung metastasis. If the drug loading capability can be

further improved, this photoactivatable organic pro-nanostimulants should have a promise for more effective and safer immunotherapy.

Using the $^1O_2$-responsive linker, Pu's group reported an organic polymer nanoenzyme (SPNK) with a NIR photoactivatable enzymatic activity for photodynamic immunometabolic therapy (Zeng et al., 2021). SPNK was constructed based on a semiconducting polymer nanoparticle as the photosensitizer, which was conjugated with kynureninase (KYNase) via PEG chain containing $^1O_2$-responsive linker. KYNase is an enzyme that catalyzes the degradation of immunosuppressive Kyn in IDO overexpressed tumors to reverse Kyn-induced immune suppression (Triplett et al., 2018). Such a photoactivation of nanoenzyme could significantly promote the proliferation and infiltration of effector T cells into B16F10 tumors in living mice, thus triggering an enhanced antitumor T cell immunity. As such, SPNK-mediated synergistic therapeutic action led to complete inhibition of primary tumors and effective suppression of distant tumors. This study provided a novel photodynamic approach for remote control of enzymatic activity to modulate immunometabolism for cancer immunotherapy. However, the synthesis conditions need to be strictly controlled to keep the activity of enzymes, and some strategies should be used to prevent degradation of enzymes by hydrolases during blood circulation.

The activation of abovementioned immunomodulatory nanoparticles relies on the generated $^1O_2$. As PDT can induces cell death, apoptosis-related biomarkers responsive nanoparticles have also been developed for cancer therapy. Zhang's group reported a peptide self-assembled nanoparticle for PDT combinational immunotherapy (Song et al., 2018a). The peptide consisted of palmitic acid and protoporphyrin IX (PpIX) as the hydrophobic part and a hydrophilic PEG conjugated with an IDO inhibitor 1-methyltryptophan (1MT) through a caspase-responsive peptide sequence, Asp-Glu-Val-Asp (DEVD). The peptide could self-assemble into nanoparticles that effectively accumulated into tumor tissues. Upon 630 nm laser irradiation, the peptide nanoparticles produced $^1O_2$ via PDT effect to induce apoptosis of cancer cells, leading to caspase-3 expression and formation of TAAs, which facilitated antitumor immune response. The expressed caspase-3 could cleave DEVD peptide sequence to release 1MT to further strengthen the immunity and activate $CD8^+$ T cells. Such synergistic effect of PDT and immunotherapy mediated by peptide nanoparticles effectively inhibited the growth of primary tumors and lung metastasis in a CT26 tumor-bearing mouse model. This study provided a unique strategy to regulate the delivery of immunotherapeutic agents with a very high efficacy, while the tissue penetration of light source needs to be further improved for their applications of large and deep-seated tumors.

Controlled antitumor immunity have been achieved by photodynamic activatable nanoparticles through regulating the activation of immunotherapeutic agents, while they still have some limitations. The endogenous ROS existed in the biological systems potentially results in off-target activation of drugs and thereby induces side effects. The biosafety of products for ROS-responsive moieties after photoactivation is questionable and needs to be systematically investigated. In addition, all existing photodynamic activatable nanoparticles only respond to visible or NIR-I light, and those that can be activated by NIR-II light have not been explored.

DISCUSSION

We herein have summarized the recent development of immunomodulatory nanoparticles with NIR photoactivatable pharmacological features for combinational immunotherapy of cancer. Due to the existences of photothermal agents or photosensitizers, these immunomodulatory nanoparticles can generate heat or ROS upon NIR photoirradiation to destroy thermal- or ROS-responsive moieties to allow on-demand release of immunotherapeutic agents, which greatly improve the bioavailability and selectivity. By combining with PTT and/or PDT, such NIR photoactivatable antitumor immunity often leads to improved therapeutic efficacy in treating tumors and preventing metastases.

Before the successful translation of NIR photoactivatable immunomodulatory nanoparticles for clinical trials, some key issues should be addressed. First, the long-term biosafety of nanoparticles in living bodies is questionable and should be systemically evaluated. Development of biodegradable or clearable nanoparticles is a good way to address this issue (Li and Pu, 2019). Second, the tissue penetration depths of NIR-I and NIR-II light are still limited and only suitable for superficial tumors. The use of light delivery technologies can achieve deep delivery of NIR light into biological tissues for treatment of deep-seated tumors (Maruoka et al., 2018). Third, it is challenging for real-time monitoring of dynamic immune activation to evaluate therapeutic efficacy. Imaging reporters that are specifically responsive to immune response can be combined with immunomodulatory nanoparticles to realize immune theranostics of cancer (He et al., 2020; Ramesh et al., 2020). In the future, these NIR photoactivatable immunomodulatory nanoparticles may show a great promise for clinical treatment of cancer and other diseases, such as infectious diseases and autoimmunity.

AUTHOR CONTRIBUTIONS

NY and MD write the original draft manuscript; JL review and edit the manuscript. All authors read and approved the final manuscript.

FUNDING

This study was supported by the Fundamental Research Funds for the Central Universities (2232021A-05) and Science and Technology Commission of Shanghai Municipality (20DZ2254900).

REFERENCES

Bordat, A., Boissenot, T., Nicolas, J., and Tsapis, N. (2019). Thermoresponsive Polymer Nanocarriers for Biomedical Applications. *Adv. Drug Deliv. Rev.* 138, 167–192. doi:10.1016/j.addr.2018.10.005

Boutros, C., Tarhini, A., Routier, E., Lambotte, O., Ladurie, F. L., Carbonnel, F., et al. (2016). Safety Profiles of Anti-CTLA-4 and Anti-PD-1 Antibodies Alone and in Combination. *Nat. Rev. Clin. Oncol.* 13, 473–486. doi:10.1038/nrclinonc.2016.58

Caster, J. M., Callaghan, C., Seyedin, S. N., Henderson, K., Sun, B., and Wang, A. Z. (2019). Optimizing Advances in Nanoparticle Delivery for Cancer Immunotherapy. *Adv. Drug Deliv. Rev.* 144, 3–15. doi:10.1016/j.addr.2019.07.009

Chen, M.-L., Yan, B.-S., Lu, W.-C., Chen, M.-H., Yu, S.-L., Yang, P.-C., et al. (2014). Sorafenib Relieves Cell-Intrinsic and Cell-Extrinsic Inhibitions of Effector T Cells in Tumor Microenvironment to Augment Antitumor Immunity. *Int. J. Cancer* 134, 319–331. doi:10.1002/ijc.28362

Chen, Q., Chen, G., Chen, J., Shen, J., Zhang, X., Wang, J., et al. (2019). Bioresponsive Protein Complex of aPD1 and aCD47 Antibodies for Enhanced Immunotherapy. *Nano Lett.* 19, 4879–4889. doi:10.1021/acs.nanolett.9b00584

Cheng, K., Ding, Y., Zhao, Y., Ye, S., Zhao, X., Zhang, Y., et al. (2018). Sequentially Responsive Therapeutic Peptide Assembling Nanoparticles for Dual-Targeted Cancer Immunotherapy. *Nano Lett.* 18, 3250–3258. doi:10.1021/acs.nanolett.8b01071

Chiang, C.-S., Lin, Y.-J., Lee, R., Lai, Y.-H., Cheng, H.-W., Hsieh, C.-H., et al. (2018). Combination of Fucoidan-Based Magnetic Nanoparticles and Immunomodulators Enhances Tumour-Localized Immunotherapy. *Nat. Nanotech* 13, 746–754. doi:10.1038/s41565-018-0146-7

Dai, Y., Su, J., Wu, K., Ma, W., Wang, B., Li, M., et al. (2019). Multifunctional Thermosensitive Liposomes Based on Natural Phase-Change Material: Near-Infrared Light-Triggered Drug Release and Multimodal Imaging-Guided Cancer Combination Therapy. *ACS Appl. Mater. Inter.* 11, 10540–10553. doi:10.1021/acsami.8b22748

Del Paggio, J. C. (2018). Cancer Immunotherapy and the Value of Cure. *Nat. Rev. Clin. Oncol.* 15, 268–270. doi:10.1038/nrclinonc.2018.27

Eun, Y., Kim, I. Y., Sun, J.-M., Lee, J., Cha, H.-S., Koh, E.-M., et al. (2019). Risk Factors for Immune-Related Adverse Events Associated with Anti-PD-1 Pembrolizumab. *Sci. Rep.* 9, 14039. doi:10.1038/s41598-019-50574-6

Feng, B., Zhou, F., Hou, B., Wang, D., Wang, T., Fu, Y., et al. (2018). Binary Cooperative Prodrug Nanoparticles Improve Immunotherapy by Synergistically Modulating Immune Tumor Microenvironment. *Adv. Mater.* 30, 1803001. doi:10.1002/adma.201803001

Fraietta, J. A., Lacey, S. F., Orlando, E. J., Pruteanu-Malinici, I., Gohil, M., Lundh, S., et al. (2018). Determinants of Response and Resistance to CD19 Chimeric Antigen Receptor (CAR) T Cell Therapy of Chronic Lymphocytic Leukemia. *Nat. Med.* 24, 563–571. doi:10.1038/s41591-018-0010-1

Gnanasammandhan, M. K., Idris, N. M., Bansal, A., Huang, K., and Zhang, Y. (2016). Near-IR Photoactivation Using Mesoporous Silica-Coated NaYF4: Yb,Er/Tm Upconversion Nanoparticles. *Nat. Protoc.* 11, 688–713. doi:10.1038/nprot.2016.035

He, S., Li, J., Lyu, Y., Huang, J., and Pu, K. (2020). Near-infrared Fluorescent Macromolecular Reporters for Real-Time Imaging and Urinalysis of Cancer Immunotherapy. *J. Am. Chem. Soc.* 142, 7075–7082. doi:10.1021/jacs.0c00659

Im, S., Lee, J., Park, D., Park, A., Kim, Y.-M., and Kim, W. J. (2018). Hypoxia-triggered Transforming Immunomodulator for Cancer Immunotherapy via Photodynamically Enhanced Antigen Presentation of Dendritic Cell. *ACS. Nano* 13, 476–488. doi:10.1021/acsnano.8b07045

Jiang, Y., Huang, J., Xu, C., and Pu, K. (2021). Activatable Polymer Nanoagonist for Second Near-Infrared Photothermal Immunotherapy of Cancer. *Nat. Commun.* 12, 1–14. doi:10.1038/s41467-021-21047-0

Jiang, Y., and Pu, K. (2018). Multimodal Biophotonics of Semiconducting Polymer Nanoparticles. *Acc. Chem. Res.* 51, 1840–1849. doi:10.1021/acs.accounts.8b00242

Jiang, Y., Zhao, X., Huang, J., Li, J., Upputuri, P. K., Sun, H., et al. (2020). Transformable Hybrid Semiconducting Polymer Nanozyme for Second Near-Infrared Photothermal Ferrotherapy. *Nat. Commun.* 11, 1857. doi:10.1038/s41467-020-15730-x

Karimi, M., Sahandi Zangabad, P., Baghaee-Ravari, S., Ghazadeh, M., Mirshekari, H., and Hamblin, M. R. (2017). Smart Nanostructures for Cargo Delivery: Uncaging and Activating by Light. *J. Am. Chem. Soc.* 139, 4584–4610. doi:10.1021/jacs.6b08313

Kuai, R., Ochyl, L. J., Bahjat, K. S., Schwendeman, A., and Moon, J. J. (2017). Designer Vaccine Nanodiscs for Personalized Cancer Immunotherapy. *Nat. Mater* 16, 489–496. doi:10.1038/nmat4822

Lei, Q., Qiu, W.-X., Hu, J.-J., Cao, P.-X., Zhu, C.-H., Cheng, H., et al. (2016). Multifunctional Mesoporous Silica Nanoparticles with thermal-responsive Gatekeeper for NIR Light-Triggered Chemo/photothermal-Therapy. *Small* 12, 4286–4298. doi:10.1002/smll.201601137

Li, J., Cui, D., Huang, J., He, S., Yang, Z., Zhang, Y., et al. (2019a). Organic Semiconducting Pro-nanostimulants for Near-Infrared Photoactivatable Cancer Immunotherapy. *Angew. Chem. Int. Ed.* 58, 12680–12687. doi:10.1002/anie.201906288

Li, J., Cui, D., Jiang, Y., Huang, J., Cheng, P., and Pu, K. (2019b). Near-Infrared Photoactivatable Semiconducting Polymer Nanoblockaders for Metastasis-Inhibited Combination Cancer Therapy. *Adv. Mater.* 31, 1905091. doi:10.1002/adma.201905091

Li, J., Luo, Y., and Pu, K. (2021). Electromagnetic Nanomedicines for Combinational Cancer Immunotherapy. *Angew. Chem. Int. Ed.* doi:10.1002/anie.202008386

Li, J., and Pu, K. (2019). Development of Organic Semiconducting Materials for Deep-Tissue Optical Imaging, Phototherapy and Photoactivation. *Chem. Soc. Rev.* 48, 38–71. doi:10.1039/c8cs00001h

Li, J., and Pu, K. (2020). Semiconducting Polymer Nanomaterials as Near-Infrared Photoactivatable Protherapeutics for Cancer. *Acc. Chem. Res.* 53, 752–762. doi:10.1021/acs.accounts.9b00569

Li, J., Yu, X., Jiang, Y., He, S., Zhang, Y., Luo, Y., et al. (2020a). Second Near-Infrared Photothermal Semiconducting Polymer Nanoadjuvant for Enhanced Cancer Immunotherapy. *Adv. Mater.* 33, 2003458. doi:10.1002/adma.202003458

Li, Y., Hu, J., Liu, X., Liu, Y., Lv, S., Dang, J., et al. (2019c). Photodynamic Therapy-Triggered On-Demand Drug Release from ROS-Responsive Core-Cross-Linked Micelles toward Synergistic Anti-cancer Treatment. *Nano Res.* 12, 999–1008. doi:10.1007/s12274-019-2330-y

Li, Z., Hu, Y., Fu, Q., Liu, Y., Wang, J., Song, J., et al. (2020b). NIR/ROS-Responsive Black Phosphorus QD Vesicles as Immunoadjuvant Carrier for Specific Cancer Photodynamic Immunotherapy. *Adv. Funct. Mater.* 30, 1905758. doi:10.1002/adfm.201905758

Lim, S., Park, J., Shim, M. K., Um, W., Yoon, H. Y., Ryu, J. H., et al. (2019). Recent Advances and Challenges of Repurposing Nanoparticle-Based Drug Delivery Systems to Enhance Cancer Immunotherapy. *Theranostics* 9, 7906–7923. doi:10.7150/thno.38425

Lin, H., Gao, S., Dai, C., Chen, Y., and Shi, J. (2017). A Two-Dimensional Biodegradable Niobium Carbide (MXene) for Photothermal Tumor Eradication in NIR-I and NIR-II Biowindows. *J. Am. Chem. Soc.* 139, 16235–16247. doi:10.1021/jacs.7b07818

Lyu, Y., Li, J., and Pu, K. (2019). Second Near-Infrared Absorbing Agents for Photoacoustic Imaging and Photothermal Therapy. *Small Methods* 3, 1900553. doi:10.1002/smtd.201900553

Maruoka, Y., Nagaya, T., Sato, K., Ogata, F., Okuyama, S., Choyke, P. L., et al. (2018). Near Infrared Photoimmunotherapy with Combined Exposure of External and Interstitial Light Sources. *Mol. Pharmaceutics* 15, 3634–3641. doi:10.1021/acs.molpharmaceut.8b00002

Mura, S., Nicolas, J., and Couvreur, P. (2013). Stimuli-responsive Nanocarriers for Drug Delivery. *Nat. Mater* 12, 991–1003. doi:10.1038/nmat3776

Nam, J., Son, S., Park, K. S., Zou, W., Shea, L. D., and Moon, J. J. (2019). Cancer Nanomedicine for Combination Cancer Immunotherapy. *Nat. Rev. Mater.* 4, 398–414. doi:10.1038/s41578-019-0108-1

Pardoll, D. M. (2012). The Blockade of Immune Checkpoints in Cancer Immunotherapy. *Nat. Rev. Cancer* 12, 252–264. doi:10.1038/nrc3239

Pei, Q., Hu, X., Zheng, X., Liu, S., Li, Y., Jing, X., et al. (2018). Light-activatable Red Blood Cell Membrane-Camouflaged Dimeric Prodrug Nanoparticles for Synergistic Photodynamic/chemotherapy. *ACS. Nano* 12, 1630–1641. doi:10.1021/acsnano.7b08219

Peng, J., Yang, Q., Xiao, Y., Shi, K., Liu, Q., Hao, Y., et al. (2019). Tumor Microenvironment Responsive Drug-Dye-Peptide Nanoassembly for Enhanced Tumor-Targeting, Penetration, and Photo-Chemo-Immunotherapy. *Adv. Funct. Mater.* 29, 1900004. doi:10.1002/adfm.201900004

Ramesh, A., Kumar, S., Brouillard, A., Nandi, D., and Kulkarni, A. (2020). A Nitric Oxide (NO) Nanoreporter for Noninvasive Real-Time Imaging of Macrophage Immunotherapy. *Adv. Mater.* 32, 2000648. doi:10.1002/adma.202000648

Scheiermann, J., and Klinman, D. M. (2014). Clinical Evaluation of CpG Oligonucleotides as Adjuvants for Vaccines Targeting Infectious Diseases and Cancer. *Vaccine* 32, 6377–6389. doi:10.1016/j.vaccine.2014.06.065

Song, W., Kuang, J., Li, C.-X., Zhang, M., Zheng, D., Zeng, X., et al. (2018a). Enhanced Immunotherapy Based on Photodynamic Therapy for Both Primary and Lung Metastasis Tumor Eradication. *ACS. Nano* 12, 1978–1989. doi:10.1021/acsnano.7b09112

Song, W., Shen, L., Wang, Y., Liu, Q., Goodwin, T. J., Li, J., et al. (2018b). Synergistic and Low Adverse Effect Cancer Immunotherapy by Immunogenic Chemotherapy and Locally Expressed PD-L1 Trap. *Nat. Commun.* 9, 2237. doi:10.1038/s41467-018-04605-x

Sun, X., Cao, Z., Mao, K., Wu, C., Chen, H., Wang, J., et al. (2020). Photodynamic Therapy Produces Enhanced Efficacy of Antitumor Immunotherapy by Simultaneously Inducing Intratumoral Release of Sorafenib. *Biomaterials* 240, 119845. doi:10.1016/j.biomaterials.2020.119845

Tang, Y., Li, Y., Hu, X., Zhao, H., Ji, Y., Chen, L., et al. (2018). "Dual Lock-And-Key"-Controlled Nanoprobes for Ultrahigh Specific Fluorescence Imaging in the Second Near-Infrared Window. *Adv. Mater.* 30, 1801140. doi:10.1002/adma.201801140

Tao, Y., Ju, E., Liu, Z., Dong, K., Ren, J., and Qu, X. (2014). Engineered, Self-Assembled Near-Infrared Photothermal Agents for Combined Tumor Immunotherapy and Chemo-Photothermal Therapy. *Biomaterials* 35, 6646–6656. doi:10.1016/j.biomaterials.2014.04.073

Triplett, T. A., Garrison, K. C., Marshall, N., Donkor, M., Blazeck, J., Lamb, C., et al. (2018). Reversal of Indoleamine 2,3-Dioxygenase-Mediated Cancer Immune Suppression by Systemic Kynurenine Depletion with a Therapeutic Enzyme. *Nat. Biotechnol.* 36, 758–764. doi:10.1038/nbt.4180

Uthaman, S., Pillarisetti, S., Mathew, A. P., Kim, Y., Bae, W. K., Huh, K. M., et al. (2020). Long Circulating Photoactivable Nanomicelles with Tumor Localized Activation and ROS Triggered Self-Accelerating Drug Release for Enhanced Locoregional Chemo-Photodynamic Therapy. *Biomaterials* 232, 119702. doi:10.1016/j.biomaterials.2019.119702

Wang, H., Han, X., Dong, Z., Xu, J., Wang, J., and Liu, Z. (2019). Hyaluronidase with pH-responsive Dextran Modification as an Adjuvant Nanomedicine for Enhanced Photodynamic-Immunotherapy of Cancer. *Adv. Funct. Mater.* 29, 1902440. doi:10.1002/adfm.201902440

Wang, W., Jin, Y., Liu, X., Chen, F., Zheng, X., Liu, T., et al. (2021). Endogenous Stimuli-Activatable Nanomedicine for Immune Theranostics for Cancer. *Adv. Funct. Mater.* 31, 2100386. doi:10.1002/adfm.202100386

Xu, L., Zhang, W., Park, H.-B., Kwak, M., Oh, J., Lee, P. C., et al. (2019). Indocyanine green and Poly I: C Containing Thermo-Responsive Liposomes Used in Immune-Photothermal Therapy Prevent Cancer Growth and Metastasis. *J. Immunotherap. Cancer* 7, 1–14. doi:10.1186/s40425-019-0702-1

Yang, C., Fu, Y., Huang, C., Hu, D., Zhou, K., Hao, Y., et al. (2020). Chlorin e6 and CRISPR-Cas9 dual-loading system with deep penetration for a synergistic tumoral photodynamic-immunotherapy. *Biomaterials* 255, 120194. doi:10.1016/j.biomaterials.2020.120194

Yang, G., Sun, X., Liu, J., Feng, L., and Liu, Z. (2016). Light-responsive, Singlet-Oxygen-Triggered On-Demand Drug Release from Photosensitizer-Doped Mesoporous Silica Nanorods for Cancer Combination Therapy. *Adv. Funct. Mater.* 26, 4722–4732. doi:10.1002/adfm.201600722

Zeng, Z., Zhang, C., Li, J., Cui, D., Jiang, Y., and Pu, K. (2021). Activatable Polymer Nanoenzymes for Photodynamic Immunometabolic Cancer Therapy. *Adv. Mater.* 33, 2007247. doi:10.1002/adma.202007247

Zhang, C., and Pu, K. (2020). Molecular and Nanoengineering Approaches towards Activatable Cancer Immunotherapy. *Chem. Soc. Rev.* 49, 4234–4253. doi:10.1039/c9cs00773c

Zhang, N., Song, J., Liu, Y., Liu, M., Zhang, L., Sheng, D., et al. (2019). Photothermal Therapy Mediated by Phase-Transformation Nanoparticles Facilitates Delivery of Anti-PD1 Antibody and Synergizes with Antitumor Immunotherapy for Melanoma. *J. Controlled Release* 306, 15–28. doi:10.1016/j.jconrel.2019.05.036

Zhen, X., Xie, C., Jiang, Y., Ai, X., Xing, B., and Pu, K. (2018). Semiconducting Photothermal Nanoagonist for Remote-Controlled Specific Cancer Therapy. *Nano Lett.* 18, 1498–1505. doi:10.1021/acs.nanolett.7b05292

Conflict of Interest: The authors declare that the research was conducted in the absence of any commercial or financial relationships that could be construed as a potential conflict of interest.

The reviewer CX declared a past co-authorship with one of the authors JL to the handling Editor.

frontiers in Chemistry

ORIGINAL RESEARCH
published: 29 July 2021
doi: 10.3389/fchem.2021.736468

Enzyme-Loaded pH-Sensitive Photothermal Hydrogels for Mild-temperature-mediated Combinational Cancer Therapy

Jindong Xia[1†], Xueqin Qing[2†], Junjian Shen[3†], Mengbin Ding[4], Yue Wang[1], Ningyue Yu[4], Jingchao Li[4] and Xiuhui Wang[5]**

[1]Department of Radiology, Shanghai Songjiang District Central Hospital, Shanghai, China, [2]Department of Pediatrics, Shanghai General Hospital, Shanghai Jiao Tong University, School of Medicine, Shanghai, China, [3]Department of Radiology, The First Affiliated Hospital of Bengbu Medical College, Bengbu, China, [4]Shanghai Engineering Research Center of Nano-Biomaterials and Regenerative Medicine, College of Chemistry, Chemical Engineering and Biotechnology, Donghua University, Shanghai, China, [5]Institute of Translational Medicine, Shanghai University, Shanghai, China

OPEN ACCESS

Edited by:
Houjuan Zhu,
Institute of Materials Research and Engineering (A*STAR), Singapore

Reviewed by:
Xijian Liu,
Shanghai University of Engineering Sciences, China
Ming Zhao,
Massachusetts Institute of Technology, United States

***Correspondence:**
Jingchao Li
jcli@dhu.edu.cn
Xiuhui Wang
wxh200801@163.com

[†]These authors contributed equally to this work.

Specialty section:
This article was submitted to Nanoscience, a section of the journal Frontiers in Chemistry

Received: 05 July 2021
Accepted: 20 July 2021
Published: 29 July 2021

Citation:
Xia J, Qing X, Shen J, Ding M, Wang Y, Yu N, Li J and Wang X (2021) Enzyme-Loaded pH-Sensitive Photothermal Hydrogels for Mild-temperature-mediated Combinational Cancer Therapy. Front. Chem. 9:736468. doi: 10.3389/fchem.2021.736468

Photothermal therapy (PTT) that utilizes hyperthermia to ablate cancer cells is a promising approach for cancer therapy, while the generated high temperature may lead to damage of surrounding normal tissues and inflammation. We herein report the construction of glucose oxidase (GOx)-loaded hydrogels with a pH-sensitive photothermal conversion property for combinational cancer therapy at mild-temperature. The hydrogels (defined as CAG) were formed *via* coordination of alginate solution containing pH-sensitive charge-transfer nanoparticles (CTNs) as the second near-infrared (NIR-II) photothermal agents and GOx. In the tumor sites, GOx was gradually released from CAG to consume glucose for tumor starvation and aggravate acidity in tumor microenvironment that could turn on the NIR-II photothermal conversion property of CTNs. Meanwhile, the released GOx could suppress the expression of heat shock proteins to enable mild NIR-II PTT under 1,064 nm laser irradiation. As such, CAG mediated a combinational action of mild NIR-II PTT and starvation therapy, not only greatly inhibiting the growth of subcutaneously implanted tumors in a breast cancer murine model, but also completely preventing lung metastasis. This study thus provides an enzyme loaded hydrogel platform with a pH-sensitive photothermal effect for mild-temperature-mediated combinational cancer therapy.

Keywords: hydrogels, photothermal therapy, starvation therapy, second near-infrared light, tumor metastasis, cancer therapy

INTRODUCTION

Photothermal therapy (PTT) that utilizes photoconversion to produce heat for tumor ablation has been explored as a non-invasive therapeutic strategy for cancer (Cheng et al., 2017; Jung et al., 2018; Zhao et al., 2018). In view of the high spatiotemporal controllability of light, PTT has the advantages of high treatment specificity and minimal side effects, which is different from conventional therapeutic strategies such as radiotherapy and chemotherapy (Liu et al., 2011; Ju et al., 2015; Li and Pu, 2019; 2020). High temperature (>50°C) is usually required to induce complete tumor cell death during PTT, which potentially results in damage of surrounding normal tissues and inflammation (Zhu et al., 2016; Yang et al., 2017; Gao et al., 2019). Therefore, mild PTT

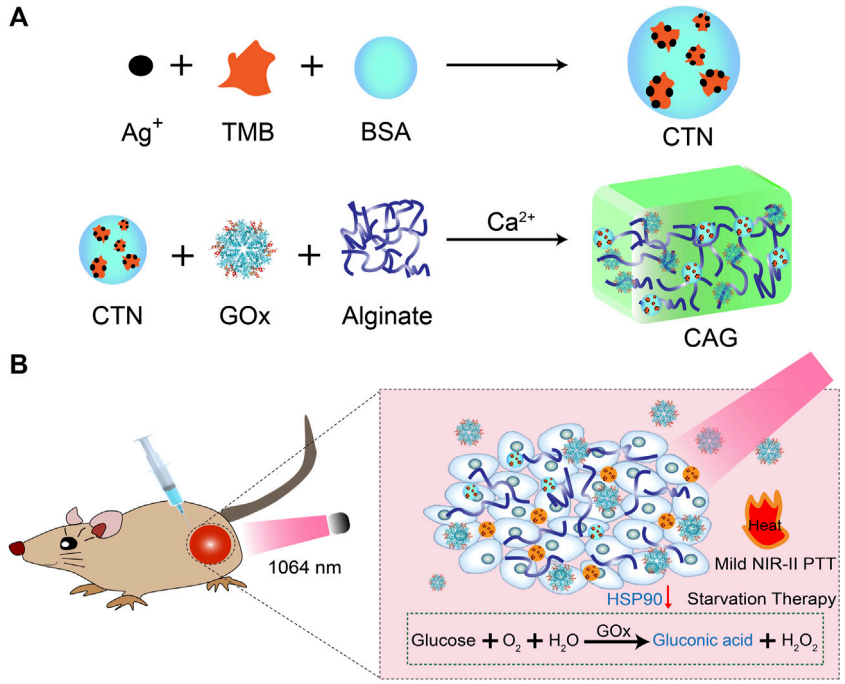

FIGURE 1 | Design and fabrication of CAG hydrogels for mild-temperature-mediated NIR-II PTT and starvation combinational therapy. **(A)** Schematic illustration of the preparation of CAG hydrogels. **(B)** Schematic illustration of working mechanism of CAG hydrogels for mild-temperature-mediated NIR-II PTT and starvation combinational therapy.

strategies at a low therapeutic temperature have attracted a great attention (Zhou et al., 2018; Ding et al., 2020; Yuan et al., 2020). However, the therapeutic efficacy of mild PTT is often compromised by the upregulated expression of heat shock proteins (HSPs) that are associated with hyperthermia-induced cell damage (Ali et al., 2016; Wang et al., 2016; Wang et al., 2017). To overcome heat resistance of cancer cells, HSP inhibitors have been used to amplify the effect of mild PTT (Tang et al., 2018). Most of existing mild PTT strategies are relied on the first near-infrared (NIR) light (NIR-I, 650–950 nm) that shows too shallow tissue penetration depth to deliver sufficient heating to the internal regions of solid tumors (Gao et al., 2021). Compared to NIR-I light, the second near-infrared (NIR-II) light (1,000–1700 nm) has greatly improved penetrating capability in biological tissues (Li et al., 2021; Luo et al., 2021; Wang et al., 2021). In this regard, it is highly desired to develop mild NIR-II PTT for tumor ablation with high safety and efficacy.

Starvation therapy that blocks the energy metabolism of cancer cells has emerged as an effective therapeutic strategy for cancer (Guo and Kohane, 2017; Zhang et al., 2017; Zhang et al., 2019). To date, some strategies such as vascular embolization, inhibition of glucose transporter, and direct intratumoral glucose consumption have been adopted to starve cancer cells (Butler et al., 2013; Liu et al., 2017; Cheng et al., 2019; Tang et al., 2021). Among them, glucose oxidase (GOx)-based starvation therapy *via* catalyzing the oxidation of glucose in tumor cells has achieved remarkable efficacy in inhibiting tumor growth (Dinda et al., 2018; Fu et al., 2018; Ranji-Burachaloo et al., 2019). However, this therapeutic model often encounters the issues of low therapeutic benefits and potential systemic toxicity (Ren et al., 2020). In addition, GOx-mediated tumor starvation can downregulate the expressions of HSPs due to the blocking of energy supply, which will contribute to enhanced PTT efficacy (Wang et al., 2012; Chen et al., 2017; Cao et al., 2020). The combination of PTT and starvation therapy has been adopted to treat tumors, which indeed achieves high antitumor efficacy with the neglect of side effects (Hu et al., 2019; Gao et al., 2020; Wang et al., 2020; He et al., 2021). Therefore, it is still highly desired to explore new strategies that integrate PTT and starvation therapy with combinational action for cancer treatment with high efficacy and safety.

In this study, we report a GOx-loaded alginate hydrogel with pH-sensitive NIR-II photothermal effect for treatment of solid tumors *via* combinational action at mild-temperature (**Figure 1A**). Alginate is used as matrix to construct hydrogels because of its excellent biocompatibility and degradability (Lee and Mooney, 2012). Alginate hydrogels have unique properties of good gelling capacity, low toxicity, excellent injectability, and low cost, and thus have been used for drug delivery, cancer therapy, molecular imaging and tissue engineering (Ouyang et al., 2019; Hernández-González et al., 2020; Johnson et al., 2020; Patrick et al., 2020). The CAG hydrogels containing pH-sensitive charge-transfer nanoparticles (CTNs) as the NIR-II photothermal agents and GOx as the starvation therapeutic agents can be locally formed *via* Ca^{2+} coordination in tumor tissues (Wang et al., 2019; Liu et al., 2021). Glucose was consumed to enable starvation therapy because of gradual release of GOx from CAG hydrogels,

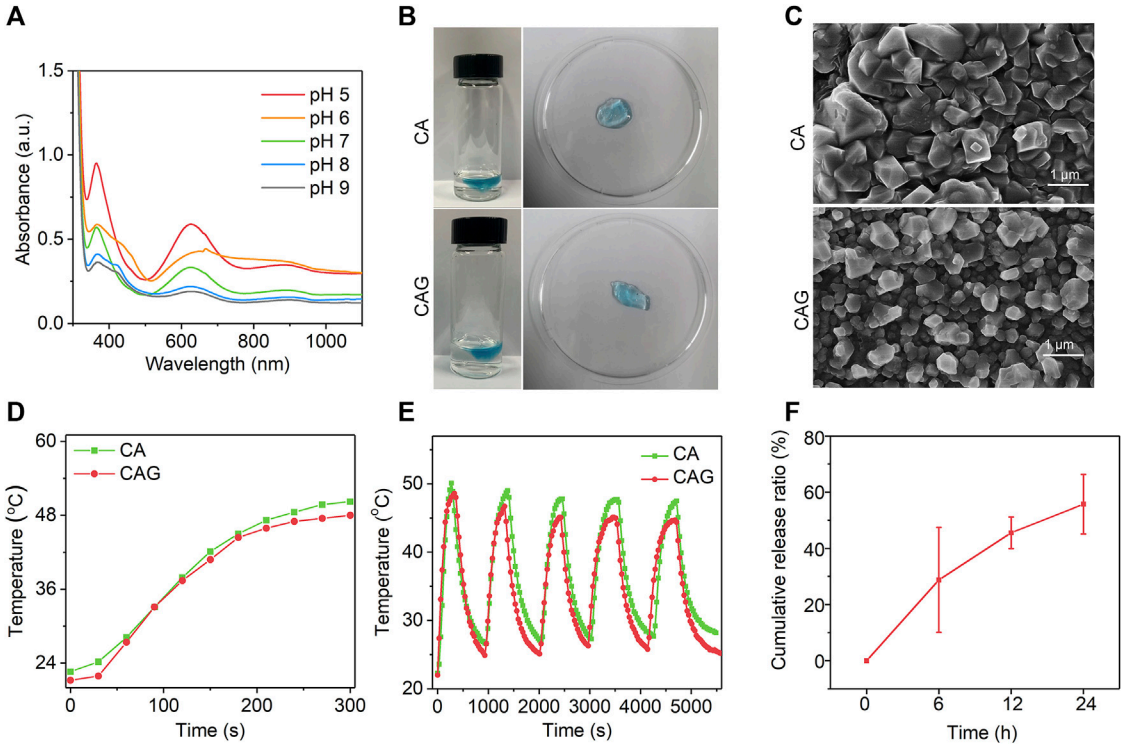

FIGURE 2 | Characterization of CAG hydrogels. **(A)** UV-vis absorption spectra of CTN at different pH conditions. **(B)** Representative SEM images of CA and CAG hydrogels. **(C)** Photographs of CA and CAG hydrogels after injecting alginate solution (5 mg/ml) containing CTN or CTN and GOx into aqueous solution at the Ca^{2+} concentration of 1.8 mM. **(D)** Temperature changes of aqueous solution containing CA or CAG under 1,064 nm laser irradiation at the powder density of 1 W/cm^2 for different time. **(E)** Evaluation of photothermal stability of CA and CAG hydrogels after five cycles of laser on/off. **(F)** Release profile of GOx from CAG hydrogels after incubation at 37°C for different time.

which also led to aggravated acidity in tumor microenvironment and inhibited expression of HSP90. As such, NIR-II PTT effect of CTNs was activated to mediate effective tumor ablation at a low temperature. Therefore, CAG-mediated combinational action of mild NIR-II PTT and starvation therapy afforded much higher therapeutic efficacy relative to sole treatment (**Figure 1B**). Such treatment could not only significantly suppress the growth of subcutaneous 4T1 tumors in living mice, but also completely prevent lung metastasis.

MATERIALS AND METHODS

Materials and Reagents

Bovine serum albumin (BSA), 3,3′,5,5′-tetramethylbenzidine (TMB), silver nitrate ($AgNO_3$) and GOx were purchased from Sigma-Aldrich (St. Louis, United States). Anhydrous $CaCl_2$ and sodium alginate were purchased from Aladdin Reagent Co. Ltd. (Shanghai, China). Cell counting kit-8 (CCK-8) and calcein-AM and propidium iodide apoptosis detection kit were purchased from Dojindo Laboratories (Kumamoto, Japan) and Dalian Meilun Biotech Co. Ltd. (Dalian, China), respectively. RPMI 1640 cell culture medium, fetal bovine serum (FBS), and penicillin-streptomycin were obtained from Gibco (Grand Island, NY, United States). TdT-mediated dUTP-biotin nick end labeling (TUNEL) kit was obtained from Roche (Sweden). Ultrapure water used in this study was prepared *via* a water purification system (PALL Cascada, MI, United States).

Synthesis of Charge-Transfer Nanoparticles

To synthesize pH-sensitive CTNs, 4.8 mg TMB dissolved in anhydrous ethanol was added into 2 ml solution containing 1.7 mg $AgNO_3$ and 3.4 mg BSA under ultrasonic oscillation at room temperature for 30 min. The products were purified by dialysis using a dialysis bag (molecular weight cut-off = 3 kDa) for 4 days to obtain CTNs.

Synthesis of CAG Hydrogels

To synthesize CAG hydrogels, 1 mg GOx and 200 mg sodium alginate were co-dissolved in 15 ml phosphate buffer saline (PBS) and then mixed with CTNs at a final concentration of 20 mg/ml. The mixed solution was then injected into 12 ml Ca^{2+} solution (1.8 mM) in a crystal bottle, forming CAG hydrogels. Similarly, CA hydrogels without GOx loading were synthesized *via* injecting CTN solution into 12 ml Ca^{2+} solution (1.8 mM) and the formed CA hydrogels were used as control.

Characterization Techniques

Dynamic light scattering (DLS) and zeta potential measurements of CTNs were used a Zetasizer Nano-series (Nano-ZS90, Malvern, United Kingdom). UV-vis-NIR absorption spectra of CTNs at different pH conditions were recorded on a Persee spectrophotometer (TU-1810, Beijing, China). Scanning electron microscopy (SEM) images of formed hydrogels were observed using a SEM (SU8010, HITACHI, Tokyo, Japan).

Photothermal Effect Evaluation

The photothermal properties of CA and CAG hydrogels were evaluated by exposing samples under 1,064 nm laser at the power density of 1 W/cm^2 for different time. In a typical experiment, the mixture of 20 μl CTN (0.96 mg/ml), 50 μL alginate (10 mg/ml) and 1 μl GOx (1 mg/ml) was added in a 96-well plate containing 30 μl Ca^{2+} aqueous solution. The temperature of mixed solution under laser irradiation was recorded using a Fotric 220s photothermal camera. Furthermore, the photothermal stability of hydrogels was investigated by turning on/off the laser for five cycles.

Evaluation of Glucose Oxidase Release From Hydrogels

CAG hydrogels were prepared as above described, and the formed CAG hydrogels were put in 5 ml PBS solution under shaking at 37°C. After incubation for different time, supernatant was collected and then centrifugated for absorption measurement to confirm the release of GOx.

In vitro Cell Apoptosis Analysis

To evaluate the *in vitro* therapeutic efficacy of hydrogels, cell apoptosis analysis was conducted. 4T1 cancer cells were seeded in 6-well plates (1×10^5 cells/well) and incubated at 37°C for 24 h. Then the cells were treated with PBS, CA, or CAG hydrogels for 24 h, followed by 1,064 nm laser irradiation at the power density of 1 W/cm^2 for 15 min. After culture for 12 h, the cells were incubated in cell culture medium containing calcein-AM/PI mixed solution for another 30 min. Fluorescence images of stained cells were captured using a fluorescence microscope (Leica DMi8, Germany). The green and red fluorescence area ratios were quantified using ImageJ software. For CCK-8 assay, 4T1 cancer cells were seeded in 96-well plates (1×10^4 cells/well) and incubated at 37°C for 24 h. Then the cells were treated with PBS, CA, or CAG at different CTN concentration for 24 h. The treated cells were irradiated by 1,064 nm laser (1 W/cm^2) for 5 min. The cells without laser irradiation were used as the control. After laser irradiation, the cells were cultured for 12 h, and then the cell culture medium was carefully removed and fresh medium containing CCK-8 agent was added into each well. After culture for another 2 h, the absorbance of each well at 450 nm was measured using a Bio-Tek ELX800 spectrophotometric microplate reader (Vermont, America). The absorbance was used to calculate the cell viability.

In vivo Evaluation of HSP90 Expression During Photothermal Therapy

The animal procedures were approved by the Animal Care and Use Committee of Donghua University. Male 4–6 week-old BALB/c nude mice (~20 g) were purchased from Shanghai SLAC Laboratory Animal Co., Ltd. 4T1 tumor-bearing mice were established by subcutaneously injecting 4T1 cancer cells (2×10^6 cells/mouse) into the right flank of each mouse. The 4T1 tumor-bearing nude mice were randomly divided into six groups when the tumor volume reached ~100 mm^3. The tumors were treated with PBS, CA, or CAG for 12 h, and then exposed under 1,064 nm laser irradiation (1 W/cm^2) for 10 min in a discontinuous manner. The temperature of tumor sites during laser irradiation was monitored using an IR thermal camera and controlled to be lower than 45°C. After treatment for 1 day, the mice were euthanized, and tumors were collected and used for immunofluorescent staining of HSP90. The fluorescence staining images of tumor sections were captured using a fluorescence microscope (Leica DMi8, Germany). The mean fluorescence intensity (MFI) of HSP90 staining was quantified using the ImageJ software.

In vivo Antitumor Efficacy Evaluation

The 4T1 tumor-bearing nude mice were treated with PBS, CA, or CAG without or with 1,064 nm laser irradiation (1 W/cm^2) for 10 min in a discontinuous manner to control tumor temperature below 45°C. After different treatments, a caliper was used to measure the tumor sizes every 2 days for 20 days. Tumor volumes were calculated as follows: volume = (length) × (width)^2/2, and relative tumor volume was calculated as V/V_0 (V_0 was the initial tumor volume). After treatments for 20 days, the mice were euthanized, and the tumors were extracted and weighed to evaluate tumor inhibition ratios. The tumors were collected for hematoxylin and eosin (H&E) and immunohistochemical TUNEL and Ki67 staining.

In vivo Anti-metastasis Efficacy Evaluation

After different treatments for 20 days, *in vivo* anti-metastasis efficacy was evaluated. The treated mice were intraperitoneally injected with 0.15 ml D-luciferin (20 mg/ml) and the peritoneum was opened to expose lungs. The lungs were then used for bioluminescence imaging using *in vivo* imaging system (VISQUE Invivo Smart-LF, Vieworks, Korea). Bioluminescence intensities of lungs were quantified using a Living Image software. To further assess the anti-metastasis efficacy of different treatments, the lungs were collected and washed with PBS, and the numbers of metastatic tumor nodes were counted. The collected lungs were then used for H&E staining to observe tumor metastasis.

In vivo Biocompatibility Evaluation

After different treatments, the body weights of 4T1 tumor-bearing nude mice were measured every 2 days for 20 days to evaluate the *in vivo* biocompatibility. After treatments for 20 days, the mice were euthanized and heart, liver, spleen, and kidney were collected and used for H&E staining.

Statistical Analysis

The significant difference between the experimental statistics is analyzed by One-way ANOVA and Tukey's multiple comparison tests. When the *p*-values were <0.05, the values were statistically regarded to be significantly different. $p < 0.05$ was indicated by (*), $p < 0.01$ by (**) and $p < 0.001$ by (***).

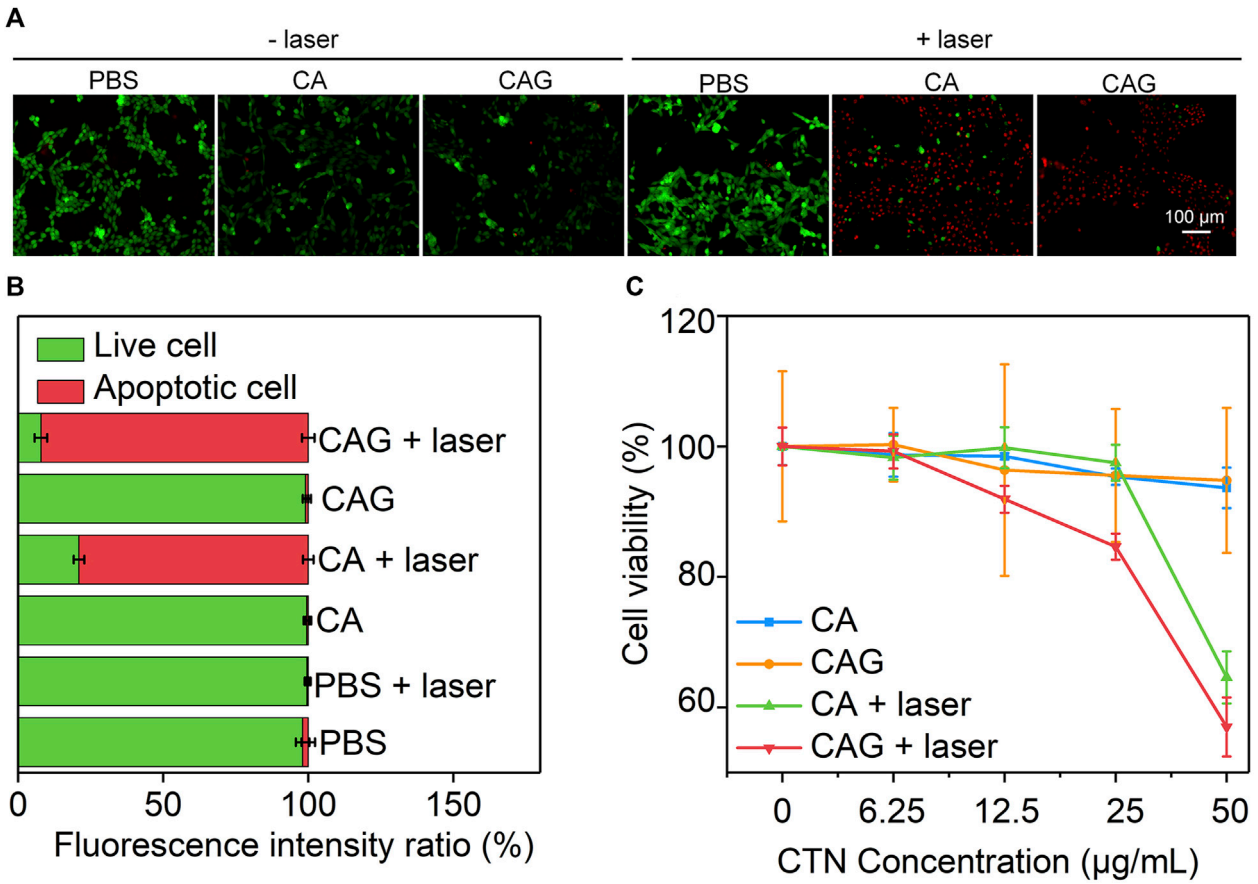

FIGURE 3 | Evaluation of *in vitro* therapeutic efficacy of hydrogels. **(A)** Fluorescence images of live (green) and dead (red) 4T1 cancer cells after incubation with PBS, CA or CAG hydrogels without or with 1,064 nm laser irradiation (1 W/cm^2) for 15 min. **(B)** Quantification of fluorescence intensity of 4T1 cancer cells after different treatments. **(C)** Cell viability of 4T1 cancer cells after incubation with PBS, CA or CAG hydrogels at different CTN concentrations without or with 1,064 nm laser irradiation (1 W/cm^2) for 5 min.

RESULTS AND DISCUSSION

Synthesis and Characterization of Hydrogels

To construct GOx-loaded pH-sensitive photothermal hydrogels, pH-sensitive CTNs with activatable NIR-II photothermal conversion property were first synthesized. Hydrodynamic diameter of CTNs was measured to be 14.7 nm (**Supplementary Figure S1**, Supporting information). The surface zeta potential of CTNs was around -22.2 mV (**Supplementary Figure S2**, Supporting information). The characteristic absorption of CTNs at different pH conditions was different and higher absorption in the NIR-II regions could be observed at acidic conditions (**Figure 2A**). The color of CTN solution gradually changed from blue to gray as the increase of pH from 5 to 9 (**Supplementary Figure S3**, Supporting information). The photothermal property of CTN solutions was different at pH = 5, 7, or 9 under 1,064 nm laser irradiation. The temperature rise of CTNs at pH = 5 was much faster than those at pH = 7 and 9 (**Supplementary Figure S4**, Supporting information). These results indicated that the synthesized CTNs were pH-sensitive photothermal agents. The pH-responsive photothermal property of CTNs may be due to different charge-transfer efficiency between the components within nanoparticles at different pH conditions (Wang et al., 2019).

As shown in **Figure 2B**, CA hydrogels with loading of CTNs and CAG hydrogels with loadings of CTNs and GOx could be formed *via* coordination reaction of alginate with Ca^{2+}. SEM images showed that the morphologies of CA and CAG were similar (**Figure 2C**), indicating that loading of CTNs and GOx did not affect the morphology of hydrogels. The photothermal performances of CA and CAG hydrogels were evaluated under 1,064 nm laser irradiation. Heating curves and thermal images showed that the temperatures increased rapidly for solutions containing CA and CAG hydrogels under 1,064 nm laser irradiation at the power density of 1 W/cm^2 for 5 min (**Figure 2D** and **Supplementary Figure S5**, Supporting information).There was no significant difference in the aspect of photothermal property between CA and CAG hydrogels, suggesting the loading of GOx showed neglectful influence on the photothermal effect of hydrogels. Moreover, the temperature

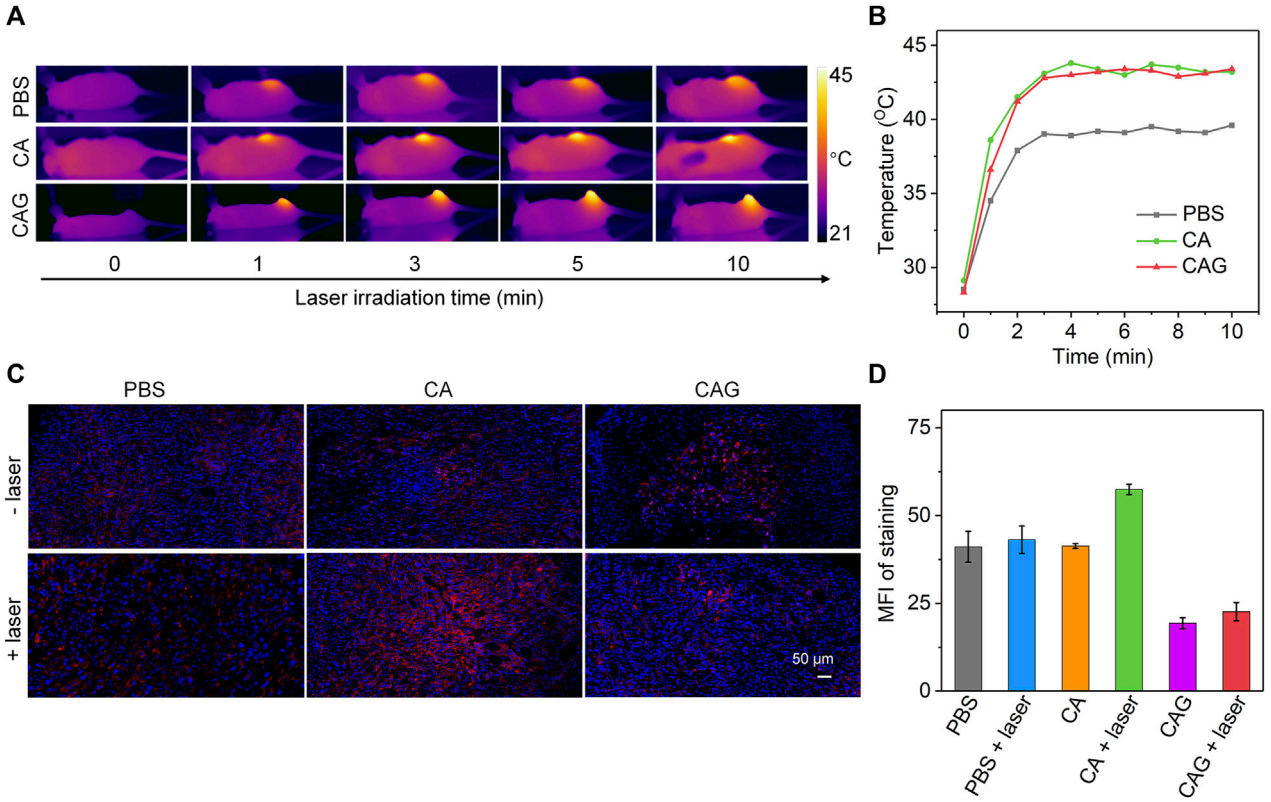

FIGURE 4 | Evaluation of mild NIR-II PTT and intratumor expression of HSP90. **(A)** *In vivo* Thermal imaging of 4T1 tumor-bearing mice after treatment with PBS, CA, or CAG hydrogels under 1,064 nm laser irradiation at the powder density of 1 W/cm^2 for 10 min. **(B)** Temperature changes of tumor sites of 4T1 tumor-bearing mice after different treatments under 1,064 nm laser irradiation (1 W/cm^2) for different time. **(C)** Immunofluorescence HSP90 staining of tumors after different treatments. The blue fluorescence signals indicated cell nucleus stained by 4′,6-diamidino-2-phenylindole (DAPI), and the red fluorescence signals indicated HSP90 stained by antibody. **(D)** Mean fluorescence intensity (MFI) of HSP90 staining in different groups.

increase of hydrogels did not have obvious changes after five cycles of laser on/off, indicating that CA and CAG hydrogels had good photothermal stability (**Figure 2E**). The release profile showed that GOx was gradually released form CAG hydrogels, and the cumulative release ratio could reach 76.0% after incubation at 37°C for 24 h (**Figure 2F**).

Evaluation of *in vitro* Therapeutic Efficacy to 4T1 Cancer Cells

In vitro therapeutic efficacy of CA and CAG hydrogels was evaluated using 4T1 cancer cells. Fluorescence images showed that obvious dead cells (red fluorescence signals) were observed in CA and CAG groups after 1,064 nm laser irradiation at the power density of 1 W/cm^2 for 15 min, while almost no dead cells were found in control and the other treatment groups (**Figure 3A**). The quantitative assay of fluorescence intensity indicated that the percentage of apoptotic cells was 79.0 and 97.8% for CA and CAG treatment and laser irradiation, respectively, while the percentage of apoptotic cells was less than 2% in the other groups (**Figure 3B**). Moreover, the therapeutic efficacy was evaluated by measuring the cell viability of 4T1 cancer cells after different treatments. Without laser irradiation, the cell viability of both CA and CAG treated cells at different CTN concentrations was higher than 90%, which indicated there was no obvious cytotoxicity for hydrogels. However, after 1,064 nm laser irradiation at the power density of 1 W/cm^2 for 5 min, the cell viability was decreased with the increase of CTN concentrations (**Figure 3C**). At the same CTN concentrations, the cell viability of 4T1 cancer cells after CAG treatment plus laser irradiation was lower relative to that after CA treatment with laser irradiation. These results suggested that CA and CAG could kill cancer cells *via* PTT effect, and the therapeutic efficacy of CAG was higher than that of CA.

Evaluation of HSP90 Expression During Photothermal Therapy

4T1 tumor-bearing mice were used as models to investigate the therapeutic efficacy of hydrogels. To achieve mild NIR-II PTT and starvation combinational therapy, the temperature of tumors during PTT should be controlled below 45°C. After treatment with PBS, CA or CAG, tumors were irradiated with 1,064 nm laser in a discontinuous manner and the tumor temperatures were monitored. During laser irradiation, the temperatures of tumor sites for CA and CAG treated mice gradually increased, and similarly reached around 44°C after

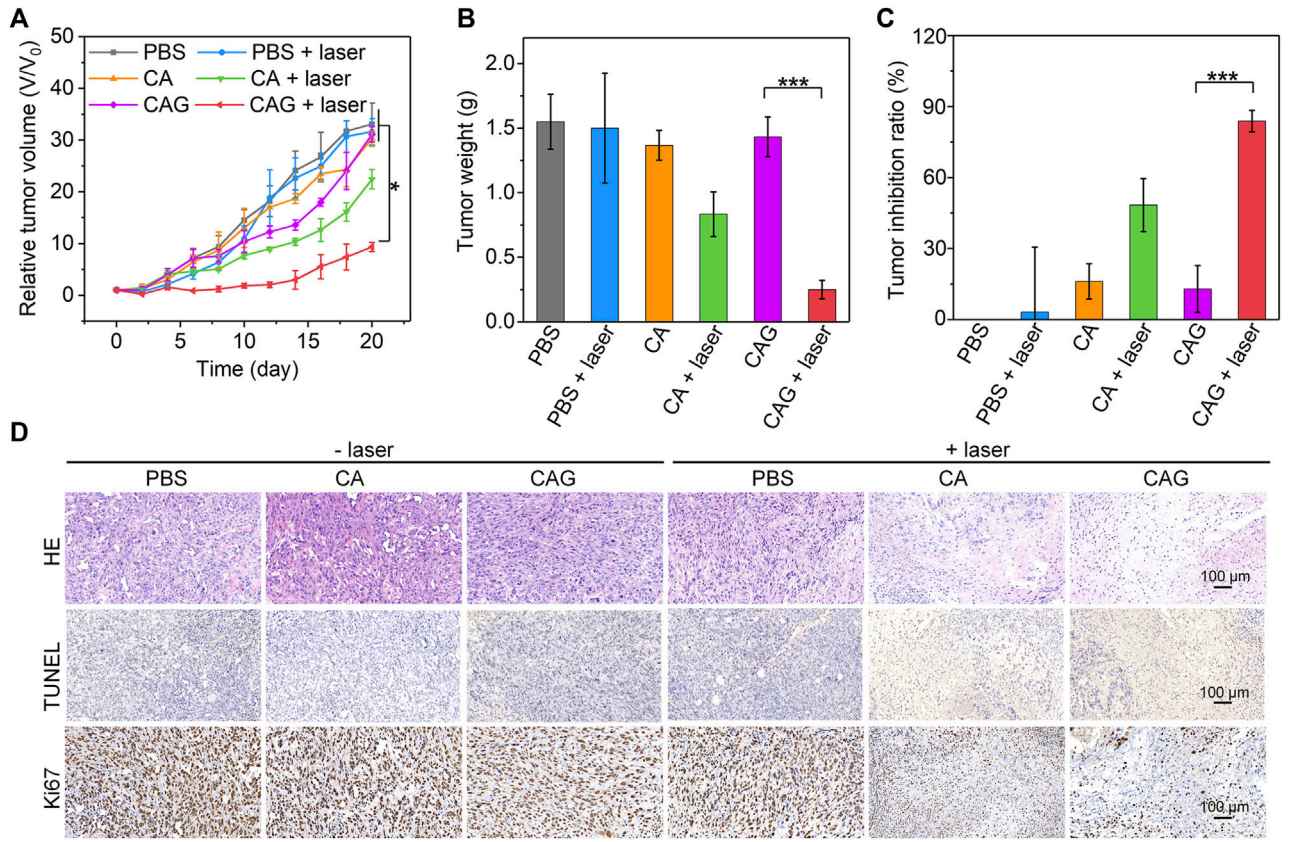

FIGURE 5 | Evaluation of *in vivo* antitumor efficacy of hydrogels. **(A)** Relative tumor volumes of 4T1 tumor-bearing mice after treatment with PBS, CA, or CAG hydrogels under 1,064 nm laser irradiation at the powder density of 1 W/cm^2 for 10 min. **(B)** Tumor weights of 4T1 tumors of mice after different treatments. **(C)** Tumor inhibition ratio of 4T1 tumors in tumor-bearing mice after different treatments. **(D)** H&E, TUNEL and Ki67 staining of 4T1 tumors from mice after different treatments.

3 min of laser irradiation and maintained at this temperature for another 7 min (**Figures 4A,B**). The tumor temperature for mice after treatment with PBS only reached around 39°C after 10 min of laser irradiation.

The expressions of HSP90 in tumor tissues after different treatments were then evaluated. As shown in the immunofluorescence staining images, the strongest staining signal was detected for the tumors after treatment with CA plus 1,064 nm laser irradiation, suggesting PTT upregulated the expression of HSP90 (**Figure 4C**). Compared to the PBS control group, the staining signals for CAG treated tumors regardless of laser irradiation were much weaker. Quantitative assay showed that the tumors after CA treatment plus laser irradiation had the highest expression level of HSP90, while the expression level of HSP90 in tumors after CAG treatment plus laser irradiation was reduced (**Figure 4D**). This indicated that CAG treatment could greatly inhibit the expression of HSP90 due to gradual release of GOx from hydrogels.

In vivo Antitumor Efficacy Evaluation

To evaluate the antitumor efficacy of hydrogels, 4T1 tumor-bearing mice were treated with PBS, CA, or CAG hydrogels, followed by 1,064 nm laser irradiation for 10 min in a discontinuous manner to maintain the maximum tumor temperature below 45°C. Compared to the PBS control group, only the growths of tumors from SA and SAC treated mice with laser irradiation were inhibited, suggesting the effective therapeutic efficacy (**Figure 5A**). The slight inhibition of tumor growth for CA treated and laser irradiated mice should be due to sole mild NIR-II PTT. The relative tumor volume in the SAC treated and laser irradiated mice were much lower than that for the mice after treatment with CA plus laser irradiation. Such a higher therapeutic efficacy for CAG was attributed to the combinational action of mild NIR-II PTT and starvation therapy. Tumor weights in CA and CAG-mediated treatment groups were lower than those in the other groups (**Figure 5B**). In particular, the tumor weight for CAG treated and laser irradiated mice were 5.7-fold lower relative to that for CAG treated mice without laser irradiation. The tumor inhibition rate for CAG treatment plus laser irradiation was calculated to be 83.0%, which was 1.7 and 6.4-fold higher than that for CA plus laser treatment and sole CAG treatment, respectively (**Figure 5C**).

To further investigate the therapeutic efficacies of hydrogels, histological staining of tumors was performed. As shown in H&E staining images, necrotic tumor cells were clearly observed in the CA and CAG treated and laser irradiated groups, while which were almost not found in

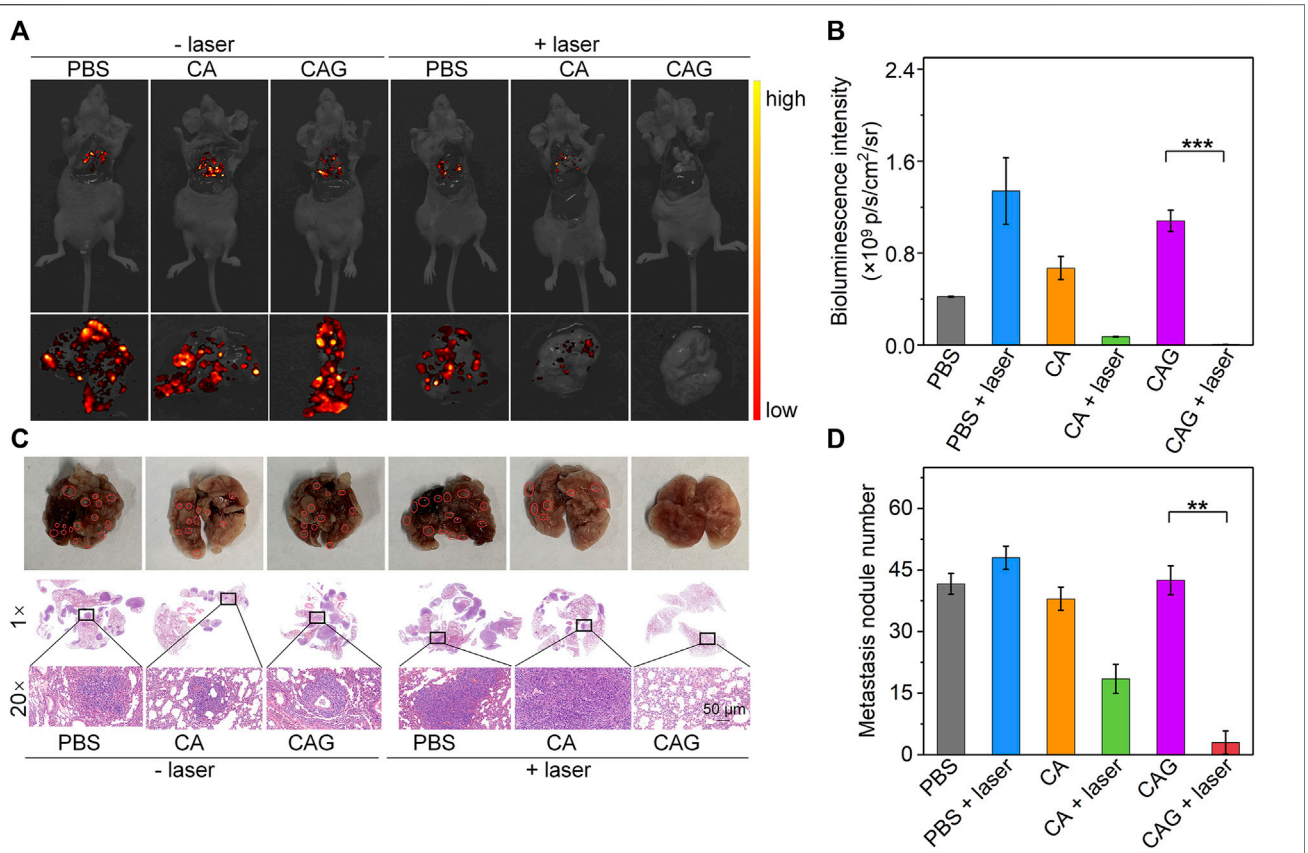

FIGURE 6 | Evaluation of *in vivo* anti-metastasis efficacy of hydrogels. **(A)** Bioluminescence images of lung from 4T1 tumor-bearing mice after treatment with PBS, CA, or CAG hydrogels under 1,064 nm laser irradiation at the powder density of 1 W/cm^2 for 10 min. **(B)** Bioluminescence intensity of lung from 4T1 tumor-bearing mice after different treatments. **(C)** Photographs and H&E staining images of lung from mice after different treatments. Red circles indicate the metastatic tumor nodes. **(D)** Number of metastatic tumor nodes of lungs from mice after different treatments.

tumors after the other treatment (**Figure 5D**). The necrosis in CAG treated and laser irradiated tumors was much more conspicuous than that in CA treated and laser irradiated tumors. The results of immunohistochemical TUNEL staining also indicated that obvious staining of necrotic cells could be found in CA and CAG treated tumors with laser irradiation, while nearly no cell necrosis was observed in the other treatment groups. The staining signal of necrotic cells in CAG treated and laser irradiated group was stronger than that in CA treated and laser irradiated group. Furthermore, the tumors after treatment with CA and CAG plus laser irradiation showed lower expressions of Ki67 as compared to the control group, indicating CA and Cag-mediated therapy could inhibit the proliferation of tumor cells. The inhibitory efficacy for CAG-mediated therapy was higher than that of CA-mediated treatment. The histological staining results were consistent with the tumor growth results, further confirming that CAG exhibited higher antitumor efficacy than CA.

The body weights of 4T1 tumor-bearing mice after different treatments for 20 days were almost the same as that of control mice (**Supplementary Figure S6**, Supporting information). H&E staining images of heart, liver, spleen and kidney from 4T1 tumor-bearing mice showed that no abnormal morphologies were found for these tissues after CA and CAG treatments plus 1,064 nm laser irradiation (**Supplementary Figure S7**, Supporting information). These results demonstrated that CA and CAG-mediated therapy did not cause obvious systematic toxicity.

In vivo Anti-metastasis Efficacy Evaluation

In addition to inhibition of tumor growth, prevention of tumor metastasis is necessary to achieve ideal treatment of tumors. Bioluminescence imaging was conducted to evaluate the anti-metastasis efficacy of hydrogels. Obvious bioluminescence signals were observed in lungs of mice after treatments with PBS, CA, or CAG without 1,064 nm laser irradiation and mice treated with PBS plus laser irradiation (**Figure 6A**). The bioluminescence signals in lungs of CA or CAG hydrogel-treated and laser irradiated mice were much lower than those in the other groups. More importantly, nearly no bioluminescence signal could be detected for mice after treatment with CAG hydrogels with 1,064 nm laser irradiation. The quantitative analysis showed that the bioluminescence intensity for CA or CAG treated mice with laser irradiation was much lower relative to those for the other treated mice (**Figure 6B**). The lowest bioluminescence intensity was found in lungs of mice after CAG treatment plus laser irradiation.

H&E staining was also used to evaluate the lung metastasis after different treatments. As shown in the photographs and H&E staining images, metastatic tumor nodes were not observed in the lungs of mice after treatment with CAG hydrogels plus laser irradiation, which however were clearly observed in lungs of mice in the other treated groups (**Figure 6C**). The treatment of CA or CAG hydrogels plus laser irradiation greatly reduced the numbers of metastatic tumor nodes as compared to the treatments of PBS, CA, or CAG without laser irradiation and PBS plus laser irradiation (**Figure 6D**). In particular, the number of tumor metastasis in lungs of CAG treated and laser irradiated mice was significantly lower than that in lungs of CAG treated mice without laser irradiation. These results suggested that CAG-mediated therapy greatly prevented lung metastasis of 4T1 tumors.

CONCLUSION

We have constructed a GOx-loaded smart hydrogel with pH-sensitive photothermal conversion property for combinational NIR-II PTT and starvation therapy of solid tumors at mild-temperature. The hydrogels (CAG) were locally formed after intratumoral injection of alginate solution containing CTN and GOx, which enabled gradual release of GOx into tumor sites. Through consuming glucose, CAG mediated starvation therapy, which not only led to exhaustion of tumor cells, but also resulted in aggravated acidity in tumor microenvironment and downregulated expression of HSP90. The NIR-II photothermal conversion property of CTNs was activated in acidic condition, which allowed for mild NIR-II PTT with a high efficacy due to the inhibited expression of HSP90. *Via* the combinational action of mild MIR-II PTT and starvation therapy, CAG was able to greatly suppress the growth of subcutaneously implanted tumors and completely prevent lung metastasis in a breast cancer murine model, while sole mild MIR-II PTT failed to do so. To the best of our knowledge, this study reports the first smart hydrogel platform with pH-sensitive NIR-II photothermal effect for mild-temperature-mediated combinational cancer therapy.

DATA AVAILABILITY STATEMENT

The original contributions presented in the study are included in the article/Supplementary Files, further inquiries can be directed to the corresponding authors.

ETHICS STATEMENT

The animal study was reviewed and approved by the Animal Care and Use Committee of Donghua University.

AUTHOR CONTRIBUTIONS

JX, XQ and JS contributed equally to this work. JL and XW conceived the idea, designed the experiments, and supervised the research. JX, XQ, JS, MD, YW, NY performed the experiments and analyzed the data. JX, XQ and JS co-wrote the manuscript. JL and XW review and edit the manuscript. All authors read and approved the final manuscript.

FUNDING

This work was financially supported by the Science and Technology Commission of Shanghai Municipality (20DZ2254900), Fundamental Research Funds for the Central Universities (2232021A-05), Shanghai Pujiang Program (20PJ1403800) and Natural Science Foundation of China (82001968).

SUPPLEMENTARY MATERIAL

The Supplementary Material for this article can be found online at: https://www.frontiersin.org/articles/10.3389/fchem.2021.736468/full#supplementary-material.

REFERENCES

Ali, M. R. K., Ali, H. R., Rankin, C. R., and El-Sayed, M. A. (2016). Targeting heat shock protein 70 using gold nanorods enhances cancer cell apoptosis in low dose plasmonic photothermal therapy. *Biomaterials* 102, 1–8. doi:10.1016/j.biomaterials.2016.06.017

Butler, E. B., Zhao, Y., Muñoz-Pinedo, C., Lu, J., and Tan, M. (2013). Stalling the engine of resistance: targeting cancer metabolism to overcome therapeutic resistance. *Cancer Res.* 73, 2709–2717. doi:10.1158/0008-5472.can-12-3009

Cao, J., Qiao, B., Luo, Y., Cheng, C., Yang, A., Wang, M., et al. (2020). A multimodal imaging-guided nanoreactor for cooperative combination of tumor starvation and multiple mechanism-enhanced mild temperature phototherapy. *Biomater. Sci.* 8, 6561–6578. doi:10.1039/d0bm01350a

Chen, W.-H., Luo, G.-F., Lei, Q., Hong, S., Qiu, W.-X., Liu, L.-H., et al. (2017). Overcoming the heat endurance of tumor cells by interfering with the anaerobic glycolysis metabolism for improved photothermal therapy. *ACS Nano* 11, 1419–1431. doi:10.1021/acsnano.6b06658

Cheng, H., Jiang, X.-Y., Zheng, R.-R., Zuo, S.-J., Zhao, L.-P., Fan, G.-L., et al. (2019). A biomimetic cascade nanoreactor for tumor targeted starvation therapy-amplified chemotherapy. *Biomaterials* 195, 75–85. doi:10.1016/j.biomaterials.2019.01.003

Cheng, X., Sun, R., Yin, L., Chai, Z., Shi, H., and Gao, M. (2017). Light-Triggered Assembly of Gold Nanoparticles for Photothermal Therapy and Photoacoustic Imaging of Tumors *In Vivo*. *Adv. Mater.* 29, 1604894. doi:10.1002/adma.201604894

Dinda, S., Sarkar, S., and Das, P. K. (2018). Glucose oxidase mediated targeted cancer-starving therapy by biotinylated self-assembled vesicles. *Chem. Commun.* 54, 9929–9932. doi:10.1039/c8cc03599g

Ding, F., Gao, X., Huang, X., Ge, H., Xie, M., Qian, J., et al. (2020). Polydopamine-coated nucleic acid nanogel for siRNA-mediated low-temperature photothermal therapy. *Biomaterials* 245, 119976. doi:10.1016/j.biomaterials.2020.119976

Fu, L.-H., Qi, C., Lin, J., and Huang, P. (2018). Catalytic chemistry of glucose oxidase in cancer diagnosis and treatment. *Chem. Soc. Rev.* 47, 6454–6472. doi:10.1039/c7cs00891k

Gao, G., Jiang, Y. W., Guo, Y., Jia, H. R., Cheng, X., Deng, Y., et al. (2020). Enzyme-Mediated Tumor Starvation and Phototherapy Enhance Mild-Temperature Photothermal Therapy. *Adv. Funct. Mater.* 30, 1909391. doi:10.1002/adfm.201909391

Gao, G., Jiang, Y. W., Sun, W., Guo, Y., Jia, H. R., Yu, X. W., et al. (2019). Molecular Targeting-Mediated Mild-Temperature Photothermal Therapy with a Smart Albumin-Based Nanodrug. *Small* 15, 1900501. doi:10.1002/smll.201900501

Gao, G., Sun, X., and Liang, G. (2021). Nanoagent-Promoted Mild-Temperature Photothermal Therapy for Cancer Treatment. *Adv. Funct. Mater.* 31, 2100738. doi:10.1002/adfm.202100738

Guo, S., and Kohane, D. S. (2017). Nanoparticulate cancer-starvation therapy. *Chem* 2, 168–170. doi:10.1016/j.chempr.2017.01.014

He, X., Hao, Y., Chu, B., Yang, Y., Sun, A., Shi, K., et al. (2021). Redox--activatable -p-hotothermal -t-herapy and -e-nzyme--m-ediated -t-umor -s-tarvation for -s-ynergistic -c-ancer -t-herapy. *Nano Today* 39, 101174. doi:10.1016/j.nantod.2021.101174

Hernández-González, A. C., Téllez-Jurado, L., and Rodríguez-Lorenzo, L. M. (2020). Alginate hydrogels for bone tissue engineering, from injectables to bioprinting: A review. *Carbohydr. Polym.* 229, 115514. doi:10.1016/j.carbpol.2019.115514

Hu, J.-J., Liu, M.-D., Gao, F., Chen, Y., Peng, S.-Y., Li, Z.-H., et al. (2019). Photo-controlled liquid metal nanoparticle-enzyme for starvation/photothermal therapy of tumor by win-win cooperation. *Biomaterials* 217, 119303. doi:10.1016/j.biomaterials.2019.119303

Johnson, K.-A., Muzzin, N., Toufanian, S., Slick, R. A., Lawlor, M. W., Seifried, B., et al. (2020). Drug-impregnated, pressurized gas expanded liquid-processed alginate hydrogel scaffolds for accelerated burn wound healing. *Acta Biomater.* 112, 101–111. doi:10.1016/j.actbio.2020.06.006

Ju, E., Dong, K., Liu, Z., Pu, F., Ren, J., and Qu, X. (2015). Tumor microenvironment activated photothermal strategy for precisely controlled ablation of solid tumors upon NIR irradiation. *Adv. Funct. Mater.* 25, 1574–1580. doi:10.1002/adfm.201403885

Jung, H. S., Verwilst, P., Sharma, A., Shin, J., Sessler, J. L., and Kim, J. S. (2018). Organic molecule-based photothermal agents: an expanding photothermal therapy universe. *Chem. Soc. Rev.* 47, 2280–2297. doi:10.1039/c7cs00522a

Lee, K. Y., and Mooney, D. J. (2012). Alginate: properties and biomedical applications. *Prog. Polym. Sci.* 37, 106–126. doi:10.1016/j.progpolymsci.2011.06.003

Li, J., and Pu, K. (2019). Development of organic semiconducting materials for deep-tissue optical imaging, phototherapy and photoactivation. *Chem. Soc. Rev.* 48, 38–71. doi:10.1039/c8cs00001h

Li, J., and Pu, K. (2020). Semiconducting polymer nanomaterials as near-infrared photoactivatable protherapeutics for cancer. *Acc. Chem. Res.* 53, 752–762. doi:10.1021/acs.accounts.9b00569

Li, J., Yu, X., Jiang, Y., He, S., Zhang, Y., Luo, Y., et al. (2021). Second Near-Infrared Photothermal Semiconducting Polymer Nanoadjuvant for Enhanced Cancer Immunotherapy. *Adv. Mater.* 33, 2003458. doi:10.1002/adma.202003458

Liu, H., Chen, D., Li, L., Liu, T., Tan, L., Wu, X., et al. (2011). Multifunctional gold nanoshells on silica nanorattles: a platform for the combination of photothermal therapy and chemotherapy with low systemic toxicity. *Angew. Chem. Int. Ed.* 50, 891–895. doi:10.1002/anie.201002820

Liu, J., Qing, X., Zhang, Q., Yu, N., Ding, M., Li, Z., et al. (2021). Oxygen-producing proenzyme hydrogels for photodynamic-mediated metastasis-inhibiting combinational therapy. *J. Mater. Chem. B* 9, 5255–5263. doi:10.1039/d1tb01009c

Liu, K., Zhang, X., Xu, W., Chen, J., Yu, J., Gamble, J. R., et al. (2017). Targeting the vasculature in hepatocellular carcinoma treatment: Starving versus normalizing blood supply. *Clin. Transl. Gastroenterol.* 8, e98. doi:10.1038/ctg.2017.28

Luo, J., Fan, M., Xiong, L., Hao, Q., Jiang, M., He, Q., et al. (2021). 1T-Phase Dirac Semimetal PdTe2 Nanoparticles for Efficient Photothermal Therapy in the NIR-II Biowindow. *ACS Appl. Mater. Inter.* 13, 27963–27971. doi:10.1021/acsami.1c06740

Ouyang, B., Liu, F., Ruan, S., Liu, Y., Guo, H., Cai, Z., et al. (2019). Localized free radicals burst triggered by NIR-II Light for augmented low-temperature photothermal therapy. *ACS Appl. Mater. Inter.* 11, 38555–38567. doi:10.1021/acsami.9b15009

Patrick, P. S., Bear, J. C., Fitzke, H. E., Zaw-Thin, M., Parkin, I. P., Lythgoe, M. F., et al. (2020). Radio-metal cross-linking of alginate hydrogels for non-invasive *in vivo* imaging. *Biomaterials* 243, 119930. doi:10.1016/j.biomaterials.2020.119930

Ranji-Burachaloo, H., Reyhani, A., Gurr, P. A., Dunstan, D. E., and Qiao, G. G. (2019). Combined Fenton and starvation therapies using hemoglobin and glucose oxidase. *Nanoscale* 11, 5705–5716. doi:10.1039/c8nr09107b

Ren, J., Zhang, L., Zhang, J., Zhang, W., Cao, Y., Xu, Z., et al. (2020). Light-activated oxygen self-supplied starving therapy in near-infrared (NIR) window and adjuvant hyperthermia-induced tumor ablation with an augmented sensitivity. *Biomaterials* 234, 119771. doi:10.1016/j.biomaterials.2020.119771

Tang, M., Ren, X., Fu, C., Ding, M., and Meng, X. (2021). Regulating glucose metabolism by nanomedicines for cancer therapy. *J. Mater. Chem. B*. doi:10.1039/d1tb00218j

Tang, X., Tan, L., Shi, K., Peng, J., Xiao, Y., Li, W., et al. (2018). Gold nanorods together with HSP inhibitor-VER-155008 micelles for colon cancer mild-temperature photothermal therapy. *Acta Pharmaceutica Sinica B* 8, 587–601. doi:10.1016/j.apsb.2018.05.011

Wang, J., Wu, C., Qin, X., Huang, Y., Zhang, J., Chen, T., et al. (2021). NIR-II light triggered nitric oxide release nanoplatform combined chemo-photothermal therapy for overcoming multidrug resistant cancer. *J. Mater. Chem. B* 9, 1698–1706. doi:10.1039/d0tb02626c

Wang, L., Schumann, U., Liu, Y., Prokopchuk, O., and Steinacker, J. M. (2012). Heat shock protein 70 (Hsp70) inhibits oxidative phosphorylation and compensates ATP balance through enhanced glycolytic activity. *J. Appl. Physiol.* 113, 1669–1676. doi:10.1152/japplphysiol.00658.2012

Wang, S., Tian, Y., Tian, W., Sun, J., Zhao, S., Liu, Y., et al. (2016). Selectively sensitizing malignant cells to photothermal therapy using a CD44-targeting heat shock protein 72 depletion nanosystem. *ACS Nano* 10, 8578–8590. doi:10.1021/acsnano.6b03874

Wang, Y., Wang, B., Zhang, L., Huang, J., Li, P., Zhao, Y., et al. (2020). Mitochondria-targeted nanospheres with deep tumor penetration for photo/starvation therapy. *J. Mater. Chem. B* 8, 7740–7754. doi:10.1039/d0tb00001a

Wang, Z., Li, S., Zhang, M., Ma, Y., Liu, Y., Gao, W., et al. (2017). Laser-Triggered Small Interfering RNA Releasing Gold Nanoshells against Heat Shock Protein for Sensitized Photothermal Therapy. *Adv. Sci.* 4, 1600327. doi:10.1002/advs.201600327

Wang, Z., Upputuri, P. K., Zhen, X., Zhang, R., Jiang, Y., Ai, X., et al. (2019). pH-sensitive and biodegradable charge-transfer nanocomplex for second near-infrared photoacoustic tumor imaging. *Nano Res.* 12, 49–55. doi:10.1007/s12274-018-2175-9

Yang, Y., Zhu, W., Dong, Z., Chao, Y., Xu, L., Chen, M., et al. (2017). 1D Coordination Polymer Nanofibers for Low-Temperature Photothermal Therapy. *Adv. Mater.* 29, 1703588. doi:10.1002/adma.201703588

Yuan, Z., Lin, C., He, Y., Tao, B., Chen, M., Zhang, J., et al. (2020). Near-infrared light-triggered nitric-oxide-enhanced photodynamic therapy and low-temperature photothermal therapy for biofilm elimination. *ACS Nano* 14, 3546–3562. doi:10.1021/acsnano.9b09871

Zhang, C., Ni, D., Liu, Y., Yao, H., Bu, W., and Shi, J. (2017). Magnesium silicide nanoparticles as a deoxygenation agent for cancer starvation therapy. *Nat. Nanotech* 12, 378–386. doi:10.1038/nnano.2016.280

Zhang, K., Fang, Y., He, Y., Yin, H., Guan, X., Pu, Y., et al. (2019). Extravascular gelation shrinkage-derived internal stress enables tumor starvation therapy with suppressed metastasis and recurrence. *Nat. Commun.* 10, 5380. doi:10.1038/s41467-019-13115-3

Zhao, P., Jin, Z., Chen, Q., Yang, T., Chen, D., Meng, J., et al. (2018). Local generation of hydrogen for enhanced photothermal therapy. *Nat. Commun.* 9, 4241. doi:10.1038/s41467-018-06630-2

Zhou, J., Li, M., Hou, Y., Luo, Z., Chen, Q., Cao, H., et al. (2018). Engineering of a nanosized biocatalyst for combined tumor starvation and low-temperature photothermal therapy. *ACS Nano* 12, 2858–2872. doi:10.1021/acsnano.8b00309

Zhu, X., Feng, W., Chang, J., Tan, Y.-W., Li, J., Chen, M., et al. (2016). Temperature-feedback upconversion nanocomposite for accurate photothermal therapy at facile temperature. *Nat. Commun.* 7, 10437. doi:10.1038/ncomms10437

Conflict of Interest: The authors declare that the research was conducted in the absence of any commercial or financial relationships that could be construed as a potential conflict of interest.

Publisher's Note: All claims expressed in this article are solely those of the authors and do not necessarily represent those of their affiliated organizations, or those of the publisher, the editors and the reviewers. Any product that may be evaluated in this article, or claim that may be made by its manufacturer, is not guaranteed or endorsed by the publisher.

frontiers in Chemistry

MINI REVIEW
published: 11 August 2021
doi: 10.3389/fchem.2021.732770

pH-Responsive DNA Motif: From Rational Design to Analytical Applications

Lin Lin Zheng[1], Jin Ze Li[1], Ying Xu Li[1], Jian Bang Gao[1], Jiang Xue Dong[2]* and Zhong Feng Gao[1]**

[1]Shandong Province Key Laboratory of Detection Technology for Tumor Makers, Collaborative Innovation Center of Tumor Marker Detection Technology, School of Chemistry and Chemical Engineering, Feixian Campus, Linyi University, Linyi, China, [2]College of Chemistry and Environmental Science, Key Laboratory of Analytical Science and Technology, Hebei University, Baoding, China

pH-responsive DNA motifs have attracted substantial attention attributed to their high designability and versatility of DNA chemistry. Such DNA motifs typically exploit DNA secondary structures that exhibit pH response properties because of the presence of specific protonation sites. In this review, we briefly summarized second structure-based pH-responsive DNA motifs, including triplex DNA, i-motif, and A^+-C mismatch base pair-based DNA devices. Finally, the challenges and prospects of pH-responsive DNA motifs are also discussed.

Keywords: pH-responsive, DNA molecular devices, triplex DNA, i-motif, A^+-C mismatch

OPEN ACCESS

Edited by:
Ruixue Duan,
Soochow University, China

Reviewed by:
Yong Pan,
Hubei University of Technology, China
Xiaoqing Yi,
Gannan Medical University, China

****Correspondence:***
Jian Bang Gao
fxgjb1963@126.com
Jiang Xue Dong
dongjx@hbu.edu.cn
Zhong Feng Gao
gaozhongfeng@lyu.edu.cn

Specialty section:
This article was submitted to Nanoscience, a section of the journal Frontiers in Chemistry

Received: *29 June 2021*
Accepted: *08 July 2021*
Published: *11 August 2021*

Citation:
Zheng LL, Li JZ, Li YX, Gao JB, Dong JX and Gao ZF (2021) pH-Responsive DNA Motif: From Rational Design to Analytical Applications. Front. Chem. 9:732770. doi: 10.3389/fchem.2021.732770

INTRODUCTION

Deoxyribonucleic acid (DNA), as the main carrier of genetic information for living organisms, has been widely studied (Zhang and Seelig, 2011; Lu et al., 2013). Because of its thermodynamic programmability, high structural features, facile synthesis, and possible conjugation to a host of molecules and nanodevices, DNA has presented an impressive potential to engineer a variety of molecular devices with applications ranging from molecular sensors to therapeutic tools (Ablasser, 2021; Kremarová et al., 2021). Thanks to those crucial properties, the functionalized DNA devices have been studied. The precise definition of the operational characteristics, especially the sensitivity, is indispensable for the development of DNA-based molecular machines to regulate the vital biological processes and sense (Ranallo et al., 2015; Manish et al., 2019). The degree of their response sensitivity to different environmental stimuli, such as metal ions (Collie and Parkinson., 2011), pH value (Gehring et al., 1993), light (Beharry et al., 2011), and enzymatic activities (Wickham et al., 2012), is determined by the magnitude of their folding structure (Simon et al., 2014).

DNA molecular devices are DNA self-assemblies induced by external stimuli, perform quasi-mechanical movement at the micro-nano scale, and have attracted increasing attention in the fields of biosensing, drug delivery, and biomedical detection (Kay and Leigh., 2015; Abendroth et al., 2015; Tani et al., 2021). By taking advantage of the high designability and the versatility of DNA chemistry, several groups have recently developed pH-dependent DNA-based nanodevices (Fu et al., 2019). Such functionalized DNA devices typically exploit DNA secondary structures that display pH dependence because of the presence of specific protonation sites. These structures include triplex DNA, i-motif, and A^+-C mismatch base pair-based DNA, displayed in **Figure 1**. The pH-responsive property is highly due to the protonation of adenine and cytosine in the A^+-C mismatch pair, triplex DNA, and i-motif, respectively (Soto et al., 2002). Different physical methods such as nuclear magnetic resonance (NMR), calorimetry, X-ray fiber, UV/Vis spectroscopy, and diffraction methods

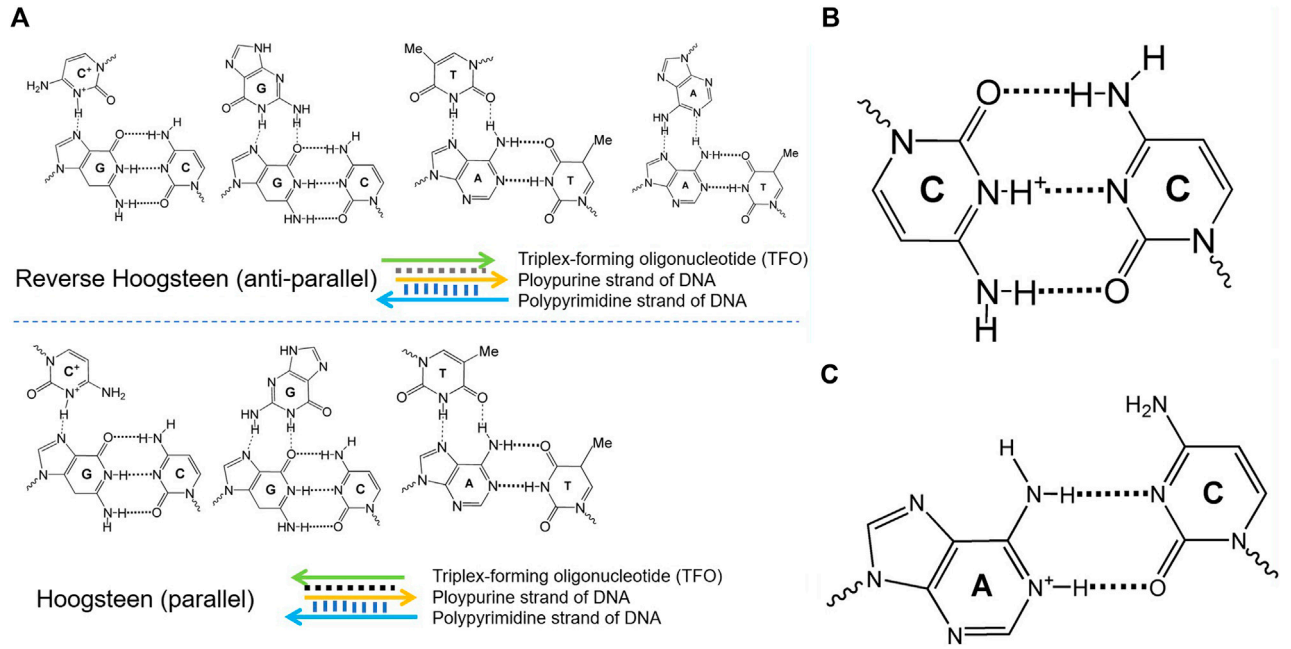

FIGURE 1 | Different conformational DNA structure configurations. **(A)** Different configurations of the parallel and antiparallel triplex DNA. **(B)** The key element C^+-C in the i-motif DNA. **(C)** The protonation center of A^+-C in the pH-dependent DNA motif.

have been applied to characterize the thermodynamic stabilities (Plum et al., 1990) kinetic properties (Maher et al., 1990), and structural features (Wärmländer et al., 2003) of the different DNA structures and their relative motifs.

In this review, we mainly described the pH-dependent DNA structures including triplex DNA, i-motif, and A^+-C mismatched DNA structures and their applications in biosensor, living cells imaging, and accurate regulation of the pH response range. Through the studies of the different pH-dependent DNA structures, we expect that the DNA nanotechnology and its related field will continue to develop rapidly. At a fundamental level, further studies should aim at greater understanding of the conformational transformation mechanisms at the nanometer scale. In terms of applications, we expect that many of these elegant DNA molecular devices will soon be used *in vivo*. These further studies could confirm the power of DNA nanotechnology in biology, material science, chemistry, and physics.

THE DIFFERENT CONFORMATIONAL PH-DEPENDENT DNA DEVICES

Triplex DNA Nanodevices

Triplex nucleic acids have recently attracted attention as part of the rich "toolbox" of the structures used to develop DNA-based nanodevices and materials. In the 1980s (Singleton and Dervan, 1992), DNA was first utilized to assemble nanostructures on the basis of the specific base-paring of single-stranded DNA overhangs, and a set of sophisticated DNA-based nanostructures have been rationally designed. Apart from the base-paired duplex structure of oligonucleotides, supramolecular DNA assemblies formed by the interaction of the double-helix DNA strand and an auxiliary single-stranded overhang were used to form triplex assemblies through Hoogsteen interactions, termed triplex-forming oligonucleotide. Different triplex structures between double-helix DNA domains and single-stranded oligonucleotides domains are demonstrated in **Figure 1**, including the parallel triplex structures composed of C^+·G-C, G·G-C, and T·A-T and antiparallel triplex structures formed by C^+·G-C, G·G-C, T·A-T, and A·A-T strands. There are different parameters such as mutations in the triplex domains, the number and kind of the triplex bridges, the pH value, and the presence of binders or ions, which would have an effect on the stability of the triplex DNA nanodevices. With the purpose of building sophisticated and functionalized molecular machines, a host of groups have devoted constant efforts to developing new mechanisms of manipulated structural reconfiguration by controlling those parameters.

Motivated by the above description, some pH-responsive triplex switch has been designed for the rational regulation of the thermodynamic property. Such triplex switch is generally combined with three key elements: pH-dependent protonation center C^+·G-C, T·A-T, and the linker connecting the

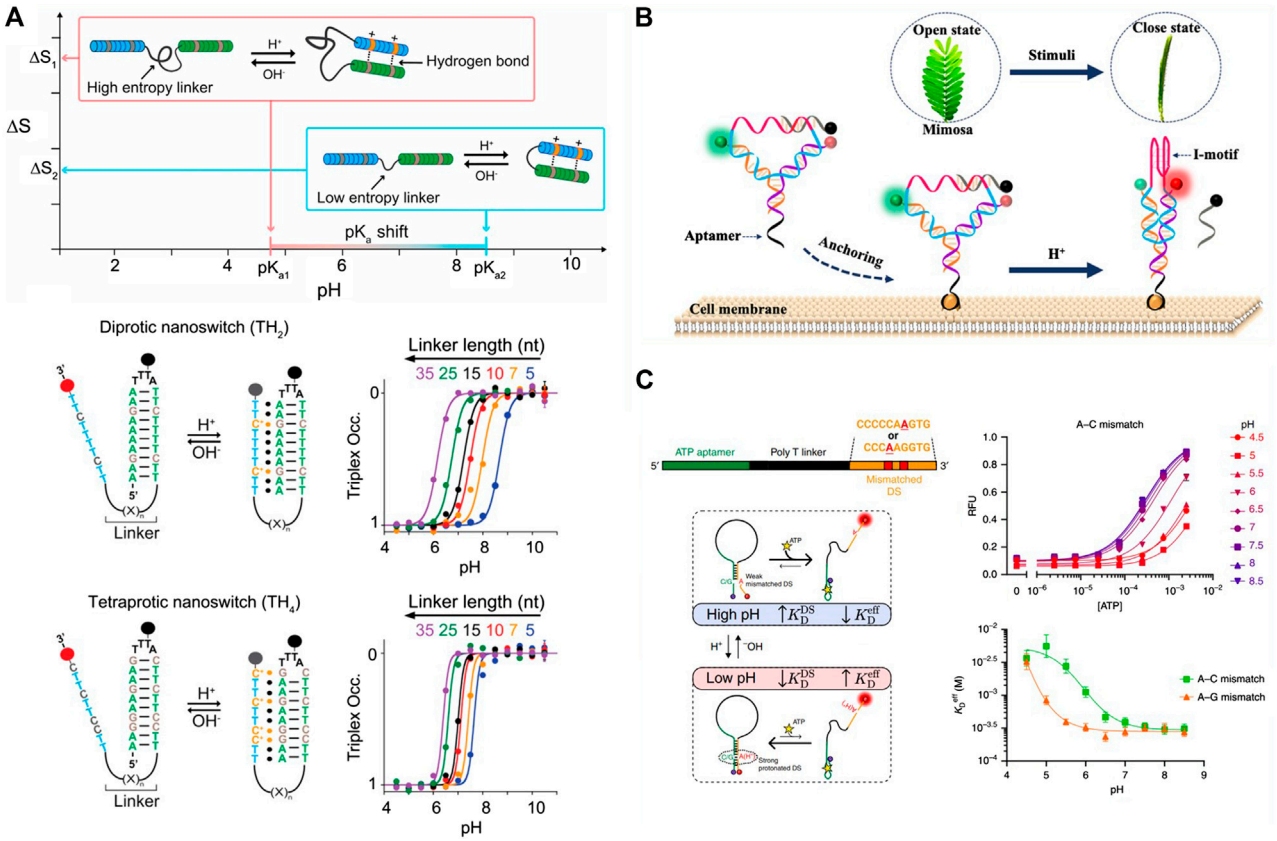

FIGURE 2 | The representative study based on the pH-dependent DNA motif. **(A)** pH triplex nanoswitches with rationally tailored pK_a (Mariottini et al., 2019), reproduced with permission. Copyright 2019, Journal of the American Chemical Society. **(B)** Y-shaped DNA nanostructure based on the i-motif DNA (Chen B et al., 2020), reproduced with permission. Copyright 2020, ACS. **(C)** pH-dependent DNA switch containing A^+-C mismatch pairs (Thompson et al., 2020), reproduced with permission. Copyright 2020, Springer Nature.

single-strand triplex-forming overhang to the hairpin duplex domain. Taking the key elements into account, Mariottini and coworkers demonstrated that the acidic constant (pK_a) of the pH-dependent nanoswitch could be rationally regulated by the design of the intrinsically disordered domain which connected with the hydrogen-bond-forming regions (Mariottini et al., 2019).To investigate this assumption, a pH-dependent triplex nucleic acid nanoswitch was designed, which can generate an intramolecular triplex conformation through the interaction of Hoogsteen between a single-strand triplex-forming overhang and the hairpin duplex domain, shown in **Figure 2A**. The gradual increase of the triplex nanoswitch destabilizing pH value could be observed when the linker length is shortened. In a nutshell, they demonstrated that the regulation of the observed pK_a is greatly attributed to a purely entropic function of the linker length, which can be weakened by improving the number of protonation centers contained in the single-stranded triplex-forming overhang. All the strategies present a predictable and versatile approach to reasonably regulate the thermodynamics and the kinetics of the synthetic structures and expand the range of their application into the designing of nanomolecular devices with a reversible pH dependence and use for controllable drug delivery.

The triplex DNA structures play a pivotal role in the designing of stimuli-responsive nucleic acid devices. The generation of the metal-organic frameworks and the substrate-loaded microcapsules based on DNA which are unlocked by the pH-stimulated conformation of the triplex nucleic acid structures have been amplified by the triplex DNA structures (Liao et al., 2016; Chen B et al., 2020). In addition, the thermodynamic property of the triplex DNA structures with protonation centers and linker led to the regulation of pK_a. Despite the reported accomplishment of applying the triplex DNA structures in nanobiotechnology, significant future challenges should be envisaged. Those preliminary results highlight the importance of the DNA triplexes in the future nanomedicine applications.

I-Motif DNA Structure

In 1993, Gueron and coworkers first reported the i-motif structure (Gehring et al., 1993). They reported that the protonated cytosine-rich (C-rich) sequences could assemble

into a four-stranded structure, intercalated motif in an acidic condition, while changing to single strands under basic or neutral conditions. Taking advantage of this finding, the *in vivo* existence of the i-motif structures has been a hot spot. Therefore, the intermolecular assembly among different C-rich strands cannot be easily controlled because of their self-association. Alternatively, different functionalized i-motif DNA units can be put into an interlocked structure to prevent the unessential interstructural association of i-motifs and make them be a potential molecular material for biosensing.

The practicability of approaches for molecular biosensing containing an adjustable dynamic range is important for understanding and controlling the essential biological processes. Nesterova and coworkers reported design strategies of sensitively pH-responsive sensor based on the nucleic acid i-motif (Nesterova and Nesterov, 2014). Through the reasonable manipulation of the i-motif and collaboration of allosteric control elements, they successfully managed to narrow the total response range to 0.2 pH and delivered a transition midpoint with 0.1 pH units precision. By incorporating three vital characteristics of reversibility of the transition range, intrinsic incorporation of i-motif folding, and incorporation adjustment, their presented strategy can be used in pH-sensitive DNA devices and can be applied to expand the manipulation of other four-strand based structures and will promote the development of the ultraresponsive elements for the signaling systems and the artificial molecular devices.

Relying on the pH-dependent i-motif, Chen and coworkers designed a Y-shaped DNA nanosensor, which can be anchored on the surface of the tumor cell by the specific recognition of an aptamer (AS1411), demonstrated in **Figure 2B** (Chen Y et al., 2020). By labeling pH-independent fluorescence pair on the Y-shaped DNA, the obvious FRET performance could be observed when putting the anchored tumor cell into different pH conditions. In an acidic solution, the C-rich single strand can fold to i-motif structure, and the FRET acceptor is excited. In a neutral condition, the i-motif was opened and the quenching strand significantly decreased the background FRET signal. The Y-shaped DNA sensor displayed a distinct narrow pH response range of 0.5 units, which can sense the tiny variation of the extracellular pH value of the tumor cells. With those advances, the Y-shaped i-motif containing sensor was successfully applied to sensing the MCF-7 cells and displayed a visual fluorescence date. The designed pH-dependent i-motif sensor has a potential for the early diagnosis of cancer and to be used in the demonstration of the cellular physiological progress related to the extracellular pH.

Over the past few years, Yamuna's group has used the i-motif structure DNA nanodevices as a pH sensor to map the temporal and spatial pH changes inside the living cells and the whole living organisms; with appropriate modifications, this method can also be applied to explore cellular endocytic pathways (Surana et al., 2011; Modi et al., 2013). These studies are crucial for the future research of the DNA nanotechnology. We can design many more molecular devices based on the i-motif structures, which can be used in early cancer diagnostics, molecular operations in the living cells, and drug delivery.

A^+-C Mismatched Base Pair-Based pH-dependent DNA Nanostructure

pH dependence DNA nanodevices lay the foundation for various indispensable applications, exclusively based on the structure of the DNA triplex and i-motif. Both structures are dissociated under near neutral solution and are stable in acidic solution with the presence of the interesting protonation site. However, strict sequence requirements are essential for them to own the pH dependence property, which greatly limits the application of the pH-dependent DNA. The i-motif based pH-dependent DNA nanostructure needs to be C-rich, and the triplex pH-dependent DNA nanostructure needs to be neither polypyrimidine nor polypurine. The capability to design general DNA sequences would help us to know more about the physicochemical nature of DNA and create more applications.

Aiming at addressing the limitation mentioned above, as early as 1992, A^+-C pair was based on the competitive binding of the non-perfectly complementary duplex DNA domain and the complementary strand, and adenine and cytosine were non-perfectly complementary base pairs in the neutral solution (Boulard et al., 1992). But in an acidic condition (e.g., pH = 5.0), adenine is protonated and then is hybridized with cytosine, forming the A^+-C mismatch base pair. In the near neutral condition (e.g., pH = 8.0), A^+ is deprotonated and the A^+-C pair dissociates. Then the A^+-C mismatch pair-based device is used in rationally designing the programmable pH-responsive DNA devices, shown in **Figure 2C** (Siegfried et al., 2010; Thompson et al., 2020).

Fu and coworkers reported a universal principle not for triplex but for i-motif forming pH-responsive DNA sequences design (Fu et al., 2019), in which the binding equilibrium changes could be controlled by the pH value of the external solution environment. To demonstrate this mechanism, they first designed a DNA strand M with the length of 20 nucleotides (nt), and a corresponding hairpin strand contained mismatch base pairs to destabilize the hairpin structure, forming MH5. When the pH value of the solution is 8, the hairpin structure of MH5 is opened and hybridized with M to generate a perfectly matched, continuous, 17-bp-long DNA duplex. When the pH value of the solution is 5, the dangling single-stranded overhang of MH5 can be hybridized back to form a hairpin structure and displace strand M. At the end of their work, they applied the design principle to the hybridization chain reaction (HCR), a common method for signal amplification. Their strategy opens new ways to a wide range of potential applications in the DNA-based nanomachines and gives new ideas into nucleic acid structures *in vivo*.

Taking advantage of the high generality and the programmability of the A^+-C pair-based DNA structure, combining it with other DNA secondary structures, a set of pH-dependent DNA nanodevices would be generated. Taking such structures into account when designing interaction or

folding of nucleic acids in such abnormal pH environment, it would greatly facilitate the development of the DNA nanodevices in the biomedical detection and the field of DNA nanotechnology.

CONCLUSION

In this review, we summarized the recent research on pH-responsive DNA motifs, including triplex DNA, i-motif, and A^+-C mismatch base pair-based DNA structures. By rationally modulating the main elements and utilizing the physicochemical nature of the pH sensitive structures, the application of those devices can be commonly used in the biochemical detection and dynamically regulating the pH response range. The variation of the DNA devices' conditions may lead to revisable conformational changes between the opening and closing states of the pH-dependent nucleic acid structure. In addition to the direct tuning, the pH value can also be fueled by the biocatalytic reaction; for example, urease or glucose oxidase (GOx) has been used in the presence of urea or glucose to motivate the production of the basic or acidic aqueous solution, respectively (Grosso et al., 2015; Gao et al., 2018). Despite the reported accomplishments in applying the pH-responsive DNA motif from rational design to analytical application, some essential future challenges can also be envisaged. For example, the self-assembly of the pH-sensitive DNA-based one-dimensional to three-dimensional nanostructures could generate stimuli-responsive, reconfigurable nanodevices acting as switchable catalytic reservoirs or novel drug carriers. The modification of those DNA nanostructures into single cell and the use of triplex DNA, i-motif structure, and A^+-C mismatched pairs as functional units modulating intercellular functions would be more and more important.

AUTHOR CONTRIBUTIONS

LZ, YL, and JL wrote the manuscript. ZG, JD, and JG reviewed and edited the manuscript. All authors revised the manuscript.

FUNDING

This work was financially supported by the National Natural Science Foundation of China (No. 31800829), the Natural Science Foundation of Hebei Province (No. B2019201397), the Project funded by China Postdoctoral Science Foundation (No. 2020M670678), and the Advanced Talents Incubation Program of Hebei University (No. 521000981136).

REFERENCES

Abendroth, J. M., Bushuyev, O. S., Weiss, P. S., and Barrett, C. J. (2015). Controlling Motion at the Nanoscale: Rise of the Molecular Machines. *ACS nano* 9, 7746–7768. doi:10.1021/acsnano.5b03367

Ablasser, A. (2021). DNA Sensor in Standby Mode during Mitosis. *Science* 371, 1204–1205. doi:10.1126/science.abg7422

Boulard, Y., Cognet, J. A. H., Gabarro-Arpa, J., Le Bret, M., Sowers, L. C., and Fazakerley, G. V. (1992). The PH Dependent Configurations of the C.A Mispair in DNA. *Nucl. Acids Res.* 20, 1933–1941. doi:10.1093/nar/20.8.1933

Chen, B., Wang, Y., Ma, W., Cheng, H., Sun, H., Wang, H., et al. (2020). A Mimosa-Inspired Cell-Surface-Anchored Ratiometric DNA Nanosensor for High-Resolution and Sensitive Response of Target Tumor Extracellular pH. *Anal. Chem.* 92, 15104–15111. doi:10.1021/acs.analchem.0c03250

Chen, Y., Wei, W., Zhu, Y., Luo, J., Liu, R., and Liu, X. (2020). Synthesis of temperature/pH Dual-Stimuli-Response Multicompartmental Microcapsules via Pickering Emulsion for Preprogrammable Payload Release. *ACS Appl. Mater. Inter.* 12, 4821–4832. doi:10.1021/acsami.9b20999

Collie, G. W., and Parkinson, G. N. (2011). The Application of DNA and RNA G-Quadruplexes to Therapeutic Medicines. *Chem. Soc. Rev.* 40, 5867–5892. doi:10.1039/c1cs15067g

Fu, W., Tang, L., Wei, G. H., Zeng, J., Zhan, R., et al. (2019). Rational Design of pH-Responsive DNA Motifs with General Sequence Compatibility. *Angew. Chem. Int. Ed.* 58, 16405–16410. doi:10.1002/anie.201906972

Gao, Z. F., Sann, E. E., Lou, X., Liu, R., Dai, J., Zuo, X., et al. (2018). Naked-eye point-of-care Testing Platform Based on a pH-Responsive Superwetting Surface: toward the Non-invasive Detection of Glucose. *NPG Asia Mater.* 10, 177–189. doi:10.1038/s41427-018-0024-7

Gehring, K., Leroy, J.-L., and Guéron, M. (1993). A Tetrameric DNA Structure with Protonated Cytosine-Cytosine Base Pairs. *Nature* 363, 561–565. doi:10.1038/363561a0

Grosso, E. D., Dallaire, A. M., Vallée-Bélisle, A., and Ricci, F. (2015). Enzyme-operated DNA-Based Nanodevices. *Nano Lett.* 15, 8407–8411. doi:10.1021/acs.nanolett.5b04566

Kay, E. R., and Leigh, D. A. (2015). Rise of the Molecular Machines. *Angew. Chem. Int. Edit.* 54, 70–72. doi:10.1016/j.sbi.2010.01.00610.1002/anie.201503375

Kremarová, M., Gulka, M., Vandenryt, T., Hruby, J., and Nesladek, M. (2021). A Label-free diamond Microfluidic DNA Sensor Based on Activenitrogen-Vacancy center Charge State Control. *ACS Appl. Mater. Inter.* 13, 18500–18510. doi:10.1021/acsami.1c01118

Liao, W.-C., Riutin, M., Parak, W. J., and Willner, I. (2016). Programmed PH-Responsive Microcapsules for the Controlled Release of CdSe/ZnS Quantum Dots. *ACS Nano* 10, 8683–8689. doi:10.1021/acsnano.6b04056

Lu, C.-H., Willner, B., and Willner, I. (2013). DNA Nanotechnology: from Sensing and DNA Machines to Drug-Delivery Systems. *ACS Nano* 7, 8320–8332. doi:10.1021/nn404613v

Maher, L. J., Dervan, P. B., and Wold, B. J. (1990). Kinetic Analysis of Oligodeoxyribonucleotide-Directed Triple-helix Formation on DNA. *Biochemistry* 29, 8820–8826. doi:10.1021/bi00489a045

Manish, D., Fatma, K., and Dash, J. (2019). Chemical Regulation of DNA I-motifs for Nanobiotechnology and Therapeutics. *Angew. Chem.* 131, 2968–2983. doi:10.1002/ange.201813288

Mariottini, D., Idili, A., Nijenhuis, M. A. D., Ercolani, G., and Ricci, F. (2019). Entropy-Based Rational Modulation of the pKa of a Synthetic pH-dependent Nanoswitch. *J. Am. Chem. Soc.* 141, 11367–11371. doi:10.1021/jacs.9b04168

Modi, S., Nizak, C., Surana, S., Halder, S., and Krishnan, Y. (2013). Two DNA Nanomachines Map pH Changes along Intersecting Endocytic Pathways inside the Same Cell. *Nat. Nanotech* 8, 459–467. doi:10.1038/nnano.2013.92

Nesterova, I. V., and Nesterov, E. E. (2014). Rational Design of Highly Responsive pH Sensors Based on DNA I-Motif. *J. Am. Chem. Soc.* 136, 8843–8846. doi:10.1021/ja501859w

Plum, G. E., Park, Y. W., Singleton, S. F., Dervan, P. B., and Breslauer, K. J. (1990). Thermodynamic Characterization of the Stability and the Melting Behavior of a DNA Triplex: a Spectroscopic and Calorimetric Study. *Proc. Natl. Acad. Sci.* 87, 9436–9440. doi:10.1073/pnas.87.23.9436

Ranallo, S., Porchetta, A., and Ricci, F. (2019). DNA-based Scaffolds for Sensing Applications. *Anal. Chem.* 91, 44–59. doi:10.1021/acs.analchem.8b05009

Ranallo, S., Rossetti, M., Plaxco, K. W., Vallée-Bélisle, A., and Ricci, F. (2015). A Modular, DNA-Based Beacon for Single-Step Fluorescence Detection of

Antibodies and Other Proteins. *Angew. Chem. Int. Ed.* 54, 13214–13218. doi:10.1002/ange.20150517910.1002/anie.201505179

Rullo, A., Reiner, A., Reiter, A., Trauner, D., Isacoff, E. Y., and Woolley, G. A. (2014). Long Wavelength Optical Control of Glutamate Receptor Ion Channels Using a Tetra-Ortho-Substituted Azobenzene Derivative. *Chem. Commun.* 50, 14613–14615. doi:10.1039/c4cc06612j

Shindo, H., Torigoe, H., and Sarai, A. (1993). Thermodynamic and Kinetic Studies of DNA Triplex Formation of an Oligohomopyrimidine and a Matched Duplex by Filter Binding Assay. *Biochemistry* 32, 8963–8969. doi:10.1021/bi00085a030

Siegfried, N. A., O'Hare, B., and Bevilacqua, P. C. (2010). Driving Forces for Nucleic Acid pKa Shifting in an A+·C Wobble: Effects of Helix Position, Temperature, and Ionic Strength. *Biochemistry* 49, 3225–3236. doi:10.1021/bi901920g

Simon, A. J., Vallée-Bélisle, A., Ricci, F., and Plaxco, K. W. (2014). Intrinsic Disorder as a Generalizable Strategy for the Rational Design of Highly Responsive, Allosterically Cooperative Receptors. *Proc. Natl. Acad. Sci. USA* 111, 15048–15053. doi:10.1073/pnas.1410796111

Singleton, S. F., and Dervan, P. B. (1992). Thermodynamics of Oligodeoxyribonucleotide-Directed Triple helix Formation: an Analysis Using Quantitative Affinity Cleavage Titration. *J. Am. Chem. Soc.* 114, 6957–6965. doi:10.1021/ja00044a002

Soto, A. M., Loo, J., and Marky, L. A. (2002). Energetic Contributions for the Formation of TAT/TAT, TAT/CGC+, and CGC+/CGC+Base Triplet Stacks. *J. Am. Chem. Soc.* 124, 14355–14363. doi:10.1021/ja026952h2002

Surana, S., Bhat, J. M., Koushika, S. P., and Krishnan, Y. (2011). An Autonomous DNA Nanomachine Maps Spatiotemporal pH Changes in a Multicellular Living Organism. *Nat. Commun.* 2, 340. doi:10.1038/ncomms1340

Tani, H., Yamaguchi, M., Enomoto, Y., Matsumura, Y., Habe, H., Nakazato, T., et al. (2021). Naked-eye Detection of Specific DNA Sequences Amplified by the Polymerase Chain Reaction with Nanocomposite Beads. *Anal. Biochem.* 617, 114114–114. doi:10.1016/j.ab.2021.114114

Thompson, I. A. P., Zheng, L., Eisenstein, M., and Soh, H. T. (2020). Rational Design of Aptamer Switches with Programmable pH Response. *Nat. Commun.* 11, 2946. doi:10.1038/s41467-020-16808-2

Wärmländer, S., Sandström, K., Leijon, M., and Gräslund, A. (2003). Base-Pair Dynamics in an Antiparallel DNA Triplex Measured by Catalyzed Imino Proton Exchange Monitored via1H NMR Spectroscopy†. *Biochemistry* 42, 12589–12595. doi:10.1021/bi034479u

Wickham, S. F. J., Bath, J., Katsuda, Y., Endo, M., Hidaka, K., Sugiyama, H., et al. (2012). A DNA-Based Molecular Motor that Can Navigate a Network of Tracks. *Nat. Nanotech* 7, 169–173. doi:10.1038/nnano.2011.253

Zhang, D. Y., and Seelig, G. (2011). Dynamic DNA Nanotechnology Using Strand-Displacement Reactions. *Nat. Chem* 3, 103–113. doi:10.1038/nchem.957

Conflict of Interest: The authors declare that the research was conducted in the absence of any commercial or financial relationships that could be construed as a potential conflict of interest.

Publisher's Note: All claims expressed in this article are solely those of the authors and do not necessarily represent those of their affiliated organizations, or those of the publisher, the editors and the reviewers. Any product that may be evaluated in this article, or claim that may be made by its manufacturer, is not guaranteed or endorsed by the publisher.

frontiers in Chemistry

ORIGINAL RESEARCH
published: 22 September 2021
doi: 10.3389/fchem.2021.744099

Injectable Hydrogel Based on Modified Gelatin and Sodium Alginate for Soft-Tissue Adhesive

Yuhang Xing[1†], Xueqin Qing[2†], Hao Xia[1†], Shiqi Hao[1], Haofang Zhu[1], Yiyan He[1,3,4], Hongli Mao[1,3,4] and Zhongwei Gu[1,3,4]**

[1]Research Institute for Biomaterials, Tech Institute for Advanced Materials, College of Materials Science and Engineering, Nanjing Tech University, Nanjing, China, [2]Department of Pediatrics, Shanghai General Hospital, School of Medicine, Shanghai Jiao Tong University, Shanghai, China, [3]NJTech-BARTY Joint Research Center for Innovative Medical Technology, Nanjing, China, [4]Suqian Advanced Materials Industry Technology Innovation Center of Nanjing Tech University, Nanjing, China

To assist or replace the traditional suture techniques for wound closure, soft-tissue adhesives with excellent adhesion strength and favorable biocompatibility are of great significance in biomedical applications. In this study, an injectable hydrogel tissue adhesive containing adipic acid dihydrazide–modified gelatin (Gel-ADH) and oxidized sodium alginate (OSA) was developed. It was found that this tissue adhesive possessed a uniform structure, appropriate swelling ratio, good injectability, and excellent hemocompatibility and cytocompatibility. The adhesion capacity of the developed adhesive with optimized component and concentration was stronger than that of the commercial adhesive Porcine Fibrin Sealant Kit. All these results suggested that the developed hydrogel was a promising candidate for a soft-tissue adhesive.

Keywords: soft-tissue adhesive, sodium alginate, gelatin, Schiff base reaction, hydrogel

OPEN ACCESS

Edited by:
Houjuan Zhu,
*Institute of Materials Research and Engineering (A*STAR), Singapore*

Reviewed by:
Shasha He,
Nanyang Technological University, Singapore
Xiaojun Zhou,
Donghua University, China

****Correspondence:***
Hongli Mao
h.mao@njtech.edu.cn
Zhongwei Gu
zwgu1006@hotmail.com

[†]These authors have contributed equally to this work and share first authorship

Specialty section:
This article was submitted to Nanoscience, a section of the journal Frontiers in Chemistry

Received: *19 July 2021*
Accepted: *02 August 2021*
Published: *22 September 2021*

Citation:
Xing Y, Qing X, Xia H, Hao S, Zhu H, He Y, Mao H and Gu Z (2021) Injectable Hydrogel Based on Modified Gelatin and Sodium Alginate for Soft-Tissue Adhesive. Front. Chem. 9:744099. doi: 10.3389/fchem.2021.744099

INTRODUCTION

Rapid hemostasis and effective wound closure are very important in wound repair. Conventional suturing is usually time consuming and cannot close the wound immediately, which can lead to a variety of pathologic scenarios, such as tissue morbidities and mortalities (Geng et al., 2020; Zhu et al., 2020). Sutureless wound closure, which primarily utilizes medical adhesives, shows adequate ability in wound sealing and healing with less pain and scars (Gowda et al., 2020; Zhou et al., 2021). In addition, compared to conventional suture, it is more acceptable by the patient. Therefore, there are different types of medical adhesives have been developed in recent years. However, most of the available adhesives have certain limitations. For example, fibrin glue has favorable biocompatibility and can facilitate wound repair, but it cannot be used alone because of its unreliable mechanical and adhesion capacity. Besides, it is rather expensive and may lead to a risk of blood-borne disease or virus infections (Du et al., 2020; Gao et al., 2020). In comparison with fibrin glue, cyanoacrylates have much stronger adhesion capacity, but the excessive heat and the cytotoxic byproducts produced in the fast polymerization process during bonding are a major concern (Lv et al., 2021). Additionally, their poor elasticity cannot accommodate the movement of soft tissues under a highly dynamic physiological environment (Li et al., 2020; Zhao et al., 2021). Therefore, development of ideal medical adhesives with good biocompatibility, sufficient mechanical property, tunable biodegradability, and rapid and strong adhesion has a great application value in wound closure and healing (Neuffer et al., 2004; Gillman et al., 2020).

Herein, by mimicking the composition of the extracellular matrix (ECM) of native tissues, a strategy to prepare adhesives with good biocompatibility and multiple functions, from polypeptide and polysaccharide, was proposed (Yang et al., 2017; Ke et al., 2020). Firstly, gelatin was modified with adipic acid dihydrazide (Gel-ADH) and sodium alginate was oxidized (OSA) with $NaIO_4$. Then, the hydrogel adhesive was prepared through the Schiff base reaction between Gel-ADH and OSA. The results showed that the Gel-ADH/OSA hydrogel had an appropriate swelling ratio, good injectability, excellent biocompatibility, and improved adhesion capacity.

MATERIALS AND METHODS

Materials

Sodium alginate (low viscosity), gelatin (from porcine skin), and sodium periodate ($NaIO_4$) were purchased from Aladdin Industrial Corporation (Shanghai, China). Dulbecco's modified Eagle medium (DMEM) and fetal bovine serum (FBS) were purchased from Life Technologies Corporation (California, United States). A Porcine Fibrin Sealant Kit was purchased from Guangzhou Bioseal Biotech Co., Ltd. All other chemicals were purchased from Sigma-Aldrich and used as received unless specified otherwise.

Preparation of OSA

Oxidized sodium alginate was synthesized as reported previously (Yuan et al., 2018). Briefly, 3.00 g raw sodium alginate (SA) was dissolved in ultrapure water (300 ml) and 4.86 g $NaIO_4$ was added. After that, the mixed solution was stirred for another 4 h without light, and then 5 ml ethylene glycol was added in the mixed solution to terminate the oxidation. The final product was dialyzed (MWCO = 3,500 Da) for 3 days in distilled water. Finally, the product was lyophilized. To confirm the characteristic peak of the aldehyde group in OSA, a Fourier transform infrared (FTIR) spectroscope (Nicolet IS 10, Thermo Scientific, United States) was used and the measurement was performed at room temperature and recorded in the 4,000–400 cm^{-1} range.

Preparation of Gel-ADH

To synthesize ADH-modified gelatin, 3.00 g gelatin and 2.40 g adipic acid dihydrazide were dissolved in 300 ml ultrapure deionized water with stirring at 55°C. Then, 0.50 g EDC and 0.50 g HOBt were added to the solution. Finally, 0.1 M HCl solution was used to adjust the pH of the abovementioned solution to 5. The mixed solution was stirred overnight. The final product was dialyzed (MWCO = 7,000 Da) for 5 days in distilled water (Hozumi et al., 2018). The ^1H NMR spectra of the Gel-ADH was measured by using a 600 Hz NMR spectrometer (JNM-ECZR-600 Hz, JEOL, United States)

Degree of Oxidation Study

The degree of oxidation was obtained by the titration method (Reakasame and Boccaccini, 2018). In brief, W g OSA, 5 ml anhydrous ethanol, and 5 ml hydroxylamine hydrochloride solution were added in a flask. Then, the solution was heated to reflux for 3 h and left to set for at least another 2 h. When the solution was cooled to room temperature, 0.1 M NaOH was used to titrate the mixture. When the color of the mixed solution became yellow, the titration was stopped and the volume (V_1) of the titrimetric NaOH solution was recorded immediately. Then, 5 ml anhydrous ethanol and 5 ml hydroxylamine hydrochloride solution were added to another flask. The previous steps were repeated and the volume (V_2) of titrimetric NaOH solution was recorded. The oxidation degree (OD) was calculated by the following **Equation**:

$$OD(\%) = 198 \times 0.1 \times \frac{V_1 - V_2}{2W} \times 100. \quad (1)$$

Preparation of Gel-ADH/OSA Hydrogels

Lyophilized OSA and Gel-ADH were dissolved in the PBS solution (pH = 7.4). The prepolymer concentration was 10, 15, and 20% (w/v), respectively. The Gel-ADH and OSA solution were added to a glass bottle to prepare the four types of hydrogels. The volume ratio of the Gel-ADH and OSA solution was 1:1 and 2:1, respectively. The prepared hydrogels were represented as 10% Gel-ADH/OSA 1:1, 15% Gel-ADH/OSA 1:1, 20% Gel-ADH/OSA 1:1, and 20% Gel-ADH/OSA 2:1 accordingly.

Gelation Time of the Gel-ADH/OSA Hydrogel

Gelation time was measured at room temperature by tilt tests. Briefly, four abovementioned types of mixed solutions were injected into glass test tubes immediately after preparation. The tube was tilted horizontally every second, and then, the time when the solution did not have any flow was recorded as the gelation time.

Swelling Behavior of the Gel-ADH/OSA Hydrogel

The hydrogel samples were lyophilized and immersed in PBS (pH = 7.4). The initial weight of the lyophilized hydrogel was recorded as W_0. After 12 and 24 h, the hydrogel samples were taken out from the PBS solution and the PBS on the surface of the hydrogels was wiped with filter papers. The weight of the hydrogels at predetermined intervals was recorded as W_t. The swelling ratio was calculated as follows:

$$Swelling\ ratio\ (\%) = \frac{W_t - W_0}{W_0} \times 100\,\%. \quad (2)$$

Micromorphology of the Gel-ADH/OSA Hydrogel

The microstructure of the lyophilized Gel-ADH/OSA hydrogel was observed by SEM (XL30 ESEM, Philips, Netherlands). The freeze-dried hydrogels were put on a platform and coated with a

gold layer. Then, the cross-sectional morphology images were observed by SEM.

Hemolytic Activity of the Gel-ADH/OSA Hydrogel

The erythrocytes were extracted from the fresh mouse blood by centrifugation (1,000 rpm, 5 min) and diluted to 5% (v/v) with PBS solution (pH = 7.4). The prepared four types of hydrogels were mixed with the erythrocytes solution and incubated for 3 h (37°C). Finally, the mixtures were centrifuged at 2,500 rpm for 10 min and the absorbance of the supernatant from each tube was obtained by using a microplate reader (MK3, Thermo, United States) at 540 nm. The percentage of hemolysis was calculated as follows:

$$Hemolysis\ (\%) = \frac{OD_{\mathrm{m}} - OD_p}{OD_{\mathrm{w}} - OD_p} \times 100\,\%, \tag{3}$$

where OD_p, OD_w, and OD_m were the absorbance of the supernatant obtained from the erythrocytes mixture with PBS, ultrapure H_2O, and prepared hydrogels, respectively. Cells treated with the PBS solution were used as a positive control, while cells treated with H_2O were used as a negative control. The hemolytic activity was measured in triplicate.

Cytocompatibility of the Gel-ADH/OSA Hydrogel

The cytocompatibility of the hydrogels to L929 cells was evaluated by the CCK-8 method (Zhang et al., 2020). Briefly, the cells were incubated in DMEM supplemented with 10% FBS and 1% penicillin–streptomycin solution at 37°C with 5% CO_2. The four abovementioned types of hydrogels were prepared in 96-well plates at 37°C, and the cells (5×10^3 cells/well) were cultured with the hydrogels. After 1 and 3 days, 10 μl of CCK-8 was added to each well and incubated for another 2 h. Finally, the absorbance of each well was obtained by using a microplate reader (MK3, Thermo, United States) at 450 nm. The hydrogel-free DMEM was used as a control. The viability of cells was measured in triplicate.

Rheological Analysis

The rheological measurements of the hydrogels were conducted by using a rheometer (MCR 302, Anton Paar, Austria) at 25°C. A 20% Gel-ADH/OSA 1:1 hydrogel was placed on a 25 mm diameter parallel plate of the rheometer. A shear-thinning test using the Gel-ADH/OSA adhesive was measured with a shear rate in the range of 0–200 1/s.

Adhesive Capacity of the Gel-ADH/OSA Hydrogel

A tissue adhesion capacity test was performed using fresh porcine skins. The porcine skins were immersed in PBS (pH = 7.4) overnight before use. Then, the porcine skins were cut into two oblong samples (6 cm × 1.5 cm). A 200 μl of Gel-ADH solution was applied on the first porcine skin, and 200 μl of OSA solution was applied on the second porcine skin. After that, two porcine skins were overlapped and the contacting area was 2 cm × 1.5 cm. Finally, the porcine skins were loaded 50 g for 5 min. The adhesion capacity (kPa) was recorded with a universal tester at a rate of 10 mm/min.

Statistical Analysis

All samples were measured in triplicate, and the data were represented as mean ± standard deviation (SD). All data were analyzed by one-way analysis of variance (*ANOVA*), and a value of $p < 0.05$ was considered to be statistically significant.

RESULTS AND DISCUSSION

Synthesis and Characterization of OSA and Gel-ADH

The preparation scheme of OSA and Gel-ADH is shown in **Figure 1**. **Figure 2A** shows the FTIR spectra of SA and OSA. Compared with the spectra of SA, a new absorption peak at 1726 cm^{-1} which is due to the aldehyde group was observed in OSA. The oxidation degree of OSA used in this study was about 79%. The ^1H NMR spectra of Gel and Gel-ADH are shown in **Figure 2B**. Compared with the curve of Gel, new methylene peaks of ADH at 2.07 and 1.46 ppm were found in the Gel-ADH, indicating that gelatin was successfully modified with adipic acid dihydrazide. The degree of substitution (DS) of ADH, defined as the number of ADH moieties per 100 carboxyl groups of gelatin, was determined from the ^1H NMR spectra (**Figure 2B**) by comparing the integrals of signals at 1.46 ($A_{1.46}$) and 2.60 ppm ($A_{2.60}$). DS, which was expressed as $A_{1.46}/(A_{1.46} + A_{2.60}) \times 100\%$ (Yan et al., 2017), was calculated to be 67%.

Characterization of the Gel-ADH/OSA Hydrogel

Without further treatment, the sol-gel transition of the Gel-ADH/OSA hydrogel occurred relatively fast, as indicated by tilt tests (**Figure 3A**). Meanwhile, the hydrogel adhesive developed here was completely transparent and would not cover the underlying tissues when used by surgeons. **Figure 3B** shows the gelation time of the Gel-ADH/OSA hydrogel with different components and concentrations. The gelation time of 10% Gel-ADH/OSA 1:1, 10% Gel-ADH/OSA 1:1, 15% Gel-ADH/OSA 1:1, and 20% Gel-ADH/OSA 2:1 was 16.7, 11.3, 8.7, and 9.3 s, respectively. For wound sealing, the gelation time of the hydrogel adhesive can affect the hemostasis of damaged tissues. Some commercial tissue adhesives have strong adhesion capacity, but the gelation time is too slow, which may not be enough to stop bleeding in the event of a sudden loss of blood (Qiao et al., 2021). Here, the gelation time of 20% Gel-ADH/OSA 1:1 and 20% Gel-ADH/OSA 2:1 was under 10 s. The Gel-ADH/OSA hydrogel with higher concentration had more amino and aldehyde groups to accelerate the Schiff base reaction rate.

An appropriate swelling ratio is an important prerequisite for medical tissue adhesive to maintain a lasting and stable adhesion

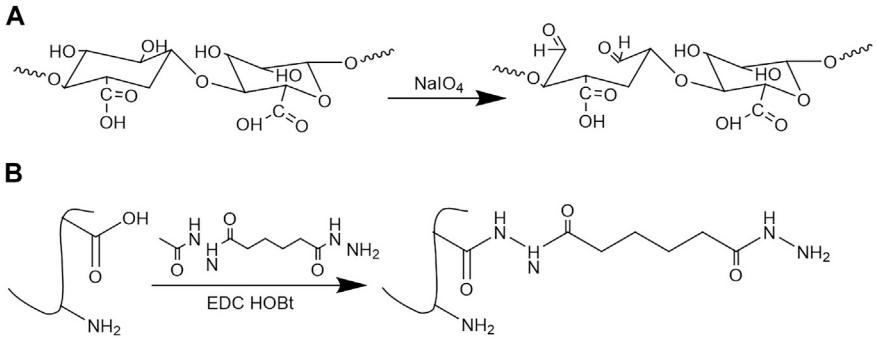

FIGURE 1 | Synthesis of **(A)** oxidized sodium alginate (OSA) and **(B)** adipic acid dihydrazide–modified gelatin (Gel-ADH).

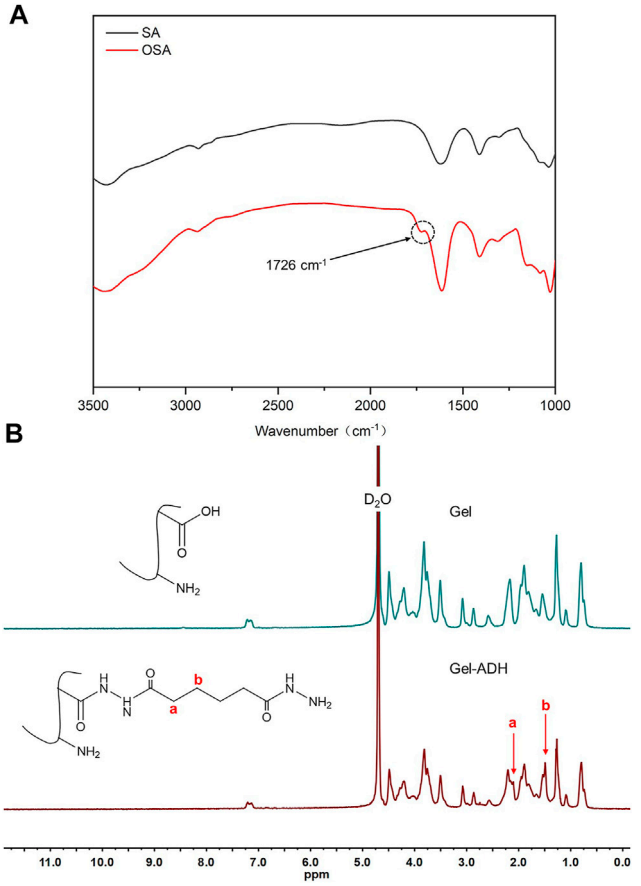

FIGURE 2 | (A) FTIR spectra of SA and OSA. **(B)** ^{1}H NMR spectra of Gel and Gel-ADH.

effect *in vivo* (Liang et al., 2021). If the swelling ratio is too high, the adhesive will squeeze the trauma area, which is not conducive to the adhesion of the wound. The swelling ratio of Gel-ADH/OSA adhesive is dependent on the prepolymer component and concentration. As shown in **Figure 3C**, with the increase of prepolymer concentration or the content of Gel-ADH, the swelling ratio decreased which may be caused by the increased internal cross-linking sites in the system. This result indicated that the dense network restricted the expansion of the hydrogel. The swelling ratio of 15% Gel-ADH/OSA 1:1, 20% Gel-ADH/OSA 1:1, and 20% Gel-ADH/OSA 2:1 was under 1,000%. However, the swelling ratio of 10% Gel-ADH/OSA 1:1 decreased after 24 h, probably because of its low concentration, resulting in faster rate of degradation. All these studies proved that Gel-ADH/OSA had good swelling ratio and excellent biodegradability.

Figure 3D shows the internal microscopic morphology of the lyophilized hydrogel characterized by scanning electron microscopy. With the increase of the Gel-ADH component and prepolymer concentration, the porosity decreased gradually. Meanwhile, a uniform microstructure usually provides better mechanical properties theoretically for hydrogels (Pourjavadi et al., 2020). The network structure of Gel-ADH/OSA adhesive presented a high degree of homogeneity.

Biocompatibility of the Gel-ADH/OSA Hydrogel *In Vitro*

It is well known that one of the key factors hindering the wide application of biomedical adhesives is their toxic and side effects on cells or their degradation products that can lead to wound tissue infection and necrosis. To investigate the biocompatibility of the Gel-ADH/OSA hydrogel, L929 cells were employed and directly incubated with the Gel-ADH/OSA hydrogel. Then, the CCK-8 assay and live/dead staining were performed on the first and third day of incubation (**Figures 4A,B**). Compared to that of the control group, cells cultured with Gel-ADH/OSA hydrogels with different compositions and concentrations showed a survival rate higher than 90% at both day 1 and day 3, indicating the hydrogels have no obvious negative effect on cell viability. This result was also consistent with the live/dead staining (**Figure 4B**). Most of the cells were stained green in all the groups.

Meanwhile, a hemolysis test was carried out to investigate the hemocompatibility of Gel-ADH/OSA hydrogels. The gross appearance of the erythrocytes after been treated with the solution of PBS, Gel-ADH/OSA hydrogels with

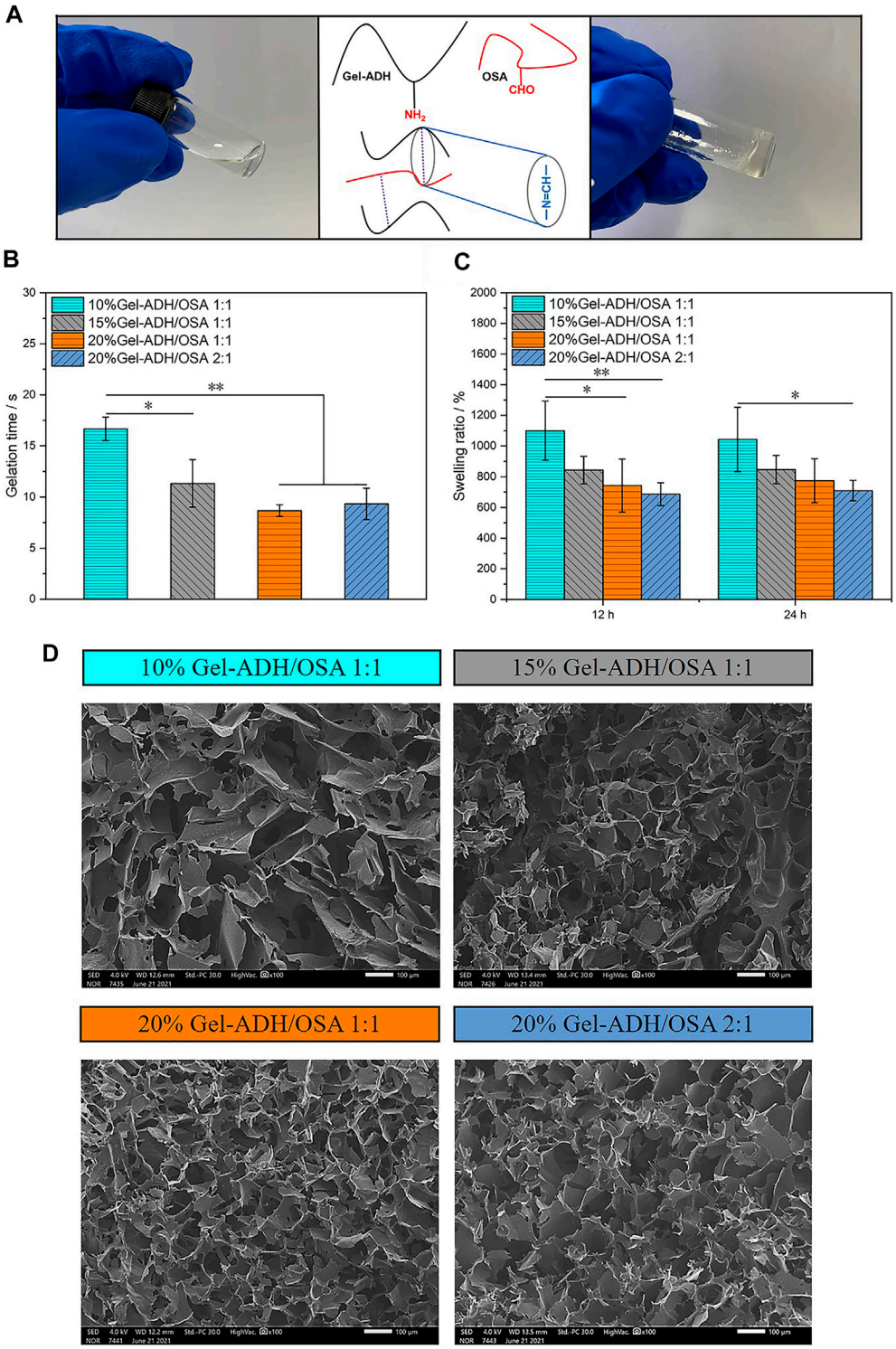

FIGURE 3 | (A) Schematic illustration of the preparation of Gel-ADH/OSA hydrogels. **(B)** Gelation time, **(C)** swelling ratio, and **(D)** SEM images of Gel-ADH/OSA hydrogels with different components and concentrations (scale bar = 100 μm, $^{*}p < 0.05$, $^{**}p < 0.01$, $n = 3$).

different compositions and concentrations, and pure water is shown in **Figure 4C**. The solutions from Gel-ADH/OSA hydrogels were found to be light red, which was similar to those of the PBS group, while the water group showed bright red color. **Figure 4D** shows the quantitative analysis result of the hemolysis test, and the hemolysis ratios of Gel-ADH/OSA

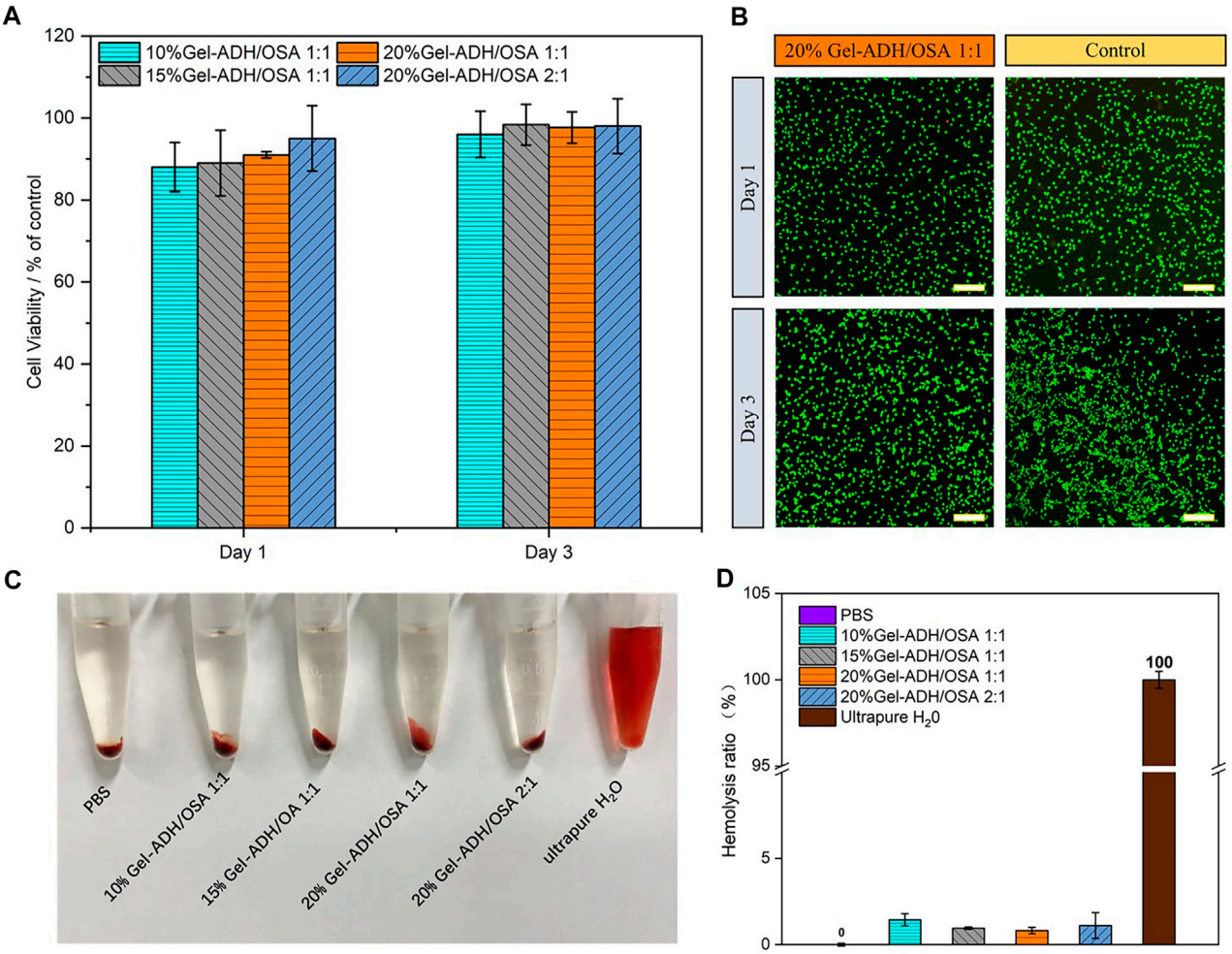

FIGURE 4 | (A) Cell viability assay of L929 cells after being incubated with Gel-ADH/OSA hydrogels with different components and concentrations for 1 and 3 days **(B)** Live/dead staining of L929 cells after being incubated with the 20% Gel-ADH/OSA 1:1 hydrogel for 1 and 3 days (scale bar = 100 μm). **(C)** Image and **(D)** quantitative analysis of the hemolytic activity of Gel-ADH/OSA hydrogels with different components and concentrations.

hydrogels were 0.82–1.44%, indicating Gel-ADH/OSA hydrogels have excellent hemocompatibility.

Rheological and Tissue Adhesion Capacity of Gel-ADH/OSA Hydrogels

To check whether the Gel-ADH/OSA adhesive has a shear-thinning property, a static shear rate sweep was performed. As shown in **Figure 5A**, with the increase of shear rate, the viscosity of the hydrogel decreased rapidly. When the shearing rate was 15 1/s, the 10% Gel-ADH/OSA 1:1 and 20% Gel-ADH/OSA 2:1 had a low viscosity of 18 Pas. When the shearing rate was 18 1/s, the 15% Gel-ADH/OSA 1:1 and 20% Gel-ADH/OSA 1:1 had a low viscosity of 9 Pas. Therefore, the Gel-ADH/OSA adhesive was shear-thinning because of dynamic Schiff base covalent bonding. As shown in **Figure 5B**, the Gel-ADH/OSA adhesive had excellent injectability in the process of application (Yang et al., 2020).

To explore the adhesion capacity of Gel-ADH/OSA hydrogels *in vitro*, standard shear and peer tests were performed (Suneetha et al., 2019) (**Figures 5C,D**). As shown in **Figure 5**, with the increase of prepolymer concentration, the shear and peer stress of Gel-ADH/OSA hydrogels increased significantly. That is because the gelatin and sodium alginate are sticky inherently, and the Gel-ADH/OSA hydrogel with higher concentration had more amino and aldehyde groups to accelerate the Schiff base reaction rate. Meanwhile, the high oxidation degree of OSA would accelerate cross-linked reactions and improve the adhesive strength of the hydrogel. Since the 20% Gel-ADH/OSA 1:1 has more sites to react with amino groups on the surface of skin tissue, the lap shear strength (45 ± 14 kPa) and peel stress (28 ± 6 kPa) were higher than those of other groups, including the commercial adhesive Porcine Fibrin Sealant Kit. Previous studies also showed that the Fibrin Sealant has limited adhesion strength (Chow et al., 2021). To further confirm the biomedical application potential of the hydrogel adhesive, wound sealing and healing investigation will be performed in the future animal studies.

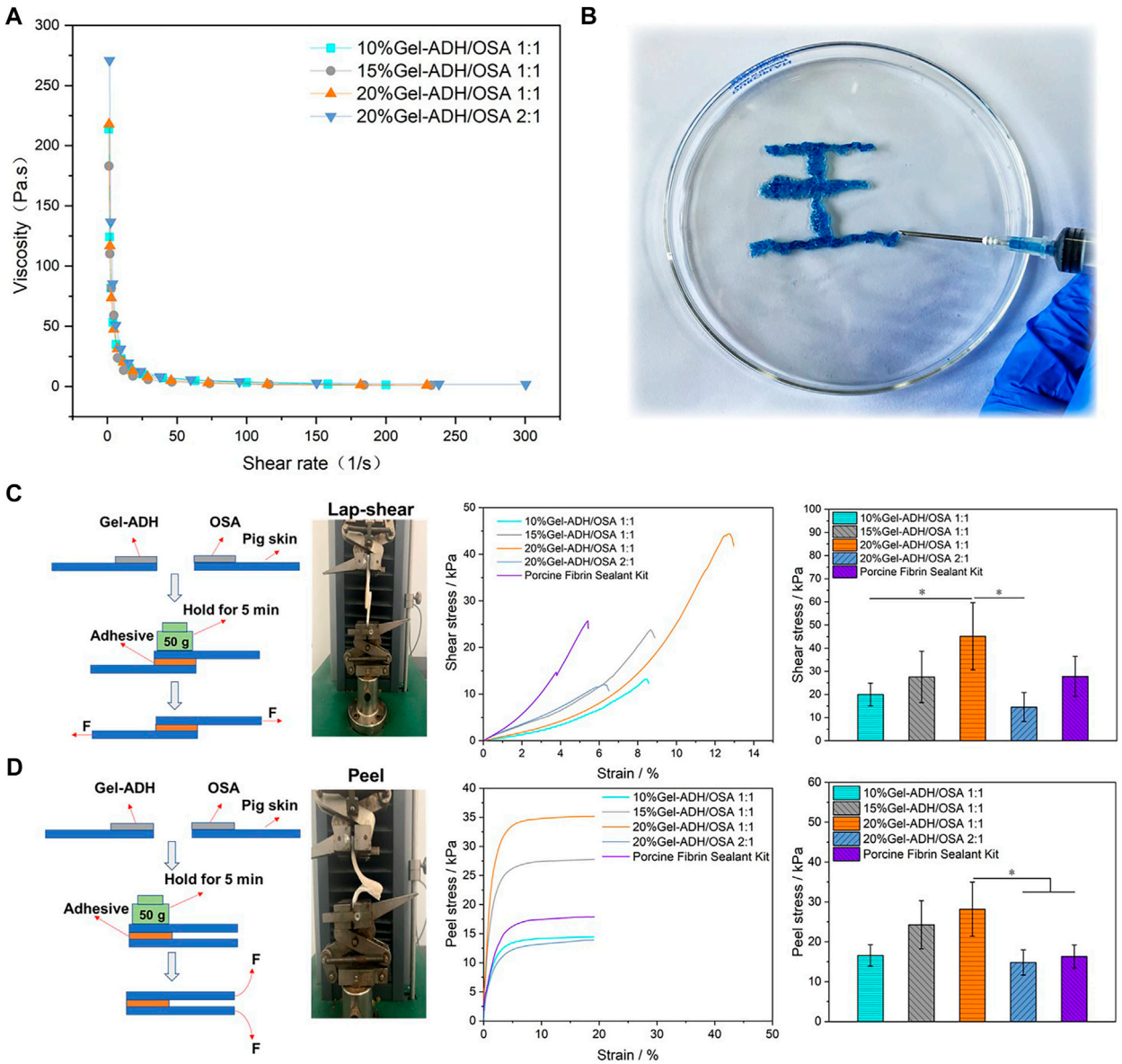

FIGURE 5 | (A) Shear-thinning ability of Gel-ADH/OSA hydrogels with different components and concentrations. **(B)** Injectability of the 20% Gel-ADH/OSA 1:1 hydrogel. A schematic and quantitative analysis of **(C)** a standard lap shear test and **(D)** a standard peel test using Gel-ADH/OSA hydrogels with different components and concentrations. A commercialized Porcine Fibrin Sealant Kit served as the control (*$p < 0.05$, $n = 3$).

CONCLUSION

In this study, an injectable hydrogel tissue adhesive was developed, and the hydrogel showed a suitable swelling ratio, good injectability, and excellent biocompatibility. We also found that the adhesion capacity was related to the prepolymer component and concentration. The 20% Gel-ADH/OSA 1:1 hydrogel showed the highest adhesion ability, which was also higher than that of the commercial Porcine Fibrin Sealant Kit. All these results suggested that the polysaccharide-based hydrogel was a promising candidate for a soft tissue adhesive.

DATA AVAILABILITY STATEMENT

The original contributions presented in the study are included in the article/Supplementary Material; further inquiries can be directed to the corresponding authors.

AUTHOR CONTRIBUTIONS

HM and ZG contributed to the conception and design of the study. YX, HX, and SH performed the experiments. YX wrote the first draft of the article. HX, SH, and HZ wrote sections of

the article. HM, XQ, YH, and ZG performed the statistical analysis and writing—review and editing. All authors contributed to article revision, read, and approved the submitted version.

FUNDING

This work was supported by the Key R&D Plan of Jiangsu Province (BE2018010-3), the National Natural Science Foundation of China (31800803, 31771067, and 32071364), and the Scientific Research Foundation for Talent Introduction of Nanjing Tech University (39803129 and 39803130).

ACKNOWLEDGMENTS

The authors gratefully acknowledge the Priority Academic Program Development of Jiangsu Higher Education Institutions (PAPD).

REFERENCES

Chow, N., Miears, H., Cox, C., and MacKay, B. (2021). Fibrin Glue and its Alternatives in Peripheral Nerve Repair. *Ann. Plast. Surg.* 86 (1), 103–108. doi:10.1097/sap.0000000000002408

Du, X., Hou, Y., Wu, L., Li, S., Yu, A., Kong, D., et al. (2020). An Anti-infective Hydrogel Adhesive with Non-swelling and Robust Mechanical Properties for Sutureless Wound Closure. *J. Mater. Chem. B* 8 (26), 5682–5693. doi:10.1039/d0tb00640h

Gao, L., Chen, J., Feng, W., Song, Q., Huo, J., Yu, L., et al. (2020). A Multifunctional Shape-Adaptive and Biodegradable Hydrogel with Hemorrhage Control and Broad-Spectrum Antimicrobial Activity for Wound Healing. *Biomater. Sci.* 8 (24), 6930–6945. doi:10.1039/d0bm00800a

Geng, H., Cui, J., and Hao, J. (2020). Mussel-Inspired Hydrogels for Tissue Healing. *Acta Chim. Sinica* 78 (2), 105–113. doi:10.6023/a19080301

Gillman, N., Lloyd, D., Bindra, R., Ruan, R., and Zheng, M. (2020). Surgical Applications of Intracorporal Tissue Adhesive Agents: Current Evidence and Future Development. *Expert Rev. Med. Devices* 17 (5), 443–460. doi:10.1080/17434440.2020.1743682

Gowda, A. H. J., Bu, Y., Kudina, O., Krishna, K. V., Bohara, R. A., Eglin, D., et al. (2020). Design of Tunable Gelatin-Dopamine Based Bioadhesives. *Int. J. Biol. Macromolecules* 164, 1384–1391. doi:10.1016/j.ijbiomac.2020.07.195

Hozumi, T., Kageyama, T., Ohta, S., Fukuda, J., and Ito, T. (2018). Injectable Hydrogel with Slow Degradability Composed of Gelatin and Hyaluronic Acid Cross-Linked by Schiff's Base Formation. *Biomacromolecules* 19 (2), 288–297. doi:10.1021/acs.biomac.7b01133

Ke, X., Dong, Z., Tang, S., Chu, W., Zheng, X., Zhen, L., et al. (2020). A Natural Polymer Based Bioadhesive with Self-Healing Behavior and Improved Antibacterial Properties. *Biomater. Sci.* 8 (15), 4346–4357. doi:10.1039/d0bm00624f

Li, D. W., Chen, J., Wang, X., Zhang, M. M., Li, C. L., and Zhou, J. (2020). Recent Advances on Synthetic and Polysaccharide Adhesives for Biological Hemostatic Applications. *Front. Bioeng. Biotechnol.* 8, 16. doi:10.3389/fbioe.2020.00926

Liang, Y., Li, Z., Huang, Y., Yu, R., and Guo, B. (2021). Dual-Dynamic-Bond Cross-Linked Antibacterial Adhesive Hydrogel Sealants with On-Demand Removability for Post-Wound-Closure and Infected Wound Healing. *Acs Nano* 15 (4), 7078–7093. doi:10.1021/acsnano.1c00204

Lv, C., Li, L., Jiao, Z., Yan, H., Wang, Z., Wu, Z., et al. (2021). Improved Hemostatic Effects by Fe3+ Modified Biomimetic PLLA Cotton-like Mat via Sodium Alginate Grafted with Dopamine. *Bioactive Mater.* 6 (8), 2346–2359. doi:10.1016/j.bioactmat.2021.01.002

Neuffer, M. C., McDivitt, J., Rose, D., King, K., Cloonan, C. C., and Vayer, J. S. (2004). Hemostatic Dressings for the First Responder: A Review. *Mil. Med.* 169 (9), 716–720. doi:10.7205/milmed.169.9.716

Pourjavadi, A., Tavakolizadeh, M., Hosseini, S. H., Rabiee, N., and Bagherzadeh, M. (2020). Highly Stretchable, Self-adhesive, and Self-healable Double Network Hydrogel Based on Alginate/polyacrylamide with Tunable Mechanical Properties. *J. Polym. Sci.* 58 (15), 2062–2073. doi:10.1002/pol.20200295

Qiao, Z., Lv, X., He, S., Bai, S., Liu, X., Hou, L., et al. (2021). A Mussel-Inspired Supramolecular Hydrogel with Robust Tissue Anchor for Rapid Hemostasis of Arterial and Visceral Bleedings. *Bioactive Mater.* 6 (9), 2829–2840. doi:10.1016/j.bioactmat.2021.01.039

Reakasame, S., and Boccaccini, A. R. (2018). Oxidized Alginate-Based Hydrogels for Tissue Engineering Applications: A Review. *Biomacromolecules* 19 (1), 3–21. doi:10.1021/acs.biomac.7b01331

Suneetha, M., Rao, K. M., and Han, S. S. (2019). Mussel-Inspired Cell/Tissue-Adhesive, Hemostatic Hydrogels for Tissue Engineering Applications. *ACS Omega* 4 (7), 12647–12656. doi:10.1021/acsomega.9b01302

Yan, S., Wang, T., Li, X., Jian, Y., Zhang, K., Li, G., et al. (2017). Fabrication of Injectable Hydrogels Based on poly(L-Glutamic Acid) and Chitosan. *RSC Adv.* 7 (28), 17005–17019. doi:10.1039/c7ra01864a

Yang, B., Song, J., Jiang, Y., Li, M., Wei, J., Qin, J., et al. (2020). Injectable Adhesive Self-Healing Multicross-Linked Double-Network Hydrogel Facilitates Full-Thickness Skin Wound Healing. *ACS Appl. Mater. Inter.* 12 (52), 57782–57797. doi:10.1021/acsami.0c18948

Yang, X., Liu, W., Li, N., Wang, M., Liang, B., Ullah, I., et al. (2017). Design and Development of Polysaccharide Hemostatic Materials and Their Hemostatic Mechanism. *Biomater. Sci.* 5 (12), 2357–2368. doi:10.1039/c7bm00554g

Yuan, L., Fan, W., Han, L., Guo, C., Yan, Z., Zhu, M., et al. (2018). Evaluation of Hydrogels for Soft Tissue Adhesives *In Vitro* and *In Vivo* Analyses. *Front. Mater. Sci.* 12 (1), 95–104. doi:10.1007/s11706-018-0405-4

Zhang, C., Yang, X., Hu, W., Han, X., Fan, L., and Tao, S. (2020). Preparation and Characterization of Carboxymethyl Chitosan/collagen Peptide/oxidized Konjac Composite Hydrogel. *Int. J. Biol. Macromolecules* 149, 31–40. doi:10.1016/j.ijbiomac.2020.01.127

Zhao, X., Hu, D. A., Wu, D., He, F., Wang, H., Huang, L. J., et al. (2021). Applications of Biocompatible Scaffold Materials in Stem Cell-Based Cartilage Tissue Engineering. *Front. Bioeng. Biotechnol.* 9, 23. doi:10.3389/fbioe.2021.603444

Zhou, J., Wu, Y., Zhang, X., Lai, J., Li, Y., Xing, J., et al. (2021). Enzyme Catalyzed Hydrogel as Versatile Bioadhesive for Tissue Wound Hemostasis, Bonding, and Continuous Repair. *Biomacromolecules* 22 (4), 1346–1356. doi:10.1021/acs.biomac.0c01329

Zhu, H., Mei, X., He, Y., Mao, H., Tang, W., Liu, R., et al. (2020). Fast and High Strength Soft Tissue Bioadhesives Based on a Peptide Dendrimer with Antimicrobial Properties and Hemostatic Ability. *ACS Appl. Mater. Inter.* 12 (4), 4241–4253. doi:10.1021/acsami.9b18720

Conflict of Interest: The authors declare that the research was conducted in the absence of any commercial or financial relationships that could be construed as a potential conflict of interest.

Publisher's Note: All claims expressed in this article are solely those of the authors and do not necessarily represent those of their affiliated organizations, or those of the publisher, the editors, and the reviewers. Any product that may be evaluated in this article, or claim that may be made by its manufacturer, is not guaranteed or endorsed by the publisher.

frontiers in Chemistry

ORIGINAL RESEARCH
published: 22 October 2021
doi: 10.3389/fchem.2021.765021

A Co-delivery System Based on a Dimeric Prodrug and Star-Shaped Polymeric Prodrug Micelles for Drug Delivery

Man Zhou[1,2], Yan Luo[1,2], Weijia Zeng[2], Xiaoqing Yang[2], Tingting Chen[2], Lulu Zhang[2], Xiaoyan He[3], Xiuguang Yi[4], Yongxiu Li[1]* and Xiaoqing Yi[2]**

[1]College of Chemistry, School of Pharmacy, Nanchang University, Nanchang, China, [2]Key Laboratory of Prevention and Treatment of Cardiovascular and Cerebrovascular Diseases, Ministry of Education, Key Laboratory of Biomaterials and Biofabrication in Tissue Engineering of Jiangxi Province, College of Pharmacy, Gannan Medical University, Ganzhou, China, [3]School of Life Sciences, Anhui Medical University, Hefei, China, [4]School of Chemistry and Chemical Engineering, Jinggangshan University, Ji'an, China

OPEN ACCESS

Edited by:
Zhong Feng Gao,
Linyi University, China

Reviewed by:
Hong Yi,
Nagoya University, Japan
Jun Wang,
Foshan University, China

***Correspondence:**
Xiaoyan He
hexiaoyan@ahmu.edu.cn
Yongxiu Li
yxli@ncu.edu.cn
Xiaoqing Yi
keyi0115@126.com

Specialty section:
This article was submitted to Nanoscience, a section of the journal Frontiers in Chemistry

Received: *26 August 2021*
Accepted: *14 September 2021*
Published: *22 October 2021*

Citation:
Zhou M, Luo Y, Zeng W, Yang X, Chen T, Zhang L, He X, Yi X, Li Y and Yi X (2021) A Co-delivery System Based on a Dimeric Prodrug and Star-Shaped Polymeric Prodrug Micelles for Drug Delivery. Front. Chem. 9:765021. doi: 10.3389/fchem.2021.765021

Chemotherapy is one of the commonly used therapies for the treatment of malignant tumors. Insufficient drug-loading capacity is the major challenge for polymeric micelle–based drug delivery systems of chemotherapy. Here, the redox-responsive star-shaped polymeric prodrug (PSSP) and the dimeric prodrug of paclitaxel (PTX) were prepared. Then the dimeric prodrug of PTX (diPTX, diP) was loaded into the core of the star-shaped polymeric prodrug micelles of PSSP by hydrophobic interaction forming the redox-responsive prodrug micelles of diPTX@PSSP for intracellular drug release in tumor cells. The hydrodynamic diameter of diPTX@PSSP nanoparticles was 114.3 nm ± 2.1 (PDI = 0.219 ± 0.016), and the micelles had long-term colloidal stability and the drug-loading content (DLC) of diPTX and PTX is 16.7 and 46.9%, respectively. The prepared micelles could broke under the reductive microenvironment within tumor cells, as a result, the dimeric prodrug of diP and polymeric prodrug micelles of PSSP were rapidly disassembled, leading to the rapid release of intracellular drugs. *In vitro* release studies showed that under the condition of reduced glutathione (GSH) (10 mM), the release of PTX was significantly accelerated with approximately 86.6% released within 21 h, and the released PTX in cytoplasm could promote the disintegration of microtubules and induce cell apoptosis. These results indicated that the new type of this reduction-sensitive nanodrug delivery system based on dimeric prodrug@polymeric prodrug micelles would be a promising technology in chemotherapy.

Keywords: drug delivery, dimeric prodrug, polymeric prodrug micelles, high drug loading, reduction-sensitive

INTRODUCTION

Polymeric micelles with a well-defined core-shell structure, which can improve the solubility, bioavailability, and circulation half-life of hydrophobic drugs thus became a promising nano-carrier for cancer treatment (Feng et al., 2020; Gauger et al., 2020; Yi et al., 2021a). Due to the unique physiological property of tumor blood vessels, polymer micelles usually from 50 to 150 nm can be passively enriched in tumor tissues through the enhanced permeability and retention (EPR)

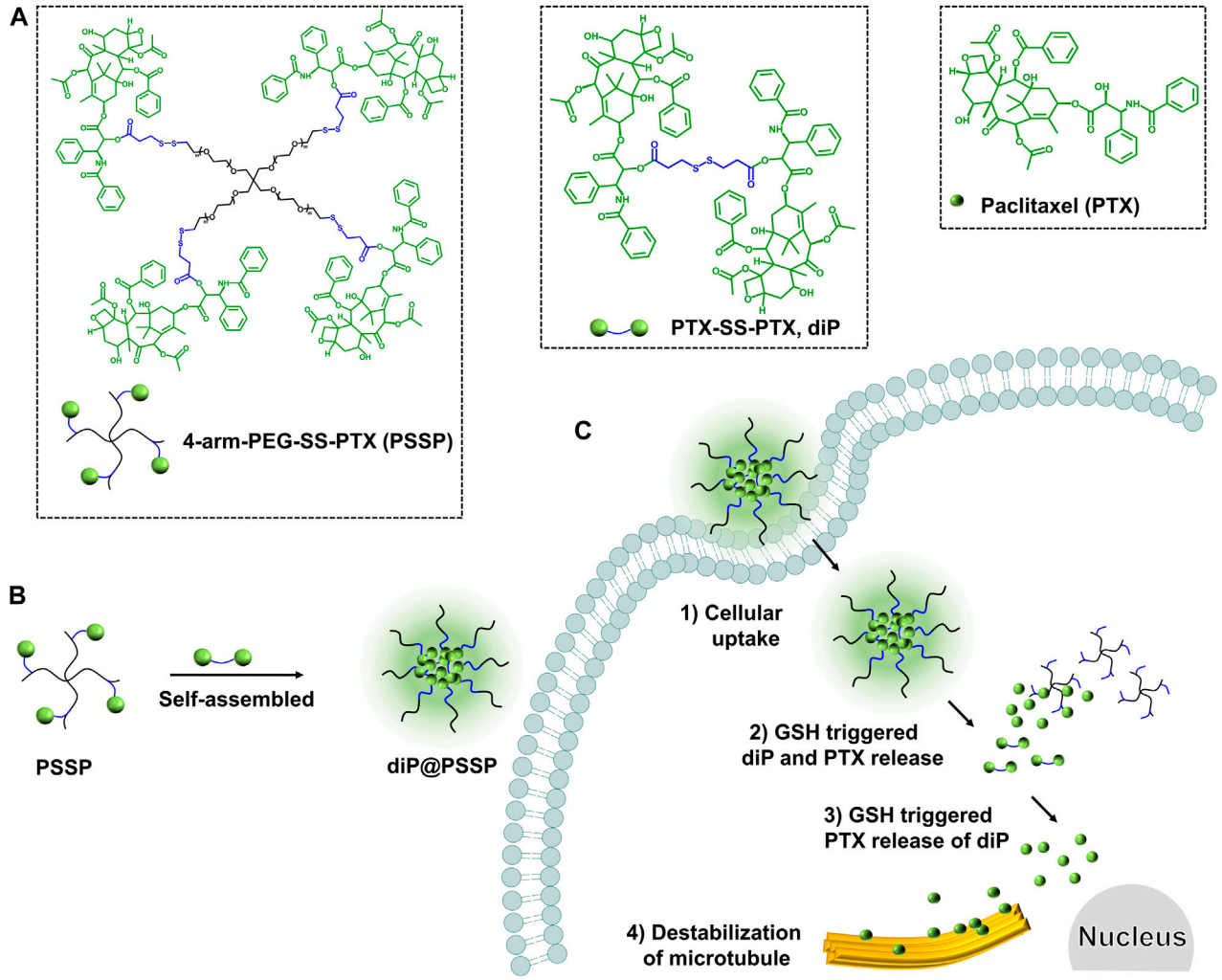

SCHEME 1 | A reduction-sensitive nanodrug delivery system based on dimeric prodrug@polymeric prodrug micelles for drug delivery. **(A)** The structure of the star-shaped polymeric prodrug (4-arm PEG-SS-PTX, PSSP) and reduction-sensitive dimer-PTX (PTX-SS-PTX, diP) with disulfide linker. **(B)** diP was encapsulated into the core of PSSP micelles to obtain diP@PSSP micelles by hydrophobic effect. **(C)** PTX release mechanism of diP@PSSP micelles in tumor cells.

effect (Yi et al., 2021b; Ghosh and Biswas, 2021; Kaur et al., 2021). Although nano-sized polymeric micelles can efficiently accumulate in tumor tissues, insufficient drug loading is still one of the main challenges for polymeric micelles in the drug delivery system.

The prodrug is obtained by directly coupling the drug and the carrier through chemical bonds, which can accurately control the drug loading and increase the solubility and stability of the drug (Deng et al., 2021; Du et al., 2021; Yang et al., 2021). It thus changes the biodistribution, improves pharmacokinetics and pharmacodynamics, increases therapeutic effect, and reduces side effect (Dhiman et al., 2021; Wang et al., 2021). FDA-approved polymers such as PLGA, PEG, and dextran have been widely used in the development of polymer-drug conjugates (prodrugs) (Li et al., 2017; Hong et al., 2020; Zeng et al., 2020; An et al., 2021). The therapeutic effect of nano-drug not only depends on the enrichment effect of nanoparticles in tumor tissues, but also on the exposure amount of free drugs. In order to achieve controlled drug release in tumor cells, many efforts have been devoted to introduction of chemical bonds between drugs and polymers, which are the intrinsic stimuli of the tumor microenvironment, such as acidity, redox potential, and specific enzymes (Chakroun et al., 2020; Hao et al., 2020; Sun and Zhong, 2020; Uthaman et al., 2020). For redox potential, the concentration of glutathione (GSH) in tumor cells is much higher than that in the extracellular. Among them, the concentration of tumor cells is much higher than that in the normal cells (~2 μmol) (Tang et al., 2020). The disulfide bonds introduced in the polymeric prodrug micelles can be reduced at high levels of GSH in the cytoplasm, leading to the dissociation of the carriers and subsequent intracellular release of the drug (Chen et al., 2018; Wang et al., 2020). Therefore, designing reduction-sensitive disulfide bonds as bridge bonds to construct polymeric prodrug nanoparticles is a common strategy for drug delivery systems.

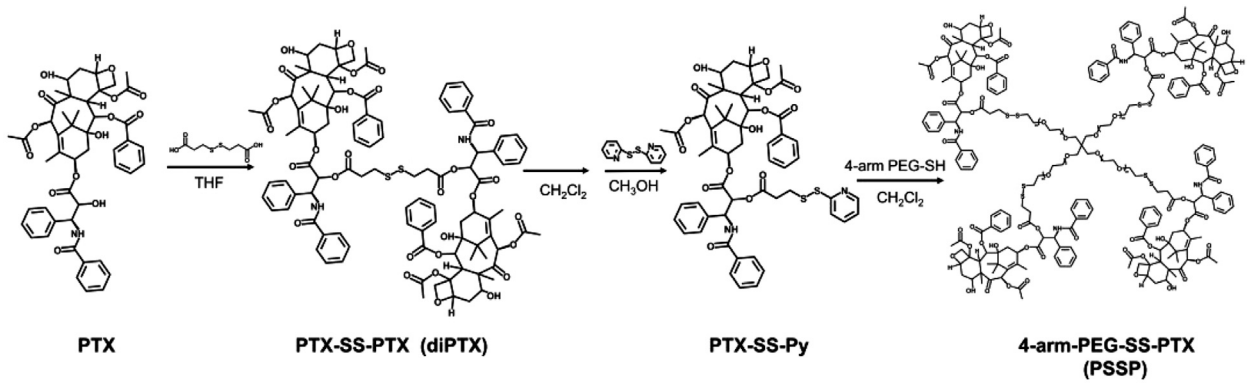

FIGURE 1 | Facile synthesis of the redox-sensitive dimeric prodrug of dimer-PTX (PTX-SS-PTX, diP) and the star-shaped polymeric prodrug of 4-arm PEG-SS-PTX (PSSP).

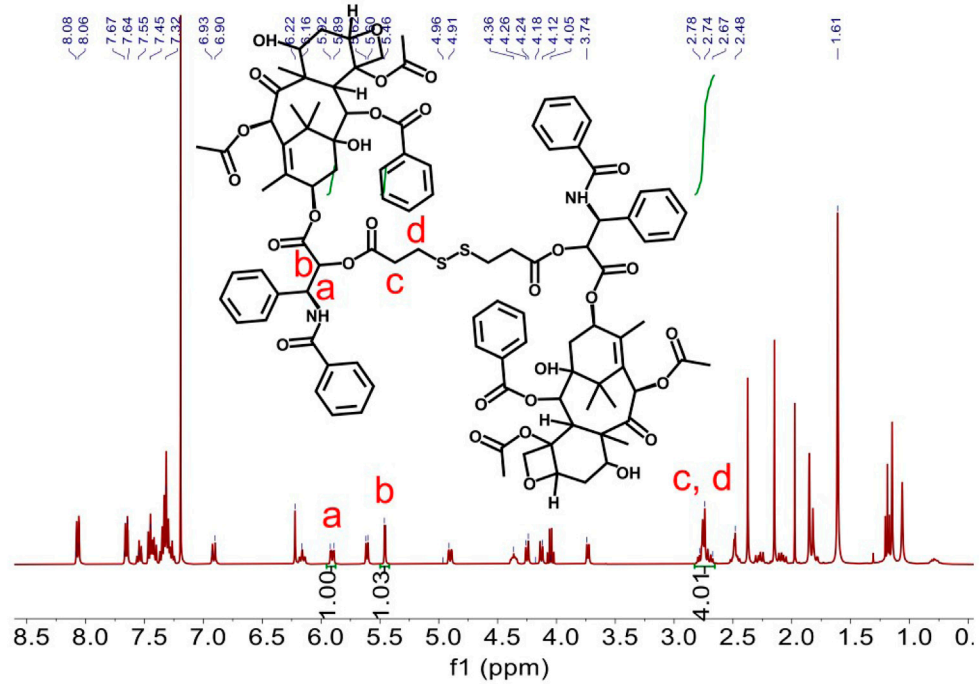

FIGURE 2 | ^{1}H NMR spectrum (400 MHz, $CDCl_3$) of diPTX.

Moreover, polymer prodrugs can also be used as drug carriers to load other drugs for combination therapy (Yi et al., 2016; Lu et al., 2020). It is worth noting that the drug loading and encapsulation efficiency of small hydrophobic drugs loaded by amphiphilic polymers are usually low (less than 10%) (Shen et al., 2017; Wang et al., 2017). This result may be mainly attributed to the formation of large drug aggregates through the packing of drug molecules with a long-range order (Cai et al., 2015). The design of the dimeric prodrug has emerged as one of the new potential strategies for increasing drug loading by hydrophobic interactions, due to the fact that drug dimers can prevent large particle formation (He et al., 2018). Furthermore, the dimeric prodrug possess the stronger intermolecular hydrophobic interactions than the free drug because of the increased surface area and the enhanced tendency of the prodrug to aggregate (Pei et al., 2018; Li et al., 2020; Zuo et al., 2020). Therefore, the design of the drug delivery system based on dimeric prodrug can improve drug loading effectively.

In order to obtain the nanodrug delivery system with a high drug-loading content (DLC), in this study, a prodrug micelle with DLC composed of a redox-responsive star-shaped polymeric prodrug of paclitaxel (PTX) and a redox-responsive dimeric prodrug of PTX was established to inhibit the growth of

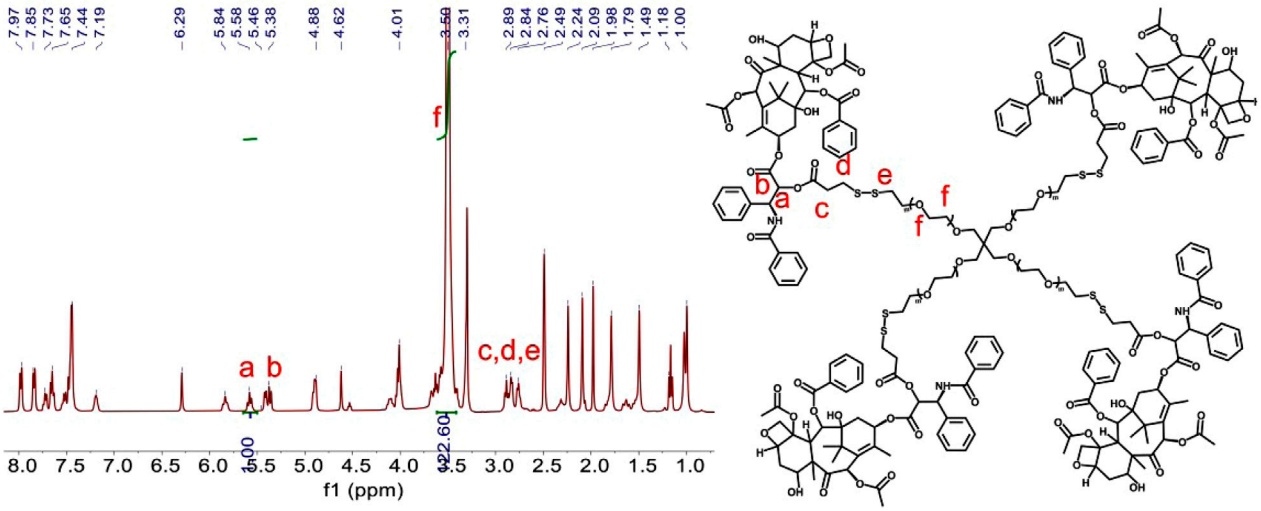

FIGURE 3 | ^{1}H NMR spectrum (400 MHz, *d*-DMSO) of PSSP.

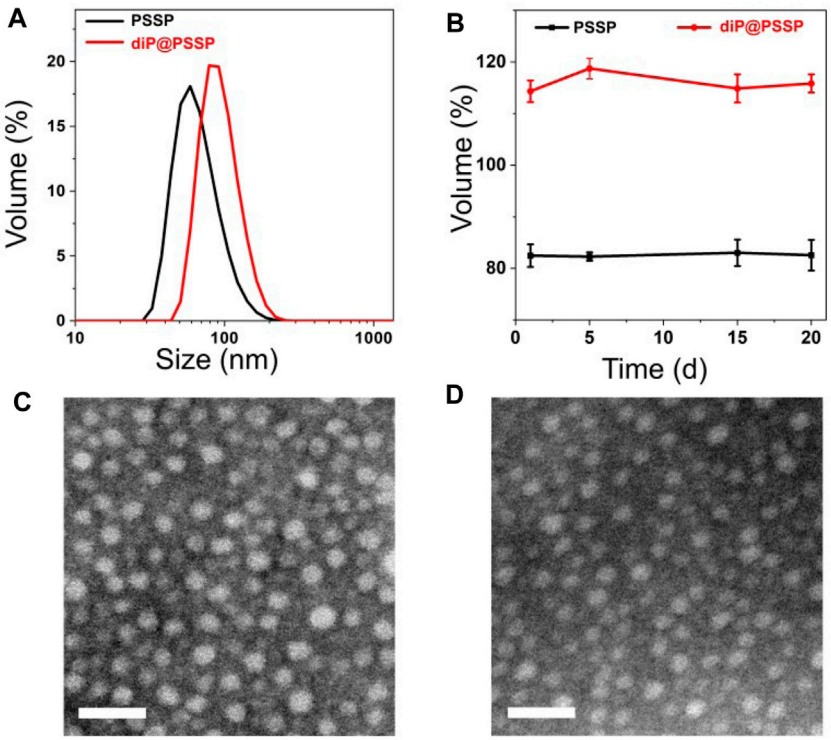

FIGURE 4 | (A) Hydrodynamic size distribution of PSSP and diP@PSSP micelles. **(B)** Stability assay of PSSP and diP@PSSP micelles in PBS during 20-day storage at room temperature. The TEM images of **(C)** PSSP and **(D)** diP@PSSP micelles. The scale bar is 100 nm.

tumor cells. As shown in **Scheme 1**, the star-shaped polymeric prodrug (4-arm-PEG-SS-PTX, PSSP) and the reduction-sensitive dimer-PTX (PTX-SS-PTX, diP) with disulfide linker were synthesized by a thiol-disulfide exchange reaction and an esterification reaction, respectively. Then the dimeric prodrug of diP was loaded into the hydrophobic core of the polymeric prodrug of PSSP micelles by the hydrophobic interaction to obtain diP@PSSP micelles. The diP@PSSP micelle has good stability, the size of the diP@PSSP micelle is 114.3 nm ± 2.1 (PDI = 0.219 ± 0.016), and the DLC of diPTX and PTX is 16.7 and 46.9%, respectively. This diP@PSSP micelle is specifically internalized into tumor cells by EPR effect and the disulfide

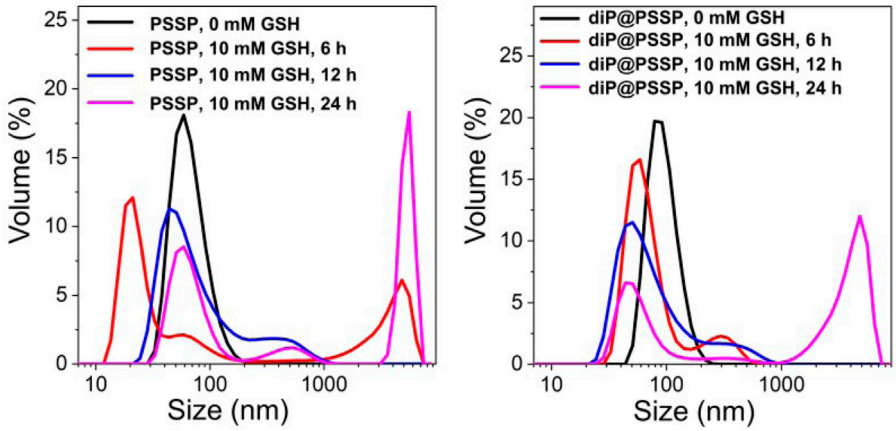

FIGURE 5 | The size changes of **(A)** PSSP and **(B)** diP@PSSP micelles in response to 10 mM GSH at pH 7.4 determined by DLS, respectively.

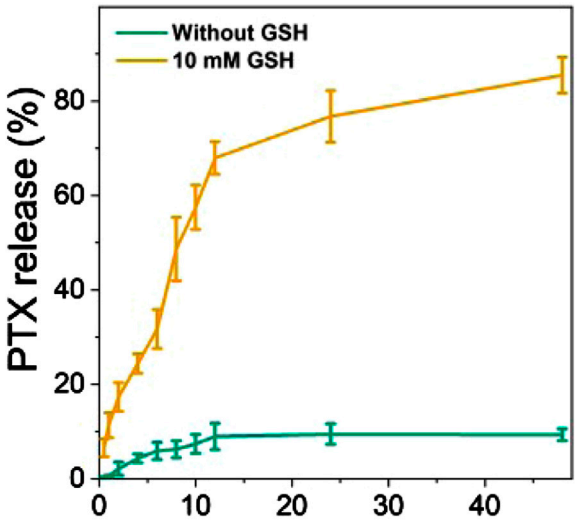

FIGURE 6 | PTX was released from a PBS solution of diP@PSSP micelles containing 0.1% (w/v) Tween 80 (pH 7.4, 0.1 M) at 37°C, with or without 10 mM GSH.

bond could be cleaved immediately under the condition of high concentration of GSH, thereby releasing PTX and diPTX. Subsequently, the released diPTX and PTX could also be released from the dimeric prodrug of diP. Finally, the released drug would disrupt the balance of microtubule polymerization and depolymerization to inhibit the growth of tumor cells.

RESULTS AND DISCUSSION

Characterization of the Prepared Prodrug

Redox-sensitive disulfides were introduced into the dimer prodrug and polymer prodrug to control drug release, the synthetic route of the redox-sensitive dimeric prodrug of dimer-PTX (PTX-SS-PTX, diP), and the star-shaped polymeric prodrug (4-arm-PEG-SS-PTX, PSSP) was shown in **Figure 1A**. The PTX reacted with 3,3′-dithiobispropionic acid to obtain the prodrug of diP by the esterification reaction (Yi et al., 2021a). Characterization was obtained by ^{1}H NMR, The signal at δ 2.5–2.8 is assigned to the methylene proton beside the disulfide bond and the ester group in deuterated dichloromethane, and the integral ratio of δ 2.5–2.8 is about four times than that of δ 5.46, which shows the successful synthesis of the dimeric prodrug of diP (**Figure 2**). Next, diP was treated with DTT to afford PTX-SH by the redox reaction and then PTX-SH reacted with excess 2,2′- dipyridyl disulfide to obtain the product of pyridyl disulfide-PTX (PTX-SS-Py) by the thiol-exchange reaction. The ^{1}H NMR spectrum of PTX-SS-Py was shown in **Supplementary Figure S1**; the shift at δ 8.71 was attributed to methyne proton of the pyridyl disulfide group and the integral of δ 8.71 and δ 5.85 is close to 1:1, and the mass data of PTX-SS-Py was 1,051.3357; the result was close to the theoretical value (calcd $[M + H]^+$ = 1,051.3351) (**Supplementary Figure S2**), which shows the successful synthesis of the PTX-SS-Py. Finally, the star-shaped polymeric prodrug of PSSP was synthesized *via* the thiol-exchange reaction between 4-arm PEG-SH and PTX-SS-Py. The characteristic peaks of PTX-SS-Py units (δ 5.54, 5.46, 5.38, 2.89, 2.84, and 2.76) and PEG units (δ 3.50, 3.31) were observed for PSSP (**Figure 3**). Moreover, the intensity ratio of the two signals at δ 5.58 and δ 3.50 on PTX units and PEG units, respectively, is close to 1:124, indicating that the PSSP with a four-armed star-shaped amphiphilic polymer was prepared successfully. The above shows that the redox-sensitive dimeric prodrug of diP and the star-shaped polymeric prodrug of PSSP were synthesized successfully.

Characterization of the Micelles

The hydrophobic dimeric prodrug of diP was encapsulated in the polymeric prodrug micelles of PSSP to prepare diP@PSSP micelles. The DLC of diP and PTX were determined and calculated by high-performance liquid chromatography (HPLC) to be 16.7 and 46.9%, respectively. The size of micelles is one of the key parameters affecting their stability *in vivo*. The average diameters of the prepared PSSP and diP@PSSP micelles were 83.1 ± 0.4 nm (PDI

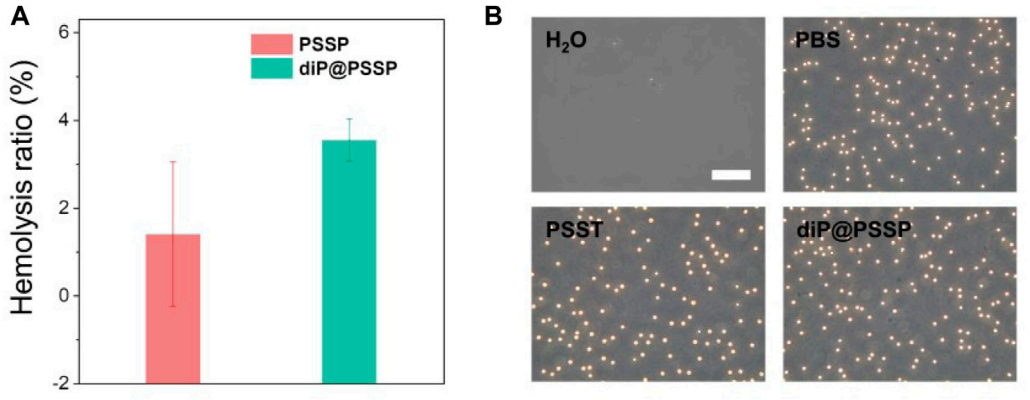

FIGURE 7 | (A) The hemolysis ratio induced by PSSP and diP@PSSP micelles with the concentration of 200 μg ml^{-1} incubated at 37°C for 6 h in dark. **(B)** Optical microscopic observation of the dispersion states of the RBCs after incubated with H_2O, PBS, PSSP, and diP@PSSP micelles for 6 h. Scale bar: 50 μm.

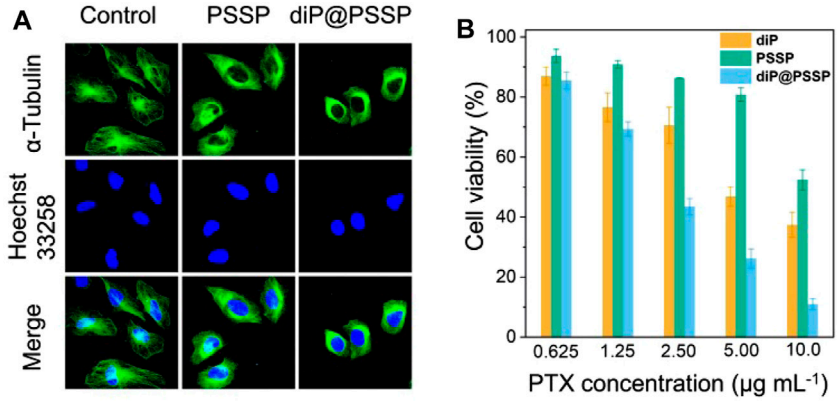

FIGURE 8 | (A) Detection of microtubules in HeLa cells after incubation with PSSP and diP@PSSP micelles for 8 h, respectively. **(B)** Viability of HeLa cells treated with diP, PSSP, and diP@PSSP nanoparticles under different concentration for 48 h, respectively. Scale bar: 20 μm.

= 0.124 ± 0.016) and 114.3 ± 2.1 nm (PDI = 0.219 ± 0.016), respectively, determined by the dynamic light scattering (DLS) (**Figure 4A**). The PSSP and diP@PSSP micelles have good stability, while their size remained essentially unchanged during 20-day storage at room temperature (**Figure 4B**). The morphology of PSSP and diP@PSSP micelles were investigated by a transmission electron microscope (TEM). The micelles showed spherical morphology and the sizes were smaller than the micelles obtained by DLS, which might be caused by the collapse of the hydrophilic PEG shell in the dry state (Wu et al., 2020) (**Figures 4C,D**). This size of micelles ranged from 50 to 150 nm could passively target the tumor with high efficiency through EPR effect (Kang et al., 2020; Kuang et al., 2020). Then the character of the reduction-sensitive was verified in this drug delivery system, DLS was used to monitor the size change of PSSP and diP@PSSP micelles in response to 10 mM GSH (**Figure 5**). The results showed that the PSSP and diP@PSSP micelles were quickly destabilized by GSH to form smaller and larger aggregates simultaneously within 6 h, the particle size distribution continued to change with the increase of time. This may be due to GSH triggering the cleavage of the disulfide bond of PSSP and diP to form water-soluble PEG and release water-insoluble PTX. The above results indicate that PSSP and diP@PSSP micelles were prepared successfully by self-assembly, and the PSSP and diP@PSSP micelles have good size distribution and excellent reduction responsiveness.

Drug Release and Cytotoxicity Assay

The PTX release behaviors of the diP@PSSP micelles in reduction environment of 10 mM GSH were evaluated *in vitro*, the results were shown in **Figure 6**. Only less than 10% of the PTX was cumulative released at pH 7.4 in absence of 10 mM GSH within 48 h, which simulates the physicochemical environment of blood circulation. This indicates that the micelle of diP@PSSP have good stability to inhibit premature drug leakage, which may be due to the hydrophobic interaction between PTX and diPTX and the stable disulfide bond of the conjugated PTX (Yang et al., 2019). However, a significant increase in drug release was observed at the condition of

10 mM GSH. The cumulative drug release of diP@PSSP micelles was about 85% within 48 h. These results show that the disulfide bonds collapse occurred under the activation of GSH, which can accelerate the release of PTX from diP@PSSP micelles (Su et al., 2018). In order to verify the prepared prodrug micelles in a short period of time is not seriously destructive to red blood cells (RBCs), the hemolysis of PSSP and diP@PSSP micelles was studied (Chibhabha et al., 2020). As shown in **Figure 7A**, the prepared micelles had no obvious corrosive effect on the behavior of RBCs. In addition, PSSP and diP@PSSP micelles exerted neglectable hemolysis (<5.0%) for RBCs at the concentration of 200 μg ml^{-1} (**Figure 7B**). The results show that the prepared PSSP and diP@PSSP micelles were safe drug delivery systems with good biocompatibility.

It is well known that PTX is a hydrophobic drug that induces apoptosis in tumor cells by promoting microtubule disintegration. Microtubule is a kind of natural biological macromolecule existing in cells, which can continuously change its assembly and disassembly state in a few seconds in life activities (Chan and Coen, 2020). In order to studied the effect of polymeric prodrug PSSP and diP@PSSP micelles on microtubules of HeLa cells, the morphology of microtubules was observed by CLSM after the HeLa cells were incubated with the PSSP and diP@PSSP micelles for 8 h. As shown in **Figure 8A**, compared with the control group, PSSP and diP@PSSP micelles showed significant contraction effect on the microtubules of HeLa cells. This is due to the presence of PTX in PSSP and diP@PSSP micelles, and the PTX released under reduction condition in tumor microenvironment can bind to specific sites of tubulin to prevent its depolymerization. To study the cytotoxicity of the diP, PSSP, and diP@PSSP micelles, the HeLa cells were incubated with these samples at the concentrations of 1.25, 2.50, and 5.00 μg ml^{-1} for 48 h. As shown in **Figure 8B**, the diP, PSSP, and diP@PSSP micelles exhibited toxicity in HeLa cells, indicating the tumor cells are very sensitive to these redox-responsive prodrugs. The inhibitory effect of PSSP micelles on HeLa cells growth was weaker than that of diP, which might be related to the protective shell of PEG. Moreover, the cell viability of diP@PSSP on HeLa cells is weaker than that of diP, which may be attributed to two reasons, one is that the solubility of diP is enhanced by PSSP carrier to facilitate its phagocytosis by cells and the other is that the released PTX in tumor environment exerts its drug effect. In general, diP@PSSP micelles with high drug loading not only have good biocompatibility but also can achieve controlled drug release in tumor cells and inhibit the growth of tumor cell.

CONCLUSION

In summary, a new type of drug delivery system of diP@PSSP with high DLC and excellent stability was developed based on prodrug–drug complexes and dimeric prodrug. The polymeric prodrug diP@PSSP micelles possessed high DLC of PTX as high as 46.9% and excellent stability. The controlled release of PTX under the 10 mM GSH could be achieved for reductive-sensitive diP@PSSP micelles. In addition, the polymeric prodrug of diP@PSSP micelles showed good biocompatibility in RBCs and therapeutic effect in HeLa cells. We hope that this strategy will be used to facilitate the provision of multiple therapeutic drugs for a variety of purposes, in particular to overcome multidrug resistance.

DATA AVAILABILITY STATEMENT

The original contributions presented in the study are included in the article/**Supplementary Material**; further inquiries can be directed to the corresponding authors.

AUTHOR CONTRIBUTIONS

XQY, XH, and YXL designed the research. MZ and XQY carried out the experiments. MZ, YL, WZ, X Yang, and X Yi performed data analysis. X Yang, TC, and LZ participated in cell experiments. XQY, XH, and YXL wrote the paper. All the authors checked the manuscript.

FUNDING

This research was supported by the National Natural Science Foundation of China (51864033; 21978127), the National Key Research Development Program of China (2019YFC0605000), Natural Science Foundation of Jinagxi Province of China (20202BAB204003), the Open Project of Key Laboratory of Prevention and Treatment of Cardiovascular and Cerebrovascular Diseases, Ministry of Education (Nos. XN201911; XN202018), and the Research Fund of Gannan Medical University (Nos. QD201903; YB201911).

SUPPLEMENTARY MATERIAL

The Supplementary Material for this article can be found online at: https://www.frontiersin.org/articles/10.3389/fchem.2021.765021/full#supplementary-material

REFERENCES

An, L., Zhang, P., Shen, W., Yi, X., Yin, W., Jiang, R., et al. (2021). A Sulfur Dioxide Polymer Prodrug Showing Combined Effect with Doxorubicin in Combating Subcutaneous and Metastatic Melanoma. *Bioactive Mater.* 6, 1365–1374. doi:10.1016/j.bioactmat.2020.10.027

Cai, K., He, X., Song, Z., Yin, Q., Zhang, Y., Uckun, F. M., et al. (2015). Dimeric Drug Polymeric Nanoparticles with Exceptionally High Drug Loading and Quantitative Loading Efficiency. *J. Am. Chem. Soc.* 137, 3458–3461. doi:10.1021/ja513034e

Chakroun, R. W., Sneider, A., Anderson, C. F., Wang, F., Wu, P. H., Wirtz, D., et al. (2020). Supramolecular Design of Unsymmetric Reverse Bolaamphiphiles for Cell-Sensitive Hydrogel Degradation and Drug Release. *Angew. Chem. Int. Ed.* 59, 4434–4442. doi:10.1002/anie.201913087

Chan, J., and Coen, E. (2020). Interaction between Autonomous and Microtubule Guidance Systems Controls Cellulose Synthase Trajectories. *Curr. Biol.* 30, 941–947. doi:10.1016/j.cub.2019.12.066

Chen, D., Zhang, G., Li, R., Guan, M., Wang, X., Zou, T., et al. (2018). Biodegradable, Hydrogen Peroxide, and Glutathione Dual Responsive Nanoparticles for Potential Programmable Paclitaxel Release. *J. Am. Chem. Soc.* 140, 7373–7376. doi:10.1021/jacs.7b12025

Chibhabha, F., Yang, Y., Ying, K., Jia, F., Zhang, Q., Ullah, S., et al. (2020). Non-invasive Optical Imaging of Retinal Aβ Plaques Using Curcumin Loaded Polymeric Micelles in APPswe/PS1ΔE9 Transgenic Mice for the Diagnosis of Alzheimer's Disease. *J. Mater. Chem. B* 8, 7438–7452. doi:10.1039/d0tb01101k

Deng, K., Yu, H., Li, J.-M., Li, K.-H., Zhao, H.-Y., Ke, M., et al. (2021). Dual-step Irradiation Strategy to Sequentially Destroy Singlet Oxygen-Responsive Polymeric Micelles and Boost Photodynamic Cancer Therapy. *Biomaterials* 275, 120959. doi:10.1016/j.biomaterials.2021.120959

Dhiman, N., Awasthi, R., Sharma, B., Kharkwal, H., and Kulkarni, G. T. (2021). Lipid Nanoparticles as Carriers for Bioactive Delivery. *Front. Chem.* 9, 580118. doi:10.3389/fchem.2021.580118

Du, Q., Lv, F., Huang, J., Tang, X., Zhao, Z., and Chen, J. (2021). A Multiple Environment-Sensitive Prodrug Nanomicelle Strategy Based on Chitosan Graftomer for Enhanced Tumor Therapy of Gambogic Acid. *Carbohydr. Polym.* 267, 118229. doi:10.1016/j.carbpol.2021.118229

Feng, H., Chu, D., Yang, F., Li, Z., Fan, B., Jin, L., et al. (2020). Hypoxia-responsive Polymeric Micelles for Enhancing Cancer Treatment. *Front. Chem.* 8, 742. doi:10.3389/fchem.2020.00742

Gauger, A. J., Hershberger, K. K., Bronstein, L. M., et al. (2020). Theranostics Based on Magnetic Nanoparticles and Polymers: Intelligent Design for Efficient Diagnostics and Therapy. *Front. Chem.* 8, 561. doi:10.3389/fchem.2020.00561

Ghosh, B., and Biswas, S. (2021). Polymeric Micelles in Cancer Therapy: State of the Art. *J. Controlled Release* 332, 127–147. doi:10.1016/j.jconrel.2021.02.016

Hao, Q., Wang, Z., Zhao, W., Wen, L., Wang, W., Lu, S., et al. (2020). Dual-responsive Polyprodrug Nanoparticles with cascade-enhanced Magnetic Resonance Signals for Deep-Penetration Drug Release in Tumor Therapy. *ACS Appl. Mater. Inter.* 12, 49489–49501. doi:10.1021/acsami.0c16110

He, X., Cai, K., Zhang, Y., Lu, Y., Guo, Q., Zhang, Y., et al. (2018). Dimeric Prodrug Self-Delivery Nanoparticles with Enhanced Drug Loading and Bioreduction Responsiveness for Targeted Cancer Therapy. *ACS Appl. Mater. Inter.* 10, 39455–39467. doi:10.1021/acsami.8b09730

Hong, Y., Che, S., Hui, B., Wang, X., Zhang, X., and Ma, H. (2020). Combination Therapy of Lung Cancer Using Layer-By-Layer Cisplatin Prodrug and Curcumin Co-encapsulated Nanomedicine. *Dddt* 14, 2263–2274. doi:10.2147/DDDT.S241291

Kang, H., Rho, S., Stiles, W. R., Hu, S., Baek, Y., Hwang, D. W., et al. (2020). Size-Dependent EPR Effect of Polymeric Nanoparticles on Tumor Targeting. *Adv. Healthc. Mater.* 9, 1901223. doi:10.1002/adhm.201901223

Kaur, J., Mishra, V., Singh, S. K., Gulati, M., Kapoor, B., Chellappan, D. K., et al. (2021). Harnessing Amphiphilic Polymeric Micelles for Diagnostic and Therapeutic Applications: Breakthroughs and Bottlenecks. *J. Controlled Release* 334, 64–95. doi:10.1016/j.jconrel.2021.04.014

Kuang, Y., Zhang, J., Xiong, M., Zeng, W., Lin, X., Yi, X., et al. (2020). A Novel Nanosystem Realizing Curcumin Delivery Based on Fe3O4@Carbon Dots Nanocomposite for Alzheimer's Disease Therapy. *Front. Bioeng. Biotechnol.* 8, 614906. doi:10.3389/fbioe.2020.614906

Li, D., Han, J., Ding, J., Chen, L., and Chen, X. (2017). Acid-sensitive Dextran Prodrug: A Higher Molecular Weight Makes a Better Efficacy. *Carbohydr. Polym.* 161, 33–41. doi:10.1016/j.carbpol.2016.12.070

Li, S., Shan, X., Wang, Y., Chen, Q., Sun, J., He, Z., et al. (2020). Dimeric Prodrug-Based Nanomedicines for Cancer Therapy. *J. Controlled Release* 326, 510–522. doi:10.1016/j.jconrel.2020.07.036

Lu, L., Zhao, X., Fu, T., Li, K., He, Y., Luo, Z., et al. (2020). An iRGD-Conjugated Prodrug Micelle with Blood-Brain-Barrier Penetrability for Anti-glioma Therapy. *Biomaterials* 230, 119666. doi:10.1016/j.biomaterials.2019.119666

Pei, Q., Hu, X., Zheng, X., Liu, S., Li, Y., Jing, X., et al. (2018). Light-activatable Red Blood Cell Membrane-Camouflaged Dimeric Prodrug Nanoparticles for Synergistic Photodynamic/chemotherapy. *Acs Nano* 12, 1630–1641. doi:10.1021/acsnano.7b08219

Shen, S., Wu, Y., Liu, Y., and Wu, D. (2017). High Drug-Loading Nanomedicines: Progress, Current Status, and Prospects. *Ijn* Vol. 12, 4085–4109. doi:10.2147/IJN.S132780

Su, L., Li, R., Khan, S., Clanton, R., Zhang, F., Lin, Y.-N., et al. (2018). Chemical Design of Both a Glutathione-Sensitive Dimeric Drug Guest and a Glucose-Derived Nanocarrier Host to Achieve Enhanced Osteosarcoma Lung Metastatic Anticancer Selectivity. *J. Am. Chem. Soc.* 140, 1438–1446. doi:10.1021/jacs.7b11462

Sun, H., and Zhong, Z. (2020). 100th Anniversary of Macromolecular Science Viewpoint: Biological Stimuli-Sensitive Polymer Prodrugs and Nanoparticles for Tumor-specific Drug Delivery. *ACS Macro Lett.* 9, 1292–1302. doi:10.1021/acsmacrolett.0c00488

Tang, H., Li, C., Zhang, Y., Zheng, H., Cheng, Y., Zhu, J., et al. (2020). Targeted Manganese Doped Silica Nano GSH-Cleaner for Treatment of Liver Cancer by Destroying the Intracellular Redox Homeostasis. *Theranostics* 10, 9865–9887. doi:10.7150/thno.46771

Uthaman, S., Pillarisetti, S., Mathew, A. P., Kim, Y., Bae, W. K., Huh, K. M., et al. (2020). Long Circulating Photoactivable Nanomicelles with Tumor Localized Activation and ROS Triggered Self-Accelerating Drug Release for Enhanced Locoregional Chemo-Photodynamic Therapy. *Biomaterials* 232, 119702. doi:10.1016/j.biomaterials.2019.119702

Wang, C., Liu, H., Liu, S., Wang, Z., and Zhang, J. (2020). pH and Redox Dual-Sensitive Covalent Organic Framework Nanocarriers to Resolve the Dilemma between Extracellular Drug Loading and Intracellular Drug Release. *Front. Chem.* 8, 488. doi:10.3389/fchem.2020.00488

Wang, H., Chen, J., Xu, C., Shi, L., Tayier, M., Zhou, J., et al. (2017). Cancer Nanomedicines Stabilized by π-π Stacking between Heterodimeric Prodrugs Enable Exceptionally High Drug Loading Capacity and Safer Delivery of Drug Combinations. *Theranostics* 7, 3638–3652. doi:10.7150/thno.20028

Wang, H., Fang, B., Peng, B., Wang, L., Xue, Y., Bai, H., et al. (2021). Recent Advances in Chemical Biology of Mitochondria Targeting. *Front. Chem.* 9, 683220. doi:10.3389/fchem.2021.683220

Wu, H., Chen, F., You, C., Zhang, Y., Sun, B., and Zhu, Q. (2020). Smart Porous Core-Shell Cuprous Oxide Nanocatalyst with High Biocompatibility for Acid-Triggered Chemo/Chemodynamic Synergistic Therapy. *Small* 16, 2001805. doi:10.1002/smll.202001805

Yang, L., Yan, G., Wang, S., Xu, J., Fang, Q., Xue, Y., et al. (2021). Dynamic Precise Dual-Drug-Backboned Nano-Prodrugs for Selective Chemotherapy. *Acta Biomater.* 129, 209–219. doi:10.1016/j.actbio.2021.05.013

Yang, X., Hu, C., Tong, F., Liu, R., Zhou, Y., Qin, L., et al. (2019). Tumor Microenvironment-Responsive Dual Drug Dimer-Loaded PEGylated Bilirubin Nanoparticles for Improved Drug Delivery and Enhanced Immune-Chemotherapy of Breast Cancer. *Adv. Funct. Mater.* 29, 1901896. doi:10.1002/adfm.201901896

Yi, X., Hu, J.-J., Dai, J., Lou, X., Zhao, Z., Xia, F., et al. (2021a). Self-guiding Polymeric Prodrug Micelles with Two Aggregation-Induced Emission Photosensitizers for Enhanced Chemo-Photodynamic Therapy. *Acs Nano* 15, 3026–3037. doi:10.1021/acsnano.0c09407

Yi, X., Zeng, W., Wang, C., Chen, Y., Zheng, L., Zhu, X., et al. (2021b). A Step-by-step Multiple Stimuli-Responsive Metal-Phenolic Network Prodrug Nanoparticles for Chemotherapy. *Nano Res.* doi:10.1007/s12274-021-3626-2

Yi, X., Zhao, D., Zhang, Q., Xu, J., Yuan, G., Zhuo, R., et al. (2016). A Co-delivery System Based on a Reduction-Sensitive Polymeric Prodrug Capable of Loading Hydrophilic and Hydrophobic Drugs for Combination Chemotherapy. *Polym. Chem.* 7, 5966–5977. doi:10.1039/c6py00900j

Zeng, X., Cheng, X., Zheng, Y., Yan, G., Wang, X., Wang, J., et al. (2020). Indomethacin-grafted and pH-Sensitive Dextran Micelles for Overcoming Inflammation-Mediated Multidrug Resistance in Breast Cancer. *Carbohydr. Polym.* 237, 116139. doi:10.1016/j.carbpol.2020.116139

Zuo, S., Sun, B., Yang, Y., Zhou, S., Zhang, Y., Guo, M., et al. (2020). Probing the Superiority of Diselenium Bond on Docetaxel Dimeric Prodrug Nanoassemblies: Small Roles Taking Big Responsibilities. *Small* 16, 2005039. doi:10.1002/smll.202005039

Conflict of Interest: The authors declare that the research was conducted in the absence of any commercial or financial relationships that could be construed as a potential conflict of interest.

Publisher's Note: All claims expressed in this article are solely those of the authors and do not necessarily represent those of their affiliated organizations, or those of the publisher, the editors and the reviewers. Any product that may be evaluated in this article, or claim that may be made by its manufacturer, is not guaranteed or endorsed by the publisher.

frontiers in Chemistry

ORIGINAL RESEARCH
published: 29 October 2021
doi: 10.3389/fchem.2021.740191

A Nanofiber Mat With Dual Bioactive Components and a Biomimetic Matrix Structure for Improving Osteogenesis Effect

Yadi Han[1†], Xiaofeng Shen[2†], Sihao Chen[1], Xiuhui Wang[3]*, Juan Du[1] and Tonghe Zhu[1]**

[1]Frontier Institute of Medical & Pharmaceutical Science and Technology, College of Chemistry and Chemical Engineering, Shanghai University of Engineering Science, Shanghai, China, [2]Department of Orthopedics, Suzhou TCM Hospital Affiliated to Nanjing University of Chinese Medicine, Suzhou, China, [3]Institute of Translational Medicine, Shanghai University, Shanghai, China

The challenge of effectively regenerating bone tissue through tissue engineering technology is that most tissue engineering scaffolds cannot imitate the three-dimensional structure and function of the natural extracellular matrix. Herein, we have prepared the poly(L-lactic acid)–based dual bioactive component reinforced nanofiber mats which were named as poly(L-lactic acid)/bovine serum albumin/nanohydroxyapatite (PLLA/BSA/nHAp) with dual bioactive components by combining homogeneous blending and electrospinning technology. The results showed that these nanofiber mats had sufficient mechanical properties and a porous structure suitable for cell growth and migration. Furthermore, the results of cell experiments *in vitro* showed that PLLA/BSA/nHAp composite nanofiber mat could preferably stimulate the proliferation of mouse osteoblastic cells (MC3T3 cells) compared with pure PLLA nanofiber mats. Based on these results, the scaffolds developed in this study are considered to have a great potential to be adhibited as bone repair materials.

Keywords: bone tissue injure, nanofiber mat, bioactive components, recognition sites, massive bone tissue regeneration

OPEN ACCESS

Edited by:
Houjuan Zhu,
*Institute of Materials Research and Engineering (A*STAR), Singapore*

Reviewed by:
Kai Wang,
Nankai University, China
Xiu Wang,
Bengbu Medical College, China

***Correspondence:**
Sihao Chen
chensh@sues.edu.cn
Xiuhui Wang
blackrabbit@shu.edu.cn
Tonghe Zhu
zhutonghe89@163.com

†These authors have contributed equally to this work

Specialty section:
This article was submitted to Nanoscience, a section of the journal Frontiers in Chemistry

Received: *12 July 2021*
Accepted: *30 August 2021*
Published: *29 October 2021*

Citation:
Han Y, Shen X, Chen S, Wang X, Du J and Zhu T (2021) A Nanofiber Mat With Dual Bioactive Components and a Biomimetic Matrix Structure for Improving Osteogenesis Effect. Front. Chem. 9:740191. doi: 10.3389/fchem.2021.740191

INTRODUCTION

Bone defects, accounting for about 50% of surgical operations, caused by various reasons are very prevalent in clinical surgery (Saravanan et al., 2019; Yuan et al., 2020; Wang et al., 2021). Treatment of complex bone defects with irregular shapes or at the interfacial zone with soft tissues, such as cartilage-to-bone, tendon-to-bone, and ligament-to-bone insertion sites remains a clinical challenge (Wang et al., 2019a; Huang et al., 2020). Autograft remains the gold standard for bone repair (Damien and Parsons, 2010; Zimmermann and Moghaddam, 2011). However, it has two fatal flaws limited in clinical practice, namely, significant donor site morbidity and poor capability for machining to accommodate irregular defects. Additionally, autogenous bone transplantation raises significant concerns about the spread of disease and immune responses (Chen et al., 2016; Ye et al., 2019). With the intersection of orthopedic surgery and tissue engineering development, bone substitutes such as ceramics and bone cement have been universally used in clinical practice. However, these materials or scaffolds are usually a three-dimensional structure mismatched with host cells, which may inhibit cell growth, vascularization, and bone regeneration (Jakus et al., 2016; Zhu et al., 2018; Wang et al., 2019b). It is necessary to develop bone tissue engineering scaffolds that

are capable of effectively replacing and regenerating fragmented large bulk bone tissue without inducing complications (Oryan et al., 2014; Wang et al., 2019c).

The hybrid fiber material, which is synthesized by electrospinning, possesses the characteristics of enhanced biocompatibility, high porosity, good mechanical properties, large specific surface area, and adjustable hydrophilicity. The micro-/nanofibers prepared by electrospinning can theoretically mimic the three-dimensional structure of an extracellular matrix (ECM), thereby facilitating the proliferation and migration of related cells in the tissue (Li et al., 2014; Rezk et al., 2018a; Aoki et al., 2020). In recent years, new technologies based on electrospinning have been applied to the fabrication of three-dimensional (3D) nanofibrous scaffolds. In these works, fabricated 3D scaffolds derived from electrospun nanofibers have been used for bone tissue engineering. Satpathy *et al.* reported a nanohydroxyapatite (nHAp) nanoparticle-doped electrospun polyvinyl alcohol (PVA)–chitosan composite nanofibrous mat, which was successfully fabricated with improved performance for the potential application as a bone tissue regeneration material. The author claims that the incorporation of HAp nanoparticles improves the biocompatibility as well as bioactivity of PVA–chitosan composite scaffolds for osteoblast, and such composite scaffolds may serve as a good template for bone tissue engineering (Satpathy et al., 2019). Ye *et al.* prepared a bone scaffold (nanohydroxyapatite/PLLA/gelatin (nHA/PLA/GEL) 3D nanofibrous scaffolds) based on combining electrospinning, homogenizing, freeze-drying, and thermal crosslinking techniques. This research concluded that the combined use of nHA and the BMP-2-derived peptides synergistically and significantly promoted BMSC osteogenic differentiation *in vitro* and bone regeneration in a rat cranial bone defect model (Ye et al., 2019).

Inorganic osteogenic nanoparticles have been extensively synthesized for a bone regeneration scaffold due to its easily modified surface (Liu et al., 2016). Sokolova et al. reported a porous scaffold, which is composed of poly(lactide–coglycolide) (PLGA) and nanohydroxyapatite (nHAp) for bone substitution. All authors in this research alleged that it is expected to enhance bone growth around an implanted scaffold or inside a scaffold for tissue engineering (Sokolova et al., 2020). Bauer et al. synthesized biphasic nHAp and whitlockite composite scaffolds with different ratios by changing the content of Mg^{2+} ions for strengthening osteogenic differentiation of human mesenchymal stem cells (hMSCs) (Bauer et al., 2020). Chen et al. prepared porous hydroxyapatite composite scaffolds through 3D bioprinting for bone tissue engineering (Chen et al., 2019). These reported scaffolds with different proportions of inorganic osteogenic nanoparticles had porous structures for facilitating cell proliferation and migration, but the matrix materials used do not have the sufficient ability to induce effective osteogenesis, which is mainly due to the lack of strong bioactive sites that recognize the host cytomembranes.

Bovine serum protein (BSA) is a globulin in bovine serum, mainly composed of proteins, peptides, hormones, etc., and it has abundant cell recognition sites to promote cell adhesion and proliferation (Li et al., 2017; Liu et al., 2020). As in previous research, a linear gradient of active protein was readily loaded into uniaxially aligned nanofibers by backfilling the active protein onto the bare regions by a graded mask of BSA (Tanes et al., 2017). Additionally, Wu et al. demonstrated a simple and general strategy by first creating a graded mask of BSA on nanofibers; it is beneficial to improve the biocompatibility of the material (Wu et al., 2018). However, they added the different gradient growth factors for the purpose of improving tissue regeneration, but the release of growth factors was difficult to control.

Poly(L-lactic acid) (PLLA) is a biodegradable material that is often used for tissue regeneration, whose degradation cycle and mechanical properties matched the growth of osteoblasts (Shim et al., 2010; Schofer et al., 2012; Qi et al., 2016; Wang et al., 2016). Beyond this, PLLA can be blended with natural active materials or inorganic particulate matter for electrospinning (Shim et al., 2010; Rajzer et al., 2018; Ye et al., 2019). However, the acidic degradation products of pure PLLA can inhibit osteoblasts and promote the growth of osteoclasts, which may have a negative effect on bone regeneration. Based on this, we believe that, by combining these bioactive factors, its drawbacks can be modified and their advantages will be magnified. The synergistic effect of these three substances will provide a biomimetic microenvironment for the growth of osteoblasts. Therefore, we will attempt to use PLLA as the base framework material, adding bioactive BSA and polyhydric nHAp dual components to neutralize the acid product as well as improve the osteogenesis effect.

MATERIALS AND METHODS

Materials

Poly(L-lactic acid) (PLLA, M_w = 125,000 g/mol) was purchased from Shenzhen MaiQi Biomaterials Co., Ltd. (Shenzhen, China). BSA (M_w = 66,446 g/mol, isoelectric point = 4.7) was purchased from Shanghai Titan Scientific Co., Ltd. (Shanghai, China). Nanohydroxyapatite (nHAp) was purchased from Shanghai Aladdin Biochemical Technology Co., Ltd. (Shanghai, China). 1,1,1,3,3,3-Hexafluoro-2-propanol (HFIP) was purchased from Shanghai Darui Fine Chemical Co., Ltd. (Shanghai, China). MC3T3 cells were obtained from Shanghai Institute of Biochemistry and Cell Biology (SIBCB, CAS, China). All culture media and reagents were purchased from Invitrogen and Sigma-Aldrich (St. Louis, MO) unless stated otherwise. All chemicals used in the experiments are analytical grade reagents and used without further purification.

Fabrication of Nanofiber Mats

The nanofibers mat was prepared by the electrospinning technology. In brief, 0.8 g PLLA and 0.08 g BSA was dissolved into 10 ml HFIP under vigorous stirring at room temperature for 24 h. Then, the HFIP solution with a uniform concentration of 1% nHAp was added into the solution for preparing PLLA/BSA/nHAp electrospinning solution. After 48 h of intense magnetic stirring, the well-mixed solution was drawn into a plastic syringe, followed by connecting it with the DC voltage and sprayed at a

feeding rate of 1.0 ml/h through a metal needle with an inner diameter of 0.8 mm at the same time. The nanofiber mat is collected on a rectangular grounded metal plate covered with an aluminum foil. The voltage and receiving distance between the needle and the metal plate was set at 10 kV and 15 cm, respectively. All processes were carried out at about 50 ± 5% relative humidity. The collected nanofibers mat was first put into a fume hood for self-volatilizing for 48 h to remove residual HFIP and then put in a vacuum drying oven for 24 h at a constant temperature for subsequent characterization and testing.

Characterization of Nanofibers and Nanofiber Mats

A scanning electron microscope (SEM, Phenom XL, Netherlands) was used to test the microscopic morphology of the nanofibers after spraying gold. The diameter distribution of nanofibers from the SEM fiber images can be measured by using ImageJ software (National Institutes of Health, MD, United States). To see the structure of single fiber, the fiber was further measured by transmission electron field electron microscopy (TEM, JEOL JEM-2100).

The apparent water contact angle (WCA) was measured three times for each sample using a contact angle instrument (OCA40, DataPhysics, Germany) when the deionized water droplet was stable at room temperature. Both WCA values of the left and right sides were measured, and an average value was applied.

The porosity of nanofiber mats was measured by the ethanol immersion method as previously described using the reported formula (Zhu et al., 2017; Du et al., 2019). In brief, 5 ml (V_1) ethanol was first filled in a measuring cylinder, and then nanofibrous mats (n = 4) were immersed in ethanol for 10 min, respectively. The resulting volume of ethanol was recorded as V_2, and the residual volume of ethanol in a measuring cylinder after removing the wet nanofibrous mats was V_3. The porosity (p) was calculated according to the following formula:

$$\mathrm{p}(\%) = (V_1 - V_3)/(V_2 - V_3). \quad (1)$$

The apparent density (ρ_a) was calculated by $\rho_a = m/v$, where m is the mass and v stands for the volume of the samples (Du et al., 2019).

The structure and properties of the nanofiber mat were analyzed by Fourier transform infrared spectroscopy (FTIR, Avatar 380, United States) in the range of 400–4,000 cm^{-1} wavenumbers at a resolution of 2 cm^{-1}. Using X-ray diffraction (XRD, Tokyo, Japan) under the condition of 40 KV tested the crystal structure of the nanofiber mat, sample scanning was performed at a 2θ angle (5°–80°). STAPT-1000 instruments (Linseis, German) were used to evaluate the thermal properties andthe thermal stability of nanofiber mats. In brief, the samples were heated from 25°C to 800°C under a flow of nitrogen (10 ml/min), and the thermogravimetric analysis (TGA) curves were measured at a heating rate of 10°C/min.

The stress–strain curves and Young's modulus of the nanofiber mats were tested in dry conditions using a general test machine (HY-940FS, Shanghai Hengyu Instrument Co., Ltd., China) (Hong et al., 2011; Zheng et al., 2013). Before the measurement, three sample strips were randomly cut from nanofiber mat for the tensile test to get an average result. The tensile speed of nanofibers mats was 5 mm/min before the sample fracture.

Cell Culture With Nanofiber Mats

MC3T3 cells were grown in a carbon dioxide incubator at 37°C and 5% CO_2. A Dulbecco's modified eagle medium (DMEM) containing 10% fetal bovine serum and 1% penicillin–streptomycin solution was used. Nanofiber mats were prepared on glass cover plates and placed at the bottom of 24-well plates, respectively. The surface of the sample was fixed by a stainless steel ring. Before inoculation, the stainless steel ring, glass cover plates, and nanofiber mat were sterilized with 75% ethanol for 12 h and then soaked in a culture medium to ensure a uniform distribution on the nanofibers mat. Then, MC3T3 cells with a certain density (1.0×10^4/well) were incubated on the nanofiber mat for cell adhesion and proliferation, and the medium was changed every 3 days. After MC3T3 cells were cultured in a 24-well plate for 1, 4, and 7 days, the cell viability was determined by the CCK-8 method. Fluorescence microscopy (Nikon, Japan) and SEM were used to observe the cell adhesion of nanofibers mats. For the immunofluorescence observation, the samples were fixed with 4% paraformaldehyde, following staining with rhodamine-conjugated phalloidin and DAPI. Finally, the residual dye of actin and nuclei of the cells were washed with PBS.

Western Blot Testing

For the determination of osteogenic-associated gene expression level of MC3T3 cells which were cocultured with different nanofiber mats, MC3T3 cells (1×10^5 cells/well) were cultured in a 6-well plate for 1, 4, and 7 days. At a period of 1, 4, and 7 days of culture, sodium dodecyl sulfate polyacrylamide gel electrophoresis was used for the protein extraction, which was then moved onto a polyvinylidene difluoride membrane surface (Merck Millipore, German). The membranes were then treated with 5% bovine serum albumin (BSA) and then incubated with monoclonal antibodies for RUNX2, OCN, and actin at 4°C overnight. The samples were then incubated with HRP-conjugated secondary goat anti-rabbit antibody (RT, 2 h), followed by the quantitative analysis using Amersham ECL Plus reagents on an Image Quant LAS 4000 (GE, United States).

Statistical Analysis

The results of all our work were expressed as mean standard deviation (SD) one-way ANOVA for data analysis, and Origin Pro 9.5 for the Tukey's test for specificity difference assessment with a significant level set at 0.05.

RESULTS AND DISCUSSION

A simple and effective strategy to regulate the preparation and construction of functional bone regeneration induced nanofibers mats with dual bioactive components via homogeneous blends

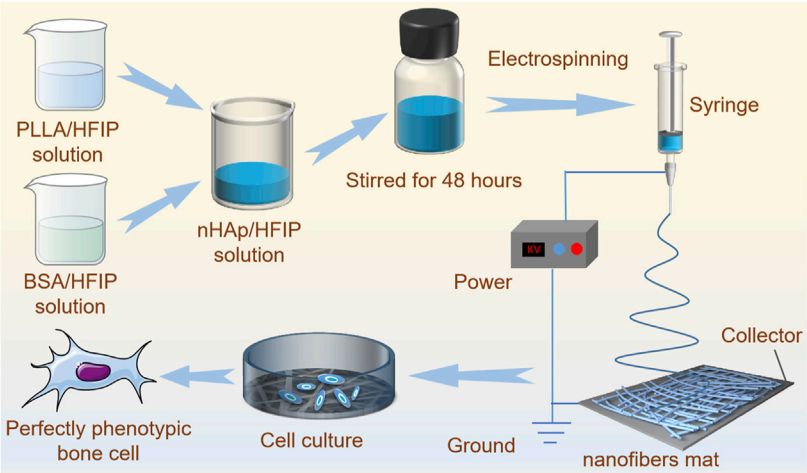

FIGURE 1 | The schematic diagram of PLLA/BSA/nHAp nanofiber mat preparation by electrospinning and mechanisms of regulating bone cellular phenotype by nanofibers.

combined with the electrospinning technology is proposed. **Figure 1** shows the fabrication process and formation mechanism of the functional scaffold with a three-dimensional structure. We prepared a uniformly dispersed mixed solution by separately dissolving the components and then blending them. This solution is easier to electrospin to form regular fibers than a solution which is prepared by "one-pot blending." The biodegradable PLLA as a frame material for mechanical support, as well as bioactive polymer BSA from a natural life source with osteogenic induction activity, and nHAp nanoparticles were combined together by electrospinning to promote bone regeneration.

Apparent Morphology and Microstructure of Prepared Nanofibers

Nanofiber-based scaffolds are very suitable material for bone repairing due to its three-dimensional structure with a biomimetic extracellular matrix, which can enhance differentiation of osteoblasts and mineralization due to their ECM-like structures (Srouji et al., 2011; Cheng et al., 2018; Kouhi et al., 2019). Bone tissue is generally composed of inorganic salts (e.g., HAp), organic fibrous matrices (collagen I), and cells. As a result, bone repair requires the application of inorganic materials to pack the defect and collagen membrane to inhibit the rapid growth of nearby soft tissues (Feng et al., 2019). Therefore, by incorporating the osteogenic active substance into an electrospun scaffold *via* the electrospinning technology, it can promote the osteogenic differentiation and bone healing.

In this study, three nanofibers mats, namely, PLLA, PLLA/BSA, and PLLA/BSA/nHAp nanofiber mats were prepared as an induction carrier for bone regeneration. PLLA, PLLA/BSA, and PLLA/BSA/nHAp nanofiber mats can also be easily processed into any shape and appearance as shown in **Figure 2A**. The three-dimensional structure of nanofiber mats is closely related to the cell phenotype. The microstructure of nanofiber mats is not only related to the electrospinning technological parameter, such as voltage, solution concentration, and receiving distance, but also related to the dispersibility of nHAp nanoparticles in polymer materials. Therefore, we have electrospun PLLA, PLLA/BSA, and PLLA/BSA/nHAp—three kinds of fibers—under the best electrospinning by adjusting parameters and tested its morphology by SEM. As shown in **Figures 2B–E**, all the nanofibers' surface renders an interconnected porous network structure by SEM, and the diameter of the nanofibers remains relatively well with ImageJ analysis software. In addition to this, we found that the PLLA, PLLA/BSA, and PLLA/BSA/nHAp nanofibers diameter, respectively, were 0.150 ± 0.044 μm, 0.110 ± 0.025 μm, and 0.150 ± 0.056 μm (**Figures 2C–2E**). Compared with pure PLLA nanofiber mats, the reduced diameter of the PLLA/BSA nanofibers may be related to the presence of positive charge in BSA, which neutralized with the negative charge output by the voltage generator during the electrospinning. On the other hand, the mercapto group in BSA is very active, which can bind to a variety of small molecules and enhance the tractive force of the droplet surface in the process of electrospinning. What is noteworthy is that, compared with the PLLA/BSA nanofiber mats, PLLA/BSA/nHAp nanofibers mat has a larger diameter, which may be due to the addition of the uniform dispersion of nHAp particles as in **Figure 2F** (red arrow). Although nHAp is uniformly mixed in the electrospinning solution, it also increased the viscosity of the mixed solution, so the diameter of PLLA/BSA/nHAp nanofibers is relatively thicker than that of PLLA/BSA nanofibers.

It is reported that a higher porosity could provide cells with more space for attachment and proliferation and also improve nutrition transport (Menon et al., 2015). As shown in **Figure 2G**, among PLLA, PLLA/BSA, and PLLA/BSA/nHAp nanofiber mats, PLLA/BSA/nHAp nanofiber mat has the largest porosity and the smallest apparent density. The porosity and apparent density of prepared nanofiber mats are related to the fiber diameter and the three-dimensional structure of mats. Although PLLA/BSA/nHAp

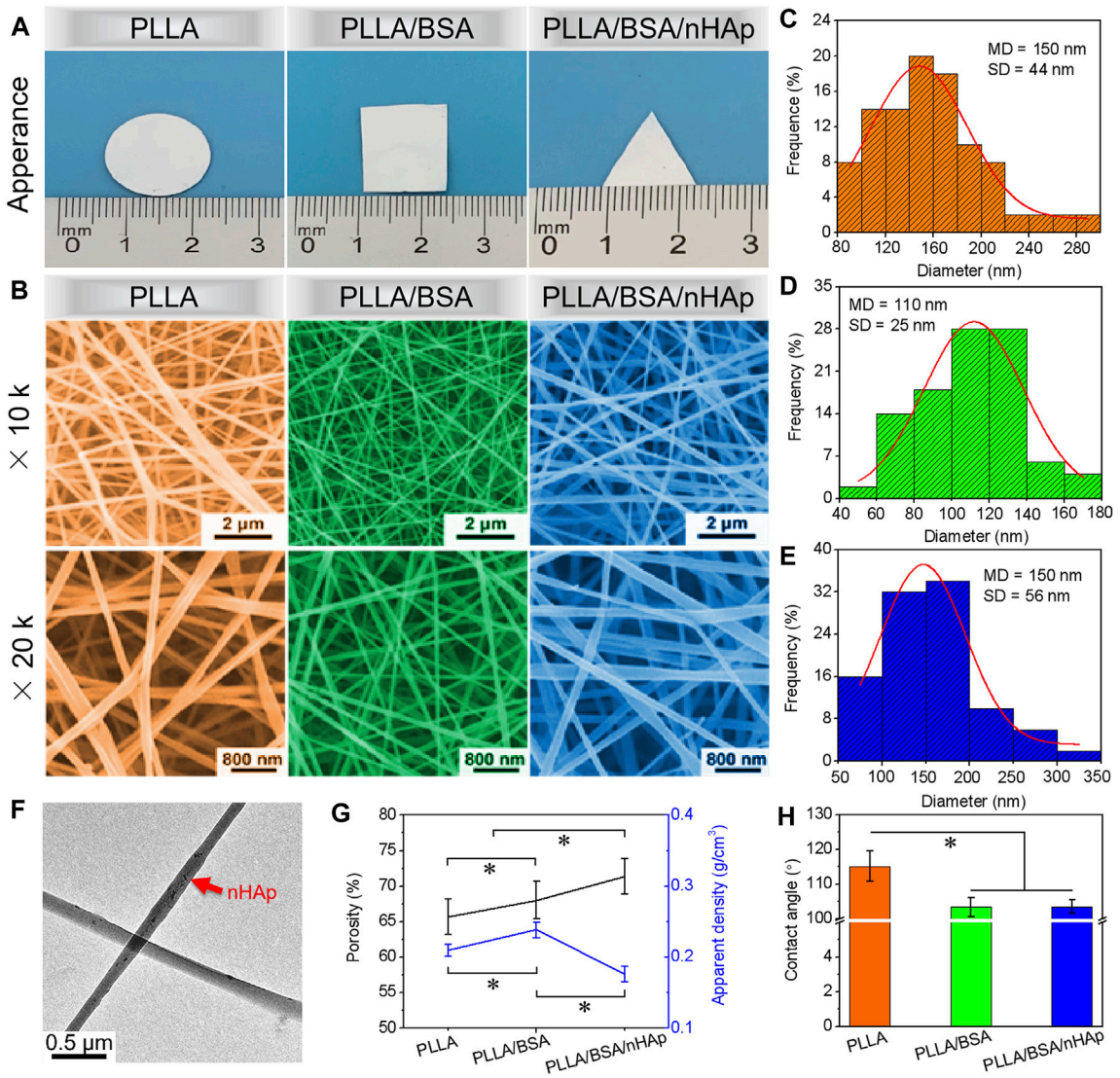

FIGURE 2 | (A) The appearance images and **(B)** SEM images at different multiples of prepared PLLA, PLLA/BSA, and PLLA/BSA/nHAp nanofibers. **(C–E)** Normal distribution of PLLA, PLLA/BSA, and PLLA/BSA/nHAp nanofibers, respectively. **(F)** TEM image of PLLA/BSA/nHAp nanofiber. **(G)** Porosity and apparent density. **(H)** Water contact angle of PLLA, PLLA/BSA, and PLLA/BSA/nHAp nanofibers mats, respectively. (*$p < 0.05$).

nanofiber mat and PLLA nanofiber mat have the same statistical average fiber diameter, the morphology of PLLA/BSA/nHAp nanofiber is not regular due to the dispersion of nanoparticles in a fiber matrix.

The hydrophilicity of biomaterials also plays an extremely important role in tissue engineering applications (Yu et al., 2020). The wetting property of the fiber mats is not only related to mats' three-dimensional structure but also related to the physical and chemical properties of the mats material itself. PLLA has weak hydrophilicity and no natural cell recognition site, which leads to a poor cell affinity. However, the natural material BSA has a lot of natural cells recognition sites and preferable cellular affinity, which could be the high potential scaffold material of bone tissue engineering. Herein, the water contact angle was used to evaluate the surface hydrophilicity of prepared nanofiber mats. As illustrated in **Figure 2H**, the dynamic change of the water contact angle was measured to evaluate the hydrophilicity of mats. The obtained results demonstrated that the water contact angle of PLLA/BSA nanofiber mat decreased compared with the PLLA nanofibers mat. This can be attributed to the hydrophobic property of PLLA. Compared with the PLLA/BSA nanofibers mat, the hydrophilicity of PLLA/BSA/nHAp nanofibers mat decreased again, indicating that nHAp further enhanced the hydrophilicity of nanofibers mat due to its rough fibrous surface structure, which may help the nanofiber mat to recruit more cells on the surface of mats.

Chemical Structure and Characteristics

The ATR-FTIR spectrum identifies materials and their interactions by determining chemical bonds (Holm et al.,

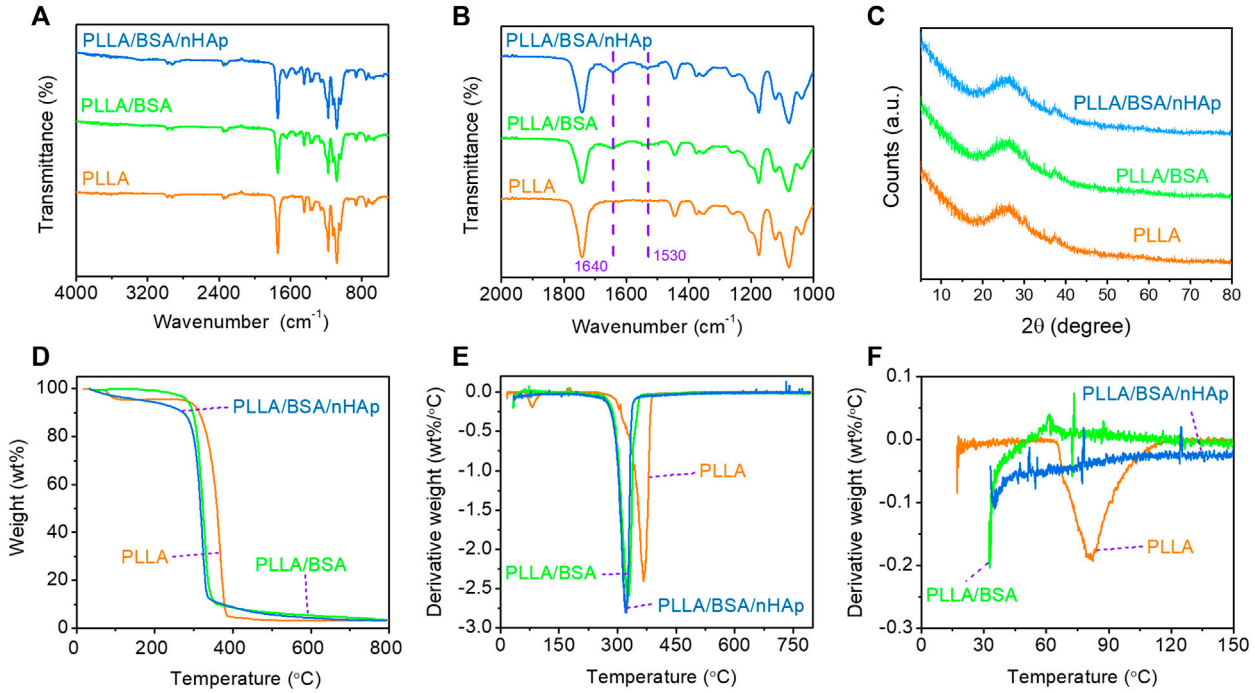

FIGURE 3 | Chemical properties of nanofibers mat include the following: **(A, B)** FTIR spectra curves of 4,000–400 cm^{-1} range and 2000–1,000 cm^{-1} range; **(C)** XRD with 5–80°range; **(D)** TGA curves with 50–800°C range, and **(E, F)** DTG curves with 0–800°C and 0–150°C range.

2007). According to **Figures 3A,B**, it can be seen from the infrared spectrum of the PLLA nanofiber mat that there was no obvious absorption peak above 3,000 cm^{-1}, which indicates that PLLA basically contains no hydroxyl and carboxyl groups. The absorption peak at 1746.09 cm^{-1} represented the stretching vibration of ester carbonyl in PLLA. The peak around 2,977.08 cm^{-1} was the -C-H- group stretching vibration of PLLA. The absorption peak at the wavelength of 1,085.34 cm^{-1} represented the stretching vibration absorption of -C-O- in PLLA. Compared with a pure PLLA nanofiber mat, the characteristic peak of both PLLA/BSA and PLLA/BSA/nHAp nanofiber mats appeared around 1,530–1,640 cm^{-1}, which may due to the presence of α-helical proteins in BSA (Patel et al., 2019). The comparison of PLLA/BSA and PLLA/BSA/nHAp nanofibers mats showed no significant change in the peak value, indicating that the addition of BSA and nHAp nanoparticles had little effect on the structure of polymer PLLA, and it also indicates that the three substances are closely bound together by an intermolecular force or hydrogen bonding.

The crystal structures of the PLLA nanofibers mat and composite nanofibers mats were accurately characterized by XRD (**Figure 3C**). The inorganic phase composition of the PLLA/BSA/nHAp nanofibers mat was studied by the XRD analysis. As previously reported, PLLA polymer is a semicrystalline material that can be identified by XRD at specific peaks at 21.5° and 29.5°. Compared with the PLLA nanofiber mat, the XRD patterns of the PLLA/BSA/nHAp nanofibers mat had little changes in the crystal structure, due to the excellent physical mixing between apatite nanoparticles and PLLA/BSA matrix.

The thermogravimetric analysis reveals the change of material mass with the increase of temperature and time to evaluate the thermal stability of the material (Zhu et al., 2017). The principle of TGA detection is to measure the residue after the thermal degradation of the sample and evaluate the thermal stability of the sample. TGA curves of nanofibers mats are shown in Figure 3D. We could simply analyze that the weight loss at 250–300°C was caused by the thermal decomposition of PLLA. In addition, there was only one turning point on the thermal degradation curves of the three materials, and the initial degradation temperature was between 250 and 300°C, which indicated that the addition of BSA and nHAp did not significantly change the thermal stability of the composites compared with the PLLA nanofiber mat. As shown in **Figures 3E,F**, the peak thermal decomposition temperatures of different components are different, and it represents the maximum rate of weight loss that occurs. The DTG curve reveals that the initial temperature of the thermal degradation of nanofibers decreases with the addition of BSA, and this is due to BSA, which is a natural active ingredient with poor thermal stability; the heating process may lead to the aggravation of an intermolecular motion in the nanofiber mat. Therefore, the maximum thermal decomposition rate corresponding to the temperature of composite nanofibers mats was reduced by further introducing BSA.

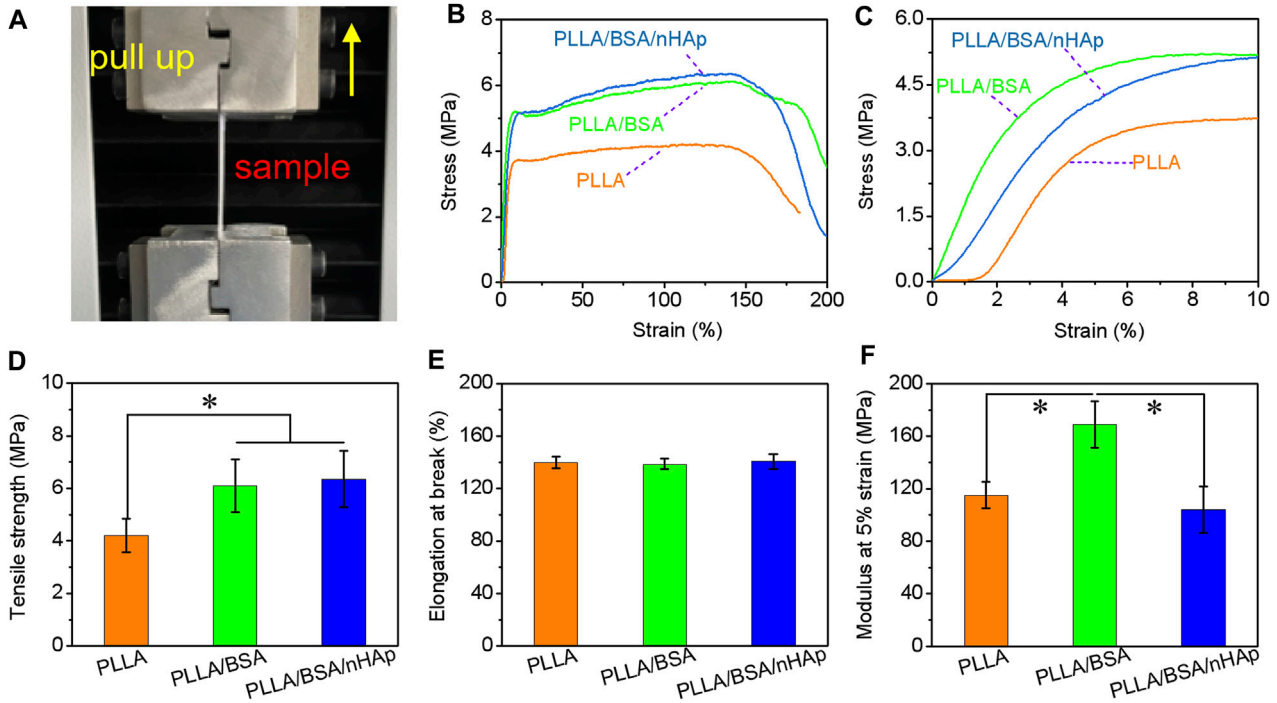

FIGURE 4 | Mechanical properties of nanofibers mats: **(A)** photographs of fracture of mat strips; **(B)** stress-strain curves from begin to break, and **(C)** stress–strain curves from begin to 10% strain; **(D)** tensile strength, **(E)** elongation at break, and **(F)** modulus at 5% strain of PLLA, PLLA/BSA, and PLLA/BSA/nHAp nanofibers mat under a dry situation. (*$p < 0.05$).

Mechanical Properties

Suitable mechanical properties similar to the bone tissue are beneficial for bone tissue repairing via a specific cell phenotype (Matinfar et al., 2019; Zhu et al., 2019). In this study, the radial stress–strain curves, modulus at 5% strain, tensile strength, and elongation at break of PLLA, PLLA/BSA, and PLLA/BSA/nHAp nanofiber mats under dry state tested by a unidirectional stretching machine were used to evaluate mats' mechanical properties (**Figure 4A**). As shown in **Figures 4B,C**, it was obvious that all the nanofiber mats showed a regular curve with a quick increase. Additionally, we can see the tensile strength of the PLLA/BSA nanofibers mat was strikingly higher than the pure PLLA nanofiber mat. This phenomenon was attributed to the coexistence of BSA and PLLA, which leads to the enhancement of the intermolecular force of electrospun solution. Much more than this, the decrease of fiber diameter and the increase of nanofiber mat density can also lead to an increase of tensile strength and initial modulus. Additionally, the introduction of BSA also further improved the tensile strength, and this may be related to the hydrogen bond interface and a serious entanglement occurred between the molecular chains of BSA and PLLA components (**Figure 4D**). The addition of BSA and nHAp did not significantly change the elongation at break of the scaffold, possibly due to nHAp and BSA evenly dispersed in the fibers (**Figure 4E**). The modulus test at 5% strain results showed that, with the addition of BSA, the modulus of the PLLA nanofiber mat was increased. But when nHAp is continued to be added, the modulus of the PLLA/BSA nanofiber mat was decreased, which is the appearance of nHAp caused by a more serious nHAp–PLLA or nHAp–BSA interface bonding.

Biocompatibility and Osteogenic Effect in *In Vitro*

As we know, the micro-/nanofibers can mimic the three-dimensional structure of the extracellular matrix, which will provide a matrix for cell adhesion and proliferation. Ensuring cell survival *in vitro* is one of the key techniques for assessing the biocompatibility of scaffolds (Rezk et al., 2018b; Du et al., 2018; Rather et al., 2020). As one of the most important elements in bone tissue engineering, MC3T3 was selected in this study to evaluate their proliferation characteristics on nanofiber mat. The proliferation of MC3T3 incubated on the surface of nanofibers mat was analyzed by using the CCK-8 assay after 1, 4, and 7 days (n = 3 for each group) of culture. From the histogram in **Figure 5A**, the results indicated that a slight increase in the proliferation profile on the PLLA/BSA composites nanofiber mat and PLLA/BSA/nHAp nanofibers mat than pure PLLA nanofibers mat was observed after 1 day of culture. The number of MC3T3 cells per mm^2 after culture for 7 days is shown in **Figure 5B**. After 7 days of culture, the number of cells on both the PLLA/BSA nanofibers mat and PLLA/BSA/nHAp nanofibers mat was more compared with the PLLA nanofibers mat. The cells showed a good proliferative activity on the surface of the PLLA/BSA/nHAp nanofiber, mat and the biocompatibility of the scaffold was good. The results indicated that PLLA/BSA/

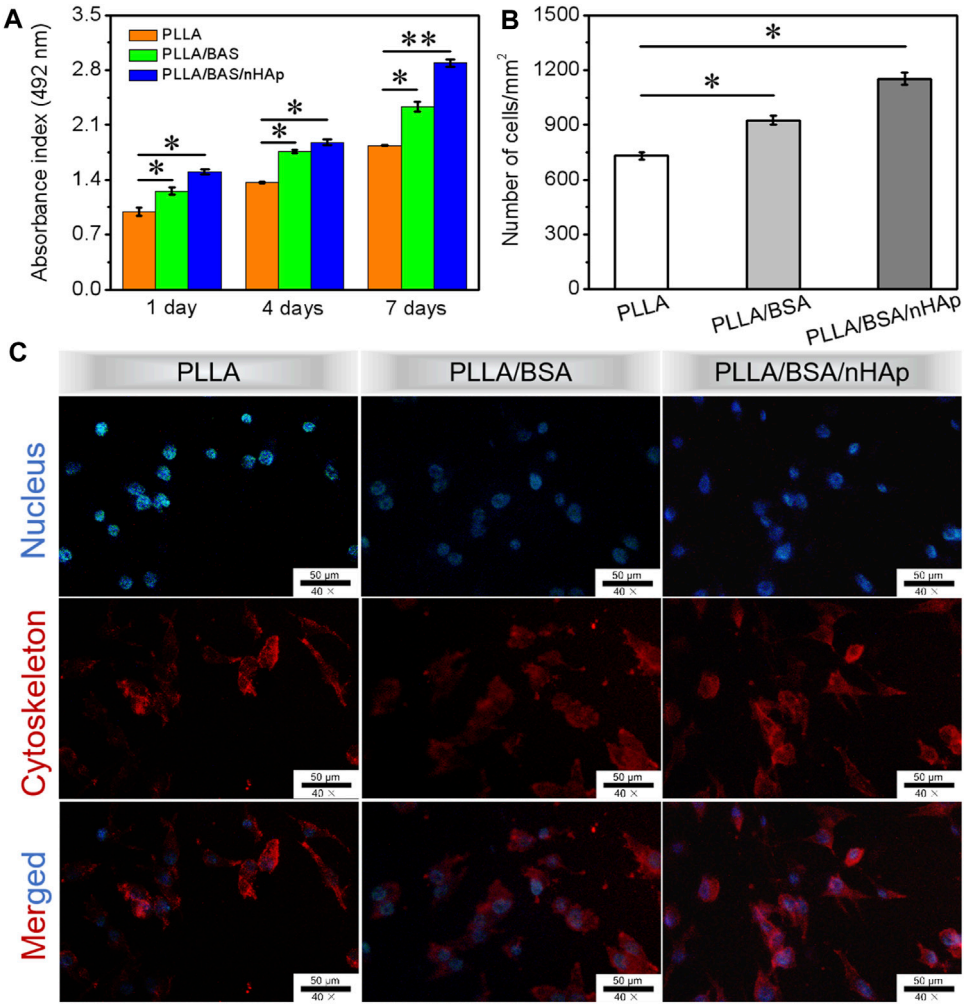

FIGURE 5 | Biocompatibility tests results: **(A)** CCK-8 assay of the proliferation viability of MC3T3 cultured for 1, 4, and 7 days. **(B)** Number of MC3T3 cells per mm^2 after culture for 7 days. **(C)** DAPI (blue)/rhodamine-conjugated phalloidin (red) staining assay after 4 days of culture. (***p < 0.01* and **p < 0.05*).

nHAp nanofiber mat with a biomimetic extracellular matrix was beneficial to the growth of osteoblasts.

DAPI and rhodamine-conjugated phalloidin were applied to staining nucleus and cytoskeleton of proliferative MC3T3 cells with blue fluorescence and red fluorescence, respectively. The morphology of the cellular activity from fluorescence microscopy images is shown in **Figure 5C** for day 4 of MC3T3 proliferation. The results indicated that MC3T3 cells cultured on the surfaces of PLLA and PLLA/BSA nanofiber mats presented a similar polygonal shape, while on the surfaces of the PLLA/BSA/nHAp nanofiber mat spread more homogeneously and presented cell-specific pseudopods, suggesting that the addition of nHAp uniformly dispersed in the PLLA/BSA nanofibrous matrix promoted the cell proliferation on nanofiber mat. Therefore, the cells might achieve rapid osteogenic differentiation on PLLA/BSA/nHAp nanofibers mat, indicating the potential application of bone tissue engineering.

After cells adhere to the surface of nanofibers mats, they entered the stage of rapid proliferation and growth. Therefore, the establishment of cell–cell interaction is essential for the subsequent differentiation and growth of cells. SEM images of MC3T3 cells proliferation after seeding on different nanofiber mats for 4 days are shown in **Figure 6A**. It can be seen that the MC3T3 was equally deposited onto the surfaces of scaffolds. Moreover, according to the results of the number of MC3T3 cells per mm^2 and percentage of cell area as in **Figures 6B,C**, MC3T3 cells on the surfaces of PLLA/BSA/nHAp nanofibers mat displayed spindle or triangular shapes and showed a greater spread property than the other two groups. The results suggested that PLLA/BSA/nHAp composite nanofiber mat could provide the appropriate environment for cell adhesion and proliferation.

The basic principle of western blot is to stain the cells or biological tissue samples treated by gel electrophoresis with

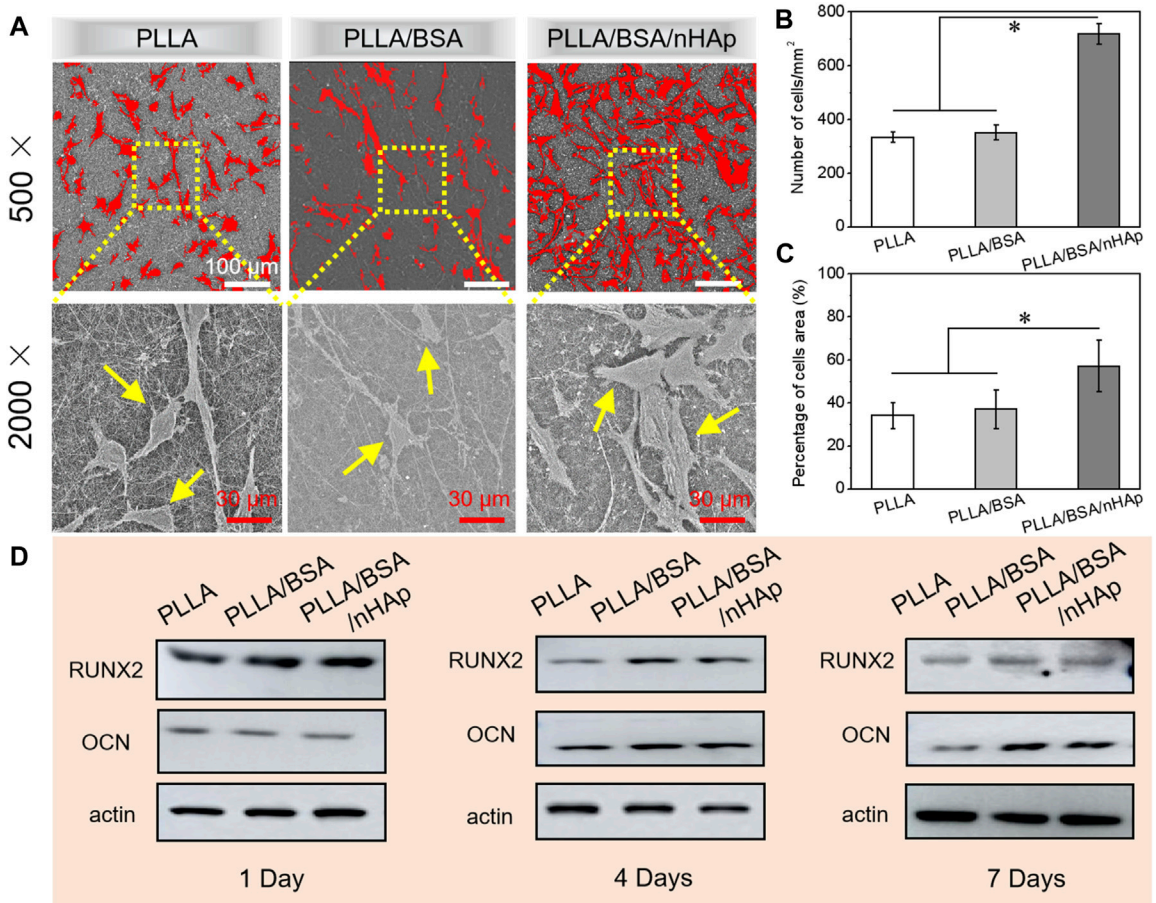

FIGURE 6 | (A) SEM images of cells after 4 days of culture *in vitro*. **(B, C)** Number of MC3T3 cells per mm^2 and percentage of cells area after 4 days' culture, respectively. **(D)** Western blot results for detecting proteins (RUNX2, OCN, and β-actin) associated with osteogenesis in MC3T3 cultured for 1, 4, and 7 days, respectively (*$p < 0.05$).

specific antibodies and obtain the information of the expression of specific proteins by analyzing the location and depth of staining. The expression of osteogenic proteins (i.e., RUNX2, OCN, and β-actin) in MC3T3 cultured with PLLA nanofiber mat, PLLA/BSA nanofiber mat, and PLLA/BSA/nHAp nanofiber mat for 1 day, 4, and 7 days were qualitatively detected by a western blot assay, respectively. As shown in **Figure 6D**, the cell cultured with the PLLA/BSA/HAp nanofibers mat was shown obviously increased the protein expression level more than the PLLA and PLLA/BSA nanofiber mat after either 4 days or 7 days. It is worth noticing that the band intensity of PLLA/BSA was the strongest among the three kinds of nanofibers mats, indicating that the osteogenesis-related protein expression levels in the group with BSA were significantly better than pure PLLA nanofibers mat after 4 days. The protein expression also showed a similar trend after 7 days, indicating that the addition of BSA and HAp induced the preferable osteogenesis effect.

CONCLUSION

In summary, a nanofiber mat with dual bioactive components and biomimetic matrix structure (PLLA/BSA/nHAp) with improved osteogenesis capability was successfully developed by homogeneous blending, following the electrospinning of poly(L-lactic acid), bovine serum albumin, and nanohydroxyapatite as comonomers in this work. PSM also exhibited salutary surface wettability and matched mechanical properties with bone tissue. A coculture with cells and an osteogenic effect in *in vitro* studies indicated that the migration and protein (RUNX2, OCN, and β-actin) associated with the osteogenesis of osteoblast can prominently speed up by the bioactive nanofibers mat. Meanwhile, the introduction of BSA and nHAp in PLLA nanofibers enables PLLA/BSA/nHAp with the capability of promoting ossification, which substantially facilitates the potential osseous regeneration to repair a large bone defect. Therefore, it is envisioned that PLLA/BSA/nHAp as promising bioactive scaffolds holds a high potential in the applications of bone tissue engineering.

DATA AVAILABILITY STATEMENT

The raw data supporting the conclusions of this article will be made available by the authors, without undue reservation.

AUTHOR CONTRIBUTIONS

All authors listed have made a substantial, direct, and intellectual contribution to the work and approved it for publication.

ACKNOWLEDGMENTS

The authors sincerely appreciate projects sponsored by the "Technology Support Project of Science and Technology Commission of Shanghai Municipality of China (19441901700, 19441901701, and 19441901702)," "National Natural Science Foundation of China (81902186, 82001968, and 82074456)," "Shanghai Rising-Star Program (20QC1401300)," "Shanghai Pujiang Program (20PJ1403800)," "China Postdoctoral Science Foundation (2019M661525)," "Shanghai Post-Doctoral Excellence Program (2019365)," and "Gusu Health Talents Project (GSWS 2020090)."

SUPPLEMENTARY MATERIAL

The Supplementary Material for this article can be found online at: https://www.frontiersin.org/articles/10.3389/fchem.2021.740191/full#supplementary-material

REFERENCES

Aoki, K., Haniu, H., Kim, Y. A., and Saito, N. (2020). The Use of Electrospun Organic and Carbon Nanofibers in Bone Regeneration. *Nanomaterials* 10, 562. doi:10.3390/nano10030562

Bauer, L., Antunović, M., Rogina, A., Ivanković, M., and Ivanković, H. (2020). Bone-mimetic Porous Hydroxyapatite/whitlockite Scaffolds: Preparation, Characterization and Interactions with Human Mesenchymal Stem Cells. *J. Mater. Sci.* 56, 3947–3969. doi:10.1007/s10853-020-05489-3

Chen, R., Wang, J., and Liu, C. (2016). Biomaterials Act as Enhancers of Growth Factors in Bone Regeneration. *Adv. Funct. Mater.* 26, 8810–8823. doi:10.1002/adfm.201603197

Chen, S., Shi, Y., Luo, Y., and Ma, J. (2019). Layer-by-layer Coated Porous 3D Printed Hydroxyapatite Composite Scaffolds for Controlled Drug Delivery. *Colloids Surf. B: Biointerfaces* 179, 121–127. doi:10.1016/j.colsurfb.2019.03.063

Cheng, G., Ma, X., Li, J., Cheng, Y., Cao, Y., Wang, Z., et al. (2018). Incorporating Platelet-Rich Plasma into Coaxial Electrospun Nanofibers for Bone Tissue Engineering. *Int. J. Pharmaceutics* 547, 656–666. doi:10.1016/j.ijpharm.2018.06.020

Damien, C. J., and Parsons, J. R. (2010). Achieve Optimum Aesthetics. *Br. Dent J.* 208, 187. doi:10.1038/sj.bdj.2010.187

Du, J., Wang, J.-H., Yu, H.-Y., Zhang, Y.-Y., Pu, L.-H., Wang, J.-C., et al. (2019). Electrospun Poly(p-dioxanone)/Poly(ester-Urethane)ureas Composite Nanofibers for Potential Heart Valve Tissue Reconstruction. *Chin. J. Polym. Sci.* 37, 560–569. doi:10.1007/s10118-019-2231-2

Du, J., Zhu, T., Yu, H., Zhu, J., Sun, C., Wang, J., et al. (2018). Potential Applications of Three-Dimensional Structure of Silk Fibroin/poly(ester-Urethane) Urea Nanofibrous Scaffold in Heart Valve Tissue Engineering. *Appl. Surf. Sci.* 447, 269–278. doi:10.1016/j.apsusc.2018.03.077

Feng, X., Li, J., Zhang, X., Liu, T., Ding, J., and Chen, X. (2019). Electrospun Polymer Micro/nanofibers as Pharmaceutical Repositories for Healthcare. *J. Controlled Release* 302, 19–41. doi:10.1016/j.jconrel.2019.03.020

Holm, N. K., Jespersen, S. K., Thomassen, L. V., Wolff, T. Y., Sehgal, P., Thomsen, L. A., et al. (2007). Aggregation and Fibrillation of Bovine Serum Albumin. *Biochim. Biophys. Acta (Bba) - Proteins Proteomics* 1774, 1128–1138. doi:10.1016/j.bbapap.2007.06.008

Hong, Y., Huber, A., Takanari, K., Amoroso, N. J., Hashizume, R., Badylak, S. F., et al. (2011). Mechanical Properties and *In Vivo* Behavior of a Biodegradable Synthetic Polymer Microfiber-Extracellular Matrix Hydrogel Biohybrid Scaffold. *Biomaterials* 32, 3387–3394. doi:10.1016/j.biomaterials.2011.01.025

Huang, J., Lin, D., Wei, Z., Li, Q., Zheng, J., Zheng, Q., et al. (2020). *Small* 16, e1905876. doi:10.1002/smll.201905876

Jakus, A. E., Rutz, A. L., Jordan, S. W., Kannan, A., Mitchell, S. M., Yun, C., et al. (2016). *Sci. Transl Med.* 8, 358ra127. doi:10.1126/scitranslmed.aaf7704

Kouhi, M., Jayarama Reddy, V., Fathi, M., Shamanian, M., Valipouri, A., and Ramakrishna, S. (2019). Poly (3-Hydroxybutyrate-Co-3-Hydroxyvalerate)/fibrinogen/bredigite Nanofibrous Membranes and Their Integration with Osteoblasts for Guided Bone Regeneration. *J. Biomed. Mater. Res.* 107, 1154–1165. doi:10.1002/jbm.a.36607

Li, D., Sun, H., Jiang, L., Zhang, K., Liu, W., Zhu, Y., et al. (2014). Enhanced Biocompatibility of PLGA Nanofibers with Gelatin/Nano-Hydroxyapatite Bone Biomimetics Incorporation. *ACS Appl. Mater. Inter.* 6, 9402–9410. doi:10.1021/am5017792

Li, H., Bo, Z., Wu, H., Li, Z., and Zhao, J. (2017). *Mat Sci. Eng. C* 70, 955–961.

Liu, W., Sun, J., Sun, Y., Xiang, Y., Yan, Y., Han, Z., et al. (2020). Multifunctional Injectable Protein-Based Hydrogel for Bone Regeneration. *Chem. Eng. J.* 394. doi:10.1016/j.cej.2020.124875

Liu, X., Bao, C., Xu, H. H. K., Pan, J., Hu, J., Wang, P., et al. (2016). Osteoprotegerin Gene-Modified BMSCs with Hydroxyapatite Scaffold for Treating Critical-Sized Mandibular Defects in Ovariectomized Osteoporotic Rats. *Acta Biomater.* 42, 378–388. doi:10.1016/j.actbio.2016.06.019

Matinfar, M., Mesgar, A. S., and Mohammadi, Z. (2019). Evaluation of Physicochemical, Mechanical and Biological Properties of Chitosan/carboxymethyl Cellulose Reinforced with Multiphasic Calcium Phosphate Whisker-like Fibers for Bone Tissue Engineering. *Mater. Sci. Eng. C* 100, 341–353. doi:10.1016/j.msec.2019.03.015

Menon, N. V., Chuah, Y. J., Phey, S., Zhang, Y., Wu, Y., Chan, V., et al. (2015). Microfluidic Assay to Study the Combinatorial Impact of Substrate Properties on Mesenchymal Stem Cell Migration. *ACS Appl. Mater. Inter.* 7, 17095–17103. doi:10.1021/acsami.5b03753

Oryan, A., Alidadi, S., Moshiri, A., and Maffulli, N. (2014). Bone Regenerative Medicine: Classic Options, Novel Strategies, and Future Directions. *J. Orthop. Surg. Res.* 9. doi:10.1186/1749-799x-9-18

Patel, P. P., Buckley, C., Taylor, B. L., Sahyoun, C. C., Patel, S. D., Mont, A. J., et al. (2019). Mechanical and Biological Evaluation of a Hydroxyapatite-Reinforced Scaffold for Bone Regeneration. *J. Biomed. Mater. Res.* 107, 732–741. doi:10.1002/jbm.a.36588

Qi, H., Ye, Z., Ren, H., Chen, N., Zeng, Q., Wu, X., et al. (2016). Bioactivity Assessment of PLLA/PCL/HAP Electrospun Nanofibrous Scaffolds for Bone Tissue Engineering. *Life Sci.* 148, 139–144. doi:10.1016/j.lfs.2016.02.040

Rajzer, I., Kurowska, A., Jabłoński, A., Jatteau, S., Śliwka, M., Ziąbka, M., et al. (2018). Layered Gelatin/PLLA Scaffolds Fabricated by Electrospinning and 3D Printing- for Nasal Cartilages and Subchondral Bone Reconstruction. *Mater. Des.* 155, 297–306. doi:10.1016/j.matdes.2018.06.012

Rather, H. A., Patel, R., Yadav, U. C. S., and Vasita, R. (2020). Dual Drug-Delivering Polycaprolactone-Collagen Scaffold to Induce Early Osteogenic Differentiation and Coupled Angiogenesis. *Biomed. Mater.* 15, 045008. doi:10.1088/1748-605x/ab7978

Rezk, A. I., Rajan Unnithan, A., Sang Kim, C., and Kim, C. S. (2018). Rational Design of Bone Extracellular Matrix Mimicking Tri-layered Composite Nanofibers for Bone Tissue Regeneration. *Chem. Eng. J.* 350, 812–823. doi:10.1016/j.cej.2018.05.185

Rezk, A. I., Rajan Unnithan, A., Sang Kim, C., and Kim, C. S. (2018). Rational Design of Bone Extracellular Matrix Mimicking Tri-layered Composite Nanofibers for Bone Tissue Regeneration. *Chem. Eng. J.* 350, 812–823. doi:10.1016/j.cej.2018.05.185

Saravanan, S., Vimalraj, S., Thanikaivelan, P., Banudevi, S., and Manivasagam, G. (2019). A Review on Injectable Chitosan/beta Glycerophosphate Hydrogels for Bone Tissue Regeneration. *Int. J. Biol. Macromolecules* 121121, 38–54. doi:10.1016/j.ijbiomac.2018.10.014

Satpathy, A., Pal, A., Sengupta, S., Das, A., Hasan, M. M., Ratha, I., et al. (2019). Bioactive Nano-Hydroxyapatite Doped Electrospun PVA-Chitosan Composite Nanofibers for Bone Tissue Engineering Applications. *J. Indian Inst. Sci.* 99, 289–302. doi:10.1007/s41745-019-00118-8

Schofer, M. D., Tünnermann, L., Kaiser, H., Roessler, P. P., Theisen, C., Heverhagen, J. T., et al. (2012). Functionalisation of PLLA Nanofiber Scaffolds Using a Possible Cooperative Effect between Collagen Type I and BMP-2: Impact on Colonization and Bone Formation *In Vivo*. *J. Mater. Sci. Mater. Med.* 23, 2227–2233. doi:10.1007/s10856-012-4697-0

Shim, I. K., Jung, M. R., Kim, K. H., Seol, Y. J., Park, Y. J., Park, W. H., et al. (2010). Novel Three-Dimensional Scaffolds of poly(L-Lactic Acid) Microfibers Using Electrospinning and Mechanical Expansion: Fabrication and Bone Regeneration. *J. Biomed. Mater. Res.* 95B, 150–160. doi:10.1002/jbm.b.31695

Sokolova, V., Kostka, K., Shalumon, K. T., Prymak, O., Chen, J.-P., and Epple, M. (2020). Synthesis and Characterization of PLGA/HAP Scaffolds with DNA-Functionalised Calcium Phosphate Nanoparticles for Bone Tissue Engineering. *J. Mater. Sci. Mater. Med.* 31, 102. doi:10.1007/s10856-020-06442-1

Srouji, S., Ben-David, D., Lotan, R., Livne, E., Avrahami, R., and Zussman, E. (2011). Slow-Release Human Recombinant Bone Morphogenetic Protein-2 Embedded within Electrospun Scaffolds for Regeneration of Bone Defect: *In Vitro* and *In Vivo* Evaluation. *Tissue Eng. A* 17, 269–277. doi:10.1089/ten.tea.2010.0250

Tanes, M. L., Xue, J., and Xia, Y. (2017). A General Strategy for Generating Gradients of Bioactive Proteins on Electrospun Nanofiber Mats by Masking with Bovine Serum Albumin. *J. Mater. Chem. B* 5, 5580–5587. doi:10.1039/c7tb00974g

Wang, C., Lai, J., Li, K., Zhu, S., Lu, B., Liu, J., et al. (2021). Cryogenic 3D Printing of Dual-Delivery Scaffolds for Improved Bone Regeneration with Enhanced Vascularization. *Bioactive Mater.* 66, 137–145. doi:10.1016/j.bioactmat.2020.07.007

Wang, L., Qiu, Y., Guo, Y., Si, Y., Liu, L., Cao, J., et al. (2019). Smart, Elastic, and Nanofiber-Based 3D Scaffolds with Self-Deploying Capability for Osteoporotic Bone Regeneration. *Nano Lett.* 19, 9112–9120. doi:10.1021/acs.nanolett.9b04313

Wang, L., Qiu, Y., Lv, H., Si, Y., Liu, L., Zhang, Q., et al. (2019). 3D Superelastic Scaffolds Constructed from Flexible Inorganic Nanofibers with Self-Fitting Capability and Tailorable Gradient for Bone Regeneration. *Adv. Funct. Mater.* 29, 1901407. doi:10.1002/adfm.201901407

Wang, S. J., Jiang, D., Zhang, Z. Z., Chen, Y. R., Yang, Z. D., Zhang, J. Y., et al. (2019). Biomimetic Nanosilica–Collagen Scaffolds for *In Situ* Bone Regeneration: Toward a Cell-Free, One-Step Surgery. *Adv. Mater.* 31, e1904341. doi:10.1002/adma.201904341

Wang, X., Lou, T., Zhao, W., Song, G., Li, C., and Cui, G. (2016). The Effect of Fiber Size and Pore Size on Cell Proliferation and Infiltration in PLLA Scaffolds on Bone Tissue Engineering. *J. Biomater. Appl.* 30, 1545–1551. doi:10.1177/0885328216636320

Wu, T., Xue, J., Li, H., Zhu, C., Mo, X., and Xia, Y. (2018). General Method for Generating Circular Gradients of Active Proteins on Nanofiber Scaffolds Sought for Wound Closure and Related Applications. *ACS Appl. Mater. Inter.* 10, 8536–8545. doi:10.1021/acsami.8b00129

Ye, K., Liu, D., Kuang, H., Cai, J., Chen, W., Sun, B., et al. (2019). Three-dimensional Electrospun Nanofibrous Scaffolds Displaying Bone Morphogenetic Protein-2-Derived Peptides for the Promotion of Osteogenic Differentiation of Stem Cells and Bone Regeneration. *J. Colloid Interf. Sci.* 534, 625–636. doi:10.1016/j.jcis.2018.09.071

Yu, M., Huang, J., Zhu, T., Lu, J., Liu, J., Li, X., et al. (2020). Liraglutide-loaded PLGA/gelatin Electrospun Nanofibrous Mats Promote Angiogenesis to Accelerate Diabetic Wound Healing via the Modulation of miR-29b-3p. *Biomater. Sci.* 8, 4225–4238. doi:10.1039/d0bm00442a

Yuan, Z., Wan, Z., Wei, P., Lu, X., Mao, J., Cai, Q., et al. (2020). *Adv. Healthc. Mater.* 9, e2000211. doi:10.1002/adhm.202000211

Zheng, F., Wang, S., Wen, S., Shen, M., Zhu, M., and Shi, X. (2013). Characterization and Antibacterial Activity of Amoxicillin-Loaded Electrospun Nano-Hydroxyapatite/poly(lactic-Co-Glycolic Acid) Composite Nanofibers. *Biomaterials* 34, 1402–1412. doi:10.1016/j.biomaterials.2012.10.071

Zhu, C., Pongkitwitoon, S., Qiu, J., Thomopoulos, S., and Xia, Y. (2018). *Adv. Mater.* 30, e1707306. doi:10.1002/adma.201870116

Zhu, T., Jiang, J., Zhao, J., Chen, S., and Yan, X. (2019). Regulating Preparation of Functional Alginate-Chitosan Three-Dimensional Scaffold for Skin Tissue Engineering. *Ijn* Vol. 14, 8891–8903. doi:10.2147/ijn.s210329

Zhu, T., Yu, K., Bhutto, M. A., Guo, X., Shen, W., Wang, J., et al. (2017). Synthesis of RGD-Peptide Modified Poly(ester-Urethane) Urea Electrospun Nanofibers as a Potential Application for Vascular Tissue Engineering. *Chem. Eng. J.* 315, 177–190. doi:10.1016/j.cej.2016.12.134

Zimmermann, G., and Moghaddam, A. (2011). Allograft Bone Matrix versus Synthetic Bone Graft Substitutes. *Injury* 42, S16–S21. doi:10.1016/j.injury.2011.06.199

Conflict of Interest: The authors declare that the research was conducted in the absence of any commercial or financial relationships that could be construed as a potential conflict of interest.

Publisher's Note: All claims expressed in this article are solely those of the authors and do not necessarily represent those of their affiliated organizations, or those of the publisher, the editors, and the reviewers. Any product that may be evaluated in this article, or claim that may be made by its manufacturer, is not guaranteed or endorsed by the publisher.

frontiers in Chemistry

ORIGINAL RESEARCH
published: 08 November 2021
doi: 10.3389/fchem.2021.789934

PPy@Fe_3O_4 Nanoparticles Inhibit Tumor Growth and Metastasis Through Chemodynamic and Photothermal Therapy in Non-small Cell Lung Cancer

Danruo Fang[1†], Hansong Jin[2†], Xiulin Huang[1], Yongxin Shi[1], Zeyu Liu[3] and Suqin Ben[1]**

[1]*Department of Respiratory and Critical Care Medicine, Shanghai General Hospital, Shanghai Jiao Tong University School of Medicine, Shanghai, China,* [2]*Department of Thoracic Surgery, Shanghai General Hospital, Shanghai Jiao Tong University School of Medicine, Shanghai, China,* [3]*Department of Respiratory and Critical Care Medicine, Shanghai Jiao Tong University Affiliated Sixth People's Hospital, Shanghai, China*

Non-small cell lung cancer (NSCLC) is considered to be a principal cause of cancer death across the world, and nanomedicine has provided promising alternatives for the treatment of NSCLC in recent years. Photothermal therapy (PTT) and chemodynamic therapy (CDT) have represented novel therapeutic modalities for cancer treatment with excellent performance. The purpose of this research was to evaluate the effects of PPy@Fe_3O_4 nanoparticles (NPs) on inhibiting growth and metastasis of NSCLC by combination of PTT and CDT. In this study, we synthesized PPy@Fe_3O_4 NPs through a very facile electrostatic absorption method. And we detected reactive oxygen species production, cell apoptosis, migration and protein expression in different groups of A549 cells and established xenograft models to evaluate the effects of PPy@Fe_3O_4 NPs for inhibiting the growth of NSCLC. The results showed that the PPy@Fe_3O_4 NPs had negligible cytotoxicity and could efficiently inhibit the cell growth and metastasis of NSCLC *in vitro*. In addition, the PPy@Fe_3O_4 NPs decreased tumor volume and growth *in vivo* and endowed their excellent MRI capability of observing the location and size of tumor. To sum up, our study displayed that the PPy@Fe_3O_4 NPs had significant synergistic effects of PTT and CDT, and had good biocompatibility and safety *in vivo* and *in vitro*. The PPy@Fe_3O_4 NPs may be an effective drug platform for the treatment of NSCLC.

Keywords: PPy@Fe_3O_4 nanoparticles, photothermal therapy, chemodynamic therapy, non-small cell lung cancer, tumor metastasis

Abbreviation: NSCLC, non-small cell lung cancer; NPs, nanoparticles; PPy, polypyrrole; MRI, magnetic resonance imaging; PTT, photothermal therapy; CDT, chemodynamic therapy; H_2O_2, hydrogen peroxide; ECM, extracellular matrix; TME, tumor microenvironment; MMPs, matrix metalloproteinases; PVA, Polyvinyl alcohol; TEM, transmission electron microscopy; FTIR, Fourier-Transformed Infrared; XRD, X-ray powder diffraction; NIR, near-infrared; CCK-8, cell counting kit-8; DCFH-DA, dichlorofluorescein-diacetate; ROS, reactive oxygen species; PBS, phosphate buffered saline; CLSM, Confocal laser scanning Microscopy; PI, propidium iodide; PVDF, polyvinylidene difluoride; HRP, horseradish peroxidase; TBST, Tris-buffered saline-Tween20; ECL, enhanced chemiluminescence; GSH, glutathione; EMT, epithelial-to-mesenchymal transition.

OPEN ACCESS

Edited by:
Houjuan Zhu,
*Institute of Materials Research and Engineering (A*STAR), Singapore*

Reviewed by:
Yanyan Jiang,
Shandong University, China
Yu Luo,
Shanghai University of Engineering Sciences, China

***Correspondence:**
Suqin Ben
bensuqin012@163.com
Zeyu Liu
liuzeyu1799@gmail.com

†These authors contributed equally to the paper

Specialty section:
This article was submitted to Nanoscience, a section of the journal Frontiers in Chemistry

Received: *05 October 2021*
Accepted: *20 October 2021*
Published: *08 November 2021*

Citation:
Fang D, Jin H, Huang X, Shi Y, Liu Z and Ben S (2021) PPy@Fe_3O_4 Nanoparticles Inhibit Tumor Growth and Metastasis Through Chemodynamic and Photothermal Therapy in Non-small Cell Lung Cancer. Front. Chem. 9:789934. doi: 10.3389/fchem.2021.789934

INTRODUCTION

Lung cancer remains the most common malignant cancer, which has the highest rates of mortality. (Nasim et al., 2019; Woodman et al., 2021) Non-small cell lung cancer (NSCLC) is one of the histological subtypes, which accounts for approximately 80–85% among lung cancers. (Oser et al., 2015) Over the last decade, considerable progress has been made in the treatment of NSCLC, helping us to understand tumor biology deeply and promoting the early detection and multimodal cancer treatment. (Herbst et al., 2018) However, metastatic lung cancer is still an incurable disease and has a median survival of only 5 months. (Riihimäki et al., 2014; Rosell and Karachaliou, 2015) At present, the conservative therapeutic methods including surgery, radiotherapy and chemotherapy are efficient modes to manage advanced lung cancer, but remain unsatisfactory for improving the therapeutic efficacy. (Luo et al., 2018) As such, continuous researches on novel therapeutic compounds and combination treatments are required to amplify clinical outcomes and to improve the survival outcomes of NSCLC.

In recent years, new advances in the bioapplication of nanomaterials substantially improved the diagnosis and treatment of tumors. (Guan et al., 2021; Zhao et al., 2021) Compared with conventional inorganic nanoparticles (NPs) and small molecule-based organic nanocarriers, polymers show excellent biocompatibility, biodegradability and minimal side effects on normal tissues. (Wang, 2016) Besides, polymer chemical structures can provide various responsive components for both external stimuli [such as light, (Hribar et al., 2011) radiofrequency, (Zhang et al., 2016) ultrasound, (Paris et al., 2015) and magnetic field (Mirvakili et al., 2020)] and internal states (such as pH, (Wang et al., 2016) temperature, (Zhang et al., 2020) enzyme, (Wei et al., 2016) and redox (Zhuang et al., 2018) environment). Recently, polypyrrole (PPy) NPs have extensively investigated as powerful photothermal agents exhibiting high photothermal conversion efficiency and exceptional photostability. (Zha et al., 2013) Meanwhile, PPy NPs are easy to fabricate, with low cost and high yield. (Phan et al., 2018; Yang et al., 2018) And it is well known that iron oxide NPs are positive contrast agents for T2 weighted magnetic resonance imaging (MRI) due to their low toxicity and superior magnetic properties. (Wei et al., 2017) In this study, since Fe^{3+} ions are used as the oxidation agents to produce PPy NPs, many ferric (Fe^{3+}) and ferrous ions (Fe^{2+}) remain in the obtained PPy NPs. And Fe ions in the PPy NPs are selected as precursors for *in situ* formation of Fe_3O_4 crystals onto the surface of pre-synthesized PPy NPs. The final products (PPy@Fe_3O_4 NPs) possess both chemodynamic therapy (CDT) and photothermal therapy (PTT) functions, holding tremendous potential for remarkable efficiency to inhibit tumor growth. PTT, which uses photothermal agents to ablate tumors by converting absorbed light energy into intense localized heat, has attracted widespread attention as a non-invasive therapeutic technology. (Chen et al., 2019) On the other hand, CDT is an emerging therapy that generates toxic hydroxyl radicals (·OH) from endogenous hydrogen peroxide (H_2O_2) using Fenton/Fenton-like reaction to control tumor progression in the tumor microenvironment (TME). (Tang et al., 2019) As generally known, compared with normal cells, cancer cells have special intracellular microenvironment with higher levels of H_2O_2 and weak acidity, which offers prerequisites to CDT application. (Yang et al., 2017, 2019; Shen et al., 2018) Thus, PPy@Fe_3O_4 NPs, which have noteworthy synergistic therapeutic effects, may play different roles in the growth and metastatic of NSCLC.

Extracellular matrix (ECM) is a complex biopolymer mixture produced by different kinds of cells in the extracellular space. The ECM not only is crucial in cell adhesion and tissue organization, but also modulates cell differentiation, activation and migration. (Pickup et al., 2014; Eble and Niland, 2019) Matrix metalloproteinases (MMPs) belong to a large family of zinc-dependent endopeptidases that are involved in ECM degradation and play essential roles in cancer progression-associated pathways, including tumor growth, invasion and migration. (Gonzalez-Avila et al., 2019) Matrix metalloproteinase 2/9/13 (MMP2/9/13) are key members of the MMP family. Among these MMPs, MMP2 and MMP9 can selectively degrade type IV collagen, promoting tumor cells migrating through the basement membrane. (Wang et al., 2018) And MMP13 has the capability to degrade native collagen fibrillar types I, II, III, and VII and is related to the ECM remodeling. MMP2, MMP9 and MMP13 have been found upregulated and enhance the migration capability of lung cancer cells (Li et al., 2019; Han et al., 2020). Meanwhile, down-regulating the expression of MMP2, MMP9 aand MMP13 can reduce tumor cell growth, proliferation and metastasis (Tan et al., 2015; Poudel et al., 2016). We are wondering if PPy@Fe_3O_4 NPs could decrease the expression of MMP2, MMP9 and MMP13.

In this research, we examined the anti-tumor efficacy of the novel PPy@Fe_3O_4 NPs *in vitro* and *in vivo*. Our results displayed that the growth of tumors was considerably inhibited by the PPy@Fe_3O_4 NPs, and the levels of MMP2, MMP9 and MMP13 decreased. These results demonstrated that PPy@Fe_3O_4 NPs were excellent MRI-guided synergistic chemodynamic/photothermal cancer therapy agents and might be promising drugs to treat NSCLC because of inhibition of tumor growth and metastasis.

MATERIALS AND METHODS

Chemicals and Reagents

Polyvinyl alcohol 1788 (PVA; Alcoholysis degree: 87.0–89.0%), iron (III) chloride anhydrous ($FeCl_3$; 99.9%) and pyrrole (99%) were purchased from Aladdin chemistry Co., Ltd. (Shanghai, China). Absolute ethyl alcohol (C_2H_5OH; AR) and ammonium hydroxide solution ($NH_3{\cdot}H_2O$; 28.0–30.0%) were purchased from Sinopharm Chemical Reagent Co., Ltd. (Shanghai, China). Deionized water (H_2O) was prepared by a Milli-Q water purification system (Millipore, Bedford, MA, United States). All the chemical reagents were used without further purification.

Preparation of PPy@Fe_3O_4 Nanoparticles

We synthesized the PPy@Fe_3O_4 NPs by a very facile electrostatic adsorption method. First, PVA (0.75 g) was added in the

deionized water (10 ml) and heated to 95°C until the solution was entirely dissolved. Later, $FeCl_3$ (0.373g, 2.30 mmol) was mixed homogeneously with the above mixture under strong magnetic stirring for 1 h. Next, pyrrole monomer (69.2μl, 0.9970 mmol) was slowly dropped, and the reaction was maintained for 4 h at 4°C under magnetic stirring. The final solution turned dark green, indicating that PPy NPs were successfully synthesized. Subsequently, the solution (2.5 ml) was taken out, mixed with deionized water (15 ml) and ethanol (2 ml) under stirring at 70°C. Afterwards, 1 ml 1.0 wt% aqueous ammonia liquid was dropped into the solution followed by stirring for 30 min. Then 1 ml of 1.0 wt% aqueous ammonia liquid was added dropwise again, and the mixture lastly maintained for 30 min at 70°C. Finally, after being washed three times by deionized water, the PPy@Fe_3O_4 NPs were collected by centrifugation (11000rpm) for 50 min.

Characterization of PPy@Fe_3O_4 NPs

The morphology and size of PPy@Fe_3O_4 NPs were determined using a JEM-200 transmission electron microscopy (TEM, JEOL, Tokyo, Japan) at 200kV acceleration voltage. The characteristic functional group and crystal structures of nanomaterials were measured using Fourier-Transformed Infrared (FTIR) spectrometer and X-ray powder diffraction (XRD) respectively.

Photothermal Effect Evaluation

Briefly, aqueous solutions of PPy@Fe_3O_4 NPs with different concentrations (100, 200 and 400 μg/ml) were separately irradiated by an 808 nm near-infrared (NIR) laser (1.0W/cm^2). The temperature profiles were monitored and recorded using a thermal imaging camera (Fotric, Shanghai, China) over time. Then the PPy@Fe_3O_4 NPs (400 μg/ml) solutions were irradiated with the NIR laser for 10 min, and cooled down to room temperature. Last, we calculated the photothermal conversion efficiency (η) by the temperature curves according to published study. (Leng et al., 2018)

Cytotoxicity Assay

We evaluated the cytotoxicity of the PPy@Fe_3O_4 NPs by cell counting kit-8 (CCK-8) assays. In detail, normal human bronchial epithelial cells (BEAS-2B) and Human lung adenocarcinoma cells (A549) were respectively seeded into 96-well plates at a density of 10^4 cells per well and cultured in pH7.4. The following day, we replaced the medium with fresh medium (pH7.4) containing the PPy@Fe_3O_4 NPs of different concentrations (25, 50, 100, 200, 400 μg/ml) for another 24 h. Then we changed the medium with 100 μl serum-free medium and 10 μl CCK-8 reagent. Following incubation for 2 h, we measured the absorbance value of wells at 450 nm using a microplate reader (Thermo, United States). The calculated formulas were listed in **Supplementary Material**.

ROS Detection Assay

The A549 cells were incubated in the culture plates and divided into four groups: 1) control; 2) PPy@Fe_3O_4 (400 μg/ml); 3) H_2O_2 (100 μM); 4) PPy@Fe_3O_4 (400 μg/ml) + H_2O_2 (100 μM). After 24 h of treatment, we used the probe solution 2, 7-dichlorodihydrofluorescein diacetate (DCFH-DA; Beyotime Biotechnology, Shanghai, China) to estimate the intracellular reactive oxygen species (ROS). After DCFH-DA treatment for 20 min, the cells were washed three times by phosphate buffered saline (PBS) buffer and blank medium was added. Finally, we acquired images using Confocal laser scanning Microscopy (CLSM, Leica Microsystems, Mannheim, Germany).

Anticancer Effect *in vitro*

The anti-cancer effect of PPy@Fe_3O_4 NPs was evaluated by the Calcine-AM/propidium iodide (PI) test (Beyotime Biotechnology, Shanghai, China) and the Annexin V-FITC/PI apoptosis kit (Multi Sciences, Hangzhou, China). To investigate the PTT effect of the PPy@Fe_3O_4 NPs, A549 cells were incubated in the culture plates at pH6.5 and divided into 6 groups; group 1 with cells only; group 2 cultured with NIR only; group 3 cultured with H_2O_2 (100 μM) only; group 4 cultured with PPy@Fe_3O_4 NPs (400 μg/ml) + NIR; group 5 cultured with PPy@Fe_3O_4 NPs (400 μg/ml) + H_2O_2 (100 μM); group6 cultured with PPy@Fe_3O_4 NPs (400 μg/ml) + H_2O_2 (100 μM) + NIR. After incubation with PPy@Fe_3O_4 NPs (400 μg/ml) for 12 h, the cells of group 2,4 and 6 were exposed to an 808 nm NIR laser (1.0 W/cm^2) for 10 min. Afterwards, we stained the A549 cells with Calcein-AM and PI for about 15 min, and images were acquired by CLSM.

And we detected cell apoptosis by Annexin V-FITC Apoptosis kit. The A549 cells in different groups were harvested and washed with PBS and Binding Buffer. Then the cells were resuspended in 500 μl Bind Buffer with 5 μl Annexin V-FITC and 10 μl PI solution to mix evenly for 5 min at room temperature in darkness. And we measured cell apoptosis immediately by flow cytometry (cytoflex LX, Beckman Coulter).

Transwell Migration Assay

In vitro migration assay, 24-well Transwell chambers with a polycarbonate filter membrane of 8 μm pore size (Corning, United States) were used to assess the effect of the PPy@Fe_3O_4 NPs on A549 cell migration. Cells were divided into control group and PPy@Fe_3O_4 group. After starvation of A549 cells for 24 h, we resuspended cells in serum-free RPMI 1640 medium and serumfree RPMI 1640 medium containing the PPy@Fe_3O_4 NPs at a concentration of 400 μg/ml respectively. Next, the A549 cells were inoculated into the upper chamber and the RPMI 1640 medium was placed in the lower chamber. After culturing for 24 h, the A549 cells that migrated to the bottom of the membranes were immobilized and stained with 1% crystal violet (Beyotime Biotechnology, Shanghai, China). Finally, the migrated cells of each groups were counted under a microscope (Leica, Germany).

Western Blotting

A549 cells ($5*10^5$) were seeded into 6-well plate and divided into the control group and the PPy@Fe_3O_4 group (400 μg/ml). After incubation for 24 h, the cells were washed by PBS and lysed in RIPA buffer. Then we removed the cell debris by centrifugation, and the supernatants were harvested and stored at −80°C. Equivalent amounts of protein (25 μg) were separated on 10% SDS-PAGE and transferred onto 0.22 um polyvinylidene

difluoride (PVDF) membranes. The membranes were blocked and subsequently incubated with primary antibodies including anti-MMP2/MMP9/MMP13 (Abclonal, China, 1:1,000 dilution) and anti-β-actin (Proteintech, China, 1:10,000 dilution). The following day, we washed the membranes three times for 10 min each time by Tris-buffered saline with Tween20 (TBST), and then incubated them in the corresponding secondary antibody (goat anti-rabbit IgG horseradish peroxidase (HRP), goat anti-mouse IgG-HRP, 1:1,000, Affinity Biosciences, China) at room temperature for 2 h. Following washing three times for 10 min with TBST buffer, the membranes were treated with enhanced chemiluminescence (ECL, EpiZyme, Shanghai, China) reagent for exposure.

Magnetic Resonance Imaging *in vivo*

For *in vivo* MRI measurements, we intratumorally injected the A549 tumor-bearing mice with 200 μl of 3 mg/ml PPy@Fe_3O_4 NPs, when tumor size reached visible size (7–9 mm in diameter). Then we scanned the mice before and 3 h after injection. Thus, we successfully acquired the high-resolution T2-weighted MRI scan images of mice by a 3.0T MRI system (Ingenia 3.0T CX, Philips Healthcare). The T2-weighted MRI parameters were as follows: pulse waiting time (TR) = 2,800 ms, echo time (TE) = 60 ms, slice width (SW) = 5.0 mm.

Tumor Treatment *in vivo*

When the tumors reached 7–9 mm in diameter, we divided the mice into four groups (n = 6 per group): 1) control; 2) PBS + NIR; 3) PPy@Fe_3O_4 NPs (3 mg/ml); 4) PPy@Fe_3O_4 NPs (3 mg/ml) + NIR. The mice of group3 and 4 were injected intravenously with 200ul PPy@Fe_3O_4 NPs (3 mg/ml) and the mice of group2 was injected intravenously with 200ul PBS. Then 8 h after injection, the mice of group2 and 4 were irradiated with 808 nm laser (1W/cm^2) for 10 min. Meanwhile, we measured the temperature changes of the tumor by a FLIR A300 thermal imaging camera. Simultaneously, tumor volume and body weight were monitored every 2 days. On day 14, the mice were sacrificed. Then the major organs were isolated for photograph or histological analysis (hematoxylin and eosin (H and E) staining), and the tumor was stained subsequently by immunohistochemistry (Ki67) and immunofluorescence (TUNEL).

Immunohistochemistry and Immunofluorescence

The tumor tissues specimens of mice were fixed in 4% paraformaldehyde for 24 h and embedded in paraffin. Then the tissue blocks were cut into sections of 3-5 um thickness. For Ki67 staining, the sections were immunostained overnight at 4°C with an anti-Ki67 antibody (Abcam). After washing in PBS, the sections were subsequently incubated with the second antibody for 1 h. Then the slides were stained with 3, 3-diaminobenzidine (DAB) and hematoxylin separately, dehydrated, and mounted. Images were captured using a microscope (Leica, Leica DMi8). For TUNEL staining, the proportion of apoptotic cells were performed by terminal deoxynucleotidyl transferase-mediated dUTP nick end labeling (TUNEL) staining kit (Servicebio, Wuhan, China). We obtained all images using a CLSM.

Statistical Analysis

All results and measurements were shown as the mean ± SD (standard deviation). Comparison between the mean values of different groups were analyzed by one way analysis of variance (ANOVA) or Student's t-test: (*) $p < 0.05$ was considered statistically significant; (**) $p < 0.01$ and (***) $p < 0.001$ was considered highly statistically significant; (****) $p < 0.0001$ was considered extremely statistically significant.

RESULTS

Synthesis and Characterization of the PPy@Fe_3O_4 NPs

We used TEM to determine the sizes and morphologies of PPy@Fe_3O_4 NPs. The PPy@Fe_3O_4 NPs are shown in **Figure 1A**, **Figure 1B** and **Supplementary Figure S1**. As we can see, the mean diameter of PPy@Fe_3O_4 NPs was measured to be 71.0 nm, and many tiny Fe_3O_4 nano-crystals were surface adsorbed on PPy NPs. The FTIR spectrum showed clearly the characteristic absorption peaks of PPy, indicating the successful formation of PPy (**Figure 1C**). And XRD patterns showed that the PPy@Fe_3O_4 NPs had characteristic peaks (**Figure 1D**), which could be indexed to the Fe_3O_4 nanocrystals (JCPDS No. 65–3,107). (Wang et al., 2020) The above results demonstrated that the PPy@Fe_3O_4 NPs had been successfully prepared.

Photothermal Performance of PPy@Fe_3O_4 Nanaparticles

As shown in **Figure 2A**, the aqueous dispersion of PPy@Fe_3O_4 NPs had a broad absorption throughout the visible to the NIR region, which demonstrated that PPy@Fe_3O_4 NPs were good potential PTT agents. We further evaluate the photothermal properties of PPy@Fe_3O_4 NPs with NIR light irradiation. With the prolonging of the irradiation time and increased concentration of PPy@Fe_3O_4 NPs, the temperature rose rapidly (**Figure 2B**). Finally, when the concentration of PPy@Fe_3O_4 NPs reached 400 μg/ml, the temperature reached about 70°C after 5 min of irradiation, which was high enough for irreversible tumor ablation (**Figure 2C**). Next, we tested the photothermal conversion efficiency (η) of PPy@Fe_3O_4 NPs, which can show the capability of converting energy of light into heat. As shown in **Figure 2D**, the η value of PPy@Fe_3O_4 NPs was figured out to be ~51.8%, which is much higher than traditional PTT agents, such as $Cu_{2-x}Se$ nanocrystals, Cu_9S_5 nanocrystals and Au nanorods. (Hessel et al., 2011; Tian et al., 2011)

In vitro Cell Cytotoxicity Assay

To assess the cytotoxic effects of PPy@Fe_3O_4 NPs, the CCK8 assay was performed on BEAS-2B and A549 cells. The cells were incubated with PPy@Fe_3O_4 NPs (0, 25, 50, 100, 200, 400 μg/ml)

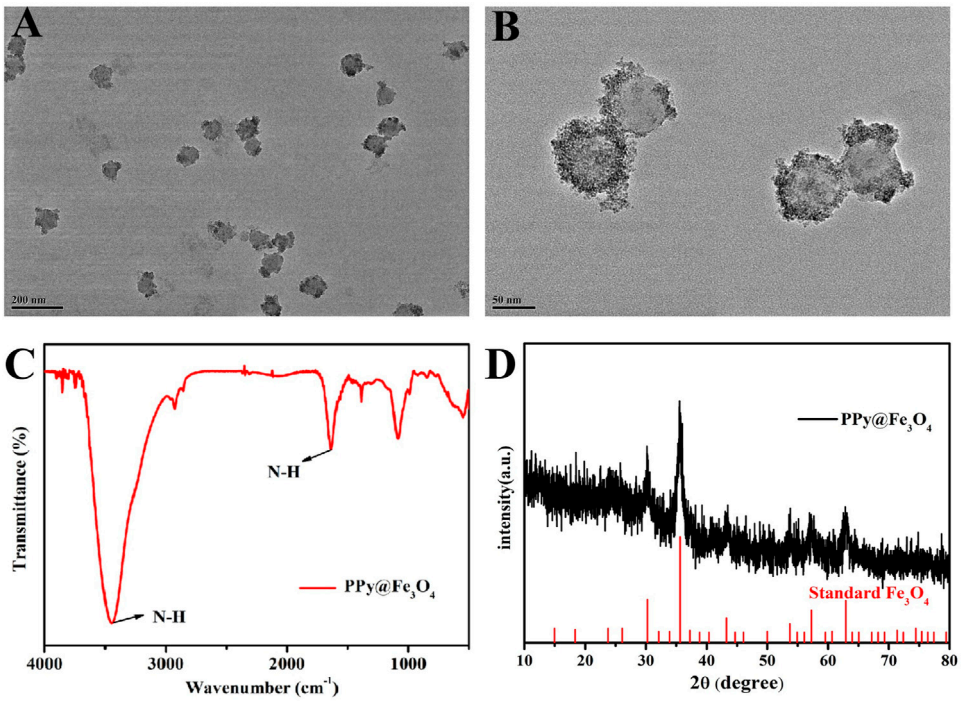

FIGURE 1 | The characterization of PPy@Fe_3O_4 NPs. **(A)** Low- and **(B)** medium-magnification TEM image of the PPy@Fe_3O_4 NPs. **(C)** FTIR spectra of PPy@Fe_3O_4 NPs. **(D)** XRD spectra of PPy@Fe_3O_4 NPs.

for 24 h to test the cell viability. The results indicated that PPy@Fe_3O_4 NPs exhibited lower cytotoxicity towards normal and cancer cells as high as 400 μg/ml (**Figure 3**), demonstrating that they have good biocompatibility.

The PPy@Fe_3O_4 NPs Increase Intracellular ROS Generation Induced by H_2O_2 and Induce Cell Apoptosis

Chemodynamic therapy is an effective therapeutic treatment that causes damage of tumor cells by producing ROS. To examine the effects of PPy@Fe_3O_4 NPs on ROS production, we detected ROS by fluorescent probe 2′, 7′-dichlorofluorescein-diacetate (DCFH-DA), which was oxidized to 2, 7′-dichlorofluorescein (DCF) in the presence of ROS. As displayed in **Figure 4A**, compared with control group, the intensity of DCF fluorescence in H_2O_2 group and PPy@Fe_3O_4 NPs group increased weakly. When treated with both H_2O_2 and PPy@Fe_3O_4 NPs, the cells displayed strong and extensive green fluorescence, indicating that PPy@Fe_3O_4 NPs could increase Fenton-induced ROS generation in the presence of H_2O_2.

Given the desirable photothermal conversion performance and significant synergistic effects, we further determined the *in vitro* therapeutic efficacy of PPy@Fe_3O_4 NPs through Calcine-AM/PI test. Living cells were stained with green fluorescent calcein AM, while dead cells were stained with red fluorescent PI (**Figure 4B**). Compared with the control group, A549 cells exhibited strong green fluorescence and no red fluorescence under exposure of NIR laser radiation, which indicated that the viability of the cells was not compromised. In contrast, H_2O_2 slightly increased the percentage of dead cells. And A549 cells showed a remarkable cell death after treatment by PPy@Fe_3O_4 NPs with NIR irradiation or PPy@Fe_3O_4 NPs with H_2O_2, suggesting that the photothermal therapy and chemodynamic therapy of the PPy@Fe_3O_4 NPs could effectively killed the A549 cells. When A549 cells were treated by the combination of PTT and CDT, very few living cells were observed. To sum up, PPy@Fe_3O_4NPs have satisfactory synergistic therapeutic effects.

We measured the influence of PPy@Fe_3O_4 NPs on cell apoptosis by using Annexin V/PI staining and flow cytometry (**Figure 4C**, **Supplementary Figure S2**). The early apoptosis cells were defined as Annexin V (+)/PI (−), and cells in the late stage of were considered as Annexin V (+)/PI (+). The flow cytometry results showed that NIR group had no evident difference compared to the control group. Nevertheless, after treatment with H_2O_2, the percentage of apoptosis cells increased to 8.9%. After treatment by PPy@Fe_3O_4 NPs with NIR irradiation and PPy@Fe_3O_4 NPs with H_2O_2, the percentage of apoptosis cells significantly increased to 42.75% and 27.35%. And most surprisingly, the apoptosis rate in the PPy@Fe_3O_4 NPs + H_2O_2 + NIR group increased highly to 76.99%, which further demonstrated that the PPy@Fe_3O_4 NPs + H_2O_2 + NIR group had the highest killing effect due to synergistic PTT and CDT.

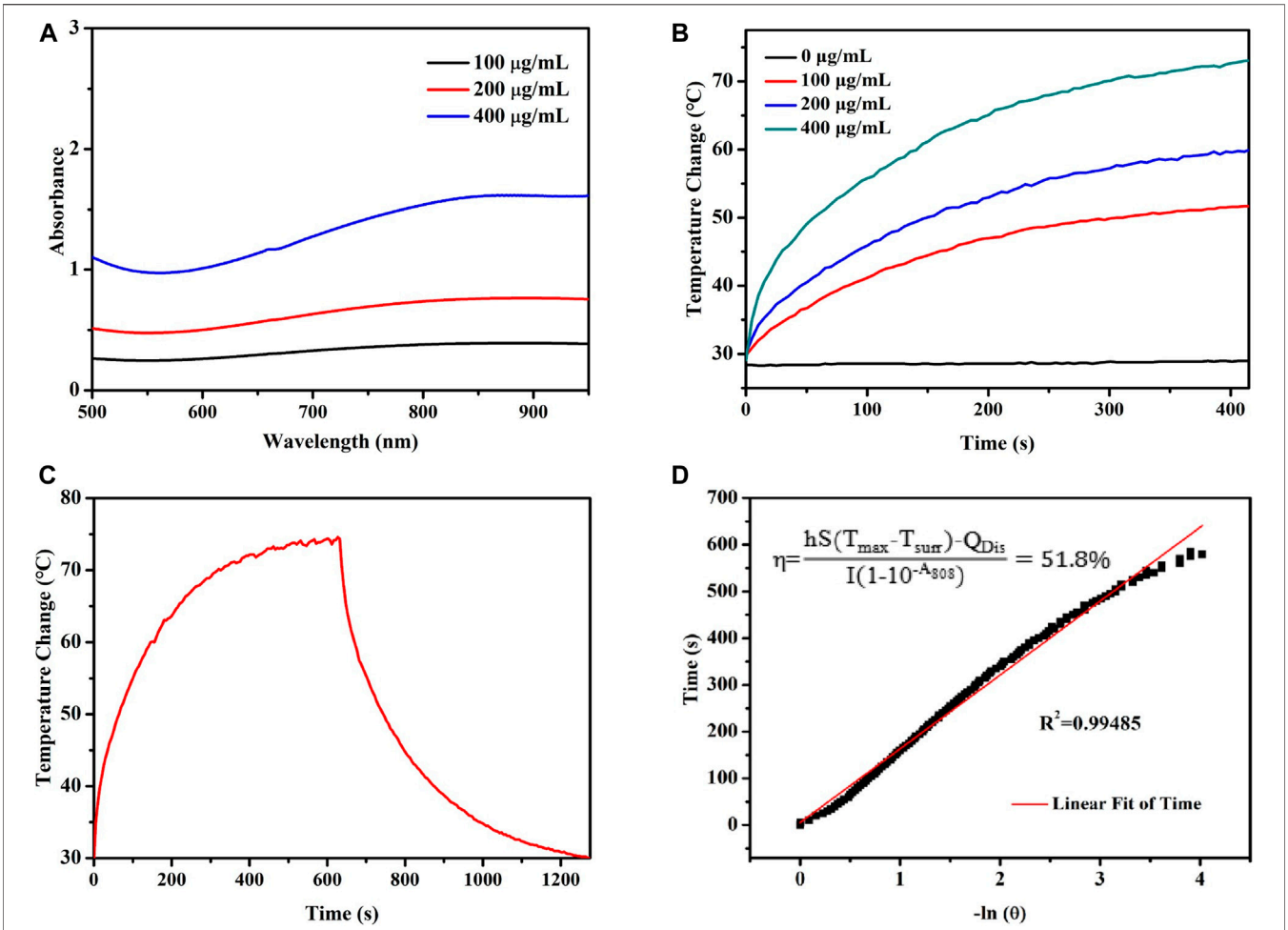

FIGURE 2 | Evaluation of the photothermal properties of the PPy@Fe_3O_4 NPs. **(A)** UV-Vis-NIR absorption spectra of PPy@Fe_3O_4 NPs. **(B)** Temperature changes of PPy@Fe_3O_4 NCs at varying concentrations for 5 min with laser irradiation. **(C)** The curves of temperature increase with irradiation and nature cooling for PPy@Fe_3O_4 NCs solution (400 μg/ml). **(D)** Linear regression with a system time constant of the cooling curve shown in **(C)**.

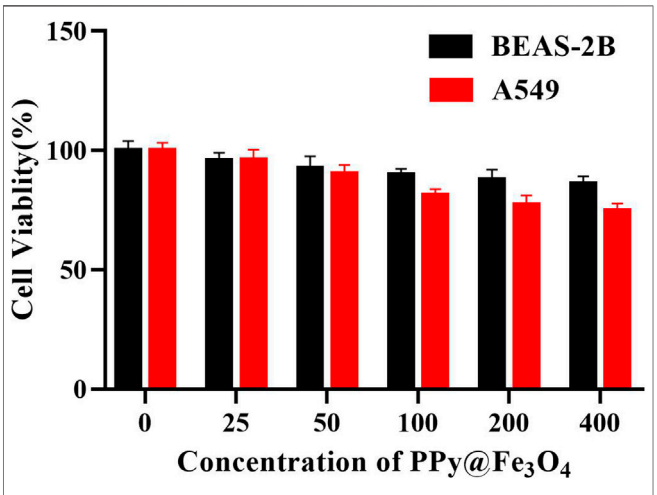

FIGURE 3 | Cell viability of A549 cells and BEAS-2B cells cultured with PPy@Fe_3O_4 NPs for 24 h at different concentrations.

The PPy@Fe_3O_4 Nanoparticles Inhibit the Migration of Lung Cancer Cells and Decrease MMP2/MMP9/MMP13 Expression Levels

To assess cell mobility in response to the PPy@Fe_3O_4 NPs, we used transwell cell cultures *in vitro*, which certified the effect of PPy@Fe_3O_4 NPs on suppressing the migration of lung cancer cells (**Figures 5A,B**).

MMP2/9/13 had been found to play vital functions in the invasion and metastasis of malignant tumors. Therefore, we examined the impact of PPy@Fe_3O_4 NPs on these protein expressions in A549 cells using western blotting (**Figure 5C**). The outcomes showed that the expressions of MMP2, MMP9 and MMP13 were obviously declined in the PPy@Fe_3O_4 NPs group compared to the control group. In summary, these experiments suggested that PPy@Fe_3O_4 NPs could suppress the growth and metastasis of A549 cells.

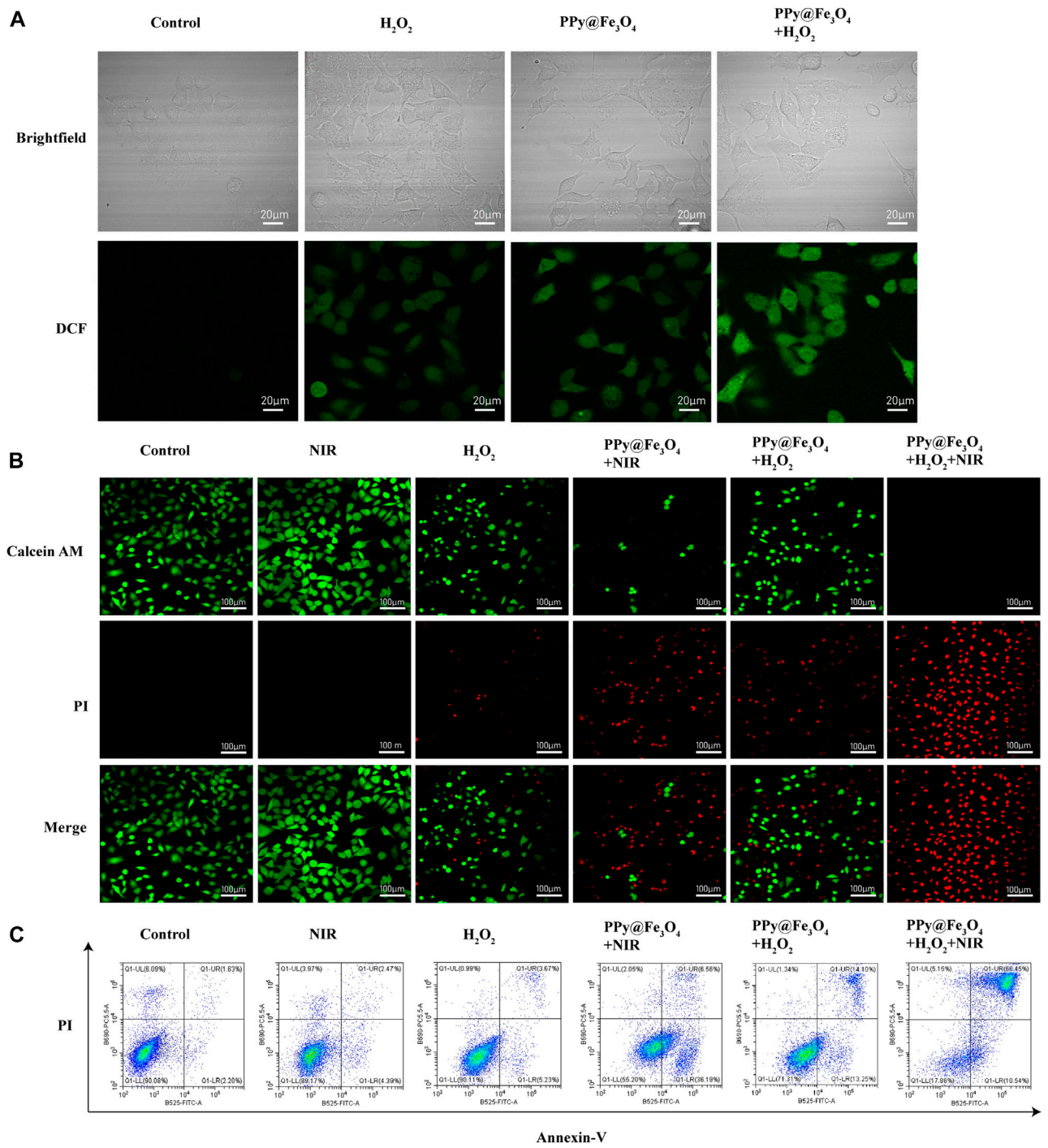

FIGURE 4 | The PPy@Fe_3O_4 NPs increase intracellular ROS generation induced by H_2O_2 and induce cell apoptosis. **(A)** Brightfield images and confocal images of ROS level in A549 cells. **(B)** Confocal images of Calcein-AM and PI co-stained A549 cells in different groups. Scale bar, 100 μm. **(C)** Cell apoptosis measured by flow cytometry.

The PPy@Fe_3O_4 Nanaparticles Inhibit the Growth of Xenograft Tumors in Nude Mice

To identify the therapeutic efficacy of PPy@Fe_3O_4 NPs on tumor growth *in vivo*, we conducted further comparative studies. 1×10^6 A549 cells were subcutaneously injected into BALB/c nude mice. When the volumes of tumors reached to approximately 100 mm^3, we divided the mice into four groups randomly: 1) control; 2) PBS + NIR; 3) PPy@Fe_3O_4 NPs; 4) PPy@Fe_3O_4 NPs + NIR. Mice of the group 2 were injected with 200ul PBS via the tail vein, and mice of

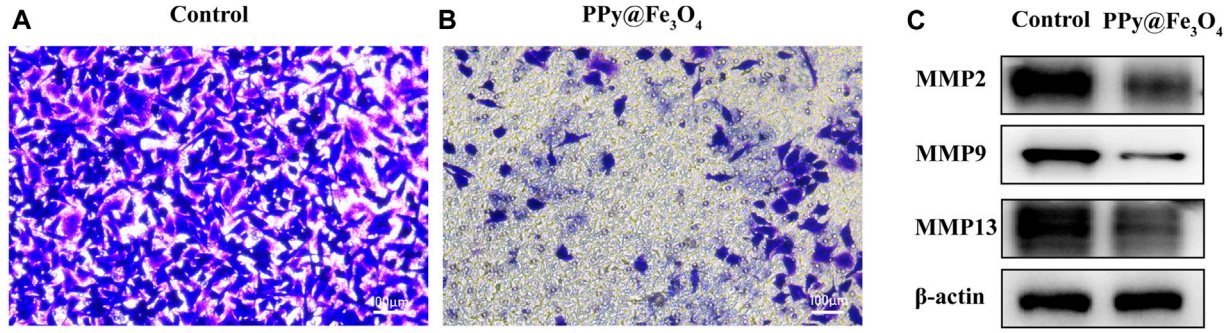

FIGURE 5 | The PPy@Fe_3O_4 NPs inhibit the migration of human lung cancer cells. **(A,B)** The migration capacity of A549 cells measured using transwell assays after PPy@Fe_3O_4 NPs (400 μg/ml) treatment for 48 h. Scale bar, 100 μm. **(C)** Protein levels of MMP2/MMP9/MMP13 in different groups.

group 3, 4 were injected with PPy@Fe_3O_4 NPs (3 mg/ml) via the tail vein. After 8 h, the mice of group 2, 4 were irradiated by an 808 nm NIR laser (1.0W/cm^2) for 10 min. Meanwhile, by using an infrared thermal camera, we found that the tumor temperature of mice injected with PPy@Fe_3O_4 NPs rapidly increased to ~53°C during irradiation, which was sufficient for ablating tumors. However, the tumor temperature of the group 2 had negligible rise (**Figures 6A,B**). After 14 days, the mice were sacrificed and the tumor volumes and body weights were recorded (**Figures 6C–E**). The growth of tumors in group 2 was similar to the control group, demonstrating that NIR alone could not inhibit tumor growth. Whereas, tumor growth in the group 3 was partially inhibited due to CDT of PPy@Fe_3O_4 NPs. Noticeably, the tumor growth in group 4 was substantially inhibited because of the synergistic effects of PTT and CDT. Representative pictures of the tumors in different groups further determined the therapeutic efficacy. There was no obvious difference in body weight among the groups, suggesting that the adverse effect of PPy@Fe_3O_4 NPs was negligible. Additionally, the main tissues and organs of different groups were collected for H&E staining to estimate the safety of various treatments (**Figure 6F**). We could not find evident damage in the group 2, 3, 4, compared to the control group, illustrating that the PPy@Fe_3O_4 NPs were biologically safe *in vivo*.

Next, we evaluated the proliferation and apoptosis of tumor cells by immunocytochemistry and immunofluorescence (**Figures 6G,H**). We noticed that PPy@Fe_3O_4 NPs could slightly reduce the expression of the proliferation marker Ki67 and increase apoptosis, compared with the control group. Moreover, treatment of PPy@Fe_3O_4 NPs with NIR further significantly decreased the level of Ki67 and caused cell apoptosis more effectively. These results clearly showed that PPy@Fe_3O_4 NPs with NIR could suppress effectively tumor growth *in vivo*.

The PPy@Fe_3O_4 Nanoparticles can Serve as Magnetic Resonance Imaging Contrast Agents to Detect Tumors

MRI offers excellent spatial resolution and tissue penetration, which is a noninvasive method for the identification and early cancer diagnosis. We used PPy@Fe_3O_4 NPs as contrast agents to evaluate the contrast-enhancing effect *in vivo* (**Figure 7A**). We treated the tumor-bearing mice with the PPy@Fe_3O_4 NPs by intratumor injection, and utilized T2 weighted MRI to observe the tumor before PPy@Fe_3O_4 NPs injection and 2 h post-injection (**Figures 7B,C**). Compared with pre-injection, we revealed that the signal intensity of tumor sites changed obviously 2 h after injection, which indicated that the PPy@Fe_3O_4 NPs might be ideal contrast agents for MRI in future applications.

DISCUSSION

For a long time, NSCLC has been a type of disease characterized by late diagnosis and resistance to therapy. (Hirsch et al., 2017) The greatest challenge in the modern nanomedicine of lung cancer is to develop promising tools for diagnosing and treating the advanced NSCLC owing to the rapid metastasis, which is the major impediment of successful treatments in the clinical procedures. Encouragingly, in this study, the PPy@Fe_3O_4 NPs showed satisfactory safety and efficacy as eminent photothermal agents for NSLC therapy. Additionally, we revealed that PPy@Fe_3O_4 NPs could suppress the proliferation, migration and metastasis of cells of NSCLC.

Polypyrrole nanoparticle, a flexible and conductive polymer, is a recognized valuable multipurpose material due to its conductive properties, outstanding stability and high absorbance in the NIR region. Therefore, it can be used in various biomedical fields, especially in the therapy of cancer. (Chiang and Chuang, 2019) Nevertheless, because of some shortcomings of PPy, such as insolubility to water, the photothermal applications of PPy-based nanoparticles are still in the development. (Chen and Cai, 2015; He et al., 2018) For overcoming these shortcomings, we formed Fe_3O_4 crystals onto the surface of PPy NPs in this study. Fe_3O_4 greatly improved the solubility and could be used as T2 contrast agents in MRI to provide diagnostic information. (Wang et al., 2012; Wei et al., 2017) And we disclosed the synergistic therapeutic effects of PPy@Fe_3O_4 NPs, including PTT and CDT. PPy@Fe_3O_4 NPs converted NIR light energy into heat energy and initiated the Fenton reaction under the mildly acidic conditions of the TME. Therefore, the

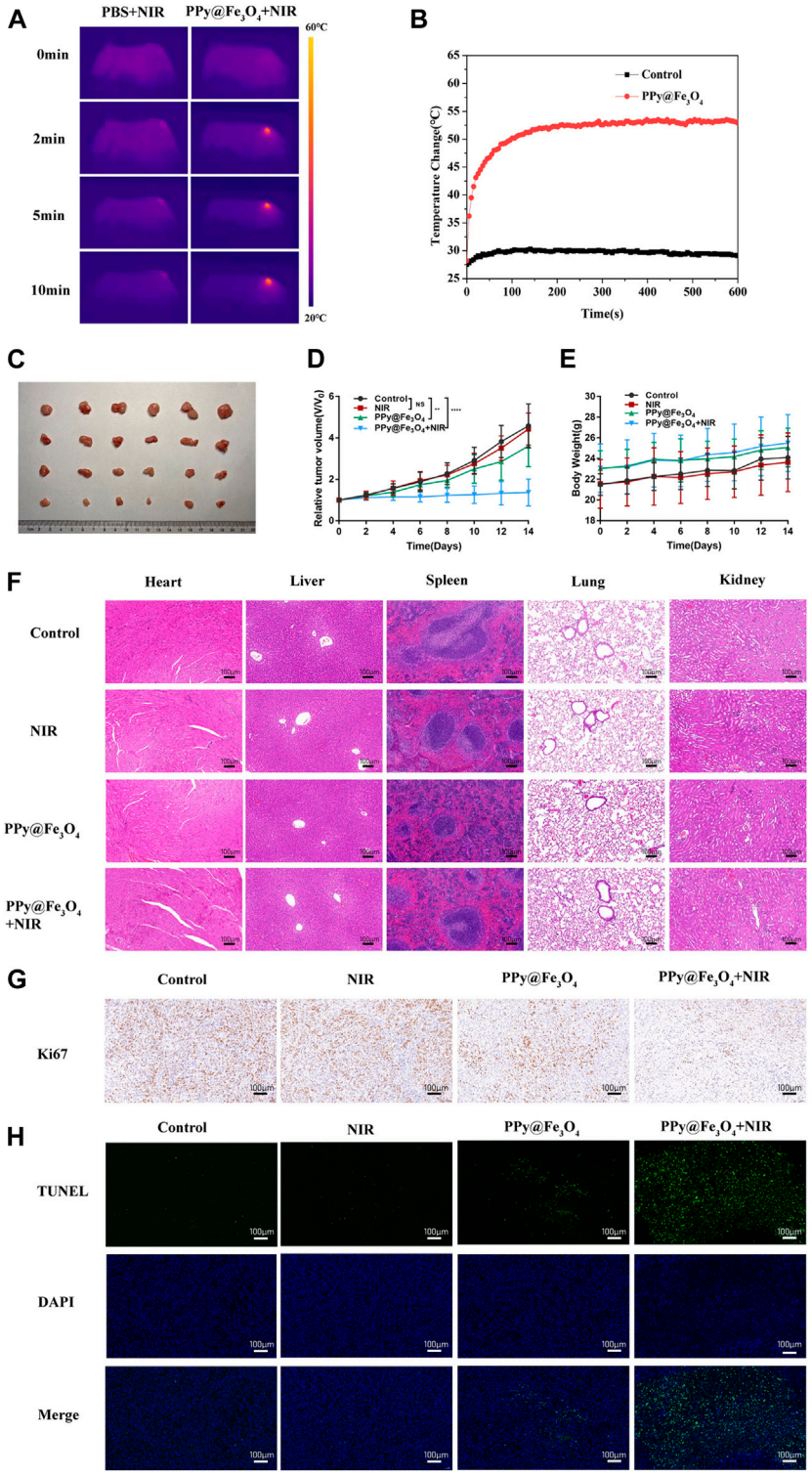

FIGURE 6 | The PPy@Fe_3O_4 NPs inhibit the growth of tumor xenografts in nude mice. **(A)** Infrared thermography pictures of A549 tumor-bearing mice treated with PBS and PPy@Fe_3O_4 NPs under irradiation (808 nm, 1.0 W/cm^2). **(B)** Profile of temperature variation of the tumor areas. **(C)** Tumor photo excised on day 14 after treatments. **(D)** Relative tumor volume and **(E)** body weight of mice in different groups. **(F)** H&E staining of main organs collected from mice in different groups. Scale bar, 100 μm. **(G)** Representative immunohistochemical stain images for Ki67 in xenograft tumors. Scale bar, 100 μm. **(H)** Representative TUNEL stain images in xenograft tumors. Blue color: DAPI staining for cell nuclei. Green color: positive apoptotic cells. Scale bar, 100 μm.

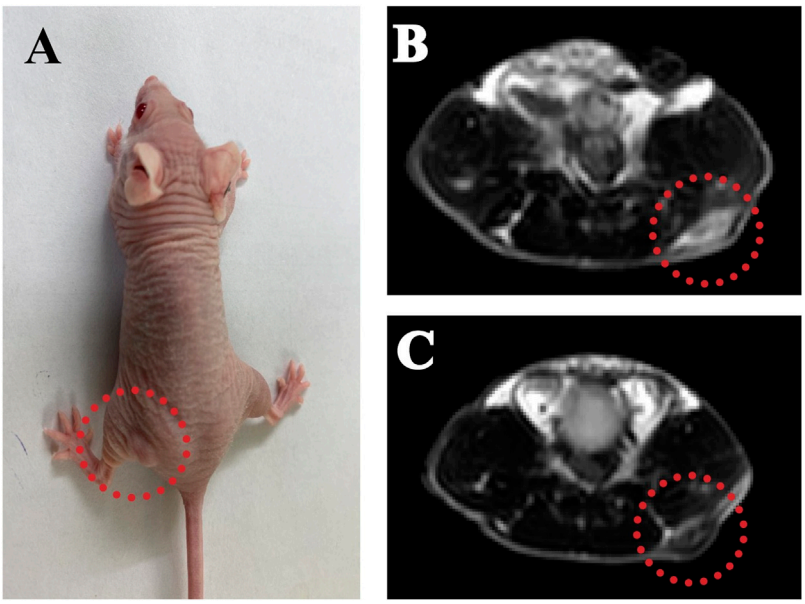

FIGURE 7 | The PPy@Fe_3O_4 NPs can serve as MRI contrast agents to detect tumors. **(A)** Representative MRI images of A549 tumor-bearing mice; **(B)** T2-weighted MRI before and **(C)** after injection of PPy@Fe_3O_4 dispersions.

apoptosis of cells would be induced and the growth and metastasis of cells would be inhibited.

In PTT, different kinds of photothermal agents contribute to the localized heating of cells and tissues. When irradiated by the light of appropriate wavelength, these agents absorb the photon energy and the singlet ground state could be converted to a singlet excited state. The excited electrons can go back to the ground state through vibrational relaxation, mediated by the interaction between the excited molecules and the surrounding molecules. Thus, the heating of the surrounding microenvironment appears due to increased kinetic energy. (Li X. et al., 2020) When the temperature reaches a certain value, cell necrosis will happen. (Knavel and Brace, 2013) Considering the high NIR photothermal conversion efficiency of PPy@Fe_3O_4 NPs, we performed a series of experiments to assess whether PPy@Fe_3O_4 NPs could be potential photothermal agents to inhibit the proliferation of lung cancer cells. We first studied the cytotoxicity of PPy NPs by CCK8 assay *in vitro* and the outcomes showed that the PPy@Fe_3O_4 NPs had negligible cytotoxicity to BEAS-2B and A549 cells as high as 400 μg/ml. Additionally, our study showed that administration of the PPy@Fe_3O_4 NPs did not induce damage to major organs, which reflected the safety of the PPy@Fe_3O_4 NPs *in vivo*. The Safety and efficiency of PPy@Fe_3O_4 NPs demonstrated that the PPy@Fe_3O_4 NPs might be perfect candidates for further clinical application of lung cancer. Then Annexin V-FITC/PI assay and Calcine-AM/PI test were performed to observe apoptosis induced by the PTT of PPy@Fe_3O_4 NPs. The results indicated that PPy@Fe_3O_4 NPs had strong apoptosis-inducing effects on A549 cells under the condition of NIR irradiation. For *in vivo* experiments, the data showed that PPy@Fe_3O_4 NPs under the NIR irradiation condition obviously caused severe tumor damage while the adjacent normal tissue would not be affected. Meanwhile, the results of the Ki67 and TUNEL assay also demonstrated that PTT of PPy@Fe_3O_4 NPs could inhibit growth and induce apoptosis of cells.

Chemodynamic therapy, which is regarded as *in-situ* treatment by Fenton and Fenton-like reactions, has received an increasing amount of attention. (Min et al., 2020) The highly oxidative •OH or O_2 generated from Fenton and Fenton-like reactions, can be stimulated by the endogenous H_2O_2 of cancer cells and catalyzed by transition metal ions or their complexes. (Li Y. et al., 2020) Briefly, PPy@Fe_3O_4 NPs dissolve ferrous ions under the mildly acidic conditions of the TME and activate the Fenton reaction. The Haber–Weiss reaction is as follows:

$$Fe^{2+} + H_2O_2 \rightarrow Fe^{3+} + \bullet OH + OH^- \quad (1)$$

$$Fe^{3+} + H_2O_2 \rightarrow Fe^{2+} + \bullet OOH + H^+ \quad (2)$$

$$Fe^{3+} + \bullet OOH \rightarrow Fe^{2+} + O_2 + H^+ \quad (3)$$

On the one hand, excessive production of •OH can oxidize vital cellular constituents, such as DNA, proteins and lipids, which can induce cell apoptosis or necrosis. (Goldstein et al., 1993) On the other hand, O_2 production mediated by Fenton reaction can alleviate tumor hypoxia, which may improve cancer therapeutic combination strategies. (Ma et al., 2016) As we all know, hypoxia is a crucial driver to drug resistance in tumor therapy. (Piao et al., 2017) Thus, the Fenton reaction can enhance the anticancer efficacy by supplying O_2 to the hypoxic TME, when used with other anticancer methods. Additionally, iron ions exert a crucial role in the process of ferroptosis, where lipid ROS level increases due to the suppression of system xc- and glutathione (GSH) synthesis. (Liu et al., 2018) GSH is the major endogen antioxidant system that leads to a decrease of ROS. (Cajas et al., 2020) Herein, Fenton reaction-based nanomaterials are of great importance in lung cancer therapy. DCFH-DA fluorescence intensity assays showed that PPy@Fe_3O_4 NPs significantly increased

ROS levels generated from A549 cells under the conditions of H_2O_2. We also found that the PPy@Fe_3O_4 NPs promoted apoptosis of the cells of lung cancer induced by H_2O_2, as revealed by the Annexin V-FITC/PI assay and Calcine-AM/PI test. Therefore, the results of these experiments draw the following conclusion that PPy@Fe_3O_4 NPs could enhance antitumor effects through ROS damage.

Migration and invasion are two essential features of tumor metastasis. In metastasis, cancer cells invade and migrate from the primary site to the extracellular matrix and surrounding basement membrane, which further colonize the distant site. (Albuquerque et al., 2021) Therefore, the inhibition of migration and invasion could suppress the progression of lung cancer and extend the survival of patients. In our research, transwell chambers were established to confirm the inhibitory efficacy of PPy@Fe_3O_4 NPs on A549 cell migration. The results showed that all PPy@Fe_3O_4 NPs significantly suppressed A549 cell migration. Moreover, tumor metastasis is a very complicated process that involves the interaction of various genes and proteins, especially MMPs. MMPs have been reported as proteolytic enzymes with the capacity of degrading the extracellular matrix components and other secreted proteins of the lungs. (Gonzalez-Avila et al., 2019) And they are also associated with endothelial basement membrane destruction. The crack in the basement membrane allows cells to enter the circulation, which transports the tumor cells to the distant extravasation site. (Bonomi, 2002) MMP2, MMP9 and MMP13 are prominent enzymes that promote tumor cell invasion and migration and regulate the progress of epithelial-to-mesenchymal transition (EMT), which is a transformation process of the epithelial cells to the mesenchymal cells and can promote cancer metastasis. (Scheau et al., 2019) Meanwhile, the levels of these proteins all had been reported to be elevated in certain lung cancer patients. (Li et al., 2019; Han et al., 2020) Here, our results indicated that MMP2, MMP9 and MMP13 were manifestly downregulated by PPy@Fe_3O_4 NPs. Thus, these findings suggested that PPy@Fe_3O_4 NPs suppressed human lung cancer cell metastasis.

CONCLUSION

In our study, we synthesized PPy@Fe_3O_4 NPs and demonstrated the safety and effectiveness of the PPy@Fe_3O_4 NPs *in vivo* and *in vitro*. The PPy@Fe_3O_4 NPs exhibited excellent synergistic effects of PTT and CDT, which could inhibit the growth and metastasis of lung cancer cells efficiently. Additionally, the PPy@Fe_3O_4 NPs was remarkable MRI contrast agents for tumors. However, the underlying mechanisms of tumor growth and metastasis need to be further discussed. Taken together, our study revealed the potential of PPy@Fe_3O_4 NPs to develop a new therapeutic strategy for NSCLC.

DATA AVAILABILITY STATEMENT

The original contributions presented in the study are included in the article/**Supplementary Material**, further inquiries can be directed to the corresponding authors.

ETHICS STATEMENT

The animal experimental protocol was reviewed and approved by the Laboratory Animal Ethics Committee of Shanghai General Hospital.

AUTHOR CONTRIBUTIONS

DF and HJ designed and conducted a series of experiments. XH analyzed the experimental data. YS proofread the manuscript and the methods. ZL supervised the experiments and reviewed the manuscript. SB provided funding and supervised the experiments. All the authors read and approved the final manuscript.

FUNDING

This work was financially supported by the National Natural Science Foundation of China (Grant 81570018).

SUPPLEMENTARY MATERIAL

The Supplementary Material for this article can be found online at: https://www.frontiersin.org/articles/10.3389/fchem.2021.789934/full#supplementary-material

REFERENCES

Albuquerque, C., Manguinhas, R., Costa, J. G., Gil, N., Codony-Servat, J., Castro, M., et al. (2021). A Narrative Review of the Migration and Invasion Features of Non-small Cell Lung Cancer Cells upon Xenobiotic Exposure: Insights from *In Vitro* Studies. *Transl. Lung Cancer Res.* 10, 2698–2714. doi:10.21037/tlcr-21-121

Bonomi, P. (2002). Matrix Metalloproteinases and Matrix Metalloproteinase Inhibitors in Lung Cancer. *Semin. Oncol.* 29, 78–86. doi:10.1053/sonc.2002.31528

Cajas, Y. N., Cañón-Beltrán, K., Ladrón de Guevara, M., Millán de la Blanca, M. G., Ramos-Ibeas, P., Gutiérrez-Adán, A., et al. (2020). Antioxidant Nobiletin Enhances Oocyte Maturation and Subsequent Embryo Development and Quality. *Int. J. Mol. Sci.* 21, 5340. doi:10.3390/ijms21155340

Chen, F., and Cai, W. (2015). Nanomedicine for Targeted Photothermal Cancer Therapy: where Are We Now? *Nanomedicine* 10, 1–3. doi:10.2217/nnm.14.186

Chen, J., Ning, C., Zhou, Z., Yu, P., Zhu, Y., Tan, G., et al. (2019). Nanomaterials as Photothermal Therapeutic Agents. *Prog. Mater. Sci.* 99, 1–26. doi:10.1016/j.pmatsci.2018.07.005

Chiang, C.-W., and Chuang, E.-Y. (2019). Biofunctional Core-Shell Polypyrrole–Polyethylenimine Nanocomplex for a Locally Sustained Photothermal with Reactive Oxygen Species Enhanced Therapeutic Effect against Lung Cancer. *Int. J. Nanomed.* 14, 1575–1585. doi:10.2147/IJN.S163299

Eble, J. A., and Niland, S. (2019). The Extracellular Matrix in Tumor Progression and Metastasis. *Clin. Exp. Metastasis* 36, 171–198. doi:10.1007/s10585-019-09966-1

Goldstein, S., Meyerstein, D., and Czapski, G. (1993). The Fenton Reagents. *Free Radic. Biol. Med.* 15, 435–445. doi:10.1016/0891-5849(93)90043-t

Gonzalez-Avila, G., Sommer, B., Mendoza-Posada, D. A., Ramos, C., Garcia-Hernandez, A. A., and Falfan-Valencia, R. (2019). Matrix Metalloproteinases Participation in the Metastatic Process and Their Diagnostic and Therapeutic Applications in Cancer. *Crit. Rev. Oncol. Hematol.* 137, 57–83. doi:10.1016/j.critrevonc.2019.02.010

Guan, S., Liu, X., Fu, Y., Li, C., Wang, J., Mei, Q., et al. (2022). A Biodegradable "Nano-Donut" for Magnetic Resonance Imaging and Enhanced Chemo/Photothermal/Chemodynamic Therapy through Responsive Catalysis in Tumor Microenvironment. *J. Colloid Interf. Sci.* 608, 344–354. doi:10.1016/j.jcis.2021.09.186

Han, L., Sheng, B., Zeng, Q., Yao, W., and Jiang, Q. (2020). Correlation between MMP2 Expression in Lung Cancer Tissues and Clinical Parameters: a Retrospective Clinical Analysis. *BMC Pulm. Med.* 20, 283. doi:10.1186/s12890-020-01317-1

He, Y., Gui, Q., Wang, Y., Wang, Z., Liao, S., and Wang, Y. (2018). A Polypyrrole Elastomer Based on Confined Polymerization in a Host Polymer Network for Highly Stretchable Temperature and Strain Sensors. *Small* 14, 1800394. doi:10.1002/smll.201800394

Herbst, R. S., Morgensztern, D., and Boshoff, C. (2018). The Biology and Management of Non-small Cell Lung Cancer. *Nature* 553, 446–454. doi:10.1038/nature25183

Hessel, C. M., Pattani, V. P., Rasch, M., Panthani, M. G., Koo, B., Tunnell, J. W., et al. (2011). Copper Selenide Nanocrystals for Photothermal Therapy. *Nano Lett.* 11, 2560–2566. doi:10.1021/nl201400z

Hirsch, F. R., Scagliotti, G. V., Mulshine, J. L., Kwon, R., Curran, W. J., Wu, Y.-L., et al. (2017). Lung Cancer: Current Therapies and New Targeted Treatments. *Lancet* 389, 299–311. doi:10.1016/S0140-6736(16)30958-8

Hribar, K. C., Lee, M. H., Lee, D., and Burdick, J. A. (2011). Enhanced Release of Small Molecules from Near-Infrared Light Responsive Polymer–Nanorod Composites. *ACS Nano* 5, 2948–2956. doi:10.1021/nn103575a

Knavel, E. M., and Brace, C. L. (2013). Tumor Ablation: Common Modalities and General Practices. *Tech. Vasc. Interv. Radiol.* 16, 192–200. doi:10.1053/j.tvir.2013.08.002

Leng, C., Zhang, X., Xu, F., Yuan, Y., Pei, H., Sun, Z., et al. (2018). Engineering Gold Nanorod-Copper Sulfide Heterostructures with Enhanced Photothermal Conversion Efficiency and Photostability. *Small* 14, 1703077. doi:10.1002/smll.201703077

Li, W., Jia, M., Wang, J., Lu, J., Deng, J., Tang, J., et al. (2019). Association of MMP9-1562C/T and MMP13-77A/G Polymorphisms with Non-small Cell Lung Cancer in Southern Chinese Population. *Biomolecules* 9, 107. doi:10.3390/biom9030107

Li, X., Lovell, J. F., Yoon, J., and Chen, X. (2020a). Clinical Development and Potential of Photothermal and Photodynamic Therapies for Cancer. *Nat. Rev. Clin. Oncol.* 17, 657–674. doi:10.1038/s41571-020-0410-2

Li, Y., Zhao, P., Gong, T., Wang, H., Jiang, X., Cheng, H., et al. (2020b). Redox Dyshomeostasis Strategy for Hypoxic Tumor Therapy Based on DNAzyme-Loaded Electrophilic ZIFs. *Angew. Chem. Int. Ed.* 59, 22537–22543. doi:10.1002/anie.202003653

Liu, T., Liu, W., Zhang, M., Yu, W., Gao, F., Li, C., et al. (2018). Ferrous-Supply-Regeneration Nanoengineering for Cancer-cell-specific Ferroptosis in Combination with Imaging-Guided Photodynamic Therapy. *ACS Nano* 12, 12181–12192. doi:10.1021/acsnano.8b05860

Luo, J., Zhu, H., Jiang, H., Cui, Y., Wang, M., Ni, X., et al. (2018). The Effects of Aberrant Expression of LncRNA DGCR5/miR-873-5p/TUSC3 in Lung Cancer Cell Progression. *Cancer Med.* 7, 3331–3341. doi:10.1002/cam4.1566

Ma, Z., Zhang, M., Jia, X., Bai, J., Ruan, Y., Wang, C., et al. (2016). Fe^{III}-Doped Two-Dimensional C_3N_4Nanofusiform: A New O_2-Evolving and Mitochondria-Targeting Photodynamic Agent for MRI and Enhanced Antitumor Therapy. *Small* 12, 5477–5487. doi:10.1002/smll.201601681

Min, H., Qi, Y., Zhang, Y., Han, X., Cheng, K., Liu, Y., et al. (2020). A Graphdiyne Oxide-Based Iron Sponge with Photothermally Enhanced Tumor-Specific Fenton Chemistry. *Adv. Mater.* 32, 2000038. doi:10.1002/adma.202000038

Mirvakili, S. M., Ngo, Q. P., and Langer, R. (2020). Polymer Nanocomposite Microactuators for On-Demand Chemical Release via High-Frequency Magnetic Field Excitation. *Nano Lett.* 20, 4816–4822. doi:10.1021/acs.nanolett.0c00648

Nasim, F., Sabath, B. F., and Eapen, G. A. (2019). Lung Cancer. *Med. Clin. North Am.* 103, 463–473. doi:10.1016/j.mcna.2018.12.006

Oser, M. G., Niederst, M. J., Sequist, L. V., and Engelman, J. A. (2015). Transformation from Non-small-cell Lung Cancer to Small-Cell Lung Cancer: Molecular Drivers and Cells of Origin. *Lancet Oncol.* 16, e165–e172. doi:10.1016/S1470-2045(14)71180-5

Paris, J. L., Cabañas, M. V., Manzano, M., and Vallet-Regí, M. (2015). Polymer-Grafted Mesoporous Silica Nanoparticles as Ultrasound-Responsive Drug Carriers. *ACS Nano* 9, 11023–11033. doi:10.1021/acsnano.5b04378

Phan, T. T. V., Bui, N. Q., Cho, S.-W., Bharathiraja, S., Manivasagan, P., Moorthy, M. S., et al. (2018). Photoacoustic Imaging-Guided Photothermal Therapy with Tumor-Targeting HA-FeOOH@PPy Nanorods. *Sci. Rep.* 8, 8809. doi:10.1038/s41598-018-27204-8

Piao, W., Hanaoka, K., Fujisawa, T., Takeuchi, S., Komatsu, T., Ueno, T., et al. (2017). Development of an Azo-Based Photosensitizer Activated under Mild Hypoxia for Photodynamic Therapy. *J. Am. Chem. Soc.* 139, 13713–13719. doi:10.1021/jacs.7b05019

Pickup, M. W., Mouw, J. K., and Weaver, V. M. (2014). The Extracellular Matrix Modulates the Hallmarks of Cancer. *EMBO Rep.* 15, 1243–1253. doi:10.15252/embr.201439246

Poudel, B., Ki, H.-H., Luyen, B. T. T., Lee, Y.-M., Kim, Y.-H., and Kim, D.-K. (2016). Triticumoside Induces Apoptosis via Caspase-dependent Mitochondrial Pathway and Inhibits Migration through Downregulation of MMP2/9 in Human Lung Cancer Cells. *Acta Biochim. Biophys. Sin.* 48, 153–160. doi:10.1093/abbs/gmv124

Riihimäki, M., Hemminki, A., Fallah, M., Thomsen, H., Sundquist, K., Sundquist, J., et al. (2014). Metastatic Sites and Survival in Lung Cancer. *Lung Cancer* 86, 78–84. doi:10.1016/j.lungcan.2014.07.020

Rosell, R., and Karachaliou, N. (2015). Relationship between Gene Mutation and Lung Cancer Metastasis. *Cancer Metastasis Rev.* 34, 243–248. doi:10.1007/s10555-015-9557-1

Scheau, C., Badarau, I. A., Costache, R., Caruntu, C., Mihai, G. L., Didilescu, A. C., et al. (2019). The Role of Matrix Metalloproteinases in the Epithelial-Mesenchymal Transition of Hepatocellular Carcinoma. *Anal. Cell Pathol.* 2019, 9423907. doi:10.1155/2019/9423907

Shen, Z., Song, J., Yung, B. C., Zhou, Z., Wu, A., and Chen, X. (2018). Emerging Strategies of Cancer Therapy Based on Ferroptosis. *Adv. Mater.* 30, 1704007. doi:10.1002/adma.201704007

Tan, M., Gong, H., Wang, J., Tao, L., Xu, D., Bao, E., et al. (2015). SENP2 Regulates MMP13 Expression in a Bladder Cancer Cell Line through SUMOylation of TBL1/TBLR1. *Sci. Rep.* 5, 13996. doi:10.1038/srep13996

Tang, Z., Liu, Y., He, M., and Bu, W. (2019). Chemodynamic Therapy: Tumour Microenvironment-Mediated Fenton and Fenton-like Reactions. *Angew. Chem. Int. Ed.* 58, 946–956. doi:10.1002/anie.201805664

Tian, Q., Jiang, F., Zou, R., Liu, Q., Chen, Z., Zhu, M., et al. (2011). Hydrophilic Cu_9S_5 Nanocrystals: a Photothermal Agent with a 25.7% Heat Conversion Efficiency for Photothermal Ablation of Cancer Cells *In Vivo*. *ACS Nano* 5, 9761–9771. doi:10.1021/nn203293t

Wang, L., Li, J., Jiang, Q., and Zhao, L. (2012). Water-soluble Fe_3O_4 Nanoparticles with High Solubility for Removal of Heavy-Metal Ions from Waste Water. *Dalton Trans.* 41, 4544–4551. doi:10.1039/c2dt11827k

Wang, W., Wang, B., Ma, X., Liu, S., Shang, X., and Yu, X. (2016). Tailor-Made pH-Responsive Poly(choline Phosphate) Prodrug as a Drug Delivery System for Rapid Cellular Internalization. *Biomacromolecules* 17, 2223–2232. doi:10.1021/acs.biomac.6b00455

Wang, X., Yang, B., She, Y., and Ye, Y. (2018). The lncRNA TP73-AS1 Promotes Ovarian Cancer Cell Proliferation and Metastasis via Modulation of MMP2 and MMP9. *J. Cel Biochem.* 119, 7790–7799. doi:10.1002/jcb.27158

Wang, X., Liu, X., Xiao, C., Zhao, H., Zhang, M., Zheng, N., et al. (2020). Triethylenetetramine-modified Hollow Fe_3O_4/SiO_2/chitosan Magnetic Nanocomposites for Removal of Cr(VI) Ions with High Adsorption Capacity and Rapid Rate. *Microporous Mesoporous Mater.* 297, 110041. doi:10.1016/j.micromeso.2020.110041

Wang, M. (2016). Emerging Multifunctional NIR Photothermal Therapy Systems Based on Polypyrrole Nanoparticles. *Polymers* 8, 373. doi:10.3390/polym8100373

Wei, X., Luo, Q., Sun, L., Li, X., Zhu, H., Guan, P., et al. (2016). Enzyme- and pH-Sensitive Branched Polymer-Doxorubicin Conjugate-Based Nanoscale Drug

Delivery System for Cancer Therapy. *ACS Appl. Mater. Inter.* 8, 11765–11778. doi:10.1021/acsami.6b02006

Wei, H., Bruns, O. T., Kaul, M. G., Hansen, E. C., Barch, M., Wiśniowska, A., et al. (2017). Exceedingly Small Iron Oxide Nanoparticles as Positive MRI Contrast Agents. *Proc. Natl. Acad. Sci. USA* 114, 2325–2330. doi:10.1073/pnas.1620145114

Woodman, C., Vundu, G., George, A., and Wilson, C. M. (2021). Applications and Strategies in Nanodiagnosis and Nanotherapy in Lung Cancer. *Semin. Cancer Biol.* 69, 349–364. doi:10.1016/j.semcancer.2020.02.009

Yang, G., Xu, L., Chao, Y., Xu, J., Sun, X., Wu, Y., et al. (2017). Hollow MnO_2 as a Tumor-Microenvironment-Responsive Biodegradable Nano-Platform for Combination Therapy Favoring Antitumor Immune Responses. *Nat. Commun.* 8, 902. doi:10.1038/s41467-017-01050-0

Yang, Y., Wang, C., Tian, C., Guo, H., Shen, Y., and Zhu, M. (2018). Fe_3O_4@MnO_2@PPy Nanocomposites Overcome Hypoxia: Magnetic-Targeting-Assisted Controlled Chemotherapy and Enhanced Photodynamic/photothermal Therapy. *J. Mater. Chem. B* 6, 6848–6857. doi:10.1039/c8tb02077a

Yang, B., Liu, Q., Yao, X., Zhang, D., Dai, Z., Cui, P., et al. (2019). FePt@MnO-Based Nanotheranostic Platform with Acidity-Triggered Dual-Ions Release for Enhanced MR Imaging-Guided Ferroptosis Chemodynamic Therapy. *ACS Appl. Mater. Inter.* 11, 38395–38404. doi:10.1021/acsami.9b11353

Zha, Z., Yue, X., Ren, Q., and Dai, Z. (2013). Uniform Polypyrrole Nanoparticles with High Photothermal Conversion Efficiency for Photothermal Ablation of Cancer Cells. *Adv. Mater.* 25, 777–782. doi:10.1002/adma.201202211

Zhang, K., Li, P., He, Y., Bo, X., Li, X., Li, D., et al. (2016). Synergistic Retention Strategy of RGD Active Targeting and Radiofrequency-Enhanced Permeability for Intensified RF & Chemotherapy Synergistic Tumor Treatment. *Biomaterials* 99, 34–46. doi:10.1016/j.biomaterials.2016.05.014

Zhang, Y., Yan, J., Avellan, A., Gao, X., Matyjaszewski, K., Tilton, R. D., et al. (2020). Temperature- and pH-Responsive Star Polymers as Nanocarriers with Potential for *In Vivo* Agrochemical Delivery. *ACS Nano* 14, 10954–10965. doi:10.1021/acsnano.0c03140

Zhao, H., Wang, J., Li, X., Li, Y., Li, C., Wang, X., et al. (2021). A Biocompatible Theranostic Agent Based on Stable Bismuth Nanoparticles for X-ray Computed Tomography/magnetic Resonance Imaging-Guided Enhanced Chemo/photothermal/chemodynamic Therapy for Tumours. *J. Colloid Interf. Sci.* 604, 80–90. doi:10.1016/j.jcis.2021.06.174

Zhuang, W., Xu, Y., Li, G., Hu, J., Ma, B., Yu, T., et al. (2018). Redox and pH Dual-Responsive Polymeric Micelles with Aggregation-Induced Emission Feature for Cellular Imaging and Chemotherapy. *ACS Appl. Mater. Inter.* 10, 18489–18498. doi:10.1021/acsami.8b02890

Conflict of Interest: The authors declare that the research was conducted in the absence of any commercial or financial relationships that could be construed as a potential conflict of interest.

Publisher's Note: All claims expressed in this article are solely those of the authors and do not necessarily represent those of their affiliated organizations, or those of the publisher, the editors and the reviewers. Any product that may be evaluated in this article, or claim that may be made by its manufacturer, is not guaranteed or endorsed by the publisher.

frontiers in Chemistry

REVIEW
published: 16 November 2021
doi: 10.3389/fchem.2021.768248

Biomimetic Nanomaterials Triggered Ferroptosis for Cancer Theranostics

Xinyu Zhang[1], *Yanling Ma*[2], *Jipeng Wan*[3], *Jia Yuan*[3], *Diqing Wang*[3], *Weiyi Wang*[3], *Xiao Sun*[3]* *and Qingwei Meng*[1]*

[1]*Department of Medical Oncology, Harbin Medical University Cancer Hospital, Harbin, China,* [2]*Department of Chemical and Biomolecular Engineering, National University of Singapore, Singapore, Singapore,* [3]*School of Chemistry and Pharmaceutical Engineering, Institute of Optical Functional Materials for Biomedical Imaging, Medical Science and Technology Innovation Center, Shandong First Medical University & Shandong Academy of Medical Sciences, Jinan, China*

Ferroptosis, as a recently discovered non-apoptotic programmed cell death with an iron-dependent form, has attracted great attention in the field of cancer nanomedicine. However, many ferroptosis-related nano-inducers encountered unexpected limitations such as immune exposure, low circulation time, and ineffective tumor targeting. Biomimetic nanomaterials possess some unique physicochemical properties which can achieve immune escape and effective tumor targeting. Especially, certain components of biomimetic nanomaterials can further enhance ferroptosis. Therefore, this review will provide a comprehensive overview on recent developments of biomimetic nanomaterials in ferroptosis-related cancer nanomedicine. First, the definition and character of ferroptosis and its current applications associated with chemotherapy, radiotherapy, and immunotherapy for enhancing cancer theranostics were briefly discussed. Subsequently, the advantages and limitations of some representative biomimetic nanomedicines, including biomembranes, proteins, amino acids, polyunsaturated fatty acids, and biomineralization-based ferroptosis nano-inducers, were further spotlighted. This review would therefore help the spectrum of advanced and novice researchers who are interested in this area to quickly zoom in the essential information and glean some provoking ideas to advance this subfield in cancer nanomedicine.

Keywords: biomimetic modification, nanomedicine, ferroptosis, diagnosis, cancer therapy

OPEN ACCESS

Edited by:
Ruixue Duan,
Soochow University, China

Reviewed by:
Satyajit Tripathy,
University of the Free State, South Africa
Jie Shen,
Zhejiang University City College, China

***Correspondence:**
Xiao Sun
sunxiao@sdfmu.edu.cn
Qingwei Meng
mengqw@hrbmu.edu.cn

Specialty section:
This article was submitted to Nanoscience, a section of the journal Frontiers in Chemistry

Received: *31 August 2021*
Accepted: *04 October 2021*
Published: *16 November 2021*

Citation:
Zhang X, Ma Y, Wan J, Yuan J, Wang D, Wang W, Sun X and Meng Q (2021) Biomimetic Nanomaterials Triggered Ferroptosis for Cancer Theranostics. Front. Chem. 9:768248. doi: 10.3389/fchem.2021.768248

INTRODUCTION

The Severe Problems in Treating Cancer and the Requirement of a New Application

From the report of the American Cancer Society, except cardiovascular diseases, tumors have become the second cause of death (Cortes et al., 2020). Similarly, according to the report from the World Health Organization, there were 9.6 million deaths caused by cancers in 2018 worldwide, which were 1/6 of the total deaths (Cortes et al., 2020). Although more and more researchers have devoted their studies toinnovating new cancer treatments, malignant tumor is affecting more patients with an increasing mortality rate (Altekruse et al., 2011). Cancer is still threatening people's health severely. Nowadays, surgery, radiotherapy, chemotherapy, immunotherapy, and biotherapy are widely used in clinical cancer treatments. However, a high risk of relapse is also found in surgery because of the incomplete tumor cutting. The

toxicity of radiotherapy and chemotherapy impairs patients' normal organ functions, whereas biotherapy is too expensive to be afforded by most of the patients (Liu et al., 2019). In the past 10 years, immunotherapy, a promising cancer treatment (Yoon et al., 2018; Adams et al., 2019; Chu et al., 2019), has been impeded to be widely used in the clinic because of the narrow anticancer spectrum, the induction of potential autoimmune toxicity, and tumor escaping from the immune system (Adams et al., 2019; Sanmamed and Chen, 2019). Therefore, a safe and effective cancer treatment is yet to be invented to improve the effectiveness of cancer treatment and ameliorate the quality of patients' life. In this case, nanotechnology can provide novel methods in treating cancers; nanomaterials can not only be used for loading and specifically targeting the chemotherapeutic drugs to the tumor sites but also have been included in other tumor treatment strategies.

The Definition, Characteristics, and Association of Ferroptosis With Chemotherapy, Radiotherapy, and Immunotherapy for Enhancing Cancer Treatment Effects

Because of different morphologies, cell death is usually divided into three groups: apoptosis, autophagy, and necrosis (Gao and Jiang, 2018). Ferroptosis is a newly discovered cell death which is different from any other regulatory cell death in morphology, biochemistry, and genetics (Dixon et al., 2012). The cells in which ferroptosis occurs have smaller mitochondria, increased mitochondrial membrane concentration, reduced or disappeared mitochondrial cristae, and the rupture of the outer mitochondrial membrane. In addition, the inhibitors of apoptosis, autophagy, and pyrolysis cannot inhibit ferroptosis (Dixon et al., 2012; Yan et al., 2021). The sensitivity of cells toward ferroptosis is related to the regulation of multiple biological pathways, including iron metabolism, amino acid and glutathione (GSH) metabolism, and lipid metabolism (Stockwell et al., 2017).

Chemotherapy, one of the most common treatments for malignant tumors, prevents cancer cell proliferation and induces "cell death." Chemotherapeutic drug resistance of tumor cells can be alleviated effectively by blocking ferroptosis. Some laboratories have reported that RSL3, the GSH peroxidase 4 (GPX4) inhibitor, can trigger ferroptosis *via* increasing reactive oxygen species (ROS) accumulation and lipid peroxidation (LPO) levels within the cells, thereby enhancing the antitumor efficacy of cisplatin (Sui et al., 2018; Zhang et al., 2020). In addition, erastin, a ferroptosis inducer, improves the antitumor effects of certain drugs such as temozolomide (Chen et al., 2015), cisplatin (Liu and Wang, 2019; Li et al., 2020), vemurafenib (Tsoi et al., 2018), and docetaxel (Zhou et al., 2019) in killing specific cancer cells.

Radiotherapy is a sufficient treatment in oncology which uses low linear energy–delivered ionizing radiation (such as X-ray or γ-rays) to kill or control malignant cells. Ionizing radiation releases free radicals directly or indirectly through the radiolysis of water to damage the cells (Bischoff et al., 2009). Several studies have shown that the ferroptosis inducers RSL3, erastin, sorafenib (SRF), and sulfasalazine synergistically enhance the radiation efficacy in the models of glioma, lung cancer, fibrosarcoma, melanoma, breast cancer, and cervical cancer (Pan et al., 2019; Lei et al., 2020; Ye et al., 2020).

Immunotherapy is a novel tumor treatment model. Programmed cell death protein 1 (PD-1) and programmed cell death ligand 1 (PD-L1) inhibitors are most widely used in this treatment to prevent PD-1 on the surface of T cells. In this case, cancer cells conduct "immune evasion" from T cells, restoring the T cell killing function toward cancer cells. Wang et al. found that with PD-1 inhibitors, the tumor volume of the tumor-bearing mouse was significantly reduced, and the lipid ROS was significantly increased at the same time (Wang et al., 2019). After applying the ferroptosis inhibitor lipoxstatin-1, the effect of PD-L1 inhibitors was reduced, which showed that ferroptosis plays an important role in immunotherapy.

The marketed drugs such as sulfasalazine (Chen et al., 2015; Ma et al., 2015; Roh et al., 2016), SRF (Louandre et al., 2013), and artemisinin and its derivatives (Roh et al., 2017; Chen et al., 2019) have been shown to induce ferroptosis in some tumors; therefore, they have great clinical value. At the same time, some of the malignant tumors such as human adrenal cortical carcinoma are very sensitive to the induction of ferroptosis, which means that ferroptosis may be directly used in the treatment of malignant tumors (Belavgeni et al., 2019). The progress of ferroptosis-related studies provides new strategies for tumor treatment sensitization and new ideas for developing new drugs.

The Advantages of Biomimetic Nanomaterials and the Potential in Combining With Ferroptosis

A nanocarrier is a new type of drug delivery system at nanoscale. Because of the unique properties and easy modification, the nanocarrier is considered as a new generation of safe and specifically targeted drug carrier (Yang et al., 2016; Han et al., 2018). Nanocarriers have been successfully applied in diagnosis and precision therapeutic drug delivery for a better curative effect and reduced side effects due to their suitable size, easy modification, strong targeting ability, high cellular uptake, and good biocompatibility (Sumer and Gao, 2008; Melancon et al., 2011), which provide a new strategy to treat malignant tumors (Weissleder and Pittet, 2008; Barreto et al., 2011; Storm and Kiessling, 2011; Hrkach et al., 2012). However, some limitations have greatly hindered the clinical transformation of nanocarriers, for example, the toxicity as well as the degradation and metabolism of nanomaterials in the human body (Chou et al., 2014; Li et al., 2016; Shen et al., 2017). If nanomaterials enter the human body, there will be complex interactions between the drug carrier and the physiological environment, such as surface dissolution, protein adsorption, and/or non-specific cellular uptake which cause unfavorable tissue distribution, immune attack, and toxicity (Blanco et al., 2015). Therefore, the biocompatibility evaluation of nanocarrier materials has drawn more attention, such as blood compatibility, immune compatibility, and systemic toxicity. Nanomaterials with good biocompatibility can minimize the immune response of the body and reduce toxicity and side effects (Grossman and Mcneil, 2012). In tradition, the biocompatibility and

TABLE 1 | Biomimetic nanomaterials for cancer theranostics.

System	Biomimetic Composition	Cancer Theranostics	Cancer Type	Ref
CCR2(+)-Fe-M1-Nvs	M1 macrophage membrane	Immunotherapy, ferroptosis	Breast cancer	Li et al. (2021)
$FePSe_3$@APP@CCM	CT26 cell membrane	MR, PA, PTI/PTT, immunotherapy	Colorectal cancer	Fang et al. (2021)
Pa-M/Ti-NCs	Leukocyte membrane	MRI/immunotherapy, ferroptosis	Mutiple	Zhang et al. (2019)
Fe_3O_4-SAS@PLT	Platelet membrane	Immunotherapy, ferroptosis	Breast cancer	Jiang et al. (2020)
mFe(SS)/DG	4T1 cell membrane	Chemo-immunotherapy, ferroptosis	Breast cancer	Yang et al. (2021)
PNP-R848	Platelet membrane	Immunotherapy	Mutiple	Bahmani et al. (2021)
RB@Exo	Exosome membrane	Chemotherapy, PTT	Melanoma tumor	Shen et al. (2020)
EV-DNs	Grapefruit extracellular vesicles	Chemotherapy	Glioma	Niu et al. (2021)
DOX-PFP-CNs@PLGA/PM	Platelet membrane	PAI/PTT and chemotherapy	Breast cancer	Li et al. (2021)
GdTPP/ZnTPP	HeLa cell membrane	MRI, FI/PDT	Cervical cancer	Wang et al. (2020)
NPN	Bacteria membrane	PTT	Breast cancer	Li et al. (2020)
FGGZA	Glucose oxidase (GOx), BSA	PDT, PTT	Breast cancer	An et al. (2020)
BCFe@SRF	BSA	PDT, ferroptosis	Liver cancer	Wang et al. (2021)
P2K-ZnP-CRL-Bfr	Bacterioferritin	PDT, ferroptosis	Amelanotic melanoma	Cioloboc et al. (2018)
SRF@Hb-Ce6	Hb	PDT, ferroptosis	Breast cancer	Xu et al. (2020)
Hb-PDA-Fe@GOD@PEG-FA	Hb, GOD	PTT, PDT, starvation therapy	Mutiple	Yuan et al. (2021)
Tf-LipoMof@PL	Transferrin	Ferroptosis, pyroptosis	Breast cancer	Xu et al. (2021)
GHZD NCs	GOx	Immunotherapy	Breast cancer	Zhao et al. (2021)
ICG/AuNR@BCNP	Albumin	FLI, PAI, IRT, BLI, MRI, PET/PTT, PDT	Glioma	Yang et al. (2020)
AQ4N/GOx@ZIF-8@CM	GOx, HepG2 cell membrane	PDT	Liver cancer	Shao et al. (2021)
NMIL-100@GOx@C	GOx, 4T1 cell membrane	Ferroptosis, starvation therapy	Breast cancer	Wan et al. (2020)
AMSNs	Arginine	MRI/chemotherapy	Mutiple	Wang et al. (2018)
ACC@DOX.Fe^{2+}-CaSi-PAMAM-FA/mPEG	Amorphous calcium carbonate	PDT	Mutiple	Xue et al. (2020)
GOx-MnCaP-DOX	MnCaP	MRI/CDT	Breast cancer	Fu et al. (2019)
OVA-Cu-HVs	$Cu_3(PO_4)_2$, OVA	Immunotherapy	Lymphoma	Liu et al. (2019)
IO-LAHP	LAHP	MRI/PDT	Glioma	Liu et al. (2019)
LDL-DHA	ω-3 PUFA	Ferroptosis	Liver cancer	Ou et al. (2017)

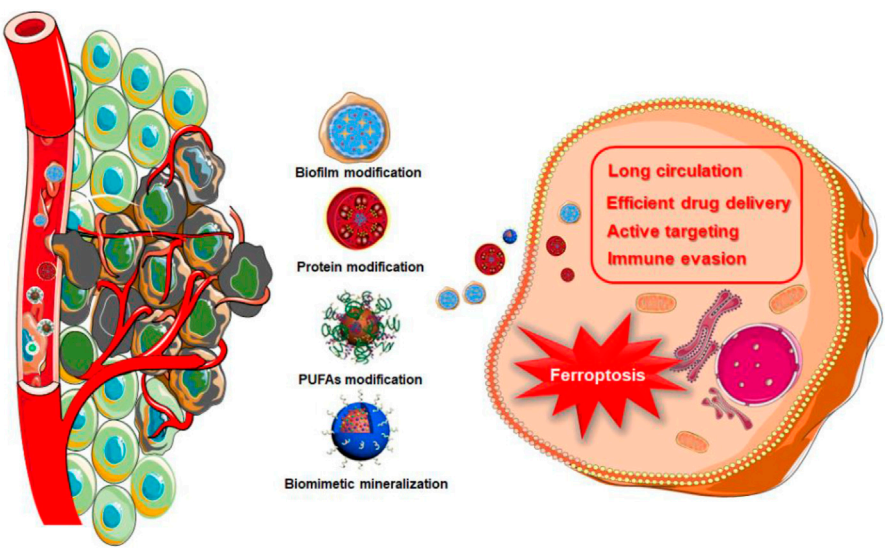

FIGURE 1 | Schematic illustration of biomimetic nanomaterials for inducing ferroptosis.

biodistribution of nanoparticles can be partially optimized by nanoparticle surface modification (for example, PEGylation) (Xu et al., 2015; Moyano et al., 2016; Ni et al., 2021).

In 1994, a s cientific research team headed by J. W. Bulte used horse spleen apolipoprotein as a raw material to synthesize a protein-encapsulated nano-single crystal superparamagnetic iron oxide as a magnetic resonance imaging (MRI) contrast agent (Bulte et al., 1994). This was the first time that the bionic technology was applied to a nanoassembly system. Since then, nano-biomimetic materials have entered a rapid developed stage. Biomimetic functionalization of nanoparticles could solve many problems in the physiological environment, endowing nanomedicines with better biological characteristics. For example, due to the antigenic diversity of the cell membrane, biomimetic modification provides a range of

functions associated with the cell origin, including immune evasion, long circulation, efficient drug delivery, and active targeting (Zhen et al., 2019; Choi et al., 2020). As showed in **Table 1**, a lot of biomimetic nanomaterials are applied in cancer theranostics in recent years. Among them, biomimetic strategies for ferroptosis therapy can be divided into biofilm modification, protein modification, polyunsaturated fatty acids (PUFAs) modification, and biomimetic mineralization **(Figure 1)**.

Since Stockwell named ferroptosis for the first time in 2012, there have been a lot of research studies conducted to study its molecular mechanism and corresponding signal transduction pathways and try to find new and more efficient ferroptosis inducers for cancer treatments. So far, various genes, small molecules, and nanomaterials have been elucidated to possess the ability of inducing cell ferroptosis (Dixon et al., 2015; Louandre et al., 2015; Yu et al., 2015; Ma et al., 2016; Shen et al., 2018). However, the lack of endogenous iron and half-helical genes or molecular reagents cannot sufficiently improve the efficiency of the Fenton reaction. In addition, the selectivity of genes and small molecules is weak, and their adverse reactions also obstruct the clinical application transformation. In this case, the introduction of nanomedicine has brought bright future for developing new ferroptosis inducers in tumor-specific treatment. Among them, the unique physicochemical properties of nanomaterials can compensate the deficiencies of traditional drugs, such as low targeting efficiency, poor solubility, and severe adverse reactions, and can also introduce new properties such as magnetism, photothermal effects and electrochemical properties (Jiang et al., 2021). Most importantly, the ferroptosis nano-inducer can make up for the lack of endogenous iron and accelerate the ferroptosis process of tumor cells by improving the efficiency of the Fenton reaction.

Ferroptosis-induced nanomaterials can be mainly divided into two categories: one is iron-based nanomaterials and the other is non–ferrous-based nanomaterials. Due to the importance of iron in ferroptosis, iron-based compounds with abundant iron ions, such as iron oxide nanoparticles (IO NPs), are the most popular nanomaterials in ferroptosis application–related research. In addition, there are also some iron-free nanomaterials which can induce cancer cell death by cooperating with endogenous iron. For example, Kim et al. created an iron-free, ultrasmall α-melanocyte–stimulating hormone and polyethylene glycol–modified silica nanoparticles which are effective ferroptosis inducers for tumor suppression and targeted therapy (Kim et al., 2016). This review mainly summarized the latest developments of biomimetic nanomaterials in the field of the development trends of ferroptosis-related tumor treatment and some considerations about the principles, advantages, and limitations of these bionic strategies.

A VARIETY OF BIONIC NANOMATERIALS ARE USED FOR FERROPTOSIS-MEDIATED TUMOR TREATMENT

Biofilm Modification

With the inspiration of the natural biological system, biofilm bionics has drawn scientists' attention (Fang et al., 2017). In recent years, various biofilms have been extracted to modify nanoparticle surfaces to produce multifunction bionic nanoparticles which are composed of nanoparticles as the core and natural biofilms as the shell. The nanoparticle core endows the bionic nanoparticle high selectivity, and biofilms also make it natural. By comparing with the attachment of nanomaterial functional groups, biofilm bionic nanomaterials are easy to prepare with better biocompatibility to lower immune rejection and toxicity. Therefore, biofilm bionic nanomaterials show great application prospects in medicine.

Leukocytes are immune cells which maintain the normal functions of the immune system, including macrophages, neutrophils, eosinophils, basophils, and lymphocytes (Xuan et al., 2015). The bionic nanomedicine of the leukocyte membrane can be constructed for targeted delivery of antitumor drugs by utilizing the mutual recognition between the leukocyte and tumor surface antigen–antibody (Molinaro et al., 2020). The receptors on the neutrophils' surface can interact with chemokines and adhesion factors in the tumor microenvironment to enrich the drug (Zhang et al., 2019; Sun et al., 2020). Kang et al. reported that NMNP-CFZ, a neutrophil membrane biomimetic nanoparticle, was able to block tumor metastasis by capturing tumor cells from the blood stream and specifically targeting the tumor microenvironment prior to metastasis (Kang et al., 2017). Macrophages are non-specific immune cells that can bind specifically to tumor surface antigens and have chemotactic properties to the tumor microenvironment. Bionic modification of the macrophage membrane can reduce the clearance rate of drug carriers *in vivo*, prolong the systemic circulation time, enrich drugs in the tumor site, significantly inhibit the tumor growth, and improve therapeutic effect (Zhao et al., 2018). Lymphocytes can be divided into NK cells, T cells, and B cells. NK cells are innate immune cells and can secrete cytokines to activate T cells and regulate immune responses (Wehner et al., 2011). The NK cell membrane has the function of tumor targeting and inducing M1-type polarization of macrophages (Deng et al., 2018).

In 2019, Xie and coworkers constructed a magnetosome Pa-M/Ti-NCs; the core of the magnetosome was a superparamagnetic and controllable Fe_3O_4 nanocluster (NCS) which was made *via* a one-pot hydrothermal approach (Wan et al., 2020). This specific structure can not only be used for MRI and magnetic targeting but also delivers a large amount of Fe ions to conduct the Fenton reaction and induce ferroptosis **(Figure 2)**. At the same time, the previously designed leukocyte membrane by using N3 covered NCS with a typical membrane protein (such as CD44 and CD45) to prolong circulation time and promote the loading of Ti, a TGF-β inhibitor within the membrane, and the coupling with the dibenzocyclooctyne-modified PD-1 antibody. After getting into the tumor, Pa and Ti worked together to create an immunogenetic microenvironment to elevate the concentration of H_2O_2 within the polarized M1 macrophage which promoted the Fenton reaction with iron ions released from NCS. The produced hydroxyl free radicals (•OH) then induced ferroptosis of tumor cells, and the exposed tumor antigens enhanced immunogenicity of the

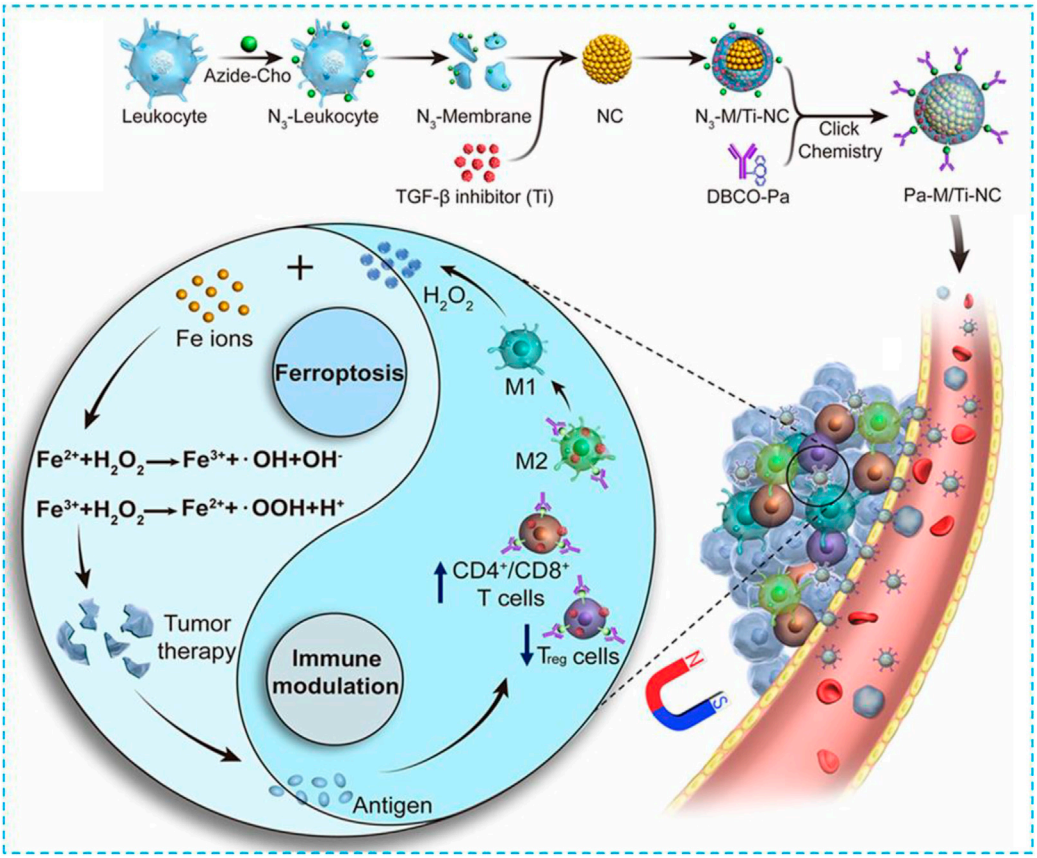

FIGURE 2 | Schematic illustration of the NMNP-CFZ nanoplatform for ferroptosis/immunomodulation synergism in cancer. Reprinted with permission from Ref. (Lyu et al., 2020) Copyright 2019 American Chemical Society.

microenvironment further. In the B16F10 xenograft model, the signal of free NCS without membrane coating was detected at the tumor site for up to 6 h. The 24-h signal did not satisfy because of the fast clearance. In comparison, the leukocyte-coated NCS could significantly inhibit phagocytosis of macrophages to increase circulation and enhance EPR, and therefore, a better antitumor effect could be achieved.

Macrophages, a subclass of leukocytes, are important effector cells in innate immunity which have great functional plasticity during tumor development and metastasis. More and more studies have proved that macrophages are used in cancer treatment for better therapeutic effects (Wan et al., 2020). Inspired by the macrophage-based cancer therapy and exosome-like drug delivery, in 2021, Li and his colleagues designed an exosome; the M1 macrophages which were transfected by CCR2 plasmids were coincubated with Fe_3O_4 nanoparticles and further extruded into exosome-like nanovesicles (denoted as CCR2 (+)-Fe-M1-NVS) to act as a nano-Fenton reactor and M2 repolarization inducer to restrict lung metastasis synergistically (Li et al., 2021). Both *in vitro* and *in vivo* experiments have found that CCR2 (+)-Fe-M1-NVS was similar to the mature macrophages which accumulated at tumor metastases through the CCR2-CCL2 (C–C chemokine-receptor 2 and -ligand 2, respectively) axis. Fe_3O_4 nanoparticles and M1-related factors (such as H_2O_2) were known as catalysts of the Fenton reaction to promote the ferroptosis of tumors and jointly induce the repolarization of macrophages, therefore stimulating tumor-specific immune responses. At the same time, the repolarization of M2 macrophages induced H_2O_2 accumulation by upregulating T-cell–stimulating factors, activated T cells, and synergistically induced ferroptosis by releasing interferon-γ, thereby inhibiting the uptake of cystine by tumor cells, leading to LPO. By investigating the cell coculture system and the 4T1 mouse xenograft model, the targeted therapy and synergistic cytotoxicity were verified.

Platelets are small fragments of the cytoplasm derived from megakaryocytes in the bone marrow. Platelets have a relatively low content in the blood, but they are super-important for body hemostatic function. When there is a wound, platelets can be quickly recruited to the wound to activate both internal and external coagulation systems for hemostasis (Senturk, 2010). Because of the fast response to vasculature damage, the recognition of circulated tumor cells, and the specific binding to the damaged area, platelet-coated nanoparticles have been widely used in cancer treatment

(Zhang et al., 2018). At the same time, endothelial reticulum endocytosis can also be reduced, and the immune escape of nanomedicine can be increased to extend the blood circulation of medicine and finally promote the efficacy of the drugs (Hu et al., 2015; Dehaini et al., 2017; Chen et al., 2019; Wang et al., 2019).

Yang et al. reported the production of a magnetic nanoparticle Fe_3O_4-SAS@PLT (Jiang et al., 2020). Sulfasalazine (SAS) is used to treat rheumatism which can inhibit not only inflammatory cell migration and the IκB kinase pathway but also cysteine intake to suppress the tumor growth and induce ferroptosis (Roh et al., 2016). The SAS activity has been proved by a clinical tumor model when the concentration is high. SAS was uptaken by magnetic nanoparticles and camouflaged by the platelet membrane; this composite was used for cancer treatment by inducing the ferroptosis effect. As a ferroptosis inducer, the synergy between Fe_3O_4 and SAS reduced the SAS dose significantly. *In vitro*, the concentration of Fe_3O_4-SAS@PLT for maximum inhibition was lower than Fe_3O_4-SAS, which indicated that PLT coating enhanced cytotoxicity because of the high binding affinity between PLT and the CD44 receptor on tumor cells (Ye et al., 2019). At the same time, PLT coating increased the cellular uptake of the nanoparticle composite. Therefore, platelet membrane coating can escape from the immune system, specifically bind to tumors, and maximize the uptake of the ferroptosis-inducible nanoparticle by the tumor which showed a great potential in treating tumor metastases.

In recent years, cancer cell–coated nanocarriers have drawn researchers' attention. This type of biomimetic membrane can camouflage nanomedicine as cancer cells to deliver drugs to the tumor site *via* mutual cancer cell recognition and adhesion to achieve effective cancer treatment (Zhang et al., 2019; Zhen et al., 2019). The design and application of cancer cell–coated nanocarriers have become hot topics for cancer diagnosis and treatment. Cancer cells could endow nanoparticles the ability to target the tumor specifically and escape from the immune system to improve the accumulation of nanoparticles in the tumor (Zhang et al., 2019; Zhen et al., 2019). Yang et al. reported a novel nanoplatform mFe (SS)/DG as ROS–ferroptosis–glycolysis regulators for the anticancer immune cycle (Yang et al., 2021). Constructed by Fe^{3+} and disulfide (-S-S-)-containing organic ligand, the nanosystem with a suitable surface and structure can effectively load GOx and doxorubicin (DOX) and can be further coated by the 4T1 cell membrane to decrease immune clearance and realize efficient tumor targeting. This nanoplatform can consume intracellular GSH *via* -S-S- bond and catalyze glucose to generate excessive ROS in tumor sites, improve cascade-amplified ferroptosis, and elicit immunogenic cell death in combination with DOX. By combining tumor metabolism and immune function, the biomimetic nanoplatform provides a potential antitumor strategy.

Tang et al. designed a nanoreactor which was composed of cancer cell–coated organic iron framework and GOx (Wan et al., 2020). In this nanoreactor, GOx catalyzed the production of H_2O_2 from glucose for the induction of the ferroptosis effect. When the nanoreactor reached the tumor site, MOF collapsed because of the release of Fe^{2+} from high concentration of GSH reduced Fe^{3+} worked with GOx to produce H_2O_2 **(Figure 3)**; then the Fenton reaction between H_2O_2 and Fe^{2+} released •OH to promote the ferroptosis effect. The fluorescent intensity of the cancer cell–coated nanoreactor NMIL-100@RhB@C was as twice as NMIL-100@RhB and could be endocytosed easier by 4T1 cells. Furthermore, the detection of the antiphagocytosis ability of NMIL-100@RhB@C and NMIL-100@RhB against macrophages (Raw 264.7) indicated that fluorescent intensity increased twice in NMIL-100@RhB incubated Raw264.7. NMIL-100@RhB@C–injected mice showed higher fluorescent intensity on the tumor site, especially within the tumor site, than NMIL-100@RhB–injected mice which proved that the cancer-coated nanoreactor can specifically bind to the tumor site. During nanoreactor transportation, the cancer cell coating can protect the nanoreactor from proteinase and immune system degradation, and therefore, high concentration of GOx can reach and be endocytosed by the tumor. Overall, these cascade reactions provided a safer and more efficient way to inhibit the tumor growth by triggering both ferroptosis and tumor cell starvation.

The cell membrane biomimetic nanoprobe is a new type of probe which actively identifies specific tumor cells *via* the EPR effect or molecular targets to shift tumor therapy from the tissue and organ level to the molecular level. At the same time, the cell membrane nanoprobe restricts the clearance of the reticuloendothelial system and prolongs the circulation time in the body significantly. Therefore, it has unique advantages in tumor-targeted precision therapy. Although the design of biomimetic cell membranes has bright prospects, new problems have also existed. For example, how to stabilize the biological effects of heterogeneous white blood cells in the body is unignorable. Whether the cancer cell membrane will express oncogenes and whether its biological safety can be guaranteed are also yet to be studied. After the cancer cell membrane enters the body, the changes of the internal immune system can be triggered. At the same time, some issues may be encountered, such as how to produce abundant various cell membrane nanoprobes efficiently, simplify the production process with reduced cost, and how to ensure the activity and stability of biofilm materials which will be the direction of future research. In addition, how to improve interactions between the biofilm and the tumor site to improve its recognition ability also should be considered because there may be limited opportunities for nanomaterials *in vivo* to establish contacts with the tumor before clearance.

Protein Modification

Proteins are big molecules with biological functions. The protein nanocarrier system is composed of different structures and functions of animals and plants or recombinant proteins and drugs which have good biocompatibility, biodegradability, low antigenicity, high stability, and drug loading capacity and are easy to make (Lee et al., 2016; Sandra et al., 2019). There are a large amount of free amino acids on the protein surface, and they can

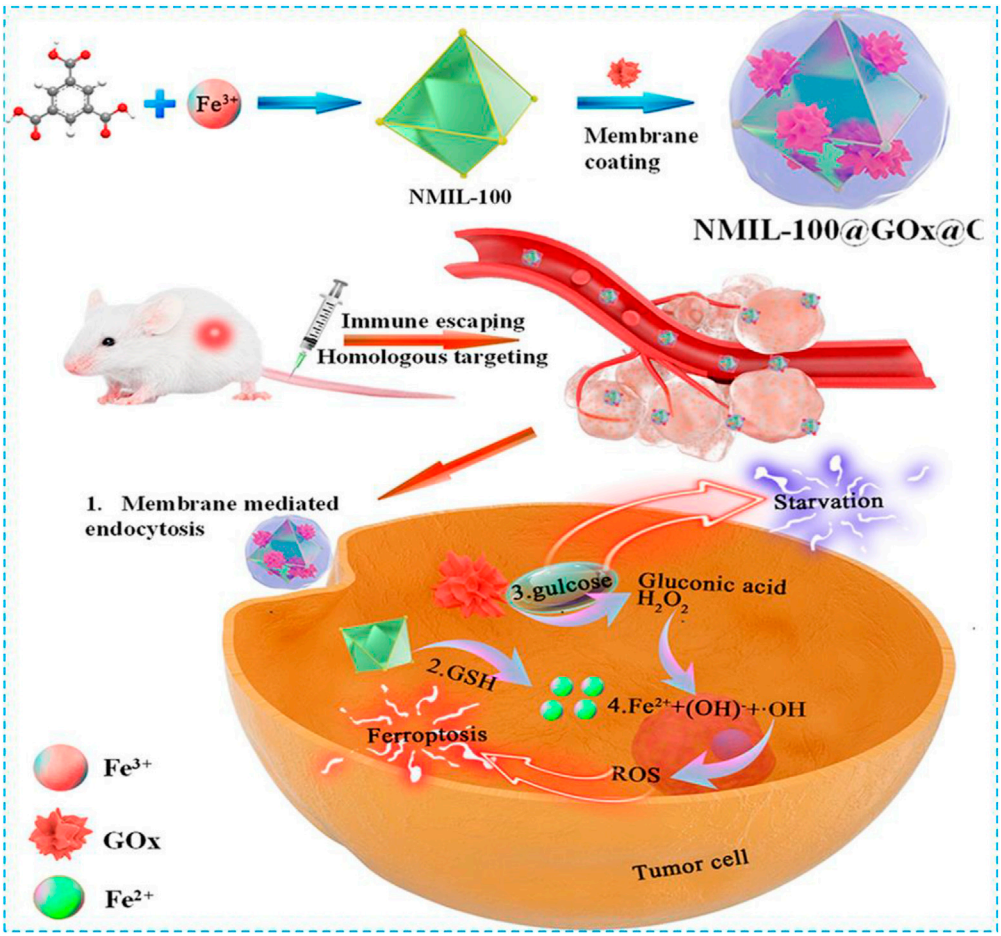

FIGURE 3 | Schematic illustration of the preparation and cascade processes for cancer therapy of NMIL-100@GOx@C. Reprinted with permission from Ref. (Wan et al., 2020). Copyright 2020 American Chemical Society.

be modified with photothermal molecules, fluorescent dyes, chemotherapeutic drugs, image probes, photosensitizers, and many other small functional molecules which make the protein nanoparticle a good nanocarrier to prolong anticancer drug loading and circulating for improved cancer imaging and treatment (Wang et al., 2015). For example, due to its good biocompatibility and stability, bovine serum albumin (BSA) is often used for nanomaterials' surface modification. In the process of stripping lamellar MoS_2, an effective stripping agent and stabilizer, BSA can achieve the large-scale preparation of ultrathin MoS_2 nanosheets under ultrasonic conditions. In another study, as a template, BSA is expected to enable the programmed preparation of TMD QDs to improve their biocompatibility and stability (Wang et al., 2020). In addition, in ferroptosis-related studies, iron ion–based proteins (hemoglobin, ferritin, etc.) are often involved in enhancing the level of iron ions, or some functional proteins such as GOx are often associated with H_2O_2 production.

Hemoglobin (Hb) is one of the most well-studied natural and red endogenous proteins to transfer oxygen in the blood vessels (Liu et al., 2018). Because of high oxygen capability, it is always used to donate oxygen in photodynamic therapy. Hb has four heme groups, which contain irons and can be used as iron supplements in the ferroptosis effect (Xu et al., 2020). These iron ions can be released in the presence of H_2O_2 and produce •OH *via* the Fenton reaction (Xu et al., 2020). Li and colleagues constructed a nanoplatform SRF@Hb-Ce6 *via* loading SRF to the Hb-coated photosensitizer Ce6 **(Figure 4)** (Xu et al., 2020). Both oxygen and irons in Hb brought opportunities for the combination of PDT and ferroptosis effect. In this nano platform, high oxygen concentration promoted PDT efficiency significantly; SRF and intrinsic iron in Hb greatly elevated lipid peroxide production and suppressed GPX4 to induce strong ferroptosis effects. This nanoplatform could also enhance T-cell infiltration at the tumor site and the release of IFN-γ to downregulate SLC3A2 and SLC7A11 which increased the sensitivity of tumors toward ferroptosis. By comparing with free Ce6, the fluorescent image of SRF@Hb-Ce6 showed a stronger intensity at the tumor site which indicated SRF@Hb-Ce6 had specific binding.In the *in vivo* study, SRF@Hb-Ce6-treated tumor-bearing mice had smaller tumor sizes and higher survival rates. Therefore, SRF@Hb-Ce6 can promote both PDT

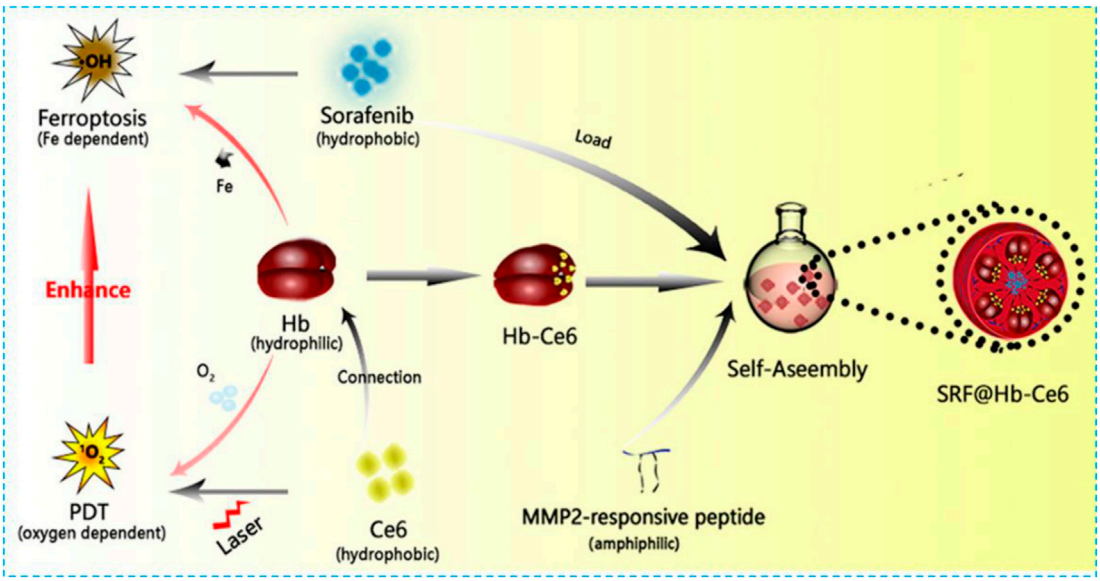

FIGURE 4 | Schematic illustration showing the components of SRF@Hb-Ce6, the synthesis process, and the combined PDT and ferroptosis therapy. Reprinted with permission from Ref. (Xu et al., 2020). Copyright 2020 American Chemical Society.

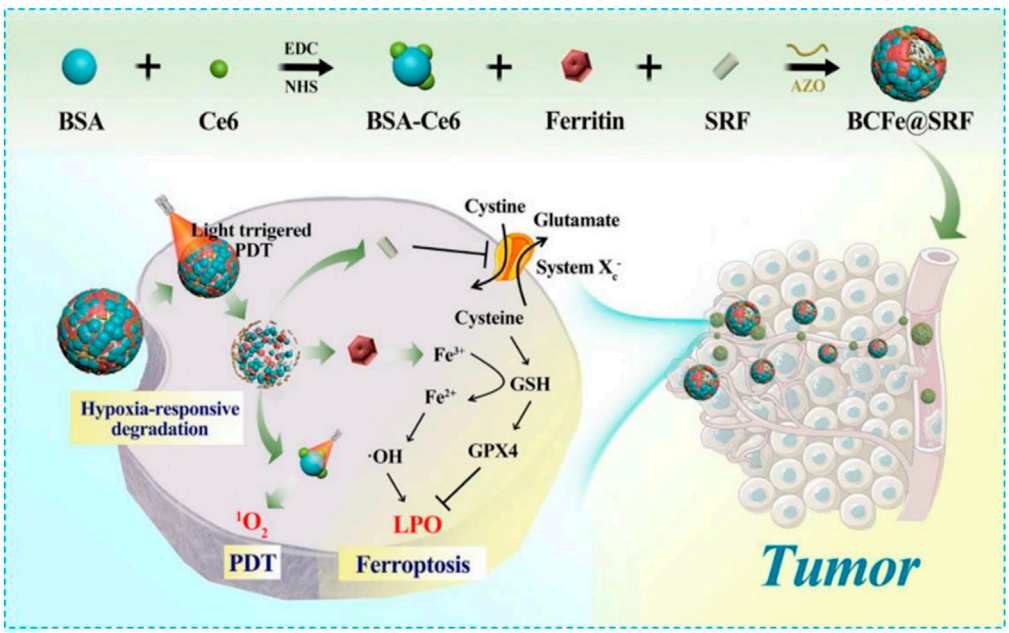

FIGURE 5 | Schematic illustration showing fabrication procedures and antitumor mechanisms of the BCFe@SRF nanoreactor for the synergistic PDT and ferroptosis therapy. Reprinted with permission from Ref. (Wang et al., 2021). Copyright 2021 The Author(s).

and the ferroptosis effect, which showed us a promising strategy in treating cancer safely via the combination of two treatments.

Ferritin is a protein which can store irons. It has been identified by overexpressed TFR1 as a new type of missile platform (Liang et al., 2014; Truffi et al., 2016). In addition, the stored irons, released from ferritin intracellular autophagy, can induce ferroptosis easily (Ensor et al., 2002; Miyamoto et al., 2003; Phillips et al., 2014; Gao et al., 2016; Hou et al., 2016; Keshet et al., 2018; Yang et al., 2021). Therefore, with intrinsic iron absorption capacity and difficult-to-identify characteristics, ferritin has more advantages than inorganic materials or MOF materials in treating ferroptosis. In 2021, Wang et al. covalently

linked BSA-Ce6 (Ce6 coupled BSA) and ferritin by azobenzene (Azo) to fabricate a new hypoxia-responsive device BcFe@SRF for SRF loading which provided an unparalleled opportunity for the synergistic treatment of high-efficiency photodynamic (PDT) and ferroptosis **(Figure 5)**. The designed BcFe@SRF had suitable particle size, stable dispersion, and excellent tumor-homing performance. Importantly, in a hypoxia environment, BcFe@SRF could be gradually degraded and release BSA-Ce6, ferritin, and SRF for triggering PDT, the iron-catalyzed Fenton reaction, and destroying tumors' antioxidant defenses, respectively. Apart from the PDT effect, studies have also found that BcFe@SRF-mediated low-oxygen laser irradiation could not only promote the production of LPO but also depleted intracellular GSH and reduced the expression of GPX4. In summary, the BcFe@SRF nanoreactor uses a variety of ways to promote the accumulation of intracellular ROS and exerts significant antitumor effects both *in vitro* and *in vivo*.

Transferrin (TF) is a glycoprotein to carry irons and mediate iron endocytosis when it binds to the transferrin receptor (TFR) (Torti and Torti, 2013). TF has been proved to be expressed in various types of cancer cells. (Johnsen et al., 2017) The upregulated TFR level on the surface of cancer cells enhances TF-mediated iron endocytosis and can therefore be a sufficient and specific cancer treatment (Weed et al., 1963; Daniels et al., 2012). More Fe^{3+} can be captured by extra TF to further accelerate TFR endocytosis. Shen et al. constructed a nanosphere TF-LipoMof@PL by coating the TF-modified pH-sensitive lipid membrane on piperlongumine (PL)-loaded MOF (Xu et al., 2021). The lipid membrane could promote TF-mediated iron endocytosis to provide a prerequisite of the ferroptosis effect. As a ferroptosis inducer, PL provided H_2O_2 for producing ROS via the Fenton reaction. *In vitro*, the TF-precipitated nanosystem showed higher tumor cytotoxicity. ICP-MS–measured intracellular iron levels showed TF-LipoMof@PL-applied cancer cell had the highest iron level, which means TF could increase iron endocytosis. The *in vivo* study had similar results, among 4T1-transplanted mice with a high TFR expression level; TF-LipoMof@PL-treated cells had the highest ROS level and induced the strongest iron effect. Therefore, TF-LipoMof@PL had the best anticancer effect.

GOx is a natural enzyme; H_2O_2 can be released when it oxidizes dextrose to gluconic acid in the present of oxygen (Wang et al., 2016). The tumor growth is highly dependent on glucose supply; tumor cells will be too starving to grow once glucose supply is stopped (Zhang et al., 2018; Xie et al., 2019; Yang et al., 2019). GOx-inducing glucose oxidation could lower the glucose level, which makes it attractive in cancer treatment. This treatment is the so-called starvation therapy (Fu et al., 2018; Yu et al., 2018; Zhang et al., 2018; Fu et al., 2019; Hanjun et al., 2019; Xie et al., 2019). At the same time, a high level of H_2O_2 was produced during GOx catalyzation which can cooperate with the iron-based nanomaterial to promote ferroptosis (Bankar et al., 2009; Fu et al., 2018; Hanjun et al., 2019). An et al. designed a 4,4′-azonzenecarboxylic acid (Azo)–BSA–modified zeolitic imidazolate framework (ZIF) nanoplatform with Fe^{3+}-gallic acid and GOx encapsulation (designated as FGGZA) (An et al., 2020). FGGZA achieved sustained Fe^{2+}/H_2O_2 supply and decreased pH and O_2 levels, which can significantly improve the ferroptosis reaction microenvironment. In a hypoxic microenvironment, azo achieved charge reversal, leading to selective tumor aggregation based on efficient cell internalization activated by hypoxia. This reasonably designed biomimetic nanosystem will present great potential in clinical transformation of ferroptosis tumor treatment.

As the main component of protein, amino acid modification is also considered to be an effective biomimetic method. Due to the lack of arginine (Arg) succinate synthase (ASS) in a variety of tumors, such as breast cancer, renal cell carcinoma, melanoma, and hepatocellular carcinoma, the tumor cells themselves cannot produce Arg (Ensor et al., 2002; Phillips et al., 2014; Keshet et al., 2018). Considering that the consumption of Arg at tumor sites will lead to the demand for Arg-modified nanomaterials, Arg is considered a targeted part of tumor diagnosis and treatment. In 2018, Wang et al. used a one-pot method to fabricate an Arg-rich manganese silicate nanobubble (AMSN)–based ferroptosis inducer which was endowed the high-efficiency GSH depletion capacity to inactivate GPX4 to induce ferroptosis (**Figure 6)** (Wang et al., 2018). In this case, Arg acted as a surface-capping ligand to provide ideal water dispersibility, biocompatibility, and tumor-homing ability. In comparison with traditional nanoparticles, the ultrathin surface layer and nanobubble structure of Arg significantly improved the rate of GSH depletion in AMSNs and inactivated tumor cells by GPX4. Fer-1 and DFO can remarkably reduce the toxicity of AMSNs. As the concentration of AMSNs and the incubation time increased, the protein expression level of GPX4 decreased and the activity of GPX4 reduced. Then, fluorescein dichlorodiacetate (DCFH-DA) proved that as AMSNs depleted GSH, the level of reactive oxygen species in the cell increased. The level of LPO was monitored by the specific probe C11-BODIPY581/591. The fluorescence intensity of AMSNs was stronger than that of the control group, and it was proportional to the concentration and the incubation time. These results indicated that ferroptosis plays a crucial role in AMSN-induced cell death. In addition, the degradation of AMSNs during GSH depletion caused Mn ions and drug release to enhance the contrast of T1-weighted MRI and the effect of chemotherapy. Different from the iron-based nanomaterials which induce ferroptosis through the Fenton reaction or manganese-based nanomaterials which only provide auxiliary functions to consume GSH in tumor treatment, AMSN can directly induce ferroptosis *in vitro* and *in vivo*, and therefore, high-efficiency tumor targeted therapy can be achieved.

In the process of protein nanomaterial–induced ferroptosis, apart from the high structural stability, excellent biocompatibility, and wonderful biodegradability of protein nanocarriers, the natural properties of proteins can be used, such as the iron-rich protein, or the protein improves the transport efficiency of iron which can increase the concentration of endosomal iron ions and improve the effect of ferroptosis further. However, these protein nanoparticles still have shortcomings. For example, the size of protein nanoparticles cannot be precisely controlled if they are prepared by covalent or non-covalent binding due to uncontrollable self-assembly

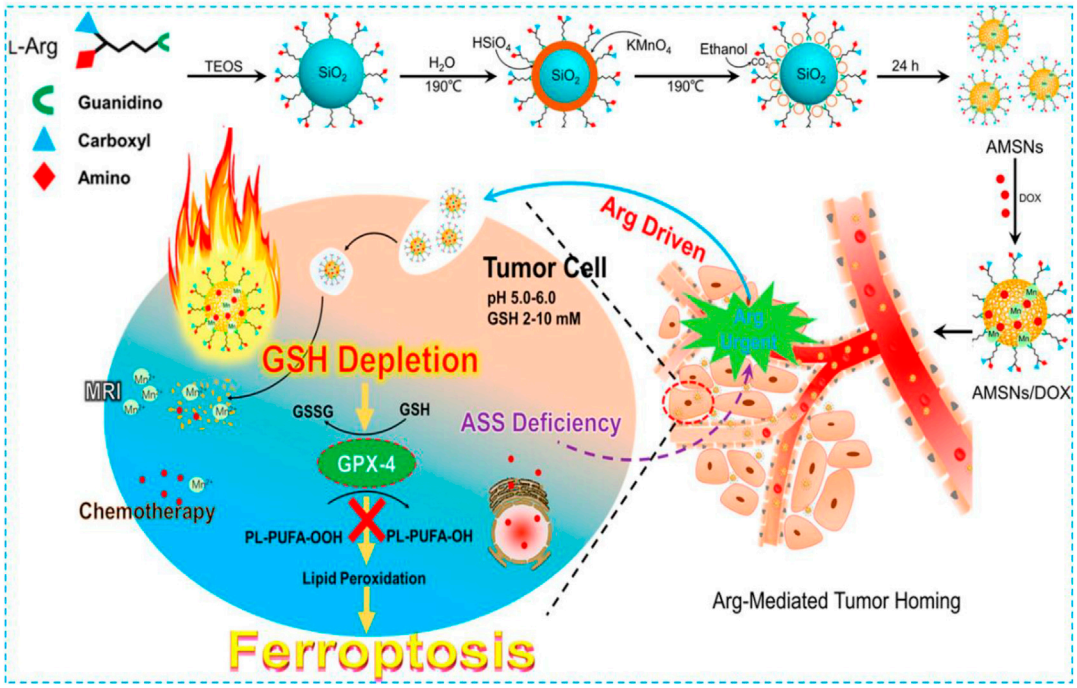

FIGURE 6 | Schematic illustration of the preparation and ferroptosis-induced cancer therapy of AMSNs. Reprinted with permission from Ref. (Wang et al., 2018). Copyright 2018 American Chemical Society.

behavior. Some proteins are difficult and expensive to be obtained, such as ferritin. More attention should be paid to maintain protein activity in appropriate temperature and buffer solution to avoid inactivation during the process of the experiment. At the same time, immunogenicity brought by the enzyme itself should also be concerned. Due to the large size and the fixed three-dimensional structure of some proteins, it is more difficult to modify the surface of some nanomaterials than long-chain polymers (e.g., PEG and PVP). In addition, the macrophage system uptakes nanomaterials significantly because of the wide size distribution and easy aggregation which reduce the concentration of protein nanoparticles in the tumor site. Furthermore, many excellent inorganic nanomaterials cannot directly interact with proteins, which limits the application of inorganic nanomaterials in tumor diagnosis and treatment. Therefore, it is still necessary to continue to explore protein nanoparticles with precise and controllable size to overcome the existing drawbacks listed before.

Polyunsaturated Fatty Acid Modification

PUFAs are important components of the phospholipid bilayer which is crucial in maintaining the fluidity of the cell membrane. Excess PUFAs will be oxidized into •OH by Fe^{2+} via the Fenton reaction. These •OH can further oxidize PUFAs in a chain reaction to produce a large amount of LPO and finally induce cell ferroptosis. In 2017, Zhou et al. used hydrophobic linoleic acid hydrogen peroxide (LAHP) and hydrophilic oligoethylene glycol to modify phosphate groups on the surface of IO NPs to develop a Fenton reaction–based nanosystem (**Figure 7**) (Zhou et al., 2017). Under this circumstance, IO NPs with a diameter of 22 nm were used as carriers of LAHP polymers with surface anchoring groups. Hydrophilic polymers grafted with oligoethylene glycol units were used as end-capping molecules on the surface of IO NPs; therefore, IO-LAHP nanoparticles possessed water dispersibility, proton permeability, and biocompatibility. At the same time, H^+ could penetrate the polymer brush to dissociate Fe^{2+} from the surface of the IO-LAHP nanoparticles as an iron source and realize the on-demand release of Fe^{2+} by the nanosystem under tumor acidic conditions. As one of the main products of LPO, LAHP was decomposed into free radicals and $^1O_2$ by catalytic ions (such as $Fe^{2+}$and Ce^{4+}) through the Russell mechanism (Miyamoto et al., 2003; Miyamoto et al., 2006). After intravenous injection of IO-LAHP nanoparticles in mice, the overall tumor growth was significantly inhibited. By evaluating the efficiency of IO-LAHP nanoparticles in producing activated $^1O_2$ and in cancer treatment *in vitro* and *in vivo*, LAHP-modified IO NPs can treat cancer effectively through the non-photodynamic process when $^1O_2$ is produced in engineering biochemical reactions.

Similarly, the addition of exogenous PUFA DHA to tumor cells provides a new possible nanomaterial construction which induced ferroptosis by promoting LPO because cancer cells tend to actively take up lipoproteins to meet the lipids' demands for rapid membrane turnover (Favre, 1992). At the same time, the lipoprotein platform can transport lipids in the plasma naturally, and it is also a particularly suitable carrier for omega-3 PUFAs (ω-3 PUFAs) (Gotto et al., 1986). Based on this knowledge, in 2017, Ou et al. uniformly incorporated w-3 PUFA

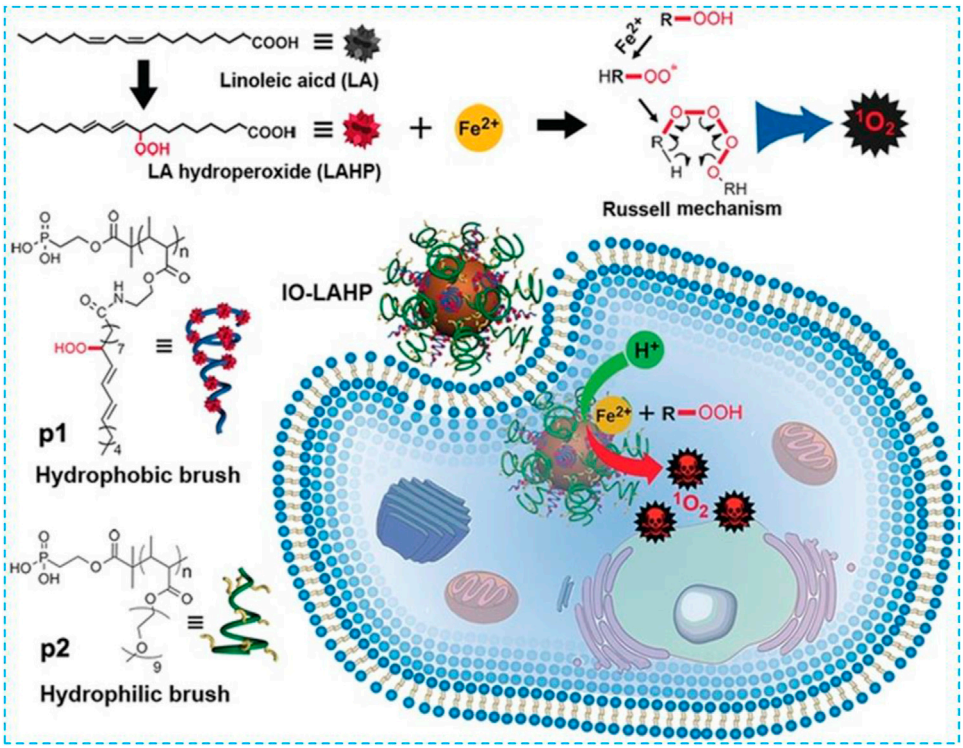

FIGURE 7 | Preparation and ferroptosis-mediated cancer therapy of IO-LAHP. Reprinted with permission from Ref. (Zhou et al., 2017). Copyright 2017 Wiley-VCH.

docosahexaenoic acid (DHA) into a low-density lipoprotein (LDL) to construct LDL-DHA nanoparticles (Ou et al., 2017). After treating using LDL-DHA, both rat and human liver cancer cells underwent significant LPO, GSH depletion, and the deactivation of the lipid antioxidant GPX4. The antitumor effect of LDL-DHA nanoparticles was evaluated in mice with HepG2 xenografts. PBS, LDL-TO and LDL-DHA, and Fer-1 or LDHA + Fer-1 were injected intratumorally to treat tumor-bearing mice, and the growth of the tumor treated by the low-density lipoprotein DHA was significantly inhibited. The combination of Fer-1 and LDL-DHA can remarkably antagonize the GPX4 activity, level of LPO, and tumor volumes which were treated by LDL-DHA alone.

So far, many studies have proved that ω-3 PUFAs have cytotoxicity toward various cancer cell cultures in a dose-dependent manner (Lindskog et al., 2006; Lim et al., 2009). However, the dosage required to induce anticancer effects in the culture is hard to achieve (Conquer and Holub, 1998) through dietary intake which may explain the inconsistent results from the treatment of established tumors through dietary intake of ω-3 PUFAs (Noguchi et al., 1997; Swamy et al., 2008; Gleissman et al., 2011). Poor solubility in water and easy forming of emboli make direct intravascular injection of ω-3 PUFAs inviable (Mellor and Soni, 2001). Even in cell culture experiments, organic solvents such as ethanol or dimethyl sulfoxide are needed to dissolve the ω-3 PUFAs in the growth media. Therefore, nanoparticles should be good tools to treat tumors. Ferroptosis can be regulated during unsaturated fatty acid metabolism; unsaturated fatty acid–loaded nanoparticles also have great prospects in this field. However, considering the uncertainty of the degree of ferroptosis induced by a single unsaturated fatty acid, more combinations of nanomaterials should be considered, such as with small-molecule ferroptosis inducers or iron-based nanomaterials to design more advanced nanomaterials in the treatment of tumor ferroptosis.

Biomimetic Mineralization

Biomineralization is a common process in which inorganic ions are combined with biological macromolecules to generate hard biomaterials in organisms. Organisms (bacteria, plants, animals, etc.) with different compositions can generate minerals in the body, endowing them on specific biological functions. The biological mineralization is a highly controlled process that exists naturally and is regulated by the genetics of the organism. It can achieve the precise control of the assembly of the crystal shape and structure from the molecular level to mesoscopic level, attracting more attention of scientists in the biomedical field. For example, the nanodrug slow-release system based on biomineralization has received extensive attention in cancer treatment due to easy preparation and modification, good biocompatibility, and biodegradability; therefore, a multifunction nanoplatform related to biomineralization has been developed for a variety of biomedical applications (Srivastava et al., 2018).

$CaCO_3$ is one of the most common inorganic materials found in nature. Because of the low cost, bio-absorbility, and good biocompatibility, $CaCO_3$ has attracted wide attention of many

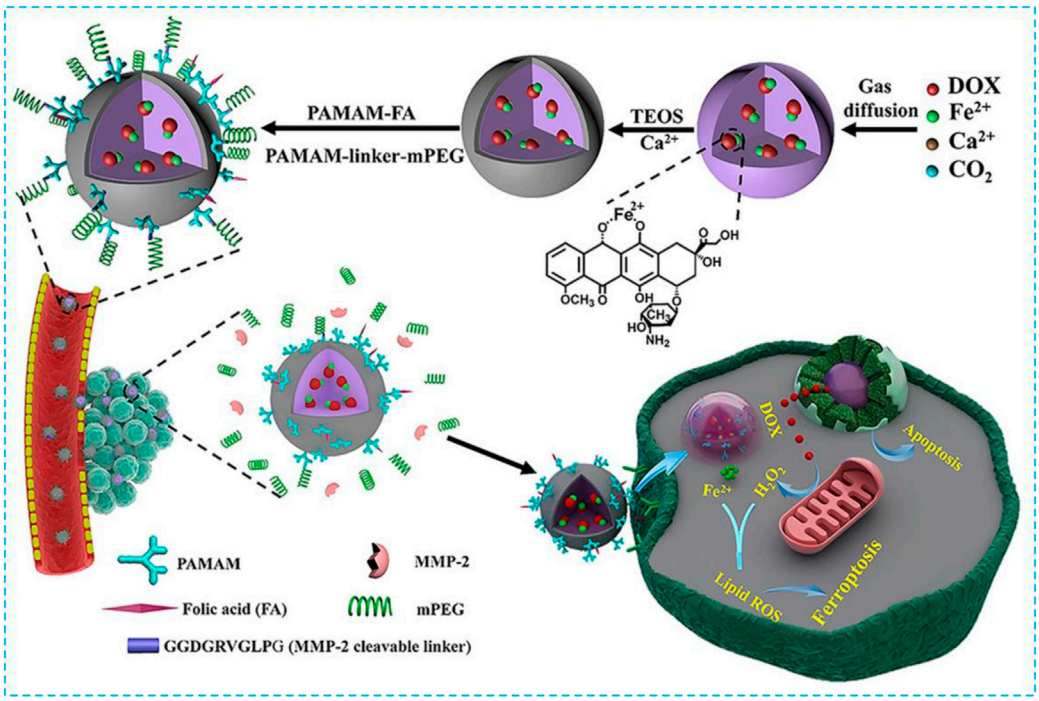

FIGURE 8 | Synthesis scheme of ACC@DOX.Fe^{2+}-CaSi-PAMAM-FA/mPEG and its complementary ferroptosis/apoptosis-based therapeutic action. Reprinted with permission from Ref. (Xue et al., 2020). Copyright 2020 The Authors.

researchers and scientists (Mao et al., 2016). However, high crystallization made $CaCO_3$ degrade slowly in the biological environment, which would impede drug release and therefore block the progression of its application as a drug release system (Maleki Dizaj et al., 2015). The development and application of the amorphous calcium carbonate (ACC) nanostructure has finally solved these intrinsic limitations. Compared with the $CaCO_3$ crystal, ACC nanoparticles have a higher energy level and can be hydrolyzed easily within cells. After a series of experiments (Min et al., 2015; Dong et al., 2018; Wang et al., 2018), the advantages of the ACC nanodrug carrier have been demonstrated. Zhao's group obtained an ACC-based, pH-sensitive drug delivery system by co-condensing DOX and a calcium precursor which can only release DOX under an acidic tumor microenvironment to kill cancer cells (Zhao et al., 2015). Furthermore, organic-modified ACC can further improve the bio-functionality and biocompatibility of nanocomposites without changing its original clinical advantages.

Luo et al. chelated DOX with Fe^{2+} and co-condensed with the calcium precursor to construct an ACC-coated Fe^{2+}-DOX core in a one-step process based on amorphous ACC which can be used for tumor targeting and ferroptosis treatment (**Figure 8**) (Xue et al., 2020). In this case, the combination of DOX and Fe^{2+} can not only be loaded sufficiently into ACC but also minimize the sensitivity of ferrous towards oxidative stress before it releases from the host cell so that the biodegradable ACC can work with DOX and Fe^{2+} synergistically. The thin CaSi layer covered at the core is coupled with PAMAM to endow the specific tumor binding and provide a balance between circulatory life and tumor-specific uptake. DOX can be released within the cancer cells when acid-induced ACC degradation has occurred and H_2O_2 produced Fe^{2+}-promoted ferroptosis. This nanocomposite has showed a strong ferroptosis effect and will be used in clinic.

Compared with synthetic nanomaterials, these biosynthetic nanominerals have good physiological stability, biodegradability, and biological activity and simple and economical synthesis process, and only need a simple bionic water system. Therefore, the design of a variety of nano-biominerals by combining biomineralization technology and ferroptosis for tumor treatment has broad application prospects in tumors. However, biomimetic-mineralized nanomaterials also faced many problems. For example, some biomimetic-mineralized nanomaterials about urinary calculus, such as calcium oxalate, calcium phosphate, and uric acid, may not degrade well *in vivo* and require further manual intervention to remove them. Because the biomimetic mineralization is highly ordered, it is difficult to control the reaction process during the artificial preparation, and some reaction conditions are relatively demanding. In addition, biomimetic mineralized nanomaterials synthesized *in vitro* may also cause immune reaction in a certain degree when applied *in vivo*. In addition to genetic regulation and other biological methods to control the synthesis of biomimetic mineralized materials, scientists still need to make unremitting efforts to further explore the generation mechanism and action properties of biomimetic mineralization.

CONCLUSION, FRESH PERSPECTIVE, AND FUTURE DIRECTIONS

Due to the antiapoptotic effect of tumor cells caused by overexpression of apoptosis-inhibiting proteins and multidrug resistance, apoptosis-based treatment strategies cannot achieve satisfactory therapeutic effects. Ferroptosis, a novel non-apoptotic programmed cell death, has become a hot topic in cancer research and has gradually attracted wide attention in the field of cancer nanomedicine. The emergence of biomimetic nanomaterials brings new opportunities for the clinical translation of ferroptosis-triggered nanomaterials. Synthetic nanoparticles are combined with natural biological materials to create biomimetic nanomedicine inspired by nature. These nanomaterials not only have the adjustability and flexibility of synthetic materials but also have the functionality and biocompatibility of natural materials, thus giving nanomaterials many advantages such as good versatility and a long *in vivo* cycle. Moreover, some components of biomimetic materials can enhance ferroptosis more effectively. This review summarized the latest research studies in the field of biomimetic nanomaterials to trigger ferroptosis of tumor cells and enhance tumor therapy. We hope that this review will provide new ideas and insights for the application of biomimetic nanomaterials in the biomedical field.

Despite the rapid progress of ferroptosis-based cancer therapeutics, the potential clinical applications of ferroptosis nanomedicine still face many challenges. For example, there are significant differences in the sensitivity of ferroptosis toward various species and tissues. And the sensitivity of ferroptosis inducers (SRF, erastin, etc) is also diverse. Therefore, it is of great significance to search for biological indicators that can reflect the sensitivity of cells and individuals to ferroptosis and to develop new ferroptosis inducers to improve the level of tumor diagnosis and treatment. In addition, several studies have shown that the combination of different therapies (e.g., PDT and PTT) with ferroptosis therapy through nanotechnology can achieve better therapeutic effects, further overcoming the barriers of ferroptosis treatment (Wang et al., 2021; Yuan et al., 2021).

There are still a lot of difficulties in the large-scale application of biomimetic nanoparticles to trigger ferroptosis due to the difficulties existed in the preparation, storage, and application process of some biomimetic nanoparticles. Theoretically, while bionic methods can effectively reduce the response of the body, there is still a lack of long-term tracking validation in *in vivo* experiments which need more exploration by excellent scientists. Because of the deficiency of the iron content for some ferroptosis nano-inducers, iron ion loading and the controlled release capacity of ferroptosis nano-inducers should be intensified to improve the distribution of iron in the cancer cells and thus improve anticancer efficiency. Although biomimetic modification can endow nanomedicine good biocompatibility, some of the nanomaterial components are difficult to be degraded or may generate toxic products after degradation. Therefore, in the process of designing biomimetic nanodrugs, the safety of the proposed component should be considered.

In conclusion, as a novel tumor treatment and multidisciplinary research, ferroptosis induced by biomimetic-based nanotumor therapy has a high therapeutic efficiency in killing cancer cells and reducing the toxicity and side effects on normal cells/tissues. Compared with the traditional cancer treatment, it shows obvious advantages and clinical transformation potential. After the listed limitations of this field have been fully addressed in future, the progress of cancer biomedicine discovery will be promoted greatly and benefit more cancer patients.

AUTHOR CONTRIBUTIONS

XZ designed and edited the manuscript. YM helped editing English language. JW and JY researched data and drew picture. DW and WW helped drawing the table. XS and QM designed and supervised the whole process. All authors read and approved the final manuscript.

ACKNOWLEDGMENTS

We acknowledge the funding provided by the National Natural Science Foundation of China (81672931), Shandong Health System Outstanding Young Talent Project, and the Overseas Science and Technology Talents Project of Shandong Province. And we gratefully acknowledge contributions of Menghan Liu, Ying Luo, Yan Wang, and Yuting Sun from Shandong First Medical University and the Shandong Academy of Medical Sciences in information query.

REFERENCES

Adams, S., Gatti-Mays, M. E., Kalinsky, K., Korde, L. A., Sharon, E., Amiri-Kordestani, L., et al. (2019). Current Landscape of Immunotherapy in Breast Cancer. *JAMA Oncol.* 5 (8), 1205–1214. doi:10.1001/jamaoncol.2018.7147

Altekruse, S., Kosary, C., Krapcho, M., Neyman, N., Aminou, R., Waldron, W., et al. (2011). *SEER Cancer Statistics Review, 1975–2007*. Bethesda, MD: Natl. Cancer Inst. 1975–2007.

An, P., Gu, D., Gao, Z., Fan, F., Jiang, Y., and Sun, B. (2020). Hypoxia-augmented and Photothermally-Enhanced Ferroptotic Therapy with High Specificity and Efficiency. *J. Mater. Chem. B* 8 (1), 78–87. doi:10.1039/C9TB02268F

Bahmani, B., Gong, H., Luk, B. T., Haushalter, K. J., DeTeresa, E., Previti, M., et al. (2021). Intratumoral Immunotherapy Using Platelet-Cloaked Nanoparticles Enhances Antitumor Immunity in Solid Tumors. *Nat. Commun.* 12 (1), 1–12. doi:10.1038/s41467-021-22311-z

Bankar, S. B., Bule, M. V., Singhal, R. S., and Ananthanarayan, L. (2009). Glucose Oxidase - an Overview. *Biotechnol. Adv.* 27 (4), 489–501. doi:10.1016/j.biotechadv.2009.04.003

Barreto, J. A., O'Malley, W., Kubeil, M., Graham, B., Stephan, H., and Spiccia, L. (2011). Nanomaterials: Applications in Cancer Imaging and Therapy. *Adv. Mater.* 23 (12), H18–H40. doi:10.1002/adma.201100140

Belavgeni, A., Bornstein, S. R., von Mässenhausen, A., Tonnus, W., Stumpf, J., Meyer, C., et al. (2019). Exquisite Sensitivity of Adrenocortical Carcinomas to

Induction of Ferroptosis. *Proc. Natl. Acad. Sci. USA* 116 (44), 22269–22274. doi:10.1073/pnas.1912700116

Bischoff, P., Altmeyer, A., and Dumont, F. (2009). Radiosensitising Agents for the Radiotherapy of Cancer: Advances in Traditional and Hypoxia Targeted Radiosensitisers. *Expert Opin. Ther. Patents* 19 (5), 643–662. doi:10.1517/13543770902824172

Blanco, E., Shen, H., and Ferrari, M. (2015). Principles of Nanoparticle Design for Overcoming Biological Barriers to Drug Delivery. *Nat. Biotechnol.* 33 (9), 941–951. doi:10.1038/nbt.3330

Bulte, J. W. M., Douglas, T., Mann, S., Frankel, R. B., Moskowitz, B. M., Brooks, R. A., et al. (1994). Magnetoferritin: Characterization of a Novel Superparamagnetic MR Contrast Agent. *J. Magn. Reson. Imaging* 4 (3), 497–505. doi:10.1002/jmri.1880040343

Chen, L., Li, X., Liu, L., Yu, B., Xue, Y., and Liu, Y. (2015). Erastin Sensitizes Glioblastoma Cells to Temozolomide by Restraining xCT and Cystathionine-γ-Lyase Function. *Oncol. Rep.* 33 (3), 1465–1474. doi:10.3892/or.2015.3712

Chen, Y., Mi, Y., Zhang, X., Ma, Q., Song, Y., Zhang, L., et al. (2019). Dihydroartemisinin-induced Unfolded Protein Response Feedback Attenuates Ferroptosis via PERK/ATF4/HSPA5 Pathway in Glioma Cells. *J. Exp. Clin. Cancer Res.* 38 (1), 402. doi:10.1186/s13046-019-1413-7

Chen, Y., Zhao, G., Wang, S., He, Y., Han, S., Du, C., et al. (2019). Platelet-membrane-camouflaged Bismuth Sulfide Nanorods for Synergistic Radio-Photothermal Therapy against Cancer. *Biomater. Sci.* 7 (8), 3450–3459. doi:10.1039/C9BM00599D

Choi, B., Park, W., Park, S.-B., Rhim, W.-K., and Han, D. K. (2020). Recent Trends in Cell Membrane-Cloaked Nanoparticles for Therapeutic Applications. *Methods* 177, 2–14. doi:10.1016/j.ymeth.2019.12.004

Chou, L. Y. T., Zagorovsky, K., and Chan, W. C. W. (2014). DNA Assembly of Nanoparticle Superstructures for Controlled Biological Delivery and Elimination. *Nat. Nanotech* 9 (2), 148–155. doi:10.1038/nnano.2013.309

Chu, D. K., Wood, R. A., French, S., Fiocchi, A., Jordana, M., Waserman, S., et al. (2019). Oral Immunotherapy for Peanut Allergy (PACE): a Systematic Review and Meta-Analysis of Efficacy and Safety. *Lancet* 393 (10187), 2222–2232. doi:10.1016/S0140-6736(19)30420-9

Cioloboc, D., Kennedy, C., Boice, E. N., Clark, E. R., and Kurtz, D. M. (2018). Trojan Horse for Light-Triggered Bifurcated Production of Singlet Oxygen and Fenton-Reactive Iron within Cancer Cells. *Biomacromolecules* 19 (1), 178–187. doi:10.1021/acs.biomac.7b01433

Conquer, J. A., and Holub, B. J. (1998). Effect of Supplementation with Different Doses of DHA on the Levels of Circulating DHA as Non-esterified Fatty Acid in Subjects of Asian Indian Background. *J. Lipid Res.* 39 (2), 286–292. doi:10.1016/S0022-2275(20)33890-6

Cortes, J., Perez-García, J. M., Llombart-Cussac, A., Curigliano, G., El Saghir, N. S., Cardoso, F., et al. (2020). Enhancing Global Access to Cancer Medicines. *CA A. Cancer J. Clin.* 70 (2), 105–124. doi:10.3322/caac.21597

Daniels, T. R., Bernabeu, E., Rodríguez, J. A., Patel, S., Kozman, M., Chiappetta, D. A., et al. (2012). The Transferrin Receptor and the Targeted Delivery of Therapeutic Agents against Cancer. *Biochim. Biophys. Acta (Bba) - Gen. Subj.* 1820 (3), 291–317. doi:10.1016/j.bbagen.2011.07.016

Dehaini, D., Wei, X., Fang, R. H., Masson, S., Angsantikul, P., Luk, B. T., et al. (2017). Erythrocyte-Platelet Hybrid Membrane Coating for Enhanced Nanoparticle Functionalization. *Adv. Mater.* 29 (16), 1606209. doi:10.1002/adma.201606209

Deng, G., Sun, Z., Li, S., Peng, X., Li, W., Zhou, L., et al. (2018). Cell-Membrane Immunotherapy Based on Natural Killer Cell Membrane Coated Nanoparticles for the Effective Inhibition of Primary and Abscopal Tumor Growth. *ACS Nano* 12 (12), 12096–12108. doi:10.1021/acsnano.8b05292

Dixon, S. J., Lemberg, K. M., Lamprecht, M. R., Skouta, R., Zaitsev, E. M., Gleason, C. E., et al. (2012). Ferroptosis: An Iron-dependent Form of Nonapoptotic Cell Death. *Cell* 149 (5), 1060–1072. doi:10.1016/j.cell.2012.03.042

Dixon, S. J., Winter, G. E., Musavi, L. S., Lee, E. D., Snijder, B., Rebsamen, M., et al. (2015). Human Haploid Cell Genetics Reveals Roles for Lipid Metabolism Genes in Nonapoptotic Cell Death. *ACS Chem. Biol.* 10 (7), 1604–1609. doi:10.1021/acschembio.5b00245

Dong, Z., Feng, L., Hao, Y., Chen, M., Gao, M., Chao, Y., et al. (2018). Synthesis of Hollow Biomineralized CaCO3-Polydopamine Nanoparticles for Multimodal Imaging-Guided Cancer Photodynamic Therapy with Reduced Skin Photosensitivity. *J. Am. Chem. Soc.* 140 (6), 2165–2178. doi:10.1021/jacs.7b11036

Ensor, C. M., Holtsberg, F. W., Bomalaski, J. S., and Clark, M. A. (2002). Pegylated Arginine Deiminase (ADI-SS PEG20,000 Mw) Inhibits Human Melanomas and Hepatocellular Carcinomas *In Vitro* and *In Vivo*. *Cancer Res.* 62 (19), 5443–5450.

Fang, R. H., Jiang, Y., Fang, J. C., and Zhang, L. (2017). Cell Membrane-Derived Nanomaterials for Biomedical Applications. *Biomaterials* 128, 69–83. doi:10.1016/j.biomaterials.2017.02.041

Fang, X., Wu, X., Li, Z., Jiang, L., Lo, W. S., Chen, G., et al. (2021). Biomimetic Anti-PD-1 Peptide-Loaded 2D FePSe 3 Nanosheets for Efficient Photothermal and Enhanced Immune Therapy with Multimodal MR/PA/Thermal Imaging. *Adv. Sci.* 8 (2), 2003041. doi:10.1002/advs.202003041

Favre, G. (1992). Targeting of Tumor Cells by Low Density Lipoproteins: Principle and Use of Ellipticin Derivatives. *C R. Seances Soc. Biol. Fil.* 186 (1-2), 73–87.

Fu, L.-H., Qi, C., Lin, J., and Huang, P. (2018). Catalytic Chemistry of Glucose Oxidase in Cancer Diagnosis and Treatment. *Chem. Soc. Rev.* 47 (17), 6454–6472. doi:10.1039/C7CS00891K

Fu, L. H., Qi, C., Hu, Y. R., Lin, J., and Huang, P. (2019). Glucose Oxidase-Instructed Multimodal Synergistic Cancer Therapy. *Adv. Mater.* 31 (21), 1808325. doi:10.1002/adma.201808325

Fu, L.-H., Hu, Y.-R., Qi, C., He, T., Jiang, S., Jiang, C., et al. (2019). Biodegradable Manganese-Doped Calcium Phosphate Nanotheranostics for Traceable Cascade Reaction-Enhanced Anti-tumor Therapy. *ACS Nano* 13 (12), 13985–13994. doi:10.1021/acsnano.9b05836

Gao, M., and Jiang, X. (2018). To Eat or Not to Eat - the Metabolic Flavor of Ferroptosis. *Curr. Opin. Cel Biol.* 51, 58–64. doi:10.1016/j.ceb.2017.11.001

Gao, M., Monian, P., Pan, Q., Zhang, W., Xiang, J., and Jiang, X. (2016). Ferroptosis Is an Autophagic Cell Death Process. *Cell Res.* 26 (9), 1021–1032. doi:10.1038/cr.2016.95

Gleissman, H., Segerström, L., Hamberg, M., Ponthan, F., Lindskog, M., Johnsen, J. I., et al. (2011). Omega-3 Fatty Acid Supplementation Delays the Progression of Neuroblastoma *In Vivo*. *Int. J. Cancer* 128 (7), 1703–1711. doi:10.1002/ijc.25473

Gotto, A. M., Pownall, H. J., and Havel, R. J. (1986). [1] Introduction to the Plasma Lipoproteins. *Methods Enzymol.* 128, 3–41. doi:10.1016/0076-6879(86)28061-1

Grossman, J. H., and Mcneil, S. E. (2012). Nanotechnology in Cancer Medicine. *Phys. Today* 65 (8), 38–42. doi:10.1063/pt.3.1678

Han, X., Li, Y., Xu, Y., Zhao, X., Zhang, Y., Yang, X., et al. (2018). Reversal of Pancreatic Desmoplasia by Re-Educating Stellate Cells with a Tumour Microenvironment-Activated Nanosystem. *Nat. Commun.* 9 (1), 3390. doi:10.1038/s41467-018-05906-x

Hao, H., Sun, M., Li, P., Sun, J., Liu, X., and Gao, W. (2019). *In Situ* Growth of a Cationic Polymer from the N-Terminus of Glucose Oxidase to Regulate H2O2 Generation for Cancer Starvation and H2O2 Therapy. *ACS Appl. Mater. Inter.* 11 (10), 9756–9762. doi:10.1021/acsami.8b20956

Hou, W., Xie, Y., Song, X., Sun, X., Lotze, M. T., Zeh, H. J., et al. (2016). Autophagy Promotes Ferroptosis by Degradation of Ferritin. *Autophagy* 12 (8), 1425–1428. doi:10.1080/15548627.2016.1187366

Hrkach, J., Von Hoff, D., Ali, M. M., Andrianova, E., Auer, J., Campbell, T., et al. (2012). Preclinical Development and Clinical Translation of a PSMA-Targeted Docetaxel Nanoparticle with a Differentiated Pharmacological Profile. *Sci. Transl. Med.* 4 (128), 128ra39. doi:10.1126/scitranslmed.3003651

Hu, C.-M. J., Fang, R. H., Wang, K.-C., Luk, B. T., Thamphiwatana, S., Dehaini, D., et al. (2015). Nanoparticle Biointerfacing by Platelet Membrane Cloaking. *Nature* 526 (7571), 118–121. doi:10.1038/nature15373

Jiang, Q., Wang, K., Zhang, X., Ouyang, B., Liu, H., Pang, Z., et al. (2020). Platelet Membrane-Camouflaged Magnetic Nanoparticles for Ferroptosis-Enhanced Cancer Immunotherapy. *Small* 16 (22), 2001704. doi:10.1002/smll.202001704

Jiang, X., He, C., and Lin, W. (2021). Supramolecular Metal-Based Nanoparticles for Drug Delivery and Cancer Therapy. *Curr. Opin. Chem. Biol.* 61, 143–153. doi:10.1016/j.cbpa.2021.01.005

Johnsen, K. B., Burkhart, A., Melander, F., Kempen, P. J., Vejlebo, J. B., Siupka, P., et al. (2017). Targeting Transferrin Receptors at the Blood-Brain Barrier Improves the Uptake of Immunoliposomes and Subsequent Cargo Transport into the Brain Parenchyma. *Sci. Rep.* 7 (1), 10396. doi:10.1038/s41598-017-11220-1

Kang, T., Zhu, Q., Wei, D., Feng, J., Yao, J., Jiang, T., et al. (2017). Nanoparticles Coated with Neutrophil Membranes Can Effectively Treat Cancer Metastasis. *ACS Nano* 11 (2), 1397–1411. doi:10.1021/acsnano.6b06477

Keshet, R., Szlosarek, P., Carracedo, A., and Erez, A. (2018). Rewiring Urea Cycle Metabolism in Cancer to Support Anabolism. *Nat. Rev. Cancer* 18 (10), 634–645. doi:10.1038/s41568-018-0054-z

Kim, S. E., Zhang, L., Ma, K., Riegman, M., Chen, F., Ingold, I., et al. (2016). Ultrasmall Nanoparticles Induce Ferroptosis in Nutrient-Deprived Cancer Cells and Suppress Tumour Growth. *Nat. Nanotech* 11 (11), 977–985. doi:10.1038/nnano.2016.164

Lee, E. J., Lee, N. K., and Kim, I.-S. (2016). Bioengineered Protein-Based Nanocage for Drug Delivery. *Adv. Drug Deliv. Rev.* 106, 157–171. doi:10.1016/j.addr.2016.03.002

Lei, G., Zhang, Y., Koppula, P., Liu, X., Zhang, J., Lin, S. H., et al. (2020). The Role of Ferroptosis in Ionizing Radiation-Induced Cell Death and Tumor Suppression. *Cel Res* 30 (2), 146–162. doi:10.1038/s41422-019-0263-3

Li, L., Fu, S., Chen, C., Wang, X., Fu, C., Wang, S., et al. (2016). Microenvironment-Driven Bioelimination of Magnetoplasmonic Nanoassemblies and Their Multimodal Imaging-Guided Tumor Photothermal Therapy. *ACS Nano* 10 (7), 7094–7105. doi:10.1021/acsnano.6b03238

Li, M., Li, S., Zhou, H., Tang, X., Wu, Y., Jiang, W., et al. (2020). Chemotaxis-driven Delivery of Nano-Pathogenoids for Complete Eradication of Tumors post-phototherapy. *Nat. Commun.* 11 (1), 1126. doi:10.1038/s41467-020-14963-0

Li, Y., Yan, H., Xu, X., Liu, H., Wu, C., and Zhao, L. (2020). Erastin/Sorafenib Induces Cisplatin-Resistant Non-Small Cell Lung Cancer Cell Ferroptosis through Inhibition of the Nrf2/xCT Pathway. *Oncol. Lett.* 19 (1), 323–333. doi:10.3892/ol.2019.11066

Li, L., Fu, J., Wang, X., Chen, Q., Zhang, W., Cao, Y., et al. (2021). Biomimetic "Nanoplatelets" as a Targeted Drug Delivery Platform for Breast Cancer Theranostics. *ACS Appl. Mater. Inter.* 13 (3), 3605–3621. doi:10.1021/acsami.0c19259

Li, P., Gao, M., Hu, Z., Xu, T., Chen, J., Ma, Y., et al. (2021). Synergistic Ferroptosis and Macrophage Re-polarization Using Engineering Exosome-Mimic M1 Nanovesicles for Cancer Metastasis Suppression. *Chem. Eng. J.* 409, 128217. doi:10.1016/j.cej.2020.128217

Liang, M., Fan, K., Zhou, M., Duan, D., Zheng, J., Yang, D., et al. (2014). H-ferritin-nanocaged Doxorubicin Nanoparticles Specifically Target and Kill Tumors with a Single-Dose Injection. *Proc. Natl. Acad. Sci.* 111 (41), 14900–14905. doi:10.1073/pnas.1407808111

Lim, K., Han, C., Dai, Y., Shen, M., and Wu, T. (2009). Omega-3 Polyunsaturated Fatty Acids Inhibit Hepatocellular Carcinoma Cell Growth through Blocking β-catenin and Cyclooxygenase-2. *Mol. Cancer Ther.* 8 (11), 3046–3055. doi:10.1158/1535-7163.MCT-09-0551

Lindskog, M., Gleissman, H., Ponthan, F., Castro, J., Kogner, P., and Johnsen, J. I. (2006). Neuroblastoma Cell Death in Response to Docosahexaenoic Acid: Sensitization to Chemotherapy and Arsenic-Induced Oxidative Stress. *Int. J. Cancer* 118 (10), 2584–2593. doi:10.1002/ijc.21555

Liu, Q., and Wang, K. (2019). The Induction of Ferroptosis by Impairing STAT3/Nrf2/GPx4 Signaling Enhances the Sensitivity of Osteosarcoma Cells to Cisplatin. *Cell Biol. Int.* 43 (11), 1245–1256. doi:10.1002/cbin.11121

Liu, W. L., Liu, T., Zou, M. Z., Yu, W. Y., Li, C. X., He, Z. Y., et al. (2018). Aggressive Man-Made Red Blood Cells for Hypoxia-Resistant Photodynamic Therapy. *Adv. Mater.* 30 (35), 1802006. doi:10.1002/adma.201802006

Liu, Y., Zhu, X., Lu, Y., Wang, X., Zhang, C., Sun, H., et al. (2019). Antigen-Inorganic Hybrid Flowers-Based Vaccines with Enhanced Room Temperature Stability and Effective Anticancer Immunity. *Adv. Healthc. Mater.* 8 (21), 1900660. doi:10.1002/adhm.201900660

Liu, Y.-H., Zang, X.-Y., Wang, J.-C., Huang, S.-S., Xu, J., and Zhang, P. (2019). Diagnosis and Management of Immune Related Adverse Events (irAEs) in Cancer Immunotherapy. *Biomed. Pharmacother.* 120, 109437. doi:10.1016/j.biopha.2019.109437

Louandre, C., Ezzoukhry, Z., Godin, C., Barbare, J.-C., Mazière, J.-C., Chauffert, B., et al. (2013). Iron-dependent Cell Death of Hepatocellular Carcinoma Cells Exposed to Sorafenib. *Int. J. Cancer* 133 (7), 1732–1742. doi:10.1002/ijc.28159

Louandre, C., Marcq, I., Bouhlal, H., Lachaier, E., Saidak, C. Z., François, C., et al. (2015). The Retinoblastoma (Rb) Protein Regulates Ferroptosis Induced by Sorafenib in Human Hepatocellular Carcinoma Cells. *Cancer Lett.* 356 (2), 971–977. doi:10.1016/j.canlet.2014.11.014

Lyu, C., Lu, G., Bao, W., Li, F., Wang, S., Zhang, F., et al. (2020). Engineering Magnetosomes with Chimeric Membrane and Hyaluronidase for Efficient Delivery of HIF-1 siRNA into Deep Hypoxic Tumors. *Chem. Eng. J.* 398, 125453. doi:10.1016/j.cej.2020.125453

Ma, M.-z., Chen, G., Wang, P., Lu, W.-h., Zhu, C.-f., Song, M., et al. (2015). Xc– Inhibitor Sulfasalazine Sensitizes Colorectal Cancer to Cisplatin by a GSH-dependent Mechanism. *Cancer Lett.* 368 (1), 88–96. doi:10.1016/j.canlet.2015.07.031

Ma, S., Henson, E. S., Chen, Y., and Gibson, S. B. (2016). Ferroptosis Is Induced Following Siramesine and Lapatinib Treatment of Breast Cancer Cells. *Cell Death Dis.* 7 (7), e2307. doi:10.1038/cddis.2016.208

Maleki Dizaj, S., Barzegar-Jalali, M., Zarrintan, M. H., Adibkia, K., and Lotfipour, F. (2015). Calcium Carbonate Nanoparticles as Cancer Drug Delivery System. *Expert Opin. Drug Deliv.* 12 (10), 1649–1660. doi:10.1517/17425247.2015.1049530

Mao, L.-B., Gao, H.-L., Yao, H.-B., Liu, L., Cölfen, H., Liu, G., et al. (2016). Synthetic Nacre by Predesigned Matrix-Directed Mineralization. *Science* 354 (6308), 107–110. doi:10.1126/science.aaf8991

Melancon, M. P., Zhou, M., and Li, C. (2011). Cancer Theranostics with Near-Infrared Light-Activatable Multimodal Nanoparticles. *Acc. Chem. Res.* 44 (10), 947–956. doi:10.1021/ar200022e

Mellor, A., and Soni, N. (2001). Fat Embolism. *Anaesthesia* 56 (2), 145–154. doi:10.1046/j.1365-2044.2001.01724.x

Min, K. H., Min, H. S., Lee, H. J., Park, D. J., Yhee, J. Y., Kim, K., et al. (2015). pH-Controlled Gas-Generating Mineralized Nanoparticles: A Theranostic Agent for Ultrasound Imaging and Therapy of Cancers. *ACS Nano* 9 (1), 134–145. doi:10.1021/nn506210a

Miyamoto, S., Martinez, G. R., Medeiros, M. H. G., and Di Mascio, P. (2003). Singlet Molecular Oxygen Generated from Lipid Hydroperoxides by the Russell Mechanism: Studies Using 18O-Labeled Linoleic Acid Hydroperoxide and Monomol Light Emission Measurements. *J. Am. Chem. Soc.* 125 (20), 6172–6179. doi:10.1021/ja029115o

Miyamoto, S., Martinez, G. R., Rettori, D., Augusto, O., Medeiros, M. H. G., and Di Mascio, P. (2006). Linoleic Acid Hydroperoxide Reacts with Hypochlorous Acid, Generating Peroxyl Radical Intermediates and Singlet Molecular Oxygen. *Proc. Natl. Acad. Sci.* 103 (2), 293–298. doi:10.1073/pnas.0508170103

Molinaro, R., Martinez, J. O., Zinger, A., De Vita, A., Storci, G., Arrighetti, N., et al. (2020). Leukocyte-mimicking Nanovesicles for Effective Doxorubicin Delivery to Treat Breast Cancer and Melanoma. *Biomater. Sci.* 8 (1), 333–341. doi:10.1039/c9bm01766f

Moyano, D. F., Liu, Y., Peer, D., and Rotello, V. M. (2016). Modulation of Immune Response Using Engineered Nanoparticle Surfaces. *Small* 12 (1), 76–82. doi:10.1002/smll.201502273

Ni, N., Su, Y., Wei, Y., Ma, Y., Zhao, L., and Sun, X. (2021). Tuning Nanosiliceous Framework for Enhanced Cancer Theranostic Applications. *Adv. Therap.* 4 (4), 2000218. doi:10.1002/adtp.202000218

Niu, W., Xiao, Q., Wang, X., Zhu, J., Li, J., Liang, X., et al. (2021). A Biomimetic Drug Delivery System by Integrating Grapefruit Extracellular Vesicles and Doxorubicin-Loaded Heparin-Based Nanoparticles for Glioma Therapy. *Nano Lett.* 21 (3), 1484–1492. doi:10.1021/acs.nanolett.0c04753

Noguchi, M., Minami, M., Yagasaki, R., Kinoshita, K., Earashi, M., Kitagawa, H., et al. (1997). Chemoprevention of DMBA-Induced Mammary Carcinogenesis in Rats by Low-Dose EPA and DHA. *Br. J. Cancer* 75 (3), 348–353. doi:10.1038/bjc.1997.57

Ou, W., Mulik, R. S., Anwar, A., McDonald, J. G., He, X., and Corbin, I. R. (2017). Low-density Lipoprotein Docosahexaenoic Acid Nanoparticles Induce Ferroptotic Cell Death in Hepatocellular Carcinoma. *Free Radic. Biol. Med.* 112, 597–607. doi:10.1016/j.freeradbiomed.2017.09.002

Pan, X., Lin, Z., Jiang, D., Yu, Y., Yang, D., Zhou, H., et al. (2019). Erastin Decreases Radioresistance of NSCLC Cells Partially by Inducing GPX4-mediated F-erroptosis. *Oncol. Lett.* 17 (3), 3001–3008. doi:10.3892/ol.2019.9888

Phillips, E., Penate-Medina, O., Zanzonico, P. B., Carvajal, R. D., Mohan, P., Ye, Y., et al. (2014). Clinical Translation of an Ultrasmall Inorganic Optical-PET Imaging Nanoparticle Probe. *Sci. Transl. Med.* 6 (260), 260ra149. doi:10.1126/scitranslmed.3009524

Roh, J.-L., Kim, E. H., Jang, H. J., Park, J. Y., and Shin, D. (2016). Induction of Ferroptotic Cell Death for Overcoming Cisplatin Resistance of Head and Neck Cancer. *Cancer Lett.* 381 (1), 96–103. doi:10.1016/j.canlet.2016.07.035

Roh, J.-L., Kim, E. H., Jang, H., and Shin, D. (2017). Nrf2 Inhibition Reverses the Resistance of Cisplatin-Resistant Head and Neck Cancer Cells to Artesunate-Induced Ferroptosis. *Redox Biol.* 11, 254–262. doi:10.1016/j.redox.2016.12.010

Sandra, F., Khaliq, N. U., Sunna, A., and Care, A. (2019). Developing Protein-Based Nanoparticles as Versatile Delivery Systems for Cancer Therapy and Imaging. *Nanomaterials* 9 (9), 1329. doi:10.3390/nano9091329

Sanmamed, M. F., and Chen, L. (2019). A Paradigm Shift in Cancer Immunotherapy: From Enhancement to Normalization. *Cell* 176 (3), 677. doi:10.1016/j.cell.2019.01.008

Senturk, T. (2010). Platelet Function in Inflammatory Diseases: Insights from Clinical Studies. *Iadt* 9 (5), 355–363. doi:10.2174/187152810793938026

Shao, F., Wu, Y., Tian, Z., and Liu, S. (2021). Biomimetic Nanoreactor for Targeted Cancer Starvation Therapy and cascade Amplificated Chemotherapy. *Biomaterials* 274, 120869. doi:10.1016/j.biomaterials.2021.120869

Shen, S., Jiang, D., Cheng, L., Chao, Y., Nie, K., Dong, Z., et al. (2017). Renal-Clearable Ultrasmall Coordination Polymer Nanodots for Chelator-Free 64Cu-Labeling and Imaging-Guided Enhanced Radiotherapy of Cancer. *ACS Nano* 11 (9), 9103–9111. doi:10.1021/acsnano.7b03857

Shen, Z., Song, J., Yung, B. C., Zhou, Z., and Chen, A. X. (2018). Emerging Strategies of Cancer Therapy Based on Ferroptosis. *Adv. Mater.* 30 (12), 1704007. doi:10.1002/adma.201704007

Shen, W.-T., Hsu, R.-S., Fang, J.-H., Hu, P.-F., Chiang, C.-S., and Hu, S.-H. (2020). Marginative Delivery-Mediated Extracellular Leakiness and T Cell Infiltration in Lung Metastasis by a Biomimetic Nanoraspberry. *Nano Lett.* 21 (3), 1375–1383. doi:10.1021/acs.nanolett.0c04122

Srivastava, P., Hira, S. K., Srivastava, D. N., Singh, V. K., Gupta, U., Singh, R., et al. (2018). ATP-decorated Mesoporous Silica for Biomineralization of Calcium Carbonate and P2 Purinergic Receptor-Mediated Antitumor Activity against Aggressive Lymphoma. *ACS Appl. Mater. Inter.* 10 (8), 6917–6929. doi:10.1021/acsami.7b18729

Stockwell, B. R., Friedmann Angeli, J. P., Bayir, H., Bush, A. I., Conrad, M., Dixon, S. J., et al. (2017). Ferroptosis: A Regulated Cell Death Nexus Linking Metabolism, Redox Biology, and Disease. *Cell* 171 (2), 273–285. doi:10.1016/j.cell.2017.09.021

Storm‡, T. L. S. A. W. E. H. G., and Kiessling†, F. (2011). Theranostic Nanomedicine. *Acc. Chem. Res.* 44 (10), 841. doi:10.1021/ar200019c

Sui, X., Zhang, R., Liu, S., Duan, T., Zhang, L. M., Han, X., et al. (2018). RSL3 Drives Ferroptosis through GPX4 Inactivation and ROS Production in Colorectal Cancer. *Front. Pharmacol.* 9, 1371. doi:10.3389/fphar.2018.01371

Sumer, B., and Gao, J. (2008). Theranostic Nanomedicine for Cancer. *Nanomedicine* 3 (2), 137–140. doi:10.2217/17435889.3.2.137

Sun, X., Ni, N., Ma, Y., Wang, Y., and Leong, D. T. (2020). Retooling Cancer Nanotherapeutics' Entry into Tumors to Alleviate Tumoral Hypoxia. *Small* 16 (41), 2003000. doi:10.1002/smll.202003000

Swamy, M. V., Citineni, B., Patlolla, J. M. R., Mohammed, A., Zhang, Y., and Rao, C. V. (2008). Prevention and Treatment of Pancreatic Cancer by Curcumin in Combination with Omega-3 Fatty Acids. *Nutr. Cancer* 60 (Suppl. 1), 81–89. doi:10.1080/01635580802416703

Torti, S. V., and Torti, F. M. (2013). Iron and Cancer: More Ore to Be Mined. *Nat. Rev. Cancer* 13 (5), 342–355. doi:10.1038/nrc3495

Truffi, M., Fiandra, L., Sorrentino, L., Monieri, M., Corsi, F., and Mazzucchelli, S. (2016). Ferritin Nanocages: A Biological Platform for Drug Delivery, Imaging and Theranostics in Cancer. *Pharmacol. Res.* 107, 57–65. doi:10.1016/j.phrs.2016.03.002

Tsoi, J., Robert, L., Paraiso, K., Galvan, C., Sheu, K. M., Lay, J., et al. (2018). Multi-stage Differentiation Defines Melanoma Subtypes with Differential Vulnerability to Drug-Induced Iron-Dependent Oxidative Stress. *Cancer Cell* 33 (5), 890–904. e895. doi:10.1016/j.ccell.2018.03.017

Wan, X., Song, L., Pan, W., Zhong, H., Li, N., and Tang, B. (2020). Tumor-Targeted Cascade Nanoreactor Based on Metal-Organic Frameworks for Synergistic Ferroptosis-Starvation Anticancer Therapy. *ACS Nano* 14 (9), 11017–11028. doi:10.1021/acsnano.9b07789

Wang, C., Chen, S., Wang, Y., Liu, X., Hu, F., Sun, J., et al. (2018). Lipase-Triggered Water-Responsive "Pandora's Box" for Cancer Therapy: Toward Induced Neighboring Effect and Enhanced Drug Penetration. *Adv. Mater.* 30 (14), 1706407. doi:10.1002/adma.201706407

Wang, Y., Yang, T., Ke, H., Zhu, A., Wang, Y., Wang, J., et al. (2015). Smart Albumin-Biomineralized Nanocomposites for Multimodal Imaging and Photothermal Tumor Ablation. *Adv. Mater.* 27 (26), 3874–3882. doi:10.1002/adma.201500229

Wang, C., Ye, Y., Hochu, G. M., Sadeghifar, H., and Gu, Z. (2016). Enhanced Cancer Immunotherapy by Microneedle Patch-Assisted Delivery of Anti-PD1 Antibody. *Nano Lett.* 16 (4), 2334–2340. doi:10.1021/acs.nanolett.5b05030

Wang, H., Wu, J., Williams, G. R., Fan, Q., Niu, S., Wu, J., et al. (2019). Platelet-membrane-biomimetic Nanoparticles for Targeted Antitumor Drug Delivery. *J. Nanobiotechnol.* 17 (1), 60. doi:10.1186/s12951-019-0494-y

Wang, W., Green, M., Choi, J. E., Gijón, M., Kennedy, P. D., Johnson, J. K., et al. (2019). CD8+ T Cells Regulate Tumour Ferroptosis during Cancer Immunotherapy. *Nature* 569 (7755), 270–274. doi:10.1038/s41586-019-1170-y

Wang, X., Wu, M., Zhang, X., Li, F., Zeng, Y., Lin, X., et al. (2021). Hypoxia-responsive Nanoreactors Based on Self-Enhanced Photodynamic Sensitization and Triggered Ferroptosis for Cancer Synergistic Therapy. *J. Nanobiotechnol.* 19 (1), 1–14. doi:10.1186/s12951-021-00952-y

Wang, J., Wang, Z., Zhong, Y., Zou, Y., Wang, C., Wu, H., et al. (2020). Central Metal-Derived Co-assembly of Biomimetic GdTPP/ZnTPP Porphyrin Nanocomposites for Enhanced Dual-Modal Imaging-Guided Photodynamic Therapy. *Biomaterials* 229, 119576. doi:10.1016/j.biomaterials.2019.119576

Wang, S., Li, F., Qiao, R., Hu, X., Liao, H., Chen, L., et al. (2018). Arginine-rich Manganese Silicate Nanobubbles as a Ferroptosis-Inducing Agent for Tumor-Targeted Theranostics. *ACS Nano* 12 (12), 12380–12392. doi:10.1021/acsnano.8b06399

Wang, S., Yang, X., Zhou, L., Li, J., and Chen, H. (2020). 2D Nanostructures beyond Graphene: Preparation, Biocompatibility and Biodegradation Behaviors. *J. Mater. Chem. B* 8 (15), 2974–2989. doi:10.1039/c9tb02845e

Weed, R. I., Reed, C. F., and Berg, G. (1963). Is Hemoglobin an Essential Structural Component of Human Erythrocyte Membranes? *J. Clin. Invest.* 42 (4), 581–588. doi:10.1172/JCI104747

Wehner, R., Dietze, K., Bachmann, M., and Schmitz, M. (2011). The Bidirectional Crosstalk between Human Dendritic Cells and Natural Killer Cells. *J. Innate Immun.* 3 (3), 258–263. doi:10.1159/000323923

Weissleder, R., and Pittet, M. J. (2008). Imaging in the Era of Molecular Oncology. *Nature* 452 (7187), 580–589. doi:10.1038/nature06917

Xie, W., Deng, W.-W., Zan, M., Rao, L., Yu, G.-T., Zhu, D.-M., et al. (2019). Cancer Cell Membrane Camouflaged Nanoparticles to Realize Starvation Therapy Together with Checkpoint Blockades for Enhancing Cancer Therapy. *ACS Nano* 13 (3), 2849–2857. doi:10.1021/acsnano.8b03788

Xu, Q., Ensign, L. M., Boylan, N. J., Schön, A., Gong, X., Yang, J.-C., et al. (2015). Impact of Surface Polyethylene Glycol (PEG) Density on Biodegradable Nanoparticle Transport in Mucus *Ex Vivo* and Distribution *In Vivo*. *ACS Nano* 9 (9), 9217–9227. doi:10.1021/acsnano.5b03876

Xu, T., Ma, Y., Yuan, Q., Hu, H., Hu, X., Qian, Z., et al. (2020). Enhanced Ferroptosis by Oxygen-Boosted Phototherapy Based on a 2-in-1 Nanoplatform of Ferrous Hemoglobin for Tumor Synergistic Therapy. *ACS Nano* 14 (3), 3414–3425. doi:10.1021/acsnano.9b09426

Xu, R., Yang, J., Qian, Y., Deng, H., Wang, Z., Ma, S., et al. (2021). Ferroptosis/pyroptosis Dual-Inductive Combinational Anti-cancer Therapy Achieved by Transferrin Decorated nanoMOF. *Nanoscale Horiz.* 6 (4), 348–356. doi:10.1039/d0nh00674b

Xuan, M., Shao, J., Dai, L., He, Q., and Li, J. (2015). Macrophage Cell Membrane Camouflaged Mesoporous Silica Nanocapsules for *In Vivo* Cancer Therapy. *Adv. Healthc. Mater.* 4 (11), 1645–1652. doi:10.1002/adhm.201500129

Xue, C.-C., Li, M.-H., Zhao, Y., Zhou, J., Hu, Y., Cai, K.-Y., et al. (2020). Tumor Microenvironment-Activatable Fe-Doxorubicin Preloaded Amorphous CaCO3 Nanoformulation Triggers Ferroptosis in Target Tumor Cells. *Sci. Adv.* 6 (18), eaax1346. doi:10.1126/sciadv.aax1346

Yan, H.-f., Zou, T., Tuo, Q.-z., Xu, S., Li, H., Belaidi, A. A., et al. (2021). Ferroptosis: Mechanisms and Links with Diseases. *Sig Transduct Target. Ther.* 6 (1), 49. doi:10.1038/s41392-020-00428-9

Yang, K., Feng, L., and Liu, Z. (2016). Stimuli Responsive Drug Delivery Systems Based on Nano-Graphene for Cancer Therapy. *Adv. Drug Deliv. Rev.* 105, 228–241. doi:10.1016/j.addr.2016.05.015

Yang, X., Yang, Y., Gao, F., Wei, J.-J., and Sun, C.-G. M.-J. (2019). Biomimetic Hybrid Nanozymes with Self-Supplied H+ and Accelerated O2 Generation for Enhanced Starvation and Photodynamic Therapy against Hypoxic Tumors. *Nano Lett.* 19 (7), 4334–4342. doi:10.1021/acs.nanolett.9b00934

Yang, Z., Du, Y., Sun, Q., Peng, Y., Wang, R., Zhou, Y., et al. (2020). Albumin-Based Nanotheranostic Probe with Hypoxia Alleviating Potentiates Synchronous Multimodal Imaging and Phototherapy for Glioma. *ACS Nano* 14 (5), 6191–6212. doi:10.1021/acsnano.0c02249

Yang, J., Ma, S., Xu, R., Wei, Y., Zhang, J., Zuo, T., et al. (2021). Smart Biomimetic Metal Organic Frameworks Based on ROS-Ferroptosis-Glycolysis Regulation for Enhanced Tumor Chemo-Immunotherapy. *J. Controlled Release* 334, 21–33. doi:10.1016/j.jconrel.2021.04.013

Yang, R. Z., Xu, W. N., Zheng, H. L., Zheng, X. F., Li, B., Jiang, L. S., et al. (2021). Involvement of Oxidative Stress-induced Annulus Fibrosus Cell and Nucleus Pulposus Cell Ferroptosis in Intervertebral Disc Degeneration Pathogenesis. *J. Cel. Physiol.* 236 (4), 2725–2739. doi:10.1002/jcp.30039

Ye, H., Wang, K., Wang, M., Liu, R., Song, H., Li, N., et al. (2019). Bioinspired Nanoplatelets for Chemo-Photothermal Therapy of Breast Cancer Metastasis Inhibition. *Biomaterials* 206, 1–12. doi:10.1016/j.biomaterials.2019.03.024

Ye, L. F., Chaudhary, K. R., Zandkarimi, F., Harken, A. D., Kinslow, C. J., Upadhyayula, P. S., et al. (2020). Radiation-Induced Lipid Peroxidation Triggers Ferroptosis and Synergizes with Ferroptosis Inducers. *ACS Chem. Biol.* 15 (2), 469–484. doi:10.1021/acschembio.9b00939

Yoon, H. Y., Selvan, S. T., Yang, Y., Kim, M. J., Yi, D. K., Kwon, I. C., et al. (2018). Engineering Nanoparticle Strategies for Effective Cancer Immunotherapy. *Biomaterials* 178, 597–607. doi:10.1016/j.biomaterials.2018.03.036

Yu, Y., Xie, Y., Cao, L., Yang, L., Yang, M., Lotze, M. T., et al. (2015). The Ferroptosis Inducer Erastin Enhances Sensitivity of Acute Myeloid Leukemia Cells to Chemotherapeutic Agents. *Mol. Cell Oncol.* 2 (4), e1054549. doi:10.1080/23723556.2015.1054549

Yu, Z., Zhou, P., Pan, W., Li, N., and Tang, B. (2018). A Biomimetic Nanoreactor for Synergistic Chemiexcited Photodynamic Therapy and Starvation Therapy against Tumor Metastasis. *Nat. Commun.* 9 (1), 5044. doi:10.1038/s41467-018-07197-8

Yuan, P., Dou, G., Liu, T., Guo, X., Bai, Y., Chu, D., et al. (2021). On-demand Manipulation of Tumorigenic Microenvironments by Nano-Modulator for Synergistic Tumor Therapy. *Biomaterials* 275, 120956. doi:10.1016/j.biomaterials.2021.120956

Zhang, C., Zhang, L., Wu, W., Gao, F., Li, R. Q., Song, W., et al. (2019). Artificial Super Neutrophils for Inflammation Targeting and HClO Generation against Tumors and Infections. *Adv. Mater.* 31 (19), 1901179. doi:10.1002/adma.201901179

Zhang, X., Sui, S., Wang, L., Li, H., Zhang, L., Xu, S., et al. (2020). Inhibition of Tumor Propellant Glutathione Peroxidase 4 Induces Ferroptosis in Cancer Cells and Enhances Anticancer Effect of Cisplatin. *J. Cel. Physiol.* 235 (4), 3425–3437. doi:10.1002/jcp.29232

Zhang, F., Li, F., Lu, G.-H., Nie, W., Zhang, L., Lv, Y., et al. (2019). Engineering Magnetosomes for Ferroptosis/Immunomodulation Synergism in Cancer. *ACS Nano* 13 (5), 5662–5673. doi:10.1021/acsnano.9b00892

Zhang, K., Meng, X., Yang, Z., Cao, Y., Cheng, Y., Wang, D., et al. (2019). Cancer Cell Membrane Camouflaged Nanoprobe for Catalytic Ratiometric Photoacoustic Imaging of MicroRNA in Living Mice. *Adv. Mater.* 31 (12), 1807888. doi:10.1002/adma.201807888

Zhang, L., Wang, Z., Zhang, Y., Cao, F., Dong, K., Ren, J., et al. (2018). Erythrocyte Membrane Cloaked Metal-Organic Framework Nanoparticle as Biomimetic Nanoreactor for Starvation-Activated Colon Cancer Therapy. *ACS Nano* 12 (10), 10201–10211. doi:10.1021/acsnano.8b05200

Zhang, X., Wang, J., Chen, Z., Hu, Q., Wang, C., Yan, J., et al. (2018). Engineering PD-1-Presenting Platelets for Cancer Immunotherapy. *Nano Lett.* 18 (9), 5716–5725. doi:10.1021/acs.nanolett.8b02321

Zhao, Y., Luo, Z., Li, M., Qu, Q., Ma, X., Yu, S.-H., et al. (2015). A Preloaded Amorphous Calcium Carbonate/Doxorubicin@Silica Nanoreactor for pH-Responsive Delivery of an Anticancer Drug. *Angew. Chem. Int. Ed.* 54 (3), 919–922. doi:10.1002/anie.201408510

Zhao, H., Li, L., Zhang, J., Zheng, C., Ding, K., Xiao, H., et al. (2018). C-C Chemokine Ligand 2 (CCL2) Recruits Macrophage-Membrane-Camouflaged Hollow Bismuth Selenide Nanoparticles to Facilitate Photothermal Sensitivity and Inhibit Lung Metastasis of Breast Cancer. *ACS Appl. Mater. Inter.* 10 (37), 31124–31135. doi:10.1021/acsami.8b11645

Zhao, Y., Xiao, X., Zou, M., Ding, B., Xiao, H., Wang, M., et al. (2021). Nanozyme-Initiated *In Situ* Cascade Reactions for Self-Amplified Biocatalytic Immunotherapy. *Adv. Mater.* 33 (3), 2006363. doi:10.1002/adma.202006363

Zhen, X., Cheng, P., and Pu, K. (2019). Recent Advances in Cell Membrane-Camouflaged Nanoparticles for Cancer Phototherapy. *Small* 15 (1), 1804105. doi:10.1002/smll.201804105

Zhou, Z., Song, J., Tian, R., Yang, Z., Lin, G. L., Zhang, G., et al. (2017). Activatable Singlet Oxygen Generation from Lipid Hydroperoxide Nanoparticles for Cancer Therapy. *Angew. Chem. Int. Ed.* 56 (23), 6492–6496. doi:10.1002/anie.201701181

Zhou, H.-H., Chen, X., Cai, L.-Y., Nan, X.-W., Chen, J.-H. X.-X., Yang, Y., et al. (2019). Erastin Reverses ABCB1-Mediated Docetaxel Resistance in Ovarian Cancer. *Front. Oncol.* 9, 1398. doi:10.3389/fonc.2019.01398

Conflict of Interest: The authors declare that the research was conducted in the absence of any commercial or financial relationships that could be construed as a potential conflict of interest.

Publisher's Note: All claims expressed in this article are solely those of the authors and do not necessarily represent those of their affiliated organizations, or those of the publisher, the editors, and the reviewers. Any product that may be evaluated in this article, or claim that may be made by its manufacturer, is not guaranteed or endorsed by the publisher.

frontiers in Chemistry

REVIEW
published: 18 November 2021
doi: 10.3389/fchem.2021.768007

Surface Treatment and Bioinspired Coating for 3D-Printed Implants

Junyi Liu†, *Nafisah Bte Mohd Rafiq*†, *Lai Mun Wong and Shijie Wang**

*Institute of Materials Research and Engineering (IMRE), A*STAR (Agency for Science, Technology and Research), Singapore, Singapore*

Three-dimensional (3D) printing technology has developed rapidly and demonstrates great potential in biomedical applications. Although 3D printing techniques have good control over the macrostructure of metallic implants, the surface properties have superior control over the tissue response. By focusing on the types of surface treatments, the osseointegration activity of the bone–implant interface is enhanced. Therefore, this review paper aims to discuss the surface functionalities of metallic implants regarding their physical structure, chemical composition, and biological reaction through surface treatment and bioactive coating. The perspective on the current challenges and future directions for development of surface treatment on 3D-printed implants is also presented.

Keywords: surface treatment, bioactive coating, hydroxyapatite, bioglass, micro-arc oxidation, 3D printing, osseointegration, metallic implant

OPEN ACCESS

Edited by:
Ruixue Duan,
Soochow University, China

Reviewed by:
Jingchao Li,
Donghua University, China
Qingqing Miao,
Soochow University, China

***Correspondence:**
Shijie Wang
sj-wang@imre.a-star.edu.sg

†*These authors have contributed equally to this work*

Specialty section:
This article was submitted to Nanoscience, a section of the journal Frontiers in Chemistry

Received: *31 August 2021*
Accepted: *22 September 2021*
Published: *18 November 2021*

Citation:
Liu J, Mohd Rafiq NB, Wong LM and Wang S (2021) Surface Treatment and Bioinspired Coating for 3D-Printed Implants. Front. Chem. 9:768007. doi: 10.3389/fchem.2021.768007

INTRODUCTION

In recent years, three-dimensional (3D) printing, also known as additive manufacturing (AM), has become an apparent choice for manufacturing technology. The manufacturing process is a bottom–up approach where raw materials are deposited layer-by-layer into a 3D object (Rayna and Striukova, 2016). The concept of 3D printing was first originated as rapid prototyping around the mid-1980s by Charles Hull (Bagaria et al., 2018). The first commercial 3D printing started with plastic, and by the mid-1990s metals had gained similar commercialization use (Duda and Raghavan, 2016). The ability to save cost, design complex shapes, and reduce waste are encouraging engineers and designers to tap into this technological capability (Vaz and Kumar, 2021). In addition, the new focus is currently channeling production of a new product design rather than choosing between AM and traditional manufacturing. 3D printing enables an effective buy-to-fly ratio reaching to equivalence, whereas conventional methods observed a 20-fold increase. A significant variation is observed due to raw materials cost, manufacturing processes, and other manufacturing-related logistics (Duda and Raghavan, 2016). This promising realization of 3D printing has since been implemented in production lines, particularly in automotive, aerospace, and medical industries, as recorded in many publications (Alison et al., 2019; Ni et al., 2019; Capasso et al., 2020).

Besides the promising attributes of 3D printing, a drawback is also commonly identified and associated with its undesirable esthetic build. Consequently, suffering from mechanical malfunction and lack of stability leads to poor performance across wide medical applications. Henceforth, this review serves to understand the various treatment methods from a biomedical point of view, mainly through understanding: 1) implant substrate parametrics such as surface uniformity, topography, wettability, and porosity, and 2) the integration of bioactive molecules and growth factor receptors to encourage key cellular activities.

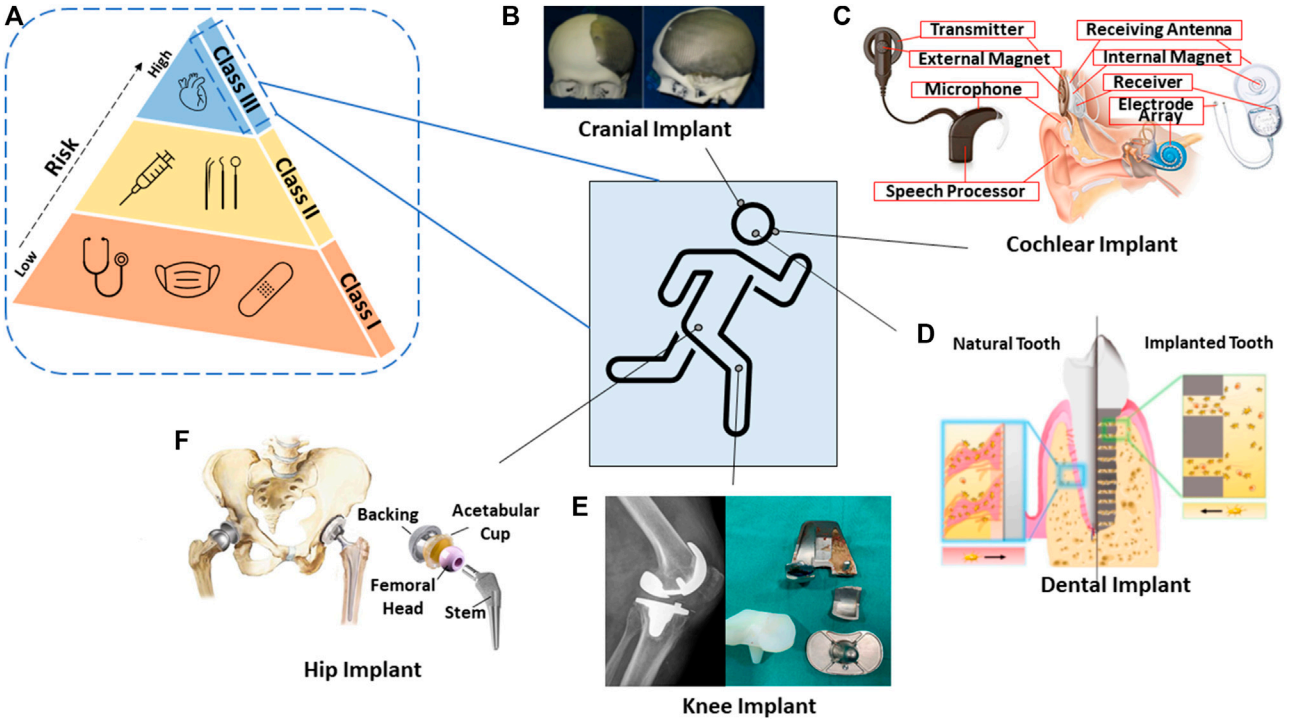

FIGURE 1 | Schematic diagram of the **(A)** risk associated within FDA-classified medical devices; and some graphics of 3D-printed biomedical applications in the human body system. **(B)** Cranial implant (Jardini et al., 2016). **(C)** Cochlear implant (Brand et al., 2014). **(D)** Dental implant (Yin et al., 2021). **(E)** Knee implant (Chithartha et al., 2020). **(F)** Hip implant (Mattei et al., 2011).

Surface treatment is commonly coupled together with bioactive coating to achieve long-term implant stability, biocompatibility, and antibacterial surface protection. Despite many surface modification methods being discovered over the last decade, with many reviews translating experimental results into a limited set of stand-alone methods, there is no concise observed relationship between the range of biomedical metallic materials and surface modification methods. This, therefore, questions the applicability of metallic materials in performing and achieving similar outcomes across various surface methods, and likewise in the reverse. This paper also aims to widen the opportunity for cross-functional coating in maximizing the likelihood of implant survival.

3D Printing Usage in Medical Application

Medical material development has been prominent over the past three decades. Throughout this time, the most notable materials used were ceramics due to their similar constituents to the human body, for example, the bone-regeneration constituent containing calcium phosphate that can be easily reproduced (Best et al., 2008). Ceramic material is categorized as bioinert or bioactive and shows strong interfacial bonding to the host tissue and osseointegration capability compared to other material classification. When it comes to medical device classification, it is subdivided into three categories implemented by the Food and Drug Administration (FDA). These are Class I, II, and III, with the latter being described as high risk to the human body, as illustrated in **Figure 1**; therefore, safety measures are adopted and required to be approved prior to mass release to the public (Johnson, 2016).

In the past, there were no systematic guidelines being introduced for materials, such as metallic, ceramic, and polymer, that could be considered for commercial biomedical devices. This resulted in more than 700 deaths and 10,000 patient injuries (Dhruva and Redberg, 2013). As the framework became gradually implemented, likewise for 3D-printed devices, similar validation and specific requirements such as design and quality control strategies came to be utilized, resulting in controlled output and consistent production of the devices (Morrison et al., 2015). Within the European Union (EU), custom-made implants, which are intended to penetrate beneath the epithelial layer such as contact lenses or devices embedded inside the body, require CE marking and have to abide by regulation (Aimar et al., 2019).

To fabricate parts of complex and intricate structures to fit nicely on the patient, for example, skull reconstruction, traditional ways involving mesh implant insertion limit dimensional precision and structural integrity. Therefore, 3D printing has an upper hand when it comes to designing complex structures which allow successful integration to the host tissue. Particularly, in 3D-printed dental implants, the flexibility of tuning micropore channel architecture consequently facilitates signaling molecules to be activated at specific sites. This is useful in recruiting cells and maintaining

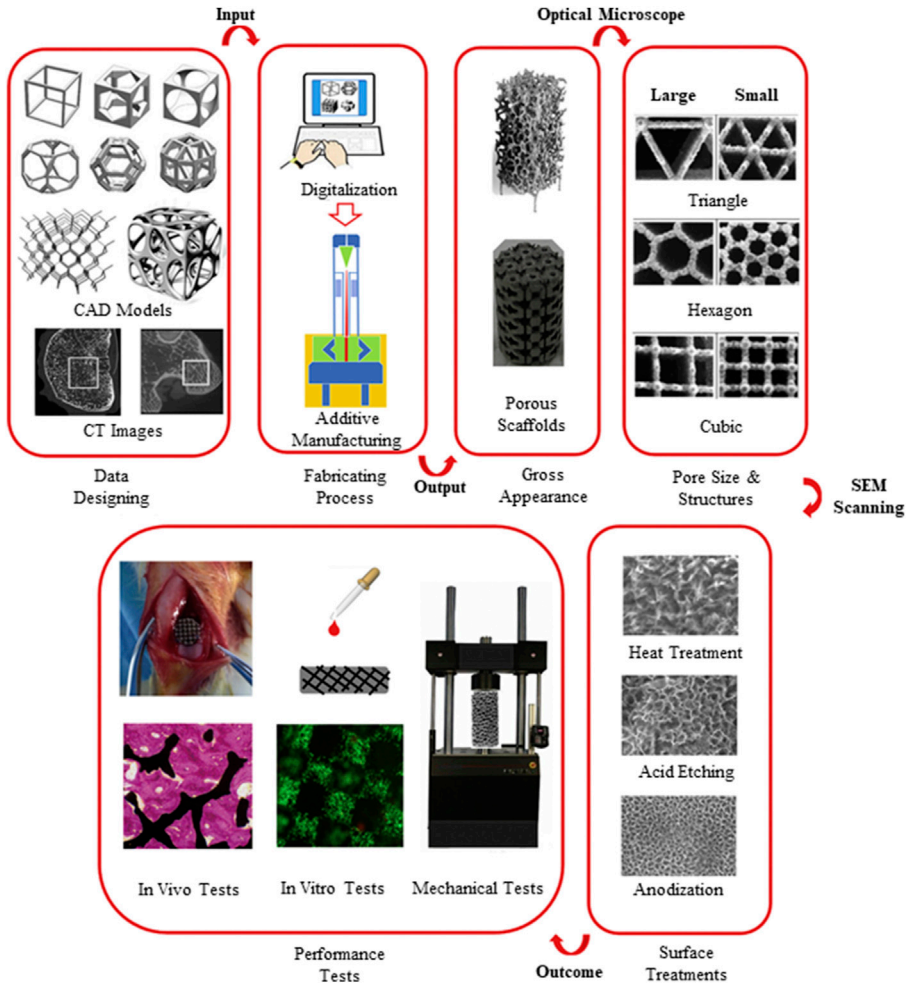

FIGURE 2 | A step-by-step approach of design control and performance evaluation to achieve successful fabrication of a 3D-printed biomedical implant (Wang et al., 2017).

alveolar height in a dental implant for better healing ability (Yin et al., 2021). The absence of surface treatment in the earlier period of pacemaker implant invention that revolves around metallic material, such as stainless steel, caused challenging mechanical fracture to its "pacemaker lead," eventually causing declining electrical stimulus. Many attempts have been made to replace the metallic alloy component, but no sign of improvement has been observed aside from more issues, including those related to corrosion (Joung, 2013). There are many significant benefits surrounding 3D printing as mentioned in many articles from its customization (Attarilar et al., 2020) to being cost effective (Schubert et al., 2014), and being ready-built in several hours (Mertz, 2013). Specifically, healthcare professionals use 3D printing to engage with patients via software, such as MIMICS or MeDraw, without requiring engineering expertise to develop and analyze models (Dai and Xu, 2021). Through 3D printing, anatomical models serve to minimize design error on patients and provide extensive practice to physicians prior to surgical procedures. As a result, this provides direct communication between physicians and patients to translate CT/MRI scans beyond a two-dimensional layout when treating life-threatening disease. This multidimensional function of 3D printing thus tackles medical issues effectively and efficiently while reducing the long waiting lists for treatment (Aimar et al., 2019). Another point that is not often emphasized or is overlooked is the open-source nature of the 3D printing files which allows vast collaboration among researchers and physicians more than just restrictive parameters published in scientific journals. The open-source database allows professionals to selectively tailor design dimensions according to the anatomical model of patients (Gross et al., 2014; Ventola, 2014). To a greater degree, open-source sharing of 3D models in the STL (Standard Tessellation Language or STereoLithography) file format has been proactively used in the immunology field, such as in the tiny replicas of microorganisms to visualize proteins and viruses (Coakley et al., 2014). In short, the importance of 3D printing has extended across vast medical applications from operation planning, as instrument guides to implant devices, and even in the field of microorganisms (Dai and Xu, 2021).

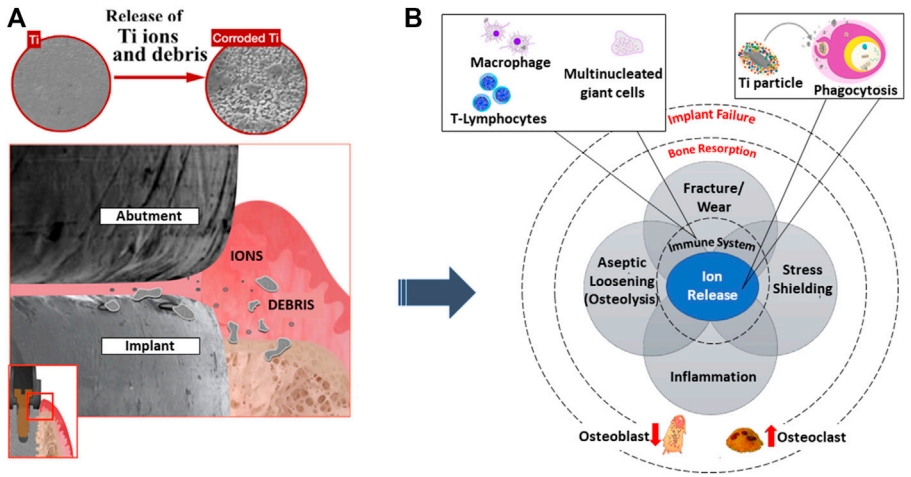

FIGURE 3 | (A) The start of foreign ions leaching, adversely affecting **(B)** immune response activities leading to bone resorption and implant failure. Image remodeled from Souza et al. (2020).

A typical procedure of a bottom–up 3D printing approach has been illustrated by Wang et al. (2017) (**Figure 2**). Particularly in orthopedic application, there are drawbacks in manufacturing porous implants using conventional methods which subsequently lead to implant failure due to lack of bone–implant integration. Depending on the final medical device customization and mechanical profile desired, a variety of surface modification techniques can be adopted, which are explored more in the Surface Modification Techniques section.

Engineering Constraints within Metallic Biomaterials

Metallic bio-devices can be divided into degradable and nondegradable types. A degradable metallic material, such as magnesium alloy, has bioactive capability and interfacial interaction between implant and tissue. The ability to degrade is preferred for temporary implant support such as plates and screws in bone healing, thereupon eliminating the unwanted surgical risk and excessive cost of a second surgery (Gu et al., 2014). By contrast, a nondegradable metallic material is classified as bioinert through the formation of a tissue fibrous capsule which isolates the implant from the surrounding tissues; however, the process does not trigger adverse interference to the biological system to a certain extent (Daghighi et al., 2013). A suitable implant can be either bioinert or bioactive as long as it does not induce toxicity. In principle, a material serving as an implant in the human body must ensure biocompatibility to the host tissue. In the medical field, the commonly used materials for orthopedic application are comprised of titanium alloy (Xiu et al., 2016), cobalt chromium alloy, and stainless steel (Balazic and Kopac, 2007), which are also categorized as nondegradable materials.

The strength-to-weight ratio of titanium alloy and magnesium alloy demonstrates similar mechanical capability to the bone, consequently exhibiting good biological integration. However, when it comes to clinical capability, these alloys tend to suffer from accelerated corrosion rate and poor cell viability when in contact with human body fluids (Kazantseva, 2018; Zhang et al., 2019; Atrens et al., 2020).

Metals are known to corrode easily but some are more resistant. This is due to the formation of a passivation layer that hinders corrosion from taking place. In general, most metals have low corrosion resistance when compared to noble metals such as gold and silver. When in contact with tissue, due to the oxygen diffusion limit contributed by the fast leakage of metal ions in the body, these ions create a high toxicity level, thereby causing adverse effects to the cells (Steinemann, 1998), as shown in **Figure 3A**. Corrosion is a common phenomenon and can be avoided through surface oxide modification. A study was conducted to identify cell proliferation between bare titanium alloy and cobalt chromium alloy against hydroxyapatite-coated metallic alloys. It was shown that there was a significant increase in cell viability when being coated (Yuan et al., 2018).

When an implant to the body is inevitable to save one's life, one needs to seriously examine the possibility of an adverse reaction of the implant to the body. **Figure 4** shows the tissue responsive effect on various common metallic implant materials. It was evident that metallic implants such as cobalt (Co), titanium (Ti) alloys, and iron (Fe) show a relatively similar polarization resistance. Yet, the contrast within tissue destruction is clear for cobalt-based materials. Depending on the implant application, careful consideration must be taken into account for any element that reacts adversely to the human body, since corrosion is also an atomic process and there is a risk of toxicity flowing into the bloodstream (Steinemann, 1998).

Stress shielding is a common phenomenon that takes place when stiffness of a metallic material exceeds the bone mechanical ability. This induces bone resorption which prevents bone growth in accordance with Wolff's law. One way to maneuver away from this issue is by designing a solid implant into the porous architecture (Carpenter et al., 2018). Titanium alloy can be fabricated into porous architecture especially for dental

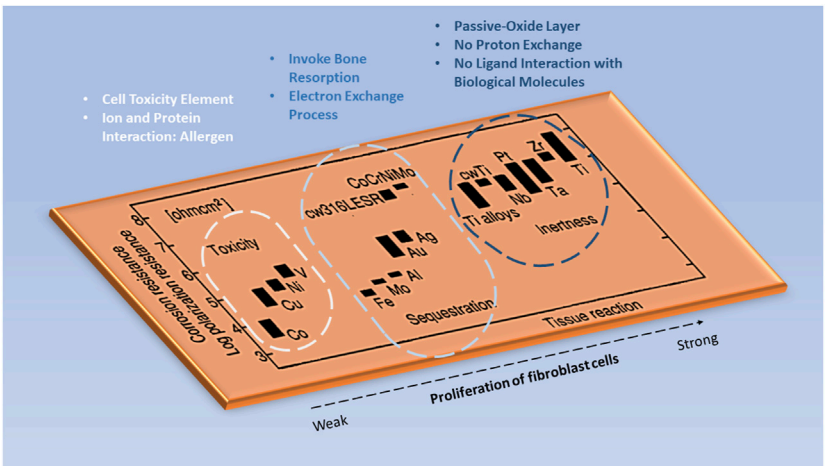

FIGURE 4 | The tissue responsive effect on various metallic elements in the implant. Image remodeled from Steinemann (1998).

implants, while still maintaining its physiochemical properties thereafter, inducing deep bone integration in the implant (osseointegration) rather than just an interfacial bond. Consequently, avoiding stress shielding as a whole prevents future implant failure (Pałka and Pokrowiecki, 2018).

In addition, titanium is known to be dangerous for casting due to metal fuming and internal oxidation processes. Hence in the traditional way, it is fabricated and machined into the desired shape of an implant (Lütjering and Williams, 2007). Through 3D printing, the mechanical aspect of titanium (low modulus, high specific strength, and low density) can be preserved leading to biocompatibility (Matassi et al., 2013). However, pure titanium is normally avoided in bone implants for load bearing due to its low yield and tensile strength (Pałka and Pokrowiecki, 2018).

Implant failure can be due to several reasons: aseptic loosening, wear, and bacterial infection (Kong et al., 2018), as illustrated in **Figure 3B**. A study was conducted by Sailer et al. (2009) gathering the percentage of metal components undergoing failure or complication. It was reported that close to 50% was caused by fracture and 24% was due to corrosion. Therefore, emphasis on early surface treatment of implants is ideal to promote successful implantation to the biological system. For example, coating such as a titanium nanotube has an antimicrobial effect which promotes osteoblast formation on the implant surface (Wang and Tang, 2019). Since a titania surface exhibits bioinert behavior when surrounding a biological environment, the physical and chemical characteristics must be restructured. The formation of nanotubular structures promotes strong mechanical interlocking to bone cells as compared to a microstructure surface. As such, the key cellular activities progress while bacterial adherence declines. The inhibition of bacteria is crucial which can result in antibiotic resistance through biofilm formation. In addition, it is reported that through the fabrication process of specific nanotubes with diameters of 30 and 80 nm, a rough surface and low water contact angle are established, eventually aiding cell growth. Likewise, the chemical compositions of oxygen and fluorine are shown to induce both cell adherence and antibacterial ability (Peng et al., 2013).

INTERFACIAL BOND: FROM MICRO-CELLULAR TO MACRO-METALLIC SUBSTRATES

When it comes to medical device design, it is imperative to consider the interaction of the material with the body system at the nano level as shown in **Figure 5A**. The process of osseointegration involves several complex chains of events. During the initial implantation stage, inflammatory cells such as monocytes, lymphocytes, and granulocytes of the white blood cells (WBCs) first arrive to aid in the healing process around the wound site as observed from a microscale perspective. The major constituents of the blood are plasma, platelets, red blood cells, and WBCs. Many proteins from the blood which are associated with the host inflammatory response, interact with the implant surface when released. However, cells require an intermediate layer to induce successful cell attachment on the implant surface. At the nanoscale, this layer consists of adsorbed water molecules, followed by protein and lipid receptors from the blood, promoting cell attachment on the implant surface. Similarly, the blood platelets release molecules who facilitate formation of fibrin clots which induce migration of mesenchymal stem cells (MSCs). The MSCs have a self-renewal capability which can be differentiated into specialized cells, for example, osteoblasts for bone formation (Gittens et al., 2014). In short, protein adsorption plays a primary role in signaling cell attachment whereby active inflammatory cells such as monocytes, lymphocytes, and granulocytes are actively engaged in the healing process (Onuki et al., 2008), thereafter aiding in the whole bone mechanism of osteoconduction, osteoinduction, and osteogenesis activities (Albrektsson and Johansson, 2001).

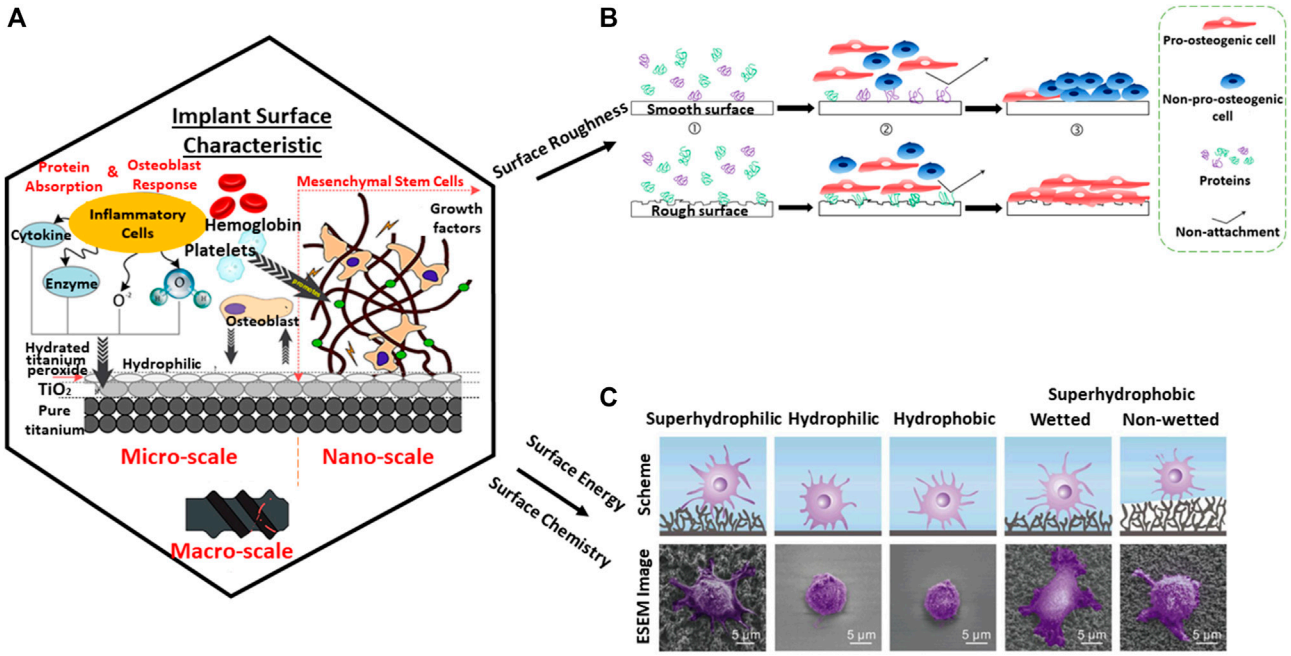

FIGURE 5 | Protein adsorption on the substrate from **(A)** nano-to-macro level which is dependent on several factors. **(B)** Surface roughness (Stich et al., 2021). **(C)** Surface chemistry and surface energy (Meng et al., 2017). Diagram adapted and adjusted from Alipal et al. (2021).

The surface of smooth implants has been studied and exhibits an anti-adhesion bond with biological tissue, in contrast to porous implants with better osseointegration capability (Zhang et al., 2014). However, porous implants are complex to fabricate. By conventional methods, fabricating implants of intricate pore structure is challenging due to manufacturing limitations. This can arise from inconsistent dimension tolerance, cost, and time. Likewise, pre-shaped implants may not suit every anatomical model of the patient, hence also causing uneven stress distribution leading to implant failure (Takemoto et al., 2005). Consequently, 3D printing becomes handy in tackling this gap and building a bridge between manufacturing and clinical trials.

Physiochemical Properties of Implants

Surface roughness, topography, wettability, and chemical composition are crucial to stimulate biocompatibility at the cellular level and interfacial bonding to the metal substrate (Tiainen et al., 2019). Surface roughness is an integral part of a material to allow bone and material interfacial bonding growth by interlocking cells to a material. It is widely known that a smooth surface provides poor stability to an implant as observed in **Figure 5B**. With surface roughness, osteoblast adsorption is observed which inhibits the osteoclast signal. As a result, full bone deposition is easily observed on the surface (Zhang et al., 2014). However, when it comes to high load-bearing application, surface roughness may pose an issue leading to high cycle fatigue. Osteolysis can occur when bonding strength within implanted bodies loosens thereafter leading to toxic ions leaching, especially when it comes to metallic elements such as cobalt (Wang et al., 2017).

Moreover, due to the lack of natural bone constituents such as bioglass and hydroxyapatite (HA) which form good chemical bonding to the bone, a metallic titanium implant in contrast has poor osseointegration and osteoinductive properties (Steinemann, 1998). It is also worth noting that despite bioceramic materials having similar bone constituents, it does not mean that they will form interfacial bonding with the bone. The key influence is heavily reliant on surface topography—the presence of surface pores hence allowing interlocking of bone cells (Davies, 2007). Similarly, a nonbonding biomaterial such as titania surfaces have the ability for bone bonding (Takatsuka et al., 1995). In hindsight, medical implants must be paired with both microstructure and macrostructure properties to achieve successful tissue integration. The surface chemical-wettability and surface energy of a contact angle below 90° at the microlevel allow for better protein adsorption and subsequently cell attachment (**Figure 5C**). From the macro-level, the pore-related parameters provide pathways for vascularization and space for bone tissue growth (Song et al., 2019).

Despite 3D printing having multiple prospects, the primary use of 3D printing over traditional manufacturing methods, especially in the medical field, is the ability to print complex lattice structural cells in precise dimensions (Wang et al., 2017). It has been mentioned that a topological feature acts as a stress distributor influencing the mechanical capability by withstanding loads; in particular, the octet truss design has shown superior results compared to other cellular structures (Parthasarathy et al., 2011), whereas triple periodic minimal surfaces promote trabecular bone simulation (Fantini et al., 2017).

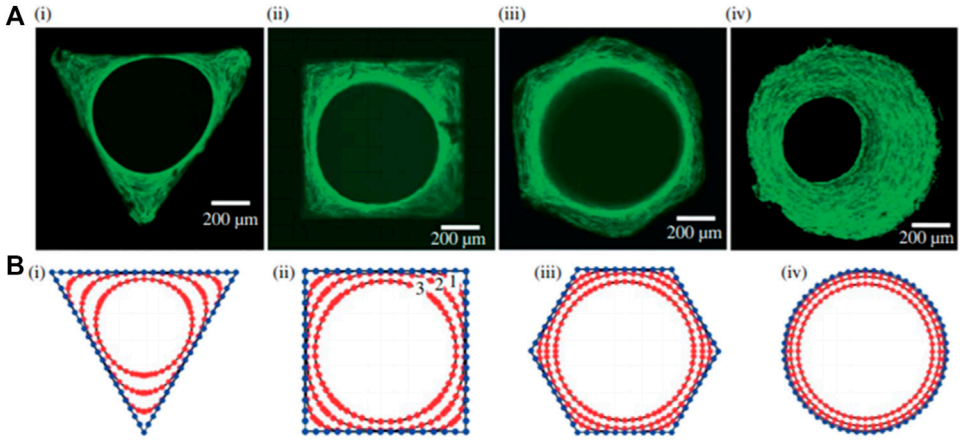

FIGURE 6 | A study on cell interaction and cell-growth concentration as pore shape changes. Reproduced from Rumpler et al. (2008).

Structural Properties of Implants

Porosity, pore interconnectivity, pore shape, and pore size are essential aspects for the functionality of a built implant, influencing the success rate of 3D printing in a biological system. Porous titanium alloy has a comparable Young's modulus to bone which does not trigger bone resorption as compared to other metallic implants. It is reported that poor bone ingrowth leads to implant loosening, henceforth tackling osseointegration bonding between bone tissue and an implant is vital (Wang et al., 2017; Pałka and Pokrowiecki, 2018). To achieve successful implantation, porous metallic implants should rejuvenate the function of the bone and promote regeneration of the damaged tissues. This is possible by establishing biocompatibility of materials with the living organism, adequate mechanical properties for load-bearing applications, and avoidance of stress shielding, since porosity influences compressive strength and elastic modulus which aid key cellular activities, such as cell adhesion, proliferation, and differentiation (Hrabe et al., 2013).

Although porosity is crucial, it is worth noting that bone ingrowth can be hindered without interconnected pore capability. With porosity, bone cells can penetrate, adhere, and encapsulate the pore structure to provide strong bone mechanisms (Takemoto et al., 2005). Adequate porosity with interconnecting pores allows formation of vascularization as a transport pathway for nutrient diffusion and metabolic waste, which help functional key cellular activities and tissue survival (Karande et al., 2004; Pałka and Pokrowiecki, 2018).

High surface-area-to-volume ratio, pore shape, and pore size are essential for cell attachment and growth. In a study by Mankani et al. (2001), it was observed that HA particles of 100–250 μm showed astounding bone growth, yet those smaller or larger than the critical size tended to show decreased bone formation. Interestingly, it was also noted that flat-sided particles showed no bone formation. It was also concluded that it was unclear how particle size and pore size could be interrelated, but it is hypothesized that the space between the particles will act as a gap indicating that pore size plays a role within bone formation. Subsequently, with the success of controlling printing design for pore sizes and shapes, 3D printing has provided flexibility for designers and engineers to adapt the mechanical behavior of bone tissue accordingly (Hrabe et al., 2013).

In an article by Rumpler et al. (2008), pores of high curvature (rounded corners) displayed more tissue growth as shown in **Figure 6**. The growth is reasoned by cell–cell neighboring interaction arising from mechanical forces, stimulating physical surface tension. High cell concentration is realized at the surface of high force. Although there is more work to be done to prove the research work, multiple articles have concluded or observed cell proliferation at the curvature as compared to other areas.

SURFACE MODIFICATION TECHNIQUES

Both surface treatment and bioactive coating have been extensively studied for their tribological properties in implants and have been recommended for use in the orthopedic field. While 3D printing allows fabrication of porous architecture, a challenge is faced in tuning surface properties to attain osseointegration with the bone, especially in metallic implants where commonly used materials such as titanium alloy are bioinert (Hwang and Choe, 2018). The release of toxic ions (Al and V) in the titanium alloy poses an actual risk to the biological system, and it is therefore essential to have a dense coating to hinder any ion leakage. Since the benefit of the titanium alloy outweighs the risk, by fine-tuning the material through the formation of a dense oxide film on its exterior or additional surface modification, an unfavorable reaction from the as-printed 3D printing products can be prevented (Song et al., 2019).

Surface Treatment

The commonly used surface treatment techniques for bio-implants such as micro-arc oxidation (MAO), laser surface texturing (LST), chemical etching, and alkali–heat treatment

TABLE 1 | Summary of the bioceramic coating method and its limitation.

Method	Material	Process	Advantage	Limitation	Reference
Micro-arc oxidation	Ti6Al4V	Electrodes: Ti/stainless steel Electrolyte: 0.065 M calcium acetate, 0.03 M monosodium phosphate, 0.065 M EDTA-2Na, 0.5 M sodium hydroxide, bath temperature at 40°C Voltage: 350 V for 5 min	Homogenous oxide film layer, antibacterial and bone-forming cells capability	A few microcracks	Xiu et al. (2016)
	Ti-xNb where x = 10, 30, and 50 wt%	Anode: Ti-xNb alloys Electrolyte: 0.15 M calcium acetate and 0.02 M calcium glycerophosphate Voltage: 280 V for 3 min	Nb content has better biocompatibility, eliminating allergic reactions and bone resorption. Mean porosity increases with increasing Nb content Ti-30Nb: Highest corrosion resistance, Ca/P ratio and HA-forming capability		Kaseem and Choe (2019)
Laser surface texturing	Ti6Al4V	Uniform ridge and groove widths are micropatterned on the sample surface Operating machine: SISMA OEM plus 6 W Laser: Q-switched diode-pumped Nd:YAG Laser beam: Circular Gaussian shape profile Spot size: 39 μm Focus beam: 160 mm f-theta objective Input aperture: 10 μm	Swift and efficient process. Reduction in wear/friction and contamination. Superhydrophilicity surface and good mechanical fixation which prevent osteolysis	Tissue response and clinical trial vary on pattern dimension and material selection	Tiainen et al. (2019) Shivakoti et al. (2021)
Chemical etching	Ti6Al4V	Immersed in 1 ml hydrofluoric acid and 50 ml H_2O solution, for 2, 5, and 10 min. Posttreatment: immediate cleansing with ethanol and ultrasonic bath	Remove unmelted powder residues in the 3D-printed part	Osseointegration capability only when paired with other methods	Song et al. (2019)
Alkali–heat treatment + HA electrochemical deposition	Ti6Al4V	Performed in 5 mol L^{-1} NaOH solution for 1 h at 60°C Heat-treated for 1 h at 600°C with heating rate 5°C min^{-1} furnace-cooled HA-electrochemical deposited parameters: Electrodes: Pt/Ti/saturated calomel Electrolyte: 2.5 mM calcium chloride hexahydrate, 1.5 mM ammonium dihydrogen phosphate, 0.15 M sodium chloride, bath temperature at 85°C	Increase surface area for protein adsorption, induce HA nucleation sites, and good cytocompatibility	Decrease in adhesive strength due to loss of surface structure during alkali treatment	Song et al. (2019)

with HA electrochemical deposition are introduced in the Surface Treatment section, and a summary of their advantages and limitations is shown in **Table 1**, for each surface treatment method adopted.

Micro-arc Oxidation

One method of treating the surface of bio-implants is through MAO, which is also known as plasma electrolytic oxidation. The MAO process relies on an electrochemical method undergoing high temperature and pressure produced by a discharge arc on the metal substrate. Subsequently inducing redistribution of the porous layer and repassivation to a fully formed passive oxide film (Liu et al., 2015). An experimental study indicated that silver-incorporated titanium oxide (TiO_2) coating through MAO can exhibit antibacterial capability and bone-forming cells (Lv et al., 2019).

In a study by Xiu et al. (2016), MAO-treated titanium alloy was adopted for a dual functionality purpose; one where a layer of microporous TiO_2 is achieved, while another for converting the bioinert titanium alloy into a bioactive surface. A one-step MAO process was applied to a 3D-printed porous Ti6Al4V scaffold to endow the scaffold with a homogeneous layer of microporous TiO_2 and significant amounts of amorphous calcium phosphate. MAO exhibits a high efficiency in the enhancement of osseointegration of porous Ti64 via optimizing the patterns of bone ingrowth and bone/implant interlocking as seen in **Figure 7**.

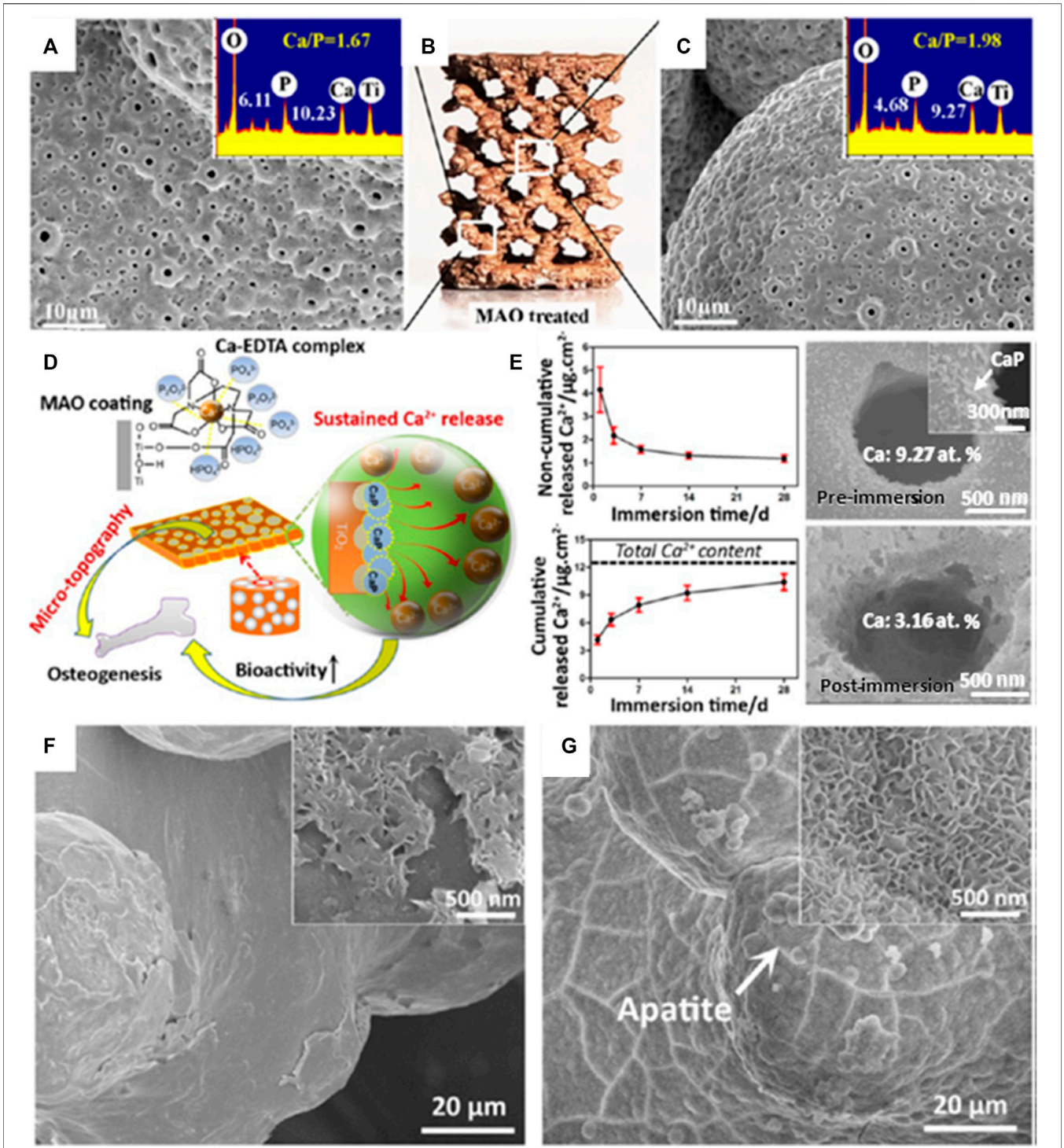

FIGURE 7 | Computer-aided design (CAD) model of multiplanar hexagonal unit cell structures with a macroscopical view of an MAO-treated scaffold **(B)**; the MAO-treated scaffold at the **(A)** outer surface and **(C)** central surfaces. **(D)** The illustrative diagram shows the simultaneous generation of microporous topography and bioactive elements on the macroporous scaffold by MAO treatment in a Ca-Ethylenediaminetetraacetic acid (EDTA)–containing electrolyte and **(E)** the noncumulative and cumulative release curves of Ca^{2+} in phosphate-buffered saline (PBS) for 28 days; scanning electron microscope (SEM) images of the implant surface before and after immersion for 28 days are shown on the right side. **(F)** SEM image of the untreated porous Ti64 scaffold immersed in stimulated body fluid (SBF) for 14 days and **(G)** SEM image of the MAO-treated scaffold immersed in SBF for 3 days. Image reproduced from Xiu et al. (2016).

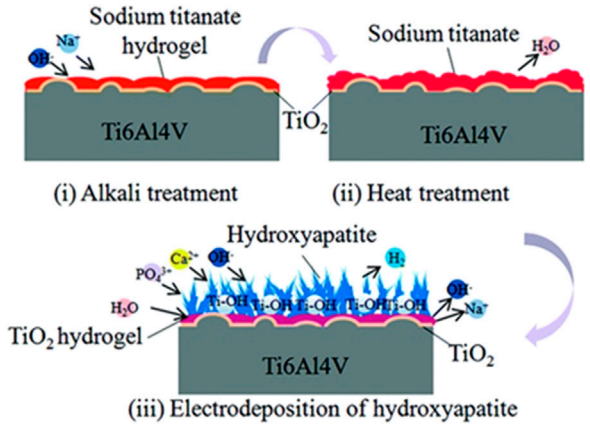

FIGURE 8 | Formation of titanium alloy coating through alkali–heat treatment and HA-electrodeposited surface treatment. Image reproduced from Song et al. (2019).

Therefore, posttreatment of 3D-printed porous titanium alloy with MAO technology might open up several possibilities for the development of bioactive customized implants in orthopedic applications. It was also noted that the 1 μm micropore between the implant and bone surface acts as an anchorage to bone bonding. Several articles have confirmed the possibility that diameter size plays a critical role in aiding natural bone remodeling (Davies, 2007; Davies et al., 2014) in contrast to a flat surface.

Laser Surface Texturing

The use of LST technology has been recommended in recent years, especially within biomedical applications due to its swift speed process, high efficiency and flexibility, its ability to reduce wear and friction, better mechanical fixation, less contamination from unwanted direct contact, and low cost (Earl et al., 2016; Grützmacher et al., 2019; Rosenkranz et al., 2019; Tiainen et al., 2019). In LST, the high-energy beam creates continuous melting and vaporization on the material, aiming at strengthening its tribological behavior (Shivakoti et al., 2021).

For medical implants, crosshatched micro/nano patterns were performed for vascularization and bone adhesion. In a study by Tiainen et al. (2019), a groove-like structure was designed on the surface that showed possibility to optimize the degree of roughness. The process allowed reproducibility, few defects, and good structural integrity which prevents osteolysis. In addition, osteoblast adhesion from superhydrophilic surfaces was observed through a process of laser texturing on the titanium alloy, which indicates surface chemistry and topography integration (Coathup et al., 2017). Overall, these parametric influences are necessary in LST to ensure better compliancy between surface properties and adherence toward biological systems (Shivakoti et al., 2021).

Chemical Etching

A previous study has shown that the 3D-printed implant (*via* selective laser melting) has a negative consequence due to unmelted powder residues formed on the printed implant surface. The adverse effect can be detrimental especially for titanium alloy containing toxic ions which may lead to further implant loosening and inflammation through osteolysis. As such, surface treatment by hydrofluoric acid chemical etchant removes toxic unmelted residual powders and even reveals a superior quality surface. The depletion of the oxide film on the titanium surface was also observed when chemically etched but was immediately rebuilt on the substrate, thus providing excellent biocompatibility and corrosion control. Hence, chemical etching is a superior surface treatment method when it comes to removing unmelted powders compared to other common methods such as sandblasting treatment (Song et al., 2019).

Alkali–Heat Treatment and HA Electrochemical Deposition

The bioinert titanium alloy induces fibrous tissues surrounding the implant in contrast to the bioactive implant. The schematic diagram of a multilayer uniform bioactive coating in **Figure 8** shows remarkable outcomes in cell cytocompatibility and cell adhesion and proliferation (Song et al., 2019).

Through subjecting implants to alkali–heat treatment, an increase in specific surface area was observed on the surface, which causes accumulation of protein adsorption forming better cell integration. The final process involves electrodeposition of HA acting as nucleation sites on the surface.

Bioactive Coating

Generally, bioceramic is not utilized for load-bearing applications due to its brittle mechanical behavior resulting from its ionic charge counterparts in contrast to metallic material. If implant failure occurs, bioceramic may pose catastrophic effects to the internal body. Despite the fact that the bulk of the implant is made from metallic material, the coating layer exhibits a bioceramic component which forms on the metallic surface. Bioceramic has great bone–tissue interaction which demonstrates biocompatibility in the biological system. Some common bioceramics are calcium phosphate, carbon nanomaterial, biphasic calcium phosphate, and bioglass. There are many advantages surrounding bioceramic coating as classified in **Figure 9**. Furthermore, bioceramic behaves as an excellent source as compared to other implant materials. It is devoid of both toxic ions such as cobalt or chromium and allergic reactions of nickel ions in stainless steel. It also minimizes disease transmission which is commonly observed in allogenic transplantation. Therefore, the intrinsic behavior of bioceramic has a pivotal role in advancing coating applications within the medical field.

Calcium Phosphate

Bioactive ceramic coating on a metal implant has been explored over the last decade (Goodman et al., 2013). For materials such as titanium, readily forming a passive layer alone is not enough for tissue integration. For this reason, HA coating has been extensively researched and is known for its ability to match bone mechanical strength, hence preventing osteoclasts, its chemical bonding to bone (Zhong et al., 2015), and has shown

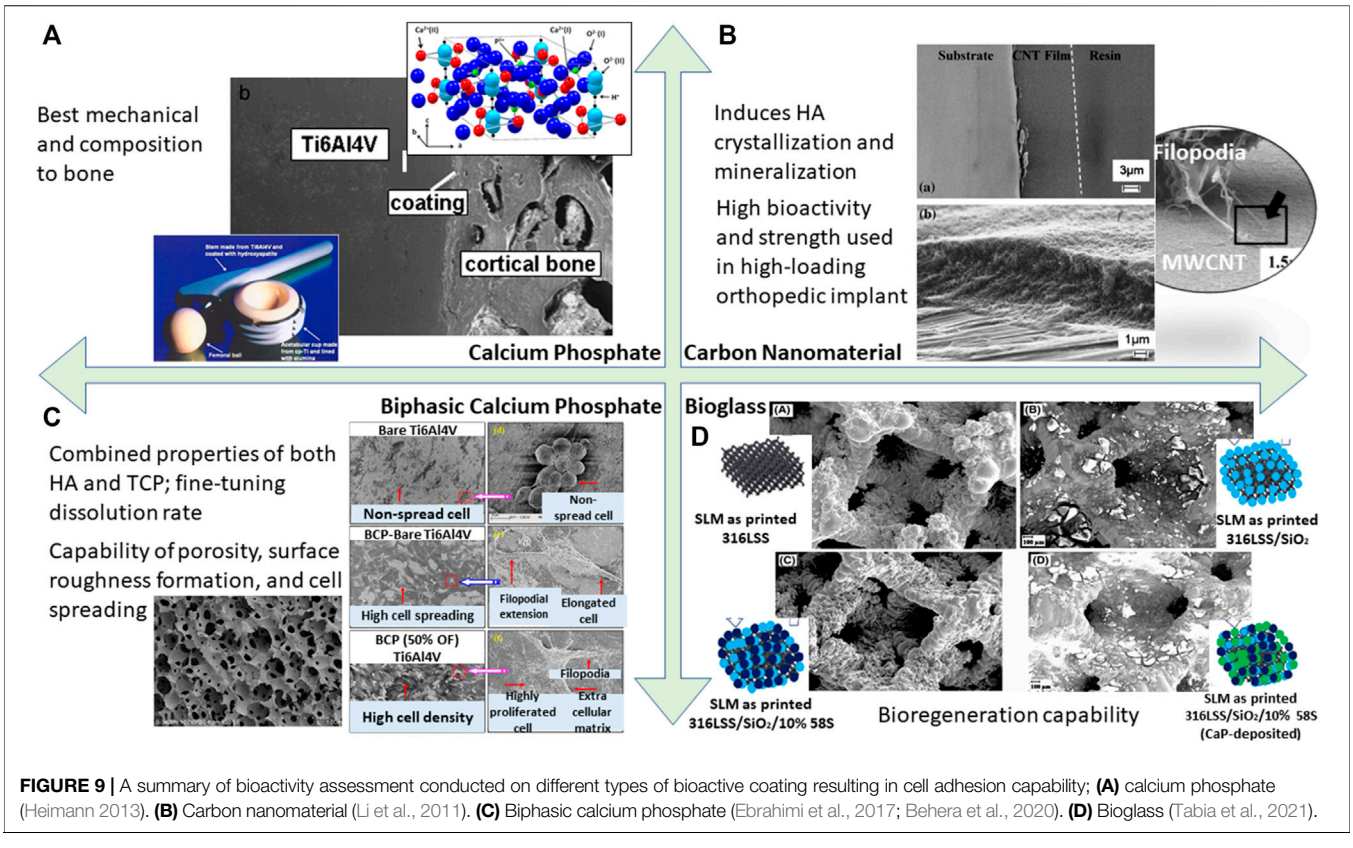

FIGURE 9 | A summary of bioactivity assessment conducted on different types of bioactive coating resulting in cell adhesion capability; **(A)** calcium phosphate (Heimann 2013). **(B)** Carbon nanomaterial (Li et al., 2011). **(C)** Biphasic calcium phosphate (Ebrahimi et al., 2017; Behera et al., 2020). **(D)** Bioglass (Tabia et al., 2021).

clinical success in inducing bone-growth fixation rather than fibrous connective tissue formation (Kienapfel et al., 1999). The HA coating also acts as a bridge to tackle bone-bonding issues by regulating the biological environment (Goodman et al., 2013). However, whether HA undergoes resorption is still controversial, depending on several factors ranging from physical (anatomical location) (Søballe et al., 1999), to biochemical (increased crystallinity reduces the resorption rate but decreases bone ingrowth) (Overgaard et al., 1999), and mechanical instability (prevent dissolution of HA) (Overgaard et al., 1999).

Carbon Nanomaterial

In the past decade, carbon nanotube (CNT) material has emerged as a tool for medical advancement such as in orthopedic coatings. Given its thermal and electrical excellence, this enables the material to act as a pathway for electrical signals from the nerve to a diseased location, hence enabling bone healing and tissue regeneration (Li et al., 2011). For metal implants, it was observed that CNT coating induces HA crystallization and mineralization. This allows the implant as a whole to be biocompatible and form good mechanical bonding to the bone (Akasaka et al., 2006). In particular, CNT has been shown to reinforce composite coating, allowing for high load-bearing application especially in the field of orthopedics. It is paired well with bioglass, polymer, and collagen. On a macroscopic level, it shows minimal porosity, hence its overall attributes can be harnessed as a promising engineering method in the field of biomedical application. There are also several studies mentioning the superior nanoscale surface properties acting for better protein adherence and cell tracking (Li et al., 2011). In addition, the fabrication of CNT was achieved at 10 μm thickness through electrophoretic deposition and even shows a strong adherence between the coating and metallic stainless steel substrate, whereas Ti-C forms a partial reaction in titanium alloy. When reinforced with HA, this coating has been shown to have the superior property of high bioactivity and strength, especially in use for high-loading orthopedic implants (Chen et al., 2005).

Biphasic Calcium Phosphate

Though calcium phosphate is evidently known to support the bone growth mechanism between the substrate and bone tissue, the distinct calcium phosphate polymorphs—tricalcium phosphate (TCP), biphasic calcium phosphate (BCP), and HA—pose different osseointegration behaviors. The bioresorption of BCP shows a complimentary functional component due to its combined properties from both HA and TCP. Although HA has better stability, it still has a slow absorption rate when compared to TCP. Likewise, TCP also has higher bioreactivity, but its rapid dissolution may be a cause of concern. Therefore, by fine-tuning these two elemental properties, BCP achieves the desired dissolution rate for specific bio-applications (Ebrahimi et al., 2017). In retrospect, BCP has a superhydrophilic surface which is protein-stimulative adherent compared to the other polymorphs which eventually accelerate the cell proliferation capability (Behera et al., 2020). In an experimental study, it was noted that uncoated titanium alloy shows globular cell morphology, indicating less cell

spreading on the surface as compared to BCP-coated titanium alloy. When textured with uniformly distributed grains, cells show even better adherence and growth on the BCP-coated surface (Behera et al., 2020).

Bioglass

Bioglass is a synthetic material made of silicon dioxide, phosphates, sodium oxide, and calcium oxide, discovered by Larry Hench (Hench and Jones 2015). Bioglass is a phenomenal material showing promising results with tissue integration. When exposed to body fluids, the material turns into a glass surface where nucleation and growth of HA crystals take place, therefore allowing osteoblast fusion into bone regeneration. Simultaneously, it was observed that because of the dissolution of bioglass, it behaves as a growth factor that sends signals to cells, allowing for better integration that is not seen when it comes to foreign materials due to a fibrous capsule surrounding the implant. In a review by Tabia et al. (2021), a 3D-printed lattice structure of a rhombic dodecahedron was formed. It was stated that this structure promotes reduction in stiffness and weight, and the addition of bioglass coating around this structure's framework promotes better bioactivity yielding to increase bone density and better bone remodeling, hence making it an excellent integration for hip implants. Another study shows that a combination of bioglass and Fe_3O_4 nanoparticles further enhanced antimicrobial activity. This nanocomposite coating inhibits infection growth and even shows outstanding corrosion protection as compared to bioglass or Fe_3O_4 on its own (Singh et al., 2020).

SUMMARY AND OUTLOOK

The advancement of 3D printing has provided many opportunities for designing intricate and porous metallic biomaterial structures. The 3D printing technique has capability to design precise and controlled topologies while maintaining excellent physical, mechanical, and biological properties. These favorable properties can be enhanced by surface treatment and bioactive coating to enable osseointegration and minimize the risk of implant-associated infections. Surface treatment is used to improve surface roughness in attempts to improve fatigue strength and biological response. With the addition of bioactive coating, significant improvement of bone in-growth capability and bone-implant bonding leads to a more rapid and durable osseointegration. In addition, the release of biofunctional ions in the phase lattice should also be considered in the evaluation of bioactive functions.

Within a biological environment, there are many considerations to be taken into account to improve the service lifetime and function of an implant. An articulate structural design of the implant–tissue interface is critical for the implant to be integrated into the body without complications. Thus, extensive understanding of the protein adsorption and cell adhesion processes at the interface between the tissue and implant surface are particularly meaningful for guiding researchers in choosing the correct surface treatment and bio-functionalization techniques. Moreover, the corrosion property of the bioactive coating also plays a critical role in implant failure. The ions or products released from the corrosion process may generate toxicity or even damage tissues. Therefore, bioactive ceramic coating produced by surface treatment, such as the MAO process, has promising biomedical applications due to its high corrosion resistance. Even better, ceramic coating on implants can be tailored according to the biomedical requirement needed, as they are tunable in their compositions and properties through additives modification, for example, addition of Ca, P, Mg, Si, Sr, etc. Future research efforts should be directed to further improve and control their physical and biological properties for bio-functionalized and long-life coatings.

AUTHOR CONTRIBUTIONS

JL and NR wrote the manuscript; LW and SW reviewed and finalized the manuscript. All authors contributed to the organization and content of the article.

REFERENCES

Aimar, A., Palermo, A., and Innocenti, B. (2019). The Role of 3D Printing in Medical Applications: A State of the Art. *J. Healthc. Eng.* 2019, 5340616. doi:10.1155/2019/5340616

Akasaka, T., Watari, F., Sato, Y., and Tohji, K. (2006). Apatite Formation on Carbon Nanotubes. *Mater. Sci. Eng. C.* 26 (4), 675–678. doi:10.1016/j.msec.2005.03.009

Albrektsson, T., and Johansson, C. (2001). Osteoinduction, Osteoconduction and Osseointegration. *Eur. Spine J.* 10 (2), S96–S101. doi:10.1007/s005860100282

Alipal, J., Mohd Pu'ad, N. A. S., Nayan, N. H. M., Sahari, N., Abdullah, H. Z., Idris, M. I., et al. (2021). An Updated Review on Surface Functionalisation of Titanium and its Alloys for Implants Applications. *Mater. Today Proc.* 42, 270–282. doi:10.1016/j.matpr.2021.01.499

Alison, L., Menasce, S., Bouville, F., Tervoort, E., Mattich, I., Ofner, A., et al. (2019). 3D Printing of Sacrificial Templates into Hierarchical Porous Materials. *Sci. Rep.* 9 (1), 409. doi:10.1038/s41598-018-36789-z

Atrens, A., Shi, Z., Mehreen, S. U., Johnston, S., Song, G.-L., Chen, X., et al. (2020). Review of Mg alloy Corrosion Rates. *J. Magnesium Alloys.* 8 (4), 989–998. doi:10.1016/j.jma.2020.08.002

Attarilar, S., Ebrahimi, M., Djavanroodi, F., Fu, Y., Wang, L., and Yang, J. (2021). 3D Printing Technologies in Metallic Implants: A Thematic Review on the Techniques and Procedures. *Int. J. Bioprint.* 7 (1), 306. doi:10.18063/ijb.v7i1.306

Bagaria, V., Bhansali, R., and Pawar, P. (2018). 3D Printing- Creating a Blueprint for the Future of Orthopedics: Current Concept Review and the Road Ahead!. *J. Clin. Orthopaedics Trauma.* 9 (3), 207–212. doi:10.1016/j.jcot.2018.07.007

Balazic, M., and Kopac, J. (2007). Improvements of Medical Implants Based on Modern Materials and New Technologies. *J. Achievements Mater. Manufacturing Eng.* 25 (2), 31–34.

Behera, R. R., Das, A., Hasan, A., Pamu, D., Pandey, L. M., and Sankar, M. R. (2020). Deposition of Biphasic Calcium Phosphate Film on Laser Surface Textured Ti-6Al-4V and its Effect on Different Biological Properties for Orthopedic Applications. *J. Alloys Comp.* 842, 155683. doi:10.1016/j.jallcom.2020.155683

Best, S. M., Porter, A. E., Thian, E. S., and Huang, J. (2008). Bioceramics: Past, Present and for the Future. *J. Eur. Ceram. Soc.* 28 (7), 1319–1327. doi:10.1016/j.jeurceramsoc.2007.12.001

Brand, Y., Senn, P., Kompis, M., Dillier, N., and Allum, J. H. (2014). Cochlear Implantation in Children and Adults in Switzerland. *Swiss Med. Wkly.* 144, w13909. doi:10.4414/smw.2014.13909

Capasso, I., Liguori, B., Verdolotti, L., Caputo, D., Lavorgna, M., and Tervoort, E. (2020). Process Strategy to Fabricate a Hierarchical Porosity Gradient in Diatomite-Based Foams by 3D Printing. *Sci. Rep.* 10 (1), 612. doi:10.1038/s41598-019-55582-0

Carpenter, R. D., Klosterhoff, B. S., Torstrick, F. B., Foley, K. T., Burkus, J. K., Lee, C. S. D., et al. (2018). Effect of Porous Orthopaedic Implant Material and Structure on Load Sharing with Simulated Bone Ingrowth: A Finite Element Analysis Comparing Titanium and PEEK. *J. Mech. Behav. Biomed. Mater.* 80, 68–76. doi:10.1016/j.jmbbm.2018.01.017

Chen, Y., Gan, C., Zhang, T., Yu, G., Bai, P., and Kaplan, A. (2005). Laser-surface-alloyed Carbon Nanotubes Reinforced Hydroxyapatite Composite Coatings. *Appl. Phys. Lett.* 86 (25), 251905. doi:10.1063/1.1951054

Chithartha, K., Thilak, J., Sukesh, A. N., and Theruvil, B. (2020). Fatigue Fracture of the Femoral Component in Total Knee Replacement. *The Knee* 27 (5), 1439–1445. doi:10.1016/j.knee.2020.06.009

Coakley, M. F., Hurt, D. E., Weber, N., Mtingwa, M., Fincher, E. C., Alekseyev, V., et al. (2014). The NIH 3D Print Exchange: A Public Resource for Bioscientific and Biomedical 3D Prints. *3D Printing and Additive Manufacturing.* 1 (3), 137–140. doi:10.1089/3dp.2014.1503

Coathup, M. J., Blunn, G. W., Mirhosseini, N., Erskine, K., Liu, Z., Garrod, D. R., et al. (2017). Controlled Laser Texturing of Titanium Results in Reliable Osseointegration. *J. Orthop. Res.* 35 (4), 820–828. doi:10.1002/jor.23340

Daghighi, S., Sjollema, J., van der Mei, H. C., Busscher, H. J., and Rochford, E. T. J. (2013). Infection Resistance of Degradable versus Non-degradable Biomaterials: An Assessment of the Potential Mechanisms. *Biomaterials* 34 (33), 8013–8017. doi:10.1016/j.biomaterials.2013.07.044

Dai, K., and Xu, F. (2021). Medical Application of 3D Printing: A Powerful Tool for Personalised Treatment. *J. Shanghai Jiaotong Univ. (Sci.)* 26 (3), 257–258. doi:10.1007/s12204-021-2290-8

Davies, J. E. (2007). Bone Bonding at Natural and Biomaterial Surfaces. *Biomaterials* 28 (34), 5058–5067. doi:10.1016/j.biomaterials.2007.07.049

Davies, J. E., Mendes, V. C., Ko, J. C. H., and Ajami, E. (2014). Topographic Scale-Range Synergy at the Functional Bone/implant Interface. *Biomaterials* 35 (1), 25–35. doi:10.1016/j.biomaterials.2013.09.072

Dhruva, S. S., and Redberg, R. F. (2013). FDA Regulation of Cardiovascular Devices and Opportunities for Improvement. *J. Interv. Card. Electrophysiol.* 36 (2), 99–105. doi:10.1007/s10840-012-9767-1

Duda, T., and Raghavan, L. V. (2016). 3D Metal Printing Technology. *IFAC-PapersOnLine* 49 (29), 103–110. doi:10.1016/j.ifacol.2016.11.111

Earl, C., Castrejón-Pita, J. R., Hilton, P. A., and O'Neill, W. (2016). The Dynamics of Laser Surface Modification. *J. Manufacturing Process.* 21, 214–223. doi:10.1016/j.jmapro.2015.10.002

Ebrahimi, M., Botelho, M. G., and Dorozhkin, S. V. (2017). Biphasic Calcium Phosphates Bioceramics (HA/TCP): Concept, Physicochemical Properties and the Impact of Standardization of Study Protocols in Biomaterials Research. *Mater. Sci. Eng. C.* 71, 1293–1312. doi:10.1016/j.msec.2016.11.039

Fantini, M., Curto, M., and De Crescenzio, F. (2017). "TPMS for Interactive Modelling of Trabecular Scaffolds for Bone Tissue Engineering," in *Advances on Mechanics, Design Engineering and Manufacturing: Proceedings of the International Joint Conference on Mechanics, Design Engineering & Advanced Manufacturing (JCM 2016), 14-16 September, 2016, Catania, Italy*. Editors B. Eynard, V. Nigrelli, S. M. Oliveri, G. Peris-Fajarnes, and S. Rizzuti (Cham: Springer International Publishing), 425–435. doi:10.1007/978-3-319-45781-9_43

Gittens, R. A., Olivares-Navarrete, R., Schwartz, Z., and Boyan, B. D. (2014). Implant Osseointegration and the Role of Microroughness and Nanostructures: Lessons for Spine Implants. *Acta Biomater.* 10 (8), 3363–3371. doi:10.1016/j.actbio.2014.03.037

Goodman, S. B., Yao, Z., Keeney, M., and Yang, F. (2013). The Future of Biologic Coatings for Orthopaedic Implants. *Biomaterials* 34 (13), 3174–3183. doi:10.1016/j.biomaterials.2013.01.074

Gross, B. C., Erkal, J. L., Lockwood, S. Y., Chen, C., and Spence, D. M. (2014). Evaluation of 3D Printing and its Potential Impact on Biotechnology and the Chemical Sciences. *Anal. Chem.* 86 (7), 3240–3253. doi:10.1021/ac403397r

Grützmacher, P. G., Profito, F. J., and Rosenkranz, A. (2019). Multi-Scale Surface Texturing in Tribology-Current Knowledge and Future Perspectives. *Lubricants* 7 (11), 95. doi:10.3390/lubricants7110095

Gu, X.-N., Li, S.-S., Li, X.-M., and Fan, Y.-B. (2014). Magnesium Based Degradable Biomaterials: A Review. *Front. Mater. Sci.* 8 (3), 200–218. doi:10.1007/s11706-014-0253-9

Heimann, R. B. (2013). Structure, Properties, and Biomedical Performance of Osteoconductive Bioceramic Coatings. *Surf. Coat. Tech.* 233, 27–38. doi:10.1016/j.surfcoat.2012.11.013

Hench, L. L., and Jones, J. R. (2015). Bioactive Glasses: Frontiers and Challenges. *Front. Bioeng. Biotechnol.* 3, 194. doi:10.3389/fbioe.2015.00194

Hrabe, N. W., Heinl, P., Bordia, R. K., Körner, C., and Fernandes, R. J. (2013). Maintenance of a Bone Collagen Phenotype by Osteoblast-like Cells in 3D Periodic Porous Titanium (Ti-6Al-4 V) Structures Fabricated by Selective Electron Beam Melting. *Connect. Tissue Res.* 54 (6), 351–360. doi:10.3109/03008207.2013.822864

Hwang, I.-J., and Choe, H.-C. (2018). Hydroxyapatite Coatings Containing Zn and Si on Ti-6Al-4Valloy by Plasma Electrolytic Oxidation. *Appl. Surf. Sci.* 432, 337–346. doi:10.1016/j.apsusc.2017.01.313

Jardini, A. L., Larosa, M. A., Macedo, M. F., Bernardes, L. F., Lambert, C. S., Zavaglia, C. A. C., et al. (2016). Improvement in Cranioplasty: Advanced Prosthesis Biomanufacturing. *Proced. CIRP.* 49, 203–208. doi:10.1016/j.procir.2015.11.017

Johnson, J. A. (2016). FDA Regulation of Medical Devices (Accessed July 31, 2021. https://sgp.fas.org/crs/misc/R42130.pdf).

Joung, Y.-H. (2013). Development of Implantable Medical Devices: From an Engineering Perspective. *Int. Neurourol J.* 17 (3), 98. doi:10.5213/inj.2013.17.3.98

Karande, T. S., Ong, J. L., and Agrawal, C. M. (2004). Diffusion in Musculoskeletal Tissue Engineering Scaffolds: Design Issues Related to Porosity, Permeability, Architecture, and Nutrient Mixing. *Ann. Biomed. Eng.* 32 (12), 1728–1743. doi:10.1007/s10439-004-7825-2

Kaseem, M., and Choe, H.-C. (2019). Electrochemical and Bioactive Characteristics of the Porous Surface Formed on Ti-xNb Alloys via Plasma Electrolytic Oxidation. *Surf. Coat. Tech.* 378, 125027. doi:10.1016/j.surfcoat.2019.125027

Kazantseva, N. (2018). Main Factors Affecting the Structure and Properties of Titanium and Cobalt Alloys Manufactured by the 3D Printing. *J. Phys. Conf. Ser.* 1115, 042008. doi:10.1088/1742-6596/1115/4/042008

Kienapfel, H., Sprey, C., Wilke, A., and Griss, P. (1999). Implant Fixation by Bone Ingrowth. *The J. Arthroplasty.* 14 (3), 355–368. doi:10.1016/s0883-5403(99)90063-3

Kong, D., Ni, X., Dong, C., Lei, X., Zhang, L., Man, C., et al. (2018). Bio-functional and Anti-corrosive 3D Printing 316L Stainless Steel Fabricated by Selective Laser Melting. *Mater. Des.* 152, 88–101. doi:10.1016/j.matdes.2018.04.058

Li, X., Liu, X., Huang, J., Fan, Y., and Cui, F.-z. (2011). Biomedical Investigation of CNT Based Coatings. *Surf. Coat. Tech.* 206 (4), 759–766. doi:10.1016/j.surfcoat.2011.02.063

Liu, C., He, D., Yan, Q., Huang, Z., Liu, P., Li, D., et al. (2015). An Investigation of the Coating/substrate Interface of Plasma Electrolytic Oxidation Coated Aluminum. *Surf. Coat. Tech.* 280, 86–91. doi:10.1016/j.surfcoat.2015.08.050

Lütjering, G., and Williams, J. C. (2007). *Titanium*. Berlin, Heidelberg: Springer Berlin Heidelberg.

Lv, Y., Wu, Y., Lu, X., Yu, Y., Fu, S., Yang, L., et al. (2019). Microstructure, Bio-Corrosion and Biological Property of Ag-Incorporated TiO2 Coatings: Influence of Ag2O Contents. *Ceramics Int.* 45 (17), 22357–22367. doi:10.1016/j.ceramint.2019.07.265

Mankani, M. H., Kuznetsov, S. A., Fowler, B., Kingman, A., and Gehron Robey, P. (2001). *In Vivo* bone Formation by Human Bone Marrow Stromal Cells: Effect of Carrier Particle Size and Shape. *Biotechnol. Bioeng.* 72 (1), 96–107. doi:10.1002/1097-0290(20010105)72:1<96:aid-bit13>3.0.co;2-a

Matassi, F., Botti, A., Sirleo, L., Carulli, C., and Innocenti, M. (2013). Porous Metal for Orthopedics Implants, The Official Journal of the Italian Society of Osteoporosis, Mineral Metabolism, and Skeletal Diseases. *Clin. Cases Mineral Bone Metab.* 10 (2), 111–115.

Mattei, L., Di Puccio, F., Piccigallo, B., and Ciulli, E. (2011). Lubrication and Wear Modelling of Artificial Hip Joints: A Review. *Tribology Int.* 44 (5), 532–549. doi:10.1016/j.triboint.2010.06.010

Meng, J., Yang, G., Liu, L., Song, Y., Jiang, L., and Wang, S. (2017). Cell Adhesive Spectra along Surface Wettability Gradient from Superhydrophilicity to Superhydrophobicity. *Sci. China Chem.* 60 (5), 614–620. doi:10.1007/s11426-016-9031-8

Mertz, L. (2013). Dream it, Design it, Print it in 3-D: What Can 3-D Printing Do for You? *IEEE Pulse* 4 (6), 15–21. doi:10.1109/mpul.2013.2279616

Morrison, R. J., Kashlan, K. N., Flanangan, C. L., Wright, J. K., Green, G. E., Hollister, S. J., et al. (2015). Regulatory Considerations in the Design and Manufacturing of Implantable 3D-Printed Medical Devices. *Clin. Translational Sci.* 8 (5), 594–600. doi:10.1111/cts.12315

Ni, J., Ling, H., Zhang, S., Wang, Z., Peng, Z., Benyshek, C., et al. (2019). Three-dimensional Printing of Metals for Biomedical Applications. *Mater. Today Bio.* 3, 100024. doi:10.1016/j.mtbio.2019.100024

Onuki, Y., Bhardwaj, U., Papadimitrakopoulos, F., and Burgess, D. J. (2008). A Review of the Biocompatibility of Implantable Devices: Current Challenges to Overcome Foreign Body Response. *J. Diabetes Sci. Technol.* 2 (6), 1003–1015. doi:10.1177/193229680800200610

Overgaard, S., Bromose, U., Lind, M., Bünger, C., and Søballe, K. (1999). The Influence of Crystallinity of the Hydroxyapatite Coating on the Fixation of Implants. *J. Bone Jt. Surg. Br.* 81 (4), 725–731. doi:10.1302/0301-620X.81B4.0810725

Parthasarathy, J., Starly, B., and Raman, S. (2011). A Design for the Additive Manufacture of Functionally Graded Porous Structures with Tailored Mechanical Properties for Biomedical Applications. *J. Manufacturing Process.* 13 (2), 160–170. doi:10.1016/j.jmapro.2011.01.004

Pałka, K., and Pokrowiecki, R. (2018). Porous Titanium Implants: A Review. *Adv. Eng. Mater.* 20 (5), 1700648. doi:10.1002/adem.201700648

Peng, Z., Ni, J., Zheng, K., Shen, Y., Wang, X., He, G., et al. (2013). Dual Effects and Mechanism of TiO2 Nanotube Arrays in Reducing Bacterial Colonization and Enhancing C3H10T1/2 Cell Adhesion. *Int. J. Nanomedicine* 8, 3093–3105. doi:10.2147/IJN.S48084

Rayna, T., and Striukova, L. (2016). From Rapid Prototyping to home Fabrication: How 3D Printing Is Changing Business Model Innovation. *Technol. Forecast. Soc. Change.* 102, 214–224. doi:10.1016/j.techfore.2015.07.023

Rosenkranz, A., Grützmacher, P. G., Gachot, C., and Costa, H. L. (2019). Surface Texturing in Machine Elements – A Critical Discussion for Rolling and Sliding Contacts. *Adv. Eng. Mater.* 21 (8), 1900194. doi:10.1002/adem.201900194

Rumpler, M., Woesz, A., Dunlop, J. W. C., van Dongen, J. T., and Fratzl, P. (2008). The Effect of Geometry on Three-Dimensional Tissue Growth. *J. R. Soc. Interf.* 5 (27), 1173–1180. doi:10.1098/rsif.2008.0064

Sailer, I., Philipp, A., Zembic, A., Pjetursson, B. E., Hämmerle, C. H. F., and Zwahlen, M. (2009). A Systematic Review of the Performance of Ceramic and Metal Implant Abutments Supporting Fixed Implant Reconstructions. *Clin. Oral Implants Res.* 20, 4–31. doi:10.1111/j.1600-0501.2009.01787.x

Schubert, C., van Langeveld, M. C., and Donoso, L. A. (2014). Innovations in 3D Printing: a 3D Overview from Optics to Organs. *Br. J. Ophthalmol.* 98 (2), 159–161. doi:10.1136/bjophthalmol-2013-304446

Shivakoti, I., Kibria, G., Cep, R., Pradhan, B. B., and Sharma, A. (2021). Laser Surface Texturing for Biomedical Applications: A Review. *Coatings* 11 (2), 124. doi:10.3390/coatings11020124

Singh, S., Singh, G., Bala, N., and Aggarwal, K. (2020). Characterization and Preparation of Fe3O4 Nanoparticles Loaded Bioglass-Chitosan Nanocomposite Coating on Mg alloy and *In Vitro* Bioactivity Assessment. *Int. J. Biol. Macromolecules* 151, 519–528. doi:10.1016/j.ijbiomac.2020.02.208

Søballe, K., Overgaard, S., Hansen, E. S., Brokstedt-Rasmussen, H., Lind, M., and Bünger, C. (1999). A Review of Ceramic Coatings for Implant Fixation. *J. long-term effects Med. Implants* 9 (1-2), 131–151.

Song, P., Hu, C., Pei, X., Sun, J., Sun, H., Wu, L., et al. (2019). Dual Modulation of Crystallinity and Macro-/microstructures of 3D Printed Porous Titanium Implants to Enhance Stability and Osseointegration. *J. Mater. Chem. B.* 7 (17), 2865–2877. doi:10.1039/c9tb00093c

Souza, J. C. M., Apaza-Bedoya, K., Benfatti, C. A. M., Silva, F. S., and Henriques, B. (2020). A Comprehensive Review on the Corrosion Pathways of Titanium Dental Implants and Their Biological Adverse Effects. *Metals* 10 (9), 1272. doi:10.3390/met10091272

Steinemann, S. G. (1998). Titanium? the Material of Choice? *Periodontol. 2000* 17 (1), 7–21. doi:10.1111/j.1600-0757.1998.tb00119.x

Stich, T., Alagboso, F., Křenek, T., Kovářík, T., Alt, V., and Docheva, D. (2021). Implant-bone-interface: Reviewing the Impact of Titanium Surface Modifications on Osteogenic Processes *In Vitro* and *In Vivo*. *Bioeng. Translational Med.*, 1–20. doi:10.1002/btm2.10239

Tabia, Z., Bricha, M., El Mabrouk, K., and Vaudreuil, S. (2021). Manufacturing of a Metallic 3D Framework Coated with a Bioglass Matrix for Implant Applications. *J. Mater. Sci.* 56 (2), 1658–1672. doi:10.1007/s10853-020-05370-3

Takatsuka, K., Yamamuro, T., Nakamura, T., and Kokubo, T. (1995). Bone-bonding Behavior of Titanium alloy Evaluated Mechanically with Detaching Failure Load. *J. Biomed. Mater. Res.* 29 (2), 157–163. doi:10.1002/jbm.820290204

Takemoto, M., Fujibayashi, S., Neo, M., Suzuki, J., Kokubo, T., and Nakamura, T. (2005). Mechanical Properties and Osteoconductivity of Porous Bioactive Titanium. *Biomaterials* 26 (30), 6014–6023. doi:10.1016/j.biomaterials.2005.03.019

Tiainen, L., Abreu, P., Buciumeanu, M., Silva, F., Gasik, M., Serna Guerrero, R., et al. (2019). Novel Laser Surface Texturing for Improved Primary Stability of Titanium Implants. *J. Mech. Behav. Biomed. Mater.* 98, 26–39. doi:10.1016/j.jmbbm.2019.04.052

Vaz, V. M., and Kumar, L. (2021). 3D Printing as a Promising Tool in Personalized Medicine. *AAPS PharmSciTech* 22 (1), 49. doi:10.1208/s12249-020-01905-8

Ventola, C. L. (2014). Medical Applications for 3D Printing: Current and Projected Uses. *P. T* 39 (10), 704–711.

Wang, M., and Tang, T. (2019). Surface Treatment Strategies to Combat Implant-Related Infection from the Beginning. *J. Orthopaedic Translation* 17, 42–54. doi:10.1016/j.jot.2018.09.001

Wang, Z., Wang, C., Li, C., Qin, Y., Zhong, L., Chen, B., et al. (2017). Analysis of Factors Influencing Bone Ingrowth into Three-Dimensional Printed Porous Metal Scaffolds: A Review. *J. Alloys Comp.* 717, 271–285. doi:10.1016/j.jallcom.2017.05.079

Xiu, P., Jia, Z., Lv, J., Yin, C., Cheng, Y., Zhang, K., et al. (2016). Tailored Surface Treatment of 3D Printed Porous Ti6Al4V by Microarc Oxidation for Enhanced Osseointegration via Optimized Bone In-Growth Patterns and Interlocked Bone/Implant Interface. *ACS Appl. Mater. Inter.* 8 (28), 17964–17975. doi:10.1021/acsami.6b05893

Yin, S., Zhang, W., Tang, Y., Yang, G., Wu, X., Lin, S., et al. (2021). Preservation of Alveolar ridge Height through Mechanical Memory: A Novel Dental Implant Design. *Bioactive Mater.* 6 (1), 75–83. doi:10.1016/j.bioactmat.2020.07.015

Yuan, W., He, X., Zhou, X., and Zhu, Y. (2018). Hydroxyapatite Nanoparticle-Coated 3D-Printed Porous Ti6Al4V and CoCrMo Alloy Scaffolds and Their Biocompatibility to Human Osteoblasts. *j nanosci nanotechnol* 18 (6), 4360–4365. doi:10.1166/jnn.2018.15207

Zhang, B., Myers, D., Wallace, G., Brandt, M., and Choong, P. (2014). Bioactive Coatings for Orthopaedic Implants-Recent Trends in Development of Implant Coatings. *Ijms* 15 (7), 11878–11921. doi:10.3390/ijms150711878

Zhang, X., Dai, J., Zhang, R., Ba, Z., and Birbilis, N. (2019). Corrosion Behavior of Mg-3Gd-1Zn-0.4Zr alloy with and without Stacking Faults. *J. Magnesium Alloys* 7 (2), 240–248. doi:10.1016/j.jma.2019.02.009

Zhong, Z., Qin, J., and Ma, J. (2015). Electrophoretic Deposition of Biomimetic Zinc Substituted Hydroxyapatite Coatings with Chitosan and Carbon Nanotubes on Titanium. *Ceramics Int.* 41 (7), 8878–8884. doi:10.1016/j.ceramint.2015.03.145

Conflict of Interest: The authors declare that the research was conducted in the absence of any commercial or financial relationships that could be construed as a potential conflict of interest.

Publisher's Note: All claims expressed in this article are solely those of the authors and do not necessarily represent those of their affiliated organizations, or those of the publisher, the editors, and the reviewers. Any product that may be evaluated in this article, or claim that may be made by its manufacturer, is not guaranteed or endorsed by the publisher.

frontiers in Chemistry

ORIGINAL RESEARCH
published: 19 November 2021
doi: 10.3389/fchem.2021.769648

Electrochemical Biosensing Interface Based on Carbon Dots-Fe_3O_4 Nanomaterial for the Determination of *Escherichia coli* O157:H7

Xiaofeng Lin[1], *Yanqiu Mei*[1], *Chen He*[1], *Yan Luo*[1], *Min Yang*[1], *Ying Kuang*[1], *Xiaoming Ma*[2], *Huifang Zhang*[2]* *and Qitong Huang*[1]*

[1]*Key Laboratory of Prevention and Treatment of Cardiovascular and Cerebrovascular Diseases, Ministry of Education, Key Laboratory of Biomaterials and Biofabrication in Tissue Engineering of Jiangxi Province, Oil-tea in Medical Health Care and Functional Product Development Engineering Research Center in Jiangxi, School of Public Health and Health Management, School of Pharmacy, School of Medical and Information Engineering, The Science Research Center, Gannan Medical University, Ganzhou, China,* [2]*School of Chemistry and Chemical Engineering, Key Laboratory of Organo-pharmaceutical Chemistry of Jiangxi Province, Gannan Normal University, Ganzhou, China*

OPEN ACCESS

Edited by:
Zhong Feng Gao,
Linyi University, China

Reviewed by:
Miaomiao Yuan,
Sun Yat-sen University, China
占明 李,
Jiangsu University of Science and Technology, China

***Correspondence:**
Huifang Zhang
zhanghuifang93@163.com
Qitong Huang
hqt@gmu.edu.cn
hqtblue@163.com

Specialty section:
This article was submitted to Nanoscience, a section of the journal Frontiers in Chemistry

Received: *02 September 2021*
Accepted: *05 October 2021*
Published: *19 November 2021*

Citation:
Lin X, Mei Y, He C, Luo Y, Yang M, Kuang Y, Ma X, Zhang H and Huang Q (2021) Electrochemical Biosensing Interface Based on Carbon Dots-Fe_3O_4 Nanomaterial for the Determination of Escherichia coli *O157:H7. Front. Chem. 9:769648. doi: 10.3389/fchem.2021.769648*

Escherichia coli (*E. coli*) O157:H7 can cause many food safety incidents, which seriously affect human health and economic development. Therefore, the sensitive, accurate, and rapid determination of *E. coli* O157:H7 is of great significance for preventing the outbreak and spread of foodborne diseases. In this study, a carbon dots-Fe_3O_4 nanomaterial (CDs-Fe_3O_4)-based sensitive electrochemical biosensor for *E. coli* O157:H7 detection was developed. The CDs have good electrical conductivity, and the surface of carbon dots contains abundant carboxyl groups, which can be used to immobilize probe DNA. Meanwhile, the CDs can be used as a reducing agent to prepare CDs-Fe_3O_4 nanomaterial. The Fe_3O_4 nanomaterial can improve the performance of the electrochemical biosensor; it also can realize the recovery of CDs-Fe_3O_4 due to its magnetism. As expected, the electrochemical biosensor has excellent specificity of *E. coli* O157:H7 among other bacteria. The electrochemical biosensor also exhibited good performance for detecting *E. coli* O157:H7 with the detection range of 10–10^8 CFU/ml, and the detection limit of this electrochemical biosensor was 6.88 CFU/ml (3S/N). Furthermore, this electrochemical biosensor was successfully used for monitoring *E. coli* O157:H7 in milk and water samples, indicating that this electrochemical biosensor has good application prospect. More importantly, this research can provide a new idea for the detection of other bacteria and viruses.

Keywords: ***Escherichia coli* O157:H7, electrochemical biosensing interface, carbon dots, Fe_3O_4 nanomaterial, DNA biosensor**

INTRODUCTION

In recent years, food poisoning caused by foodborne pathogens has frequently occurred worldwide, which is the most prominent public health problem in the world (Hou et al., 2020; Duan et al., 2021). As one of the most hazardous foodborne pathogens, *Escherichia coli* (*E. coli*) O157:H7 can cause some diseases such as hemorrhagic colitis and hemolytic uremic syndrome. What is more, low-dose *E. coli* O157:H7 can make humans sick, and in severe cases, it can even cause kidney failure and

death. Currently, more than two million acute foodborne diseases worldwide are attributed to *E. coli* O157:H7 each year (Li et al., 2015a; Zhou et al., 2020). Therefore, it is very important to monitor the *E. coli* O157:H7 with high sensitivity. At present, some bioanalytical methods have been applied for *E. coli* O157:H7 detection, including enzyme-linked immunosorbent assay (ELISA) (Guo et al., 2016; Zhao et al., 2020), lateral flow immunochromatographic detection technology (Xie et al., 2014; Ye et al., 2020), polymerase chain reaction (PCR) (Dong et al., 2015), and so on. These alternative assays are the most rapidly used tests because of their good specificity and stability. Nevertheless, they are still faced with some limitations in detecting foodborne pathogens, including low sensitivity, complicated pretreatment, and high environmental impact. Therefore, there is an urgent need to establish a sensitive, simple, and highly specific method for detecting *E. coli* O157:H7. At present, many different electrochemical sensors have been used in food safety due to their some advantages, such as high sensitivity, economy, and accuracy (Li et al., 2015b; Li et al., 2016; Liu Y. et al., 2020; Dong et al., 2020). Therefore, electrochemical biosensors for the detection of *E. coli* O157:H7 have received extensive attention.

As is known, due to the excellent chemical, physical and biological properties of nanomaterials, they have been widely used in biomedical (Liu H. et al., 2020; Kuang et al., 2020; Thakur et al., 2020; Wu et al., 2020; Yi et al., 2021), analytical science (Chen et al., 2018; Broza et al., 2019; Jia et al., 2020; Lee et al., 2020; Mao et al., 2020; He S. et al., 2021; Mao et al., 2021), energy catalytic (Zhuang et al., 2019a; Zhuang et al., 2019b; Enesca, 2020; Zhuang et al., 2021), and other fields. Till now, some nanomaterials have been successfully used to construct electrochemical sensors for *E. coli* O157:H7 detection, such as graphene/AuNPs (You et al., 2020), reduced graphene oxide/polyaniline/Au@Pt/neutral red (rGO/PANI/Au@Pt/Nr) (Mo et al., 2019), rGO/Au@Pt (Zhu et al., 2018), rGO-poly (vinyl alcohol)/gold nanoparticles nanocomposite (AuNPs/rGO-PVA) (Qaanei et al., 2021), and so on. Although the abovementioned materials have made certain contributions to electrochemical sensors for detecting *E. coli* O157:H7, the abovementioned materials still have disadvantages, including complicated preparation, insufficient economy, and environmental protection, or low sensitivity of sensors. Therefore, it is important to prepare an easy-to-obtain, economical, and environmentally friendly functional material for the construction of electrochemical sensors for detecting *E. coli* O157:H7. As a member of "zero-dimensional" carbon nanomaterials, carbon dots (CDs) have some advantages of good biocompatibility, simple synthesis, and excellent conductivity (Zhang et al., 2019; Huang et al., 2020; Zhang and Du, 2020; He H. et al., 2021; Lin et al., 2021; Xu and Liu, 2021), and they have been successfully used to construct new electrochemical sensors, such as Pd-Au@CDs nanocomposite that we prepared for the preparation of the novel electrochemical DNA biosensor (Huang et al., 2017). Liu et al. designed an electrochemical sensor for measuring catechol based on F, N-doped CDs (Liu et al., 2019). Giang et al. constructed a wireless electrochemical biosensor based on CDs-hyaluronic acid/TiO_2/Cu^{2+} for cancer cell detection (Giang et al., 2021). Sri et al. developed a CD/polymethyl methacrylate-based electrochemical biosensor for monitoring TNF-α targeting (Sri et al., 2021).

In this study, a CDs-Fe_3O_4 nanomaterial-based electrochemical biosensor is constructed for detecting *E. coli* O157:H7, which is highly sensitive and reliable (**Figure 1**). The CDs have good electrical conductivity and large specific surface areas to improve the sensitivity of the sensor. The CDs also can be used as the reducing agent to synthesize the CDs-Fe_3O_4 nanomaterial. The Fe_3O_4 can improve the catalytic performance of the electrochemical biosensor, and it also can realize the recovery of CDs-Fe_3O_4 due to its magnetism. This electrochemical biosensor can achieve a good linear and detection limit for monitoring *E. coli* O157:H7. In addition, the biosensor has been also successfully applied to measure the *E. coli* O157:H7 in milk, indicating that the electrochemical biosensor has a broad application prospect. What is more, this study can provide a new idea for the preparation of electrochemical biosensors for other bacteria and virus detection, such as *Staphylococcus aureus* (*S. aureus*), *Listeria*, SARS-CoV-2, Hepatitis B virus, etc.

EXPERIMENTAL

Synthesis of carbon dots Fe_3O_4 nanomaterial

The preparation of CDs-Fe_3O_4 nanocomposite was based on the method of instrument preparation of our group (Kuang et al., 2020): First, 3 g of citric acid and 1 g of glucose were added in 5 ml H_2O and reacted under microwave with a radiation power of 900 W for 6 min to synthesize CDs. Second, the above solution was cooled and added 30 ml H_2O, centrifuged them at 12,000 rpm for 15 min and took the supernatant, then dialyzed the supernatant for 24 h and then freeze dried. Third, the abovementioned CD solid was dissolved in 25 ml of the aqueous solution, then 1 g of sodium acetate and 1 g of ferric chloride was added into 15 ml of CD solution, the mixed solution was sonicated for 8 h, then placed in an autoclave, and reacted at 210°C for 24 h; after cooling, they were centrifuged at 12,000 rpm for 10 min to acquire CDs-Fe_3O_4 nanomaterial.

Preparation of electrodes

First, 5.0 μl of CDs-Fe_3O_4 nanomaterial was slowly dropped on the glassy surface of the carbon electrode (GCE) to prepare a CDs-Fe_3O_4/GCE working electrode. Second, the CDs-Fe_3O_4/GCE electrode was immersed in 1 ml of 0.1 mM PBS, 8.00 mM EDC, and 8.00 mM NHS mixed solution for 3 h to activate the electrode, then it was rinsed with TE buffer solution. Third, the above electrode was immersed in 1 ml of 0.1 μM probe DNA to react for 24 h, and it was rinsed with TE buffer solution to prepare the DNA/CDs-Fe_3O_4/GCE probe electrode. Finally, the prepared electrode was stored at 4°C.

Preparation of the biosensor

The prepared DNA/CDs-Fe_3O_4/GCE was immersed into different concentrations (*C*) of *E. coli* O157:H7 solutions and reacted for 40 min at 42°C in a water bath. After the reaction, TE buffer solution was used to wash off non-specifically adsorbed

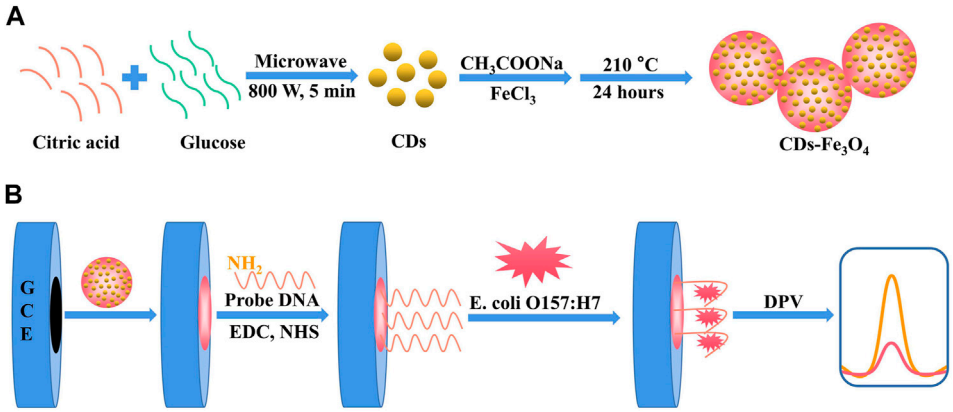

FIGURE 1 | A sensitive electrochemical DNA biosensor based on CDs/Fe_3O_4 nanocomposite is constructed for *E. coli* O157:H7 detection.

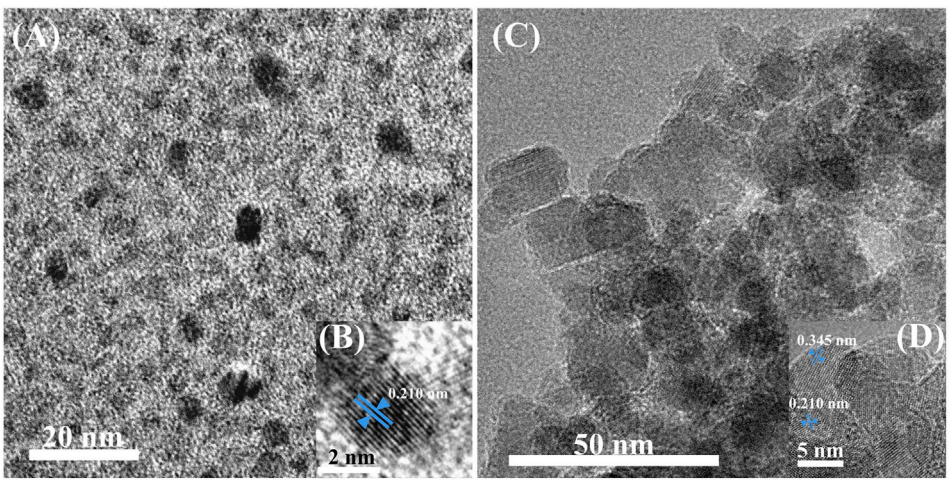

FIGURE 2 | TEM and HRTEM image of CDs **(A,B)** and carbon dots (CDs)-Fe_3O_4 nanomaterial **(C,D)**.

E. coli on the surface to obtain the *E. coli* O157:H7-DNA/CDs-Fe_3O_4/GCE. Cyclic voltammetry (CV) and differential pulse voltammetry (DPV) have characterized the layer-by-layer assembly of each modified electrode: the $[Fe(CN)_6]^{3-/4-}$ has been applied as the electrolyte. For the test parameters of CV, the potential scanning range was −0.2–0.8 V, and the scan rate(*5*) was 0.1 V/s. DPV was used to record the electrochemical signal changes before and after the identification of the electrode and different substances, and the potential interval was −0.2–0.8 V, the amplitude was 0.05 V, the pulse width was 0.05 s.

RESULTS AND DISCUSSION

Characterization of nanomaterial

Transmission electron microscopy (TEM) has characterized the morphologies of CDs and CDs-Fe_3O_4 nanomaterial. As shown in **Figure 2A**, the particle size distribution of the prepared CDs is relatively uniform, mainly at 3–4 nm. **Figure 2B** shows the high-resolution TEM (HRTEM) image of CDs. It shows that CDs have a good crystal lattice, and the lattice spacing is 0.210 nm, which is a typical (002) carbon crystal plane. As shown in **Figure 2C**, the particle size of the CDs-Fe_3O_4 nanomaterial was in the range of 15–40 nm. The HRTEM characterization of CDs-Fe_3O_4 (**Figure 2D**) shows that the nanomaterial has two lattice spacings, 0.345 and 0.210 nm, respectively. The corresponding crystal planes are (220) of the Fe_3O_4 and (002) of the carbon. The above morphology characterization can indicate that CDs-Fe_3O_4 nanomaterial has been successfully prepared.

Cyclic voltammetry behavior of electrodes

It is well known that $[Fe(CN)_6]^{3-/4-}$ is often used as a supporting electrolyte for electrochemical biosensors (Fan et al., 2018; Li et al., 2021; Nano et al., 2021). The working electrodes were electrochemically characterized by CVs in 1.0 mM $[Fe(CN)_6]^{3-/4-}$ and 0.1 M KCl solution (**Figure 3A**). On the surface of GCE, the

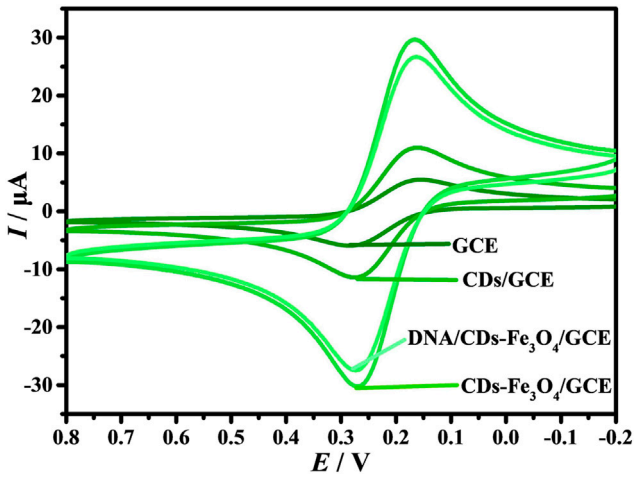

FIGURE 3 | CVs of the electrodes in the 1.0 mM $[Fe(CN)_6]^{3-/4-}$ and 0.1 M KCl solution (*v*: 0.1 V/s).

redox peak current (*I*) has good reversibility, and the oxidation peak potential (I_{pa}) and reduction peak potential (I_{pc}) are −6.616 and 5.958 A, respectively. When the CDs are modified on the surface of GCE, the I_{pa} and I_{pc} are promoted to −12.29 and 12.06 A, respectively, indicating that the prepared CDs have good conductivity. When the electrode is CDs-Fe_3O_4/GCE, the I_{pa} and I_{pc} are further enhanced, indicating that the introduction of Fe_3O_4 can improve the conductivity of the electrode. However, when the probe DNA is self-assembled on the surface of CDs-Fe_3O_4/GCE through carboxyammonia coupling reaction, the *I* decreases; the main reason is that the DNA molecules will hinder the diffusion of $[Fe(CN)_6]^{3-/4-}$ on the surface of CDs-Fe_3O_4/GCE. At the same time, the results indicate that the probe DNA was successfully modified on CDs-Fe_3O_4/GCE's surface.

Effects of scan rate

The effect of different *v* on the electrochemical response of DNA/CDs-Fe_3O_4/GCE in $[Fe(CN)_6]^{3-/4-}$ has also been studied. **Figure 4A** shows that in the process of increasing *v*, the *I* also keeps increasing. As shown in **Figure 4B**, the I_{pa} and I_{pc} show an excellent linear relationship with $v^{1/2}$, and the linear regression equations are $I_{pa} = 3.598 + 80.265\ v^{1/2}$ and $I_{pa} = -2.551 - 85.187\ v^{1/2}$, respectively. The results show that the electrochemical behavior of $[Fe(CN)_6]^{3-/4-}$ on the surface of DNA/CDs-Fe_3O_4/GCE is mainly affected by the diffusion-controlled process (Alam and Deen, 2020).

Effect of interaction time

The interaction time between the probe electrode and the target substance is one of the key factors affecting the performance of the biosensors. Therefore, the interaction time of *E. coli* O157:H7 with DNA/CDs-Fe_3O_4/GCE was studied. When the *C* of *E. coli* O157:H7 was 10 CFU/Ml, the optimum hybridization time was determined to be 40 min (**Supplementary Figure S1**). However, when the *C* of *E. coli* O157:H7 was 10^8 CFU/Ml, the optimum hybridization time was determined to be 35 min (**Supplementary Figure S2**). Therefore, in this electrochemical biosensor, the best reaction time between *E. coli* O157:H7 and DNA/CDs-Fe_3O_4/GCE is 40 min.

Specificity of the biosensor

The specificity of the electrochemical biosensor is a necessary factor to ensure the accuracy of the biosensor. Therefore, the interferences of different bacteria with 10^5 CFU/ml on the DNA/CDs-Fe_3O_4/GCE through DPV have been investigated, such as *S. aureus*, *Salmonella*, *Staphylococcus lactis* (*S. lactis*), and *Listeria*. **Figure 5A** shows that DNA/CDs-Fe_3O_4/GCE has almost no effect on other bacteria. However, the DNA/CDs-Fe_3O_4/GCE has a very strong response to *E. coli* O157:H7, and the I_{pa} drops by 53.42%. As shown in **Figure 5B**, other interfering substances have almost no effect on the determination of *E. coli* O157:H7. The above results show that the electrochemical biosensor based on DNA/CDs-Fe_3O_4/GCE for detecting *E. coli* O157:H7 has very excellent specificity and is expected to realize the determination of *E. coli* O157:H7 in real samples.

Sensitivity of the biosensor

As is known, DPV has been extensively applied in the construction of electrochemical sensors because it has good detection sensitivity. This study explores the sensitivity and

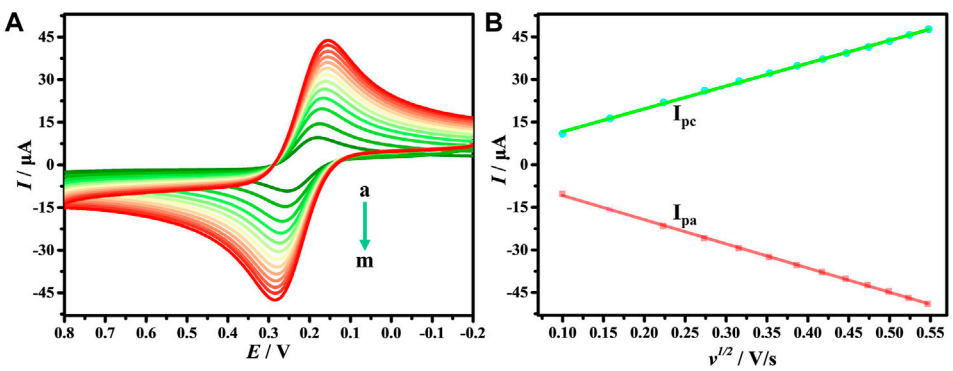

FIGURE 4 | (A) CVs of DNA/CDs-Fe_3O_4/GCE in1.0 mM $[Fe(CN)_6]^{3-/4-}$ and 0.1 M KCl solution with different *v* (a–m: 0.01, 0.025, 0.05, 0.075, 0.1, 0.125, 0.15, 0.175, 0.20, 0.225, 0.25, 0,275, 0.3 Vs^{-1}). **(B)** The relationship of redox peak current (*I*) with $v^{1/2}$.

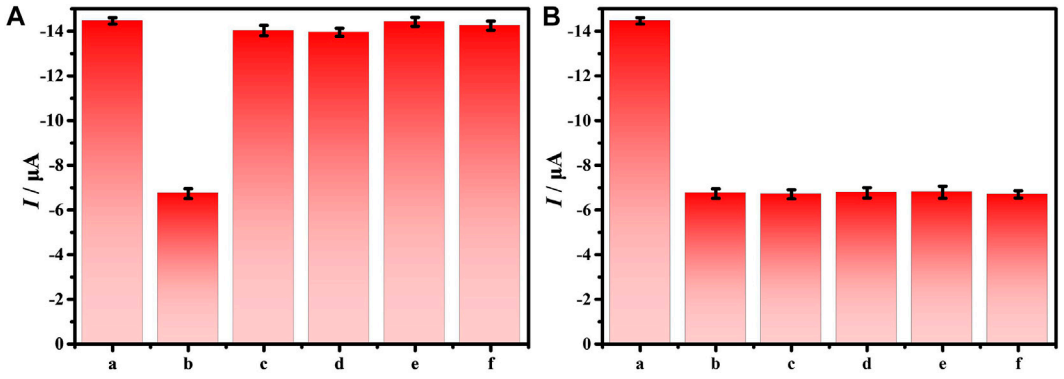

FIGURE 5 | (A) I_{pa} of 10^5 CFU/ml different bacteria on the DNA/CDs-Fe_3O_4/GCE, **(B)** I_{pa} of 10^5 CFU/ml *E. coli* O157:H7 with different bacteria on the DNA/CDs-Fe_3O_4/GCE (a: none, b: *E. coli* O157:H7, c: *S. aureus*, d: *Salmonella*, e: *S. lactis*, and f: *Listeria*).

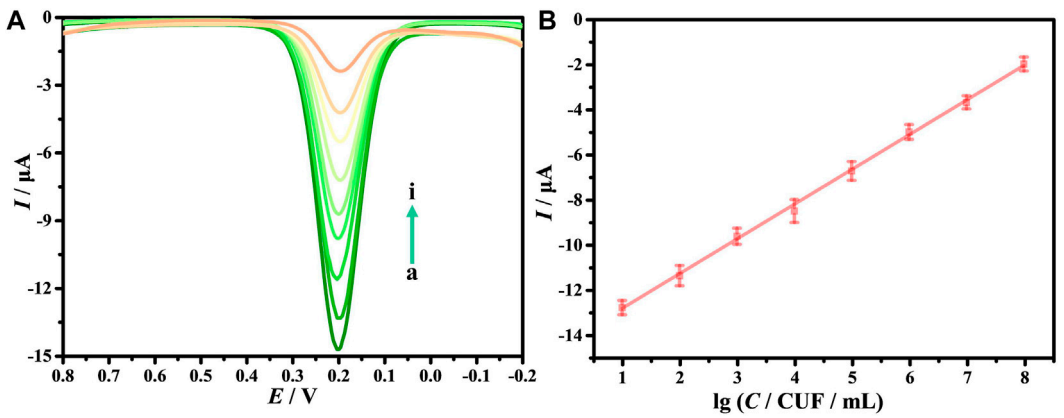

FIGURE 6 | (A) Differential pulse voltammetry (DPV) of *E. coli* O157:H7 with different concentrations (from a to i: 0, 10, 10^2, 10^3, 10^4, 10^5, 10^6, 10^7, 10^8 CFU/ml). **(B)** The relationship of I_{pa} with the lg*C*.

detection range of the electrochemical biosensors via DPV. **Figure 6A** shows that when *E. coli* O157:H7 interacts with DNA/CDs-Fe_3O_4/GCE, I_{pa} decreases as the *C* of *E. coli* O157:H7 increases. The main possible reason is *E. coli* O157:H7 has poor electrical conductivity, which affects the electrical conductivity of the working electrode's interface, leading to a weakening of the electrochemical signal. When the *C of E. coli* O157:H7 is in the range of 10–107 CFU/ml, the lg*C* and I_{pa} show a good linear relationship (**Figure 6B**): I_{pa} = 1.5422 lgC—14.387. At the same time, the detection limit (LOD) can reach 6.88 CFU/ml. Compared with other electrochemical biosensors for monitoring *E. coli* O157:H7 (**Table 1**), this electrochemical biosensor based on DNA/CDs-Fe_3O_4/GCE has very good sensitivity.

Repeatability and stability of the biosensor

To investigate the reproducibility of this biosensor, six DNA/CDs-Fe_3O_4/GCE working electrodes were prepared, and they have been applied to detect 10^5 CFU/ml of *E. coli* O157:H7 respectively. **Supplementary Figure S3** shows that the relative standard deviation (RSD) was 2.6%, which indicates the electrochemical biosensor based on DNA/CDs-Fe_3O_4/GCE for *E. coli* O157:H7 detection has good reproducibility. The stability of the electrochemical biosensor has been also studied; the DNA/CDs-Fe_3O_4/GCE was placed in a dryer at 4°C, and the above working electrode was applied to measure 10^5 CFU/ml of *E. coli* O157:H7 every 3 days. As shown in **Supplementary Figure S4** after 30 days, the I_{pa} was only dropped by 2.7%, which shows that the electrochemical biosensor based on DNA/CDs- Fe_3O_4/GCE has good stability.

Analysis of real samples

Since milk and water are often contaminated by *E. coli* O157:H7, it is very necessary to efficiently determine *E. coli* O157:H7 in milk and water. In this study, to verify the practical applicability of the biosensor, the electrochemical biosensor is used to determine the *E. coli* O157:H7 in milk and water. **Table 2**

TABLE 1 | Electrochemical biosensors for detecting *Escherichia* (*E.) coli* O157:H7.

Materials	Methods	Detection ranges (CFU/ml)	LOD (CFU/ml)	References
Graphene/AuNPs/array electrode	EIS	10^2–10^8	10^2	You et al. (2020)
rGO/Au@Pt/Screen printed carbon electrode	CV	4×10^3–4×10^8	4.5×10^2	Zhu et al. (2018)
rGO/PANI/Au@Pt/Nr/Screen printed carbon electrode	CV	8.9×10^3–8.9×10^9	2.84×10^3	Mo et al. (2019)
AuNPs/rGO-PVA/GCE	DPV	9.2–9.2×10^8	9.34	Qaanei et al. (2021)
AuNPs/3D DNA walker/GCE	DPV	10–10^4	7	Li et al. (2020)
$Cu_3(PO_4)_2$/methylene blue/Gold electrode	DPV	10^2–10^7	32	Bu et al. (2020)
Cocoon-like DNA nanostructures/Gold electrode	DPV	10–10^6	10	Bai et al. (2020)
DNA/CDs-Fe_3O_4/GCE	DPV	10–10^8	6.88	This work

TABLE 2 | Electrochemical biosensor for monitoring *E. coli* O157:H7 in milk and water samples.

Sample	Spike (CFU/ml)	Found (CFU/ml)	Recovery (%)	Detection by ELISA
Milk	10^3	9.52×10^2	95.2	9.46×10^2
	10^4	9.96×10^3	99.6	9.53×10^3
	10^5	1.02×10^5	102.0	9.91×10^4
Water	10^3	9.93×10^2	99.3	9.86×10^2
	10^4	9.89×10^3	98.9	9.81×10^3
	10^5	9.79×10^4	97.9	9.69×10^4

shows that 10^3, 10^4, and 10^5 CFU/ml of *E. coli* O157:H7 were added to the samples, and the recovery rates are between 95.2% and 102.0%, At the same time, the results were consistent with ELISA results, indicating that the method is feasible for monitoring *E. coli* O157:H7 in milk and water samples.

CONCLUSIONS

In conclusion, a sensitive electrochemical DNA biosensor has been prepared for monitoring *E. coli* O157:H7 by CDs-Fe_3O_4 nanomaterial. Under the best conditions, when the *C* of *E. coli* O157:H7 is in the range of 10–10^8 CFU/ml, the lg*C* has a good linear relationship with the I_{pa}, and the LOD reaches 6.88 CFU/ml. At the same time, the electrochemical DNA biosensor has been successfully used to determine *E. coli* O157:H7 in milk and water samples. Therefore, this research provides an effective biosensor manufacturing strategy, which is expected to provide a reference for the preparation of electrochemical DNA biosensors for other bacteria or viruses detection.

DATA AVAILABILITY STATEMENT

The original contributions presented in the study are included in the article/**Supplementary Material**. Further inquiries can be directed to the corresponding authors.

AUTHOR CONTRIBUTIONS

XL and YM handled the data curation, and preparation and writing of the original draft. CH and XM were also involved in the writing of the original draft. YL, MY, and YK edited the manuscript. HZ participated in the reviewing of the draft. QH contributed to the reviewing, editing, and writing of the manuscript.

FUNDING

This work has been supported by the National Natural Science Foundation of China (No. 82060599), the Natural Science Foundation of Jiangxi (No. 20202BABL213018), the Science and Technology Project of the Education Department of Jiangxi Province (Nos. GJJ190795, GJJ190775 and GJJ190827), the Science and Technology Project of Jiangxi Health Committee (No. 202131033), the Research Fund of Gannan Medical University (Nos. ZD201901, YQ202003, YB201905, YB201931, YB201911), and the Science and Technology Plan Post-subsidy Project of Ganzhou (No. 2019-60-174).

SUPPLEMENTARY MATERIAL

The Supplementary Material for this article can be found online at: https://www.frontiersin.org/articles/10.3389/fchem.2021.769648/full#supplementary-material

REFERENCES

Alam, A. U., and Deen, M. J. (2020). Bisphenol A Electrochemical Sensor Using Graphene Oxide and β-Cyclodextrin-Functionalized Multi-Walled Carbon Nanotubes. *Anal. Chem.* 92, 5532–5539. doi:10.1021/acs.analchem.0c00402

Bai, H., Bu, S., Liu, W., Wang, C., Li, Z., Hao, Z., et al. (2020). An Electrochemical Aptasensor Based on Cocoon-Like DNA Nanostructure Signal Amplification for the Detection of *Escherichia C* O157:H7. *Analyst* 145, 7340–7348. doi:10.1039/d0an01258k

Broza, Y. Y., Zhou, X., Yuan, M., Qu, D., Zheng, Y., Vishinkin, R., et al. (2019). Disease Detection with Molecular Biomarkers: From Chemistry of Body Fluids to Nature-Inspired Chemical Sensors. *Chem. Rev.* 119, 11761–11817. doi:10.1021/acs.chemrev.9b00437

Bu, S., Wang, K., Li, Z., Wang, C., Hao, Z., Liu, W., et al. (2020). An Electrochemical Biosensor Based on Methylene Blue-Loaded Nanocomposites as Signal-Amplifying Tags to Detect Pathogenic Bacteria. *Analyst* 145, 4328–4334. doi:10.1039/d0an00470g

Chen, B., Chen, D., Li, F., Lin, X., and Huang, Q. (2018). Graphitic Porous Carbon: Efficient Synthesis by a Combustion Method and Application as a Highly Selective Biosensor. *J. Mater. Chem. B* 6, 7684–7691. doi:10.1039/c8tb02139b

Dong, L. H., Zhang, L., Jing, J., Wang, J. N., Wang, J., and Chen, W. J. (2015). Development of Droplet Digital Polymerase Chain Reaction for Quantifying Escherichia Coli O157: H7. *Chin. J. Anal. Chem.* 43, 319–324. doi:10.11895/j.issn.0253-3820.140569

Dong, Y., Li, F., and Wang, Y. (2020). Low-Dimension Nanomaterial-Based Sensing Matrices for Antibiotics Detection: A Mini Review. *Front. Chem.* 8, 551. doi:10.3389/fchem.2020.00551

Duan, R., Fang, X., and Wang, D. (2021). A Methylene Blue Assisted Electrochemical Sensor for Determination of Drug Resistance of *Escherichia C. Front. Chem.* 9, 689735. doi:10.3389/fchem.2021.689735

Enesca, A. (2020). Enhancing the Photocatalytic Activity of SnO2-TiO2 and ZnO-TiO2 Tandem Structures toward Indoor Air Decontamination. *Front. Chem.* 8, 583270. doi:10.3389/fchem.2020.583270

Fan, T., Du, Y., Yao, Y., Wu, J., Meng, S., Luo, J., et al. (2018). Rolling Circle Amplification Triggered Poly Adenine-Gold Nanoparticles Production for Label-Free Electrochemical Detection of Thrombin. *Sensors Actuators B: Chem.* 266, 9–18. doi:10.1016/j.snb.2018.03.112

Giang, N. N., Won, H. J., Lee, G., and Park, S. Y. (2021). Cancer Cells Targeted Visible Light and Alkaline Phosphatase-Responsive TiO2/Cu2+ Carbon Dots-Coated Wireless Electrochemical Biosensor. *Chem. Eng. J.* 417, 129196. doi:10.1016/j.cej.2021.129196

Guo, Q., Han, J.-J., Shan, S., Liu, D.-F., Wu, S.-S., Xiong, Y.-H., et al. (2016). DNA-Based Hybridization Chain Reaction and Biotin-Streptavidin Signal Amplification for Sensitive Detection of *Escherichia C* O157:H7 through ELISA. *Biosens. Bioelectron.* 86, 990–995. doi:10.1016/j.bios.2016.07.049

He, H., Meng, S., Li, H., Yang, Q., Xu, Z., Chen, X., et al. (2021a). Nanoplatform Based on GSH-Responsive Mesoporous Silica Nanoparticles for Cancer Therapy and Mitochondrial Targeted Imaging. *Microchim Acta* 188, 154. doi:10.1007/s00604-021-04810-4

He, S., Huang, Q., Zhang, Y., Zhang, H., Xu, H., Li, X., et al. (2021b). Magnetic Beads-Based Multicolor Colorimetric Immunoassay for Ultrasensitive Detection of Aflatoxin B1. *Chin. Chem. Lett.* 32, 1462–1465. doi:10.1016/j.cclet.2020.09.047

Hou, K., Zhao, P., Chen, Y., Li, G., Lin, Y., Chen, D., et al. (2020). Rapid Detection of Bifidobacterium Bifidum in Feces Sample by Highly Sensitive Quartz Crystal Microbalance Immunosensor. *Front. Chem.* 8, 548. doi:10.3389/fchem.2020.00548

Huang, Q., Lin, X., Zhu, J.-J., and Tong, Q.-X. (2017). Pd-Au@carbon Dots Nanocomposite: Facile Synthesis and Application as an Ultrasensitive Electrochemical Biosensor for Determination of Colitoxin DNA in Human Serum. *Biosens. Bioelectron.* 94, 507–512. doi:10.1016/j.bios.2017.03.048

Huang, Q., Lin, X., Tong, L., and Tong, Q.-X. (2020). Graphene Quantum Dots/Multiwalled Carbon Nanotubes Composite-Based Electrochemical Sensor for Detecting Dopamine Release from Living Cells. *ACS Sustain. Chem. Eng.* 8, 1644–1650. doi:10.1021/acssuschemeng.9b06623

Jia, A., Liu, B., Liu, H., Li, Q., and Yun, Y. (2020). Interface Design of SnO2@PANI Nanotube with Enhanced Sensing Performance for Ammonia Detection at Room Temperature. *Front. Chem.* 8, 383. doi:10.3389/fchem.2020.00383

Kuang, Y., Zhang, J., Xiong, M., Zeng, W., Lin, X., Yi, X., et al. (2020). A Novel Nanosystem Realizing Curcumin Delivery Based on Fe3O4@Carbon Dots Nanocomposite for Alzheimer's Disease Therapy. *Front. Bioeng. Biotechnol.* 8, 614906. doi:10.3389/fbioe.2020.614906

Lee, H. C., Hsieh, E. Y., Yong, K., and Nam, S. (2020). Multiaxially-Stretchable Kirigami-Patterned Mesh Design for Graphene Sensor Devices. *Nano Res.* 13, 1406–1412. doi:10.1007/s12274-020-2662-7

Li, Z., Fu, Y., Fang, W., and Li, Y. (2015a). Electrochemical Impedance Immunosensor Based on Self-Assembled Monolayers for Rapid Detection of *Escherichia C* O157:H7 with Signal Amplification Using Lectin. *Sensors* 15, 19212–19224. doi:10.3390/s150819212

Li, Z., Yu, Y., Li, Z., Wu, T., and Yin, J. (2015b). The Art of Signal Transforming: Electrodes and Their Smart Applications in Electrochemical Sensing. *Anal. Methods* 7, 9732–9743. doi:10.1039/c5ay02373d

Li, Z., Ye, Z., Fu, Y., Xiong, Y., and Li, Y. (2016). A Portable Electrochemical Immunosensor for Rapid Detection of Trace Aflatoxin B1 in rice. *Anal. Methods* 8, 548–553. doi:10.1039/c5ay02643a

Li, Y., Liu, H., Huang, H., Deng, J., Fang, L., Luo, J., et al. (2020). A Sensitive Electrochemical Strategy via Multiple Amplification Reactions for the Detection of *E. C* O157: H7. *Biosens. Bioelectron.* 147, 111752. doi:10.1016/j.bios.2019.111752

Li, C., Cui, Y., Ren, J., Zou, J., Kuang, W., Sun, X., et al. (2021). Novel Cells-Based Electrochemical Sensor for Investigating the Interactions of Cancer Cells with Molecules and Screening Multitarget Anticancer Drugs. *Anal. Chem.* 93, 1480–1488. doi:10.1021/acs.analchem.0c03566

Lin, X., Xiong, M., Zhang, J., He, C., Ma, X., Zhang, H., et al. (2021). Carbon Dots Based on Natural Resources: Synthesis and Applications in Sensors. *Microchemical J.* 160, 105604. doi:10.1016/j.microc.2020.105604

Liu, L., Anwar, S., Ding, H., Xu, M., Yin, Q., Xiao, Y., et al. (2019). Electrochemical Sensor Based on F,N-Doped Carbon Dots Decorated Laccase for Detection of Catechol. *J. Electroanalytical Chem.* 840, 84–92. doi:10.1016/j.jelechem.2019.03.071

Liu, H., Yao, J., Guo, H., Cai, X., Jiang, Y., Lin, M., et al. (2020a). Tumor Microenvironment-Responsive Nanomaterials as Targeted Delivery Carriers for Photodynamic Anticancer Therapy. *Front. Chem.* 8, 758. doi:10.3389/fchem.2020.00758

Liu, Y., Zhou, M., Jin, C., Zeng, J., Huang, C., Song, Q., et al. (2020b). Preparation of a Sensor Based on Biomass Porous Carbon/Covalent-Organic Frame Composites for Pesticide Residues Detection. *Front. Chem.* 8, 643. doi:10.3389/fchem.2020.00643

Mao, X., Wan, Y., Li, Z., Chen, L., Lew, H., and Yang, H. (2020). Analysis of Organophosphorus and Pyrethroid Pesticides in Organic and Conventional Vegetables Using QuEChERS Combined with Dispersive Liquid-Liquid Microextraction Based on the Solidification of Floating Organic Droplet. *Food Chem.* 309, 125755. doi:10.1016/j.foodchem.2019.125755

Mao, X., Xiao, W., Wan, Y., Li, Z., Luo, D., and Yang, H. (2021). Dispersive Solid-Phase Extraction Using Microporous Metal-Organic Framework UiO-66: Improving the Matrix Compounds Removal for Assaying Pesticide Residues in Organic and Conventional Vegetables. *Food Chem.* 345, 128807. doi:10.1016/j.foodchem.2020.128807

Mo, X., Wu, Z., Huang, J., Zhao, G., and Dou, W. (2019). A Sensitive and Regenerative Electrochemical Immunosensor for Quantitative Detection of *Escherichia C* O157:H7 Based on Stable Polyaniline Coated Screen-Printed Carbon Electrode and rGO-NR-Au@Pt. *Anal. Methods* 11, 1475–1482. doi:10.1039/c8ay02594k

Nano, A., Furst, A. L., Hill, M. G., and Barton, J. K. (2021). DNA Electrochemistry: Charge-Transport Pathways through DNA Films on Gold. *J. Am. Chem. Soc.* 143, 11631–11640. doi:10.1021/jacs.1c04713

Qaanei, M., Taheri, R. A., and Eskandari, K. (2021). Electrochemical Aptasensor for *Escherichia coli* O157:H7 Bacteria Detection Using a Nanocomposite of Reduced Graphene Oxide, Gold Nanoparticles and Polyvinyl Alcohol. *Anal. Methods* 13, 3101–3109. doi:10.1039/d1ay00563d

Sri, S., Lakshmi, G. B. V. S., Gulati, P., Chauhan, D., Thakkar, A., and Solanki, P. R. (2021). Simple and Facile Carbon Dots Based Electrochemical Biosensor for TNF-α Targeting in Cancer Patient's Sample. *Analytica Chim. Acta* 1182, 338909. doi:10.1016/j.aca.2021.338909

Thakur, N., Thakur, S., Chatterjee, S., Das, J., and Sil, P. C. (2020). Nanoparticles as Smart Carriers for Enhanced Cancer Immunotherapy. *Front. Chem.* 8, 597806. doi:10.3389/fchem.2020.597806

Wu, X., Jiang, X., Fan, T., Zheng, Z., Liu, Z., Chen, Y., et al. (2020). Recent Advances in Photodynamic Therapy Based on Emerging Two-Dimensional Layered Nanomaterials. *Nano Res.* 13, 1485–1508. doi:10.1007/s12274-020-2750-8

Xie, Q.-Y., Wu, Y.-H., Xiong, Q.-R., Xu, H.-Y., Xiong, Y.-H., Liu, K., et al. (2014). Advantages of Fluorescent Microspheres Compared with Colloidal Gold as a Label in Immunochromatographic Lateral Flow Assays. *Biosens. Bioelectron.* 54, 262–265. doi:10.1016/j.bios.2013.11.002

Xu, Z., and Liu, Y. (2021). The Behavior of Carbonized Polymer Dots at the Nano-Bio Interface and Their Luminescent Mechanism: A Physical Chemistry Perspective. *Chin. J. Chem.* 39, 265–273. doi:10.1002/cjoc.202000334

Ye, Y., Su, W., Zhang, J., Huang, Y., Chen, W., and Huang, Y. (2020). Development of a Combined Immunochromatographic Lateral Flow Assay for Accurate and Rapid *Escherichia C* O157:H7 Detection. *Lett. Appl. Microbiol.* 71, 311–319. doi:10.1111/lam.13297

Yi, X., Zeng, W., Wang, C., Chen, Y., Zheng, L., Zhu, X., et al. (2021). A Step-by-Step Multiple Stimuli-Responsive Metal-Phenolic Network Prodrug Nanoparticles for Chemotherapy. *Nano Res.* doi:10.1007/s12274-021-3626-2

You, Z., Qiu, Q., Chen, H., Feng, Y., Wang, X., Wang, Y., et al. (2020). Laser-Induced Noble Metal Nanoparticle-Graphene Composites Enabled Flexible Biosensor for Pathogen Detection. *Biosens. Bioelectron.* 150, 111896. doi:10.1016/j.bios.2019.111896

Zhang, C., and Du, X. (2020). Electrochemical Sensors Based on Carbon Nanomaterial Used in Diagnosing Metabolic Disease. *Front. Chem.* 8, 651. doi:10.3389/fchem.2020.00651

Zhang, M., Su, R., Zhong, J., Fei, L., Cai, W., Guan, Q., et al. (2019). Red/Orange Dual-Emissive Carbon Dots for pH Sensing and Cell Imaging. *Nano Res.* 12, 815–821. doi:10.1007/s12274-019-2293-z

Zhao, Y., Zeng, D., Yan, C., Chen, W., Ren, J., Jiang, Y., et al. (2020). Rapid and Accurate Detection of *Escherichia C* O157:H7 in Beef Using Microfluidic Wax-Printed Paper-Based ELISA. *Analyst* 145, 3106–3115. doi:10.1039/d0an00224k

Zhou, S., Lu, C., Li, Y., Xue, L., Zhao, C., Tian, G., et al. (2020). Gold Nanobones Enhanced Ultrasensitive Surface-Enhanced Raman Scattering Aptasensor for Detecting *Escherichia C* O157:H7. *ACS Sens.* 5, 588–596. doi:10.1021/acssensors.9b02600

Zhu, F., Zhao, G., and Dou, W. (2018). A Non-Enzymatic Electrochemical Immunoassay for Quantitative Detection of *Escherichia coli* O157:H7 Using Au@Pt and Graphene. *Anal. Biochem.* 559, 34–43. doi:10.1016/j.ab.2018.08.016

Zhuang, Z., Huang, J., Li, Y., Zhou, L., and Mai, L. (2019a). The Holy Grail in Platinum-Free Electrocatalytic Hydrogen Evolution: Molybdenum-Based Catalysts and Recent Advances. *ChemElectroChem* 6, 3570–3589. doi:10.1002/celc.201900143

Zhuang, Z., Li, Y., Huang, J., Li, Z., Zhao, K., Zhao, Y., et al. (2019b). Sisyphus Effects in Hydrogen Electrochemistry on Metal Silicides Enabled by Silicene Subunit Edge. *Sci. Bull.* 64, 617–624. doi:10.1016/j.scib.2019.04.005

Zhuang, Z., Li, Y., Li, Y., Huang, J., Wei, B., Sun, R., et al. (2021). Atomically Dispersed Nonmagnetic Electron Traps Improve Oxygen Reduction Activity of Perovskite Oxides. *Energy Environ. Sci.* 14, 1016–1028. doi:10.1039/d0ee03701j

Conflict of Interest: The authors declare that the research was conducted in the absence of any commercial or financial relationships that could be construed as a potential conflict of interest.

frontiers in Chemistry

REVIEW
published: 06 January 2022
doi: 10.3389/fchem.2021.782307

Recent Advances in Metal/Alloy Nano Coatings for Carbon Nanotubes Based on Electroless Plating

Lei Zhang[1,2,3], *Yi Chao*[4], *Kenan Yang*[1], *Daodao Xue*[4] *and Shisheng Zhou*[4,5]*

[1]School of Mechanical and Precision Instrument Engineering, Xi'an University of Technology, Xi'an, China, [3]Western Institute of Modern Vocational Education, Xianyang, China, [2]Shaanxi Polytechnic Institute, Xianyang, China, [4]Faculty of Printing, Packaging Engineering and Digital Media Technology, Xi'an University of Technology, Xi'an, China, [5]Shaanxi Provincial Key Laboratory of Printing and Packaging Engineering, Xi'an University of Technology, Xi'an, China

A large number of researches on the electroless plating of carbon nanotubes and their applications after plating have emerged, which has attracted more and more attention. In this review article, the existing electroless plating methods for carbon nanotubes were briefly summarized, and the surface coatings were listed and analyzed in detail. At last, the related applications after electroless metal/alloy coatings of carbon nanotubes were discussed in detail. This study aims to provide a reference for the research and improvement of different electroless metals/alloys coatings of carbon nanotubes. After a clear understanding of the electroless metal/alloy coatings of carbon nanotubes, the appropriate coating can be selected according to the actual situation, so that the carbon nanotubes after plating can be used as reinforcement and modification materials for better satisfaction of the needs, and the application of plated carbon nanotubes has reference significance in more fields.

Keywords: carbon nanotubes, electroless plating, meta, alloy, nano coatings

OPEN ACCESS

Edited by:
Guoqing Wang,
Ocean University of China, China

Reviewed by:
Xiaozhou Li,
Qilu University of Technology, China
Masato Sone,
Tokyo Institute of Technology, Japan
Jian Li,
Northeast Forestry University, China

***Correspondence:**
Shisheng Zhou
zhoushisheng@xaut.edu.cn

Specialty section:
This article was submitted to Nanoscience, a section of the journal Frontiers in Chemistry

Received: *24 September 2021*
Accepted: *20 December 2021*
Published: *06 January 2022*

Citation:
Zhang L, Chao Y, Yang K, Xue D and Zhou S (2022) Recent Advances in Metal/Alloy Nano Coatings for Carbon Nanotubes Based on Electroless Plating. Front. Chem. 9:782307. doi: 10.3389/fchem.2021.782307

1 INTRODUCTION

1.1 Preamble

Carbon nanotubes (CNTs), as quasi one-dimensional nanomaterials, have been widely studied and applied since their discovery due to their excellent mechanical properties and special electrochemical, thermal and magnetic properties (Li et al., 2009). They have been widely used in interconnects (Ngo et al., 2007; Desmaris et al., 2014), energy storage (Nihei et al., 2005), transistors (Martel et al., 1998; Tans et al., 1998), touch screens (Cao et al., 2015), membrane switches and other conductive and thermally conductive materials (Han et al., 2012). These capabilities are due in large part to their extremely small size (about 1–10 nm in diameter), high aspect ratio (>1,000), high structural and chemical stability (Liu et al., 2007). However, it has been found that for some applications where metallic properties (e.g., interconnects), conductivity, thermal conductivity, and magnetism are required, the use of pure CNTs as additive materials has major limitations. As pristine CNTs have low chemical activity, large degree of entanglement, and insignificant magnetic properties, if they are directly added to metal matrix composites, they will easily agglomerate due to poor wettability and weak interfacial bonding between them and the matrix material, which will not play a proper role in strengthening the matrix material but reduce the physical and mechanical properties of the material (Zhang et al., 2015). Accordingly, it is necessary to modify CNTs to better exploit their advantages in matrix materials. Electroplating has been proved successful in fabricating film/bulk composite with good mate rial properties but not

suitable for individual hybrid metal/CNT structure. Electroless plating could be a good method to fabricate individually separated metal/CNT nanowire owing to its unique deposition process (Cha et al., 2005; Peng and Chen, 2009). Electroless plating is a simple, energy-saving and environmentally friendly electroless deposition technology. It refers to the reduction of metal ions in the plating solution to metal and deposits in the active center of the material to be plated through a controllable redox reaction with a suitable reducing agent under the condition of no external current (Maqbool et al., 2013; Jagannatham and Haridoss, 2015). The electroless plating method has the characteristics of simple process, easy operation, uniform coating, low porosity, and good wear resistance. This process does not require an external power supply during the preparation process, and the materials immersed in the plating solution can be evenly covered by the plating layer. Therefore, this technology has received widespread attention. For example, the modification of wood, fibrils (Hui et al., 2020; Chen et al., 2021) often uses electroless plating. Due to its wide range of use, high quality of plating, and the ability to obtain a complete and uniform metal/alloy coatings on the surface of metallic or nonmetallic materials of any shape. Its appearance provides a convenient way for the successful modification of carbon nanotubes. Although different from the unique anisotropic multi-channel structure characteristics of easy electroless plating of wood (Hui et al., 2021), carbon nanotubes have a large aspect ratio and a large specific surface area, excellent mechanical properties and special electrochemical, thermal and magnetic properties. Increasing the activity of carbon nanotubes through plating has a greater strengthening effect on the material in terms of mechanics, electrical conductivity, thermal conductivity, tribology, and corrosion resistance. So it can be used as a filler to be more widely used in metal matrix composite materials, magnetic composite materials, electrically and thermally conductive materials, energy storage materials and catalytic materials, etc. A large number of studies have found that high-quality metal/alloy coatings have been successfully plated on the surface of pretreated carbon nanotubes by controlling the plating conditions (Chen et al., 2000; Chen et al., 2002).

At present, the common coatings on the surface of CNTs include silver, copper, nickel and alloys (such as Ni-P, Ni-Co, Ni-Co-P, etc.), while gold and cobalt coatings are relatively rare. Plating combines the characteristics of the metal/alloy of the coating with the characteristics of the CNTs themselves, thereby imparting stronger or new properties to the CNTs (Elbasuney et al., 2019). It has been found that the coating increases the activity of CNTs, improves their physical and mechanical properties, and provides good wettability and interfacial bonding between them and the matrix material, which can be used as fillers in a wider range of applications such as metal matrix composites, magnetic composites, electrically and thermally conductive materials, energy storage materials, and catalytic materials, which have a greater strengthening effect on materials in terms of mechanics, electrical conductivity, thermal conductivity, tribology, and corrosion resistance (Esawi et al., 2009).

1.2 Synopsis

Following this introduction section, this review will, in **Section 2**, make a brief discussion of fundamental aspects of underlying electroless plating processes. In **Section 3**, this study will elaborate the classification of electroless plating metal alloy plating and its physical and mechanical properties after electroless plating. **Section 4** details the application of carbon nanotubes after electroless plating. Finally, in **Section 5**, the review ends with conclusion and future prospect.

2 METHODS FOR ELECTROLESS PLATING OF CARBON NANOTUBES

At present, there are two technological methods for electroless plating of CNTs, namely, the traditional direct coating with mixed aqueous solution and the new ultrasonic spray atomization assisted electroless plating (EPUSA). The methods for electroless plating of CNTs will be analyzed and compared in detail below.

2.1 Traditional Method

The traditional electroless plating is carried out directly in the form of mixed aqueous solution. Usually, the reducing agent and the metal salt solution in the plating bath are directly mixed in a certain proportion or added dropwise (Zhao et al., 2017). However, it takes a certain amount of time to diffuse and homogenize the components in the plating solution, which will cause spatial inhomogeneity in the entire system, and the metal salt, reduced agent and the failed uniform mixing of CNTs. In addition, CNTs will agglomerate in the plating solution, and the overall quality of the resulting plating layer is not high.

2.2 Ultrasonic Spray Atomization Method (EPUSA)

In the EPUSA method, the suspension of the metal salt solution and the reducing agent-CNTs were ultrasonically atomized into droplet form; then the two were brought into contact in the reaction vessel and the metal reaction was completed. Since each initially contained reducing agent-CNTs or metal ions was relatively limited, it could be ensured that two or more simultaneous reduction reactions occurred when contacting, so that the reduced metal nanoparticles were deposited on the active sites on the surface of the CNTs. This process was realized within micrometer scale droplets generated by ultrasonic spray atomization, for the purpose of getting higher uniformity of silver deposits/coatings on MWCNTs (Choi et al., 2014).

3 CLASSIFICATION OF ELECTROLESS PLATING ON THE SURFACE OF CARBON NANOTUBES

3.1 Carbon Nanotubes Electroless Gold Plating

Gold has excellent corrosion resistance, good electrical conductivity, thermal conductivity and processability, so it can

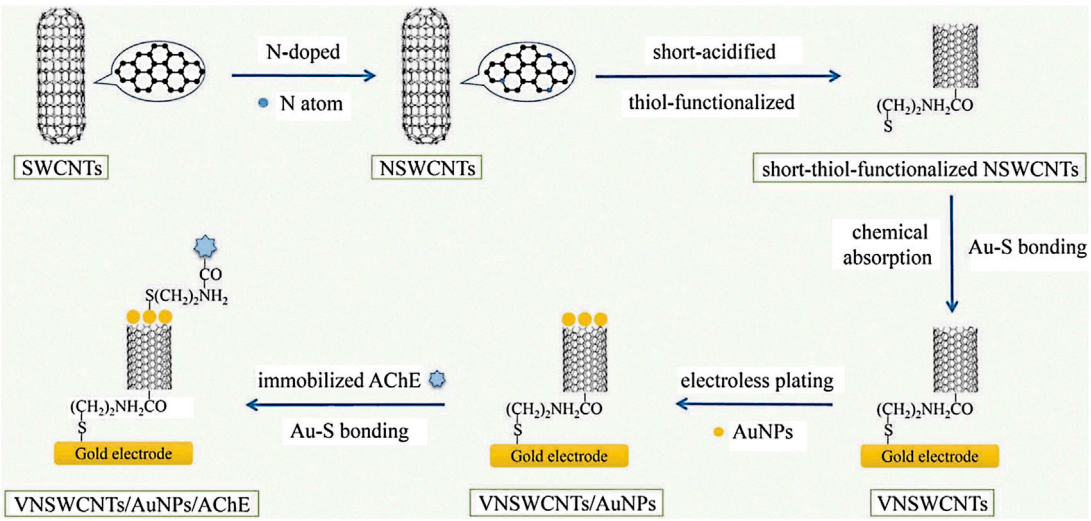

FIGURE 1 | The construction of the AChE biosensor (Xu et al., 2019) (published in Int J Environ Anal Chem 2019).

be used in electronics, communications technology, chemical technology and many other fields (Dondoi et al., 2006; Yang et al., 2014). However, as a precious metal, gold is very expensive, which largely limits its application. CNTs are very economical and have unique physical and mechanical properties, which have successfully attracted the wide attention. Researchers have combined gold with CNTs and coated them with a layer of gold nanoparticles, which not only retains the excellent properties of gold but also increases the cost-effectiveness of the coating.

Xu et al. constructed an acetylcholinesterase (AChE) biosensor based on gold nanoparticles (AuNPs) chemically plated on vertical nitrogen-doped single-walled CNTs (VNSWCNTs) (the schematic diagram for the construction process is shown in **Figure 1**). The modified gold electrode was soaked in 2 ml distilled water contained 5 μL of 50 mM HAuCl4 in HCl for 30 min. This was followed by rapid addition of 15 μL of 50 mM reducing agent NaBH4 in NaOH to the solution in the reagent bottle, then the colour was slightly lavender (Martin et al., 2010; Chaudhari et al., 2016). After standing for 30 min, the modified gold electrode was taken out to obtain an Au/VNSWCNTs/AuNPs modified electrode. Finally, this electrode was immersed in 5 mM NH2–(CH2)2–SH solution for 4 h, and the AuNPs were attached to NH2–(CH2)2–SH *via* Au–S bonding (Ju et al., 2015). The modified electrode was then coated with 10 μL (2 U/mL) AChE; after that, the amino group at the other end of NH2–(CH2)2–SH cross-linked with carboxyl bond of AChE. The AuNPs constructed by this method are considered to be more stable than the covalent self-assembled AuNPs. Due to the synergistic effect between AuNPs and VNSWCNT, the AChE biosensor prepared by this method has excellent electron transport capability, and it performs better than the biosensor in previous studies in terms of stability, sensitivity and durability (Xu et al., 2019). Besides, Feng et al. prepared the sulfhydryl-modified carbon nanotubes groups by reacting the pretreated carbon nanotubes with LiAlH4, PBr3 and NaHS in turn, and then placed them in an electroless plating solution to prepare quasi-one-dimensional gold nanowires with an average diameter of less than 50 nm. Experiments have proved that the formation mechanism of gold nanowires is that in the presence of sulfhydryl groups (-SH), gold nanoparticles self-assemble on the surface of carbon nanotubes (CNTs) (Feng, 2008).

3.2 Carbon Nanotubes Electroless Cobalt Plating

Due to the superior magnetic properties, cobalt is widely used in the manufacture of high-performance magnetic materials. Magnetic materials are important functional materials, and they play a very important role in the electronics industry and high-tech fields (Guo et al., 2006; Turtelli et al., 2006; Ruitao and Kang, 2008; Hyie et al., 2017). Electroless plating was utilized to deposit Cobalt (Co.) on the surface of multi-walled carbon nanotubes (MWCNTs), the Co-MWCNTs composites showed a higher impedance which implies a better potential absorbing property and makes Co-MWCNTs probable to be utilized in electromagnetic absorbing field (Bao et al., 2011). By chemically coating CNTs with cobalt to give them magnetic properties, they are widely used as magnetic reinforcements for composite materials.

After the pretreated carbon nanotubes are electrolessly plated with cobalt under a suitable process, it is found that the surface is uniformly and continuously covered with a layer of centered cubic nanocrystalline cobalt coating. After metallization, the carbon nanotubes still keep the original fibrous form, and the thickness of the resulting coating is about 5–15 nm. Studies have shown that changes in the pH value and plating time during the electroless plating process have a great influence on the thickness and uniformity of the coating (Wilson et al., 2011). After cobalt coating, the magnetic properties of carbon nanotubes are greatly

improved. It was found that the saturation magnetization strength of Co-MWCNTs was 2.81 emu/g and the coercivity was about 4 times higher than that of cobalt powder (308Oe) after chemical cobalt plating. Bao et al., explored the effect of metal salt concentration and pH value change on the quality of the plating during the chemical cobalt plating process. It was found that the electromagnetic properties of Co-MWCNTs composites were better than those of MWCNTs composites, and the chemical cobalt plating process improved the magnetic properties of the carbon nanotube composites, and calculations based on the measured parameters showed that the cobalt-plated carbon nanotube composites improved the microwave absorption capacity of the carbon nanotube composites (Bao et al., 2011). The Co-MWNT composites have lower surface reflection, which have the potential to be applied as the matching part in two-layer absorbing material.

3.3 Carbon Nanotubes Electroless Silver Plating

Silver has excellent ductility, electrical and thermal conductivity, and it is widely used in electrical and electronic materials, photographic materials, chemical materials, etc. The deposition of silver on CNTs allows for combination or enhancement of properties, and has been extensively studied in applications such as field emission, polymer-reinforced fillers, and composite materials (Pal and Sharma, 2015). The formation of silver plating on the surface of CNTs is achieved by the reduction of silver ions deposited on their active sites by reducing agents. With the appropriate increase of plating time, the reduced silver nanoparticles grow up along the nucleation center in the normal and tangential directions and gradually cover the whole surface of CNTs, making the density of CNTs increase and the resistivity decrease after plating (Feng and Yuan 2004). Youngseok et al. have developed a novel silver/conducting polymer composite by the incorporation of CNTs, resulting in a significant increase in electrical conductivity. The interfacial contact was improved by the electroless plating of silver on the CNTs (Oh et al., 2008).

3.3.1 Physical Properties of Silver-Plated Carbon Nanotubes

The deposition uniformity and microstructure characteristics of the silver coating on CNTs are important physical characteristics after silver plating (Daoush et al., 2009). Numerous studies have found that the more uniform the carbon nanotubes are dispersed during electroless silver plating, the more uniform the coating morphology will be. Conversely, the more uniform the silver coating, the less likely the carbon nanotubes agglomerate during the plating process, and the thickness; continuity of the coating uniformity can also be controlled by plating conditions. The silver coating on the surface of carbon nanotubes is formed by reducing and depositing silver ions on the active sites by a reducing agent. With the appropriate increase of the plating time, the reduced silver nanoparticles move toward the normal and cut along the nucleation center. It grows up and gradually covers the entire surface of the carbon nanotubes, so that the density of the carbon nanotubes increases after plating, and the resistivity decreases (Feng et al., 2005).

3.3.2 Mechanical Properties of Silver-Plated Carbon Nanotubes

The original CNTs are soft and highly entangled. The silver-plated CNTs integrate the advantages of metal and CNTs, so that the hardness and strength of the CNTs are greatly improved, and the surface contact area is increased. As a result, the friction resistance under certain loads is significantly improved compared to uncoated CNTs, making it easier to use silver-plated CNTs in microsystems with moving components (Zhang and Liu, 2016; Zhang et al., 2017; Yang et al., 2018).

3.3.3 Other Properties of Silver-Plated Carbon Nanotubes

CNTs themselves have high thermal conductivity in the axial direction but very low thermal conductivity across the axial direction. The thermal conductivity will be further increased after silver plating, because metallic silver itself has good thermal conductivity. With the tremendous increase in the power and packaging density of electronic devices in recent years, thermal management and thermal interface materials (TIM) have become more and more important.

3.4 Carbon Nanotubes Electroless Copper Plating

Copper is abundant in nature, and it has excellent electrical conductivity, thermal conductivity, ductility, corrosion resistance, wear resistance, etc. Copper is widely used in the fields of power electronics, machinery and metallurgy, transportation, light industry, new industries, and high technology (Sahraei, 2017). The surface state and structure of CNTs can be improved by electroless copper plating, so that they not only exhibit high thermal and chemical stability, but also improve their dispersibility and wettability with the substrate.

3.4.1 Physical Properties of Copper-Plated Carbon Nanotubes

Under a suitable electroless copper plating process, through scanning electron microscopy and transmission electron microscopy, it is found that a layer of centered cubic nanocrystalline copper coating is uniformly and continuously covered on the surface of the CNTs. The metalized CNTs are still intact and uniform (Arai and Endo, 2003; Yamagishi, 2003; Araia et al., 2004). In addition, compared with unplated CNTs, the copper-plated CNTs have increased density and decreased resistivity, and it has good dispersion uniformity in deionized water.

3.4.2 Mechanical Properties of Copper -Plated Carbon Nanotubes

The surface modification metallization of CNTs with copper not only increases their surface active centers and improves the bonding of nanotubes with resins or ceramics, but also maintains the excellent properties of CNTs in composites,

which greatly expands the application fields of CNTs (Wang, 2011; Wang, 2014). After sintering with metal powder (such as copper powder) as composite material, the strength of the composite material increases due to the strengthening of grain boundaries because the CNTs can prevent the growth of copper particles during the sintering process, which increases the number of non-metallic interfaces between copper particles (Han and Kim, 2013).

3.4.3 Other Properties of Copper -Plated Carbon Nanotubes

Due to the high thermal conductivity (TC) and low thermal expansion coefficient, CNTs are considered as potential enhancers for copper-based thermal management materials. The sp2 hybridized carbon atoms in CNTs lead to poor wettability between CNTs and Cu, which results in weaker interfacial bonding. Therefore, in order to better utilize the excellent thermal conductivity of CNTs and increase their activity to improve the wettability, a layer of metallic Cu was coated on the surface of CNTs (Kim, 2008). Cu itself has good thermal conductivity, and the combination of the two can not only further increase the TC of the composite, but also sufficiently improve the inter-facial bonding between CNTs and the metal matrix.

3.5 Carbon Nanotubes Electroless Nickel Plating

Nickel metal has properties such as high hardness, good toughness and excellent ferromagnetism, and it is often doped in other metals or non-metals as a second phase. CNTs are widely used as reinforcement materials in the field of composite materials. In order to make fuller use of CNTs' superior properties, the surface modification, modification and coating are often applied to CNTs. Using the chemical nickel plating process, the continuous high-strength bonded nickel plating can be deposited on the surface of CNTs, which can greatly broaden the application fields of CNTs. Therefore, the study of chemical nickel plating on CNTs has attracted great interest from researchers (Yu and Shen, 2009).

3.5.1 Physical Properties of Nickel-Plated Carbon Nanotubes

The pretreated CNTs are chemically active and hydrophilic, which can attract the metallic nickel particles to its surface. On the contrary, if there is no pretreatment before chemical plating, the metallic nickel particles will not be adsorbed on the surface of CNTs. With the appropriate increase in the deposition of nickel, the coating tends to be uniform and continuous, and there is a firm bond between metallic nickel and CNTs. Since metallic nickel is inherently well ferromagnetic, the coating CNTs with nickel makes them easy to handle with magnetic forces. Accordingly, the study on how nickel-plated CNTs respond to external magnetic fields is important for their application as fillers for magnetic materials. In addition, deposit uniformity is an important physical property and a significant advantage of the electroless nickel process. It is the ability to produce uniform thickness on parts with complex geometries and shapes. The current density effect typically associated with electroplating is not a factor here; so sharp edges, deep recesses and blind holes are readily plated to have uniform thickness with electroless nickel process. Electrodeposition leads to the excessive buildup at projections, and the edges and finish-grinding operation may be required. In such a context, electroless deposits avoid these drawbacks (Jothi et al., 2013).

3.5.2 Mechanical Properties of Nickel-Plated Carbon Nanotubes

Nickel plating of CNTs provides significant improvements in mechanical properties and reliability as well as plating of other metals. Usually, we choose suitable plated CNTs to be doped into composite materials according to different applications. As modern electronic devices require higher performance and increasingly smaller sizes, the solder joints of components in electronic packaging have become a key consideration, compared to undoped lead-free solder in which nickel-plated CNTs are doped into the Sn-58Bi solder alloy as a second phase, the nickel-plated CNTs not only enable the solder joints to cure at lower temperatures, but also have greatly improved shear strength, ductility and durability improved. The addition of nickel-plated CNTs significantly improves the performance of the composite solder because of the good mechanical and electrical properties of the CNTs themselves, and the addition of nickel metal further enhances the mechanical properties such as hardness, wear resistance and ductility (Zhang et al., 2008).

3.5.3 Other Properties of Nickel-Plated Carbon Nanotubes

Primitive CNTs have good thermal conductivity and flexibility, and CNTs are usually considered as the reinforcing phase to improve the thermal conductivity and toughness of composite materials, but the direct addition of CNTs to composite materials will cause them to aggregate under the action of van der Waals forces, making it difficult to effectively disperse in the matrix material. Electroless nickel plating can not only make CNTs uniformly distributed in the composite material but also improve its thermal conductivity, and the presence of nickel plating facilitates the application of CNTs in thermal management materials (Xiong et al., 2006).

3.6 Carbon Nanotubes Electroless Alloy Plating

Alloys have higher strength, hardness, and corrosion resistance than single metals, and can also give CNTs composites excellent properties compared to monometallic nanoparticles coated on CNTs. They have shown significant improvements in aspects such as thermal conductivity, electrical conductivity, magnetic properties, catalytic properties, corrosion resistance, and wear resistance, so they are even better than monometallic nanoparticles. The formation of composite coatings on CNTs and the effect of composite coatings on the properties of carbon nanotube composites have been extensively investigated. At present, the main alloy coatings coated on CNTs are Ni-Co

TABLE 1 | Features and types of electroless metallic alloy coatings.

Use	Alloy types
Corrosion protection	Ni-P, Ni-P-Mo, Ni-Sn-P, Co-P, Ni-Cu-P
Wear resistance	Ni-B, Ni-B-Mo, Ni-B-Sn, Co-P, Co-P-W
Magnetic	Au-Ni, Au-Co; Ni-Co-P, Ni-Co-B, Ni-Fe-P
Solderability	Sn-Pb, Ni-P
High temperature	Co-W-B, Ni-Re-P
Diffusion barrier	Ni-P

alloy, Ni-P alloy, Ni-B alloy, Co-B alloy, Ni-Co-P alloy, Ni-Co-B-P alloy, Fe-Co alloy, Ni-Cu-P alloy, Pd-Ni alloy, Sn-Cu alloy, and Ni-Pd-Sn alloy (Zhao et al., 2017). The properties given to CNTs vary because of the different alloys coated. Electroless deposited alloy features and types of metallic non-electrolytic alloy coatings are summarized in **Table 1**.

3.6.1 Physical Characteristics of Alloy-Plated Carbon Nanotubes

Like other monometallic alloys, CNTs can be coated with uniform, dense and continuous layers under appropriate coating conditions. For some heat-treated alloys, different phase transformation processes occur at different temperatures. When the heat treatment temperature is low, the alloy plating shows both amorphous and crystalline states, and as the heat treatment temperature rises, a complete crystalline structure is obtained, in which the grain size increases significantly with the increase of temperature. When Ni-Co-P alloy, Fe-Co alloy, Ni-P alloy and Co-P alloy are electrolessly plated on the surface of CNTs, the coating thickness is about 5–20 nm. The saturation magnetization, coercive force and microwave absorption characteristics of the tube are quite different, so it is very important to explore the appropriate alloy concentration ratio for the magnetic performance (Pang et al., 2011).

3.6.2 Mechanical Properties of Alloy-Plated Carbon Nanotubes

After the post-plating heat treatment process, the microhardness of the coating is greatly improved. With the moderate increase of MWCNTs concentration in the chemical plating solution, the microhardness gradually increases. The heat treatment not only reduces cracks and pores of the coating but also has the effect of grain refinement, which makes the coating become more dense and continuous, and the microhardness and strength becomes higher. The alloy-plated CNTs also showed significant improvement in ductility, stiffness, frictional properties and wear resistance, and it was found that the concentration of MWCNTs had an effect on the frictional properties and wear resistance of the coating, and the friction coefficient of the coating gradually decreased with the increase of MWCNTs concentration (Chung, 2012).

3.6.3 Other Properties of Alloy-Plated Carbon Nanotubes

CNTs electroplated with Ni-P coatings are excellent in terms of corrosion resistance, which increases after heat treatment, implying that the coating structure becomes denser and more homogeneous after heat treatment. Because of their high electrical and thermal conductivity, CNTs are often used as fillers to enhance the thermal conductivity of polymer composites. contact each other to form a thermal path.

4 APPLICATION OF CARBON NANOTUBES AFTER ELECTROLESS PLATING

4.1 Magnetic Composite

In order to obtain better efficiency in electromagnetic wave shielding, low density, designable and dimensionally stable polymeric magnetic composites have been proposed and developed. Polymer magnetic composites usually consist of two parts—a polymer that provides good compatibility and a magnetic filler, as well as the inorganic magnetic nanoparticles such as nickel, cobalt or alloys related to nickel-cobalt. CNTs are common fillers due to their excellent mechanical, thermal, and electrical properties, but unmodified CNTs cannot obtain excellent magnetic properties due to their small maximum saturation magnetization intensity. In order to optimize the performance of CNTs as magnetic fillers, they must be coated with magnetic substances to modify them. Nickel and cobalt powders are typical magnetic fillers, with high conductivity and high saturation magnetization, but with high density and high cost. Plated nickel/cobalt multi-walled CNTs obtained by chemical plating method for comprehensive cost will become magnetic fillers with high magnetic properties and medium cost (Gopiraman et al., 2013).

Jagannatham et al. electroless nickel plating on multi-walled carbon nanotubes (MWCNTs) synthesized by arc discharge method, and then discussed the influence of plating time on the morphology and magnetic properties of the coating (Jagannatham et al., 2015). Zhang et al. obtained nickel-plated multi-walled CNTs (Ni/MWCNTs) by chemical plating, and then prepared a novel polymeric magnetic composite based on thermoplastic acrylate pressure-sensitive adhesive (PSA) using Ni/MWCNTs as filler, and the results of vibrating sample magnetometer showed that the increase of Ni/MWCNTs content could improve the saturation (Zhang et al., 2012). Liang et al. chemically coated CNTs with Co-P alloy and found that the saturation magnetization intensity of homogeneous Co2P-CNTs nanocomposites was 2.81 emu g-1 (Liang et al., 2016). Wang et al. coated Fe-Co alloy nanoparticles onto Fe-filled CNTs by chemical plating and evaluated the microwave absorption properties of the samples, and the results showed that coating Fe-Co alloy nanoparticles followed by heat treatment can improve the soft magnetic properties of Fe-filled CNTs, resulting in more effective microwave absorption (Chen et al., 2008).

4.2 Mechanical and Frictional Performance Improvement Materials

CNTs have become one of the most promising materials in the electronic field in the future due to their excellent mechanical properties, friction properties, and electrical and thermal

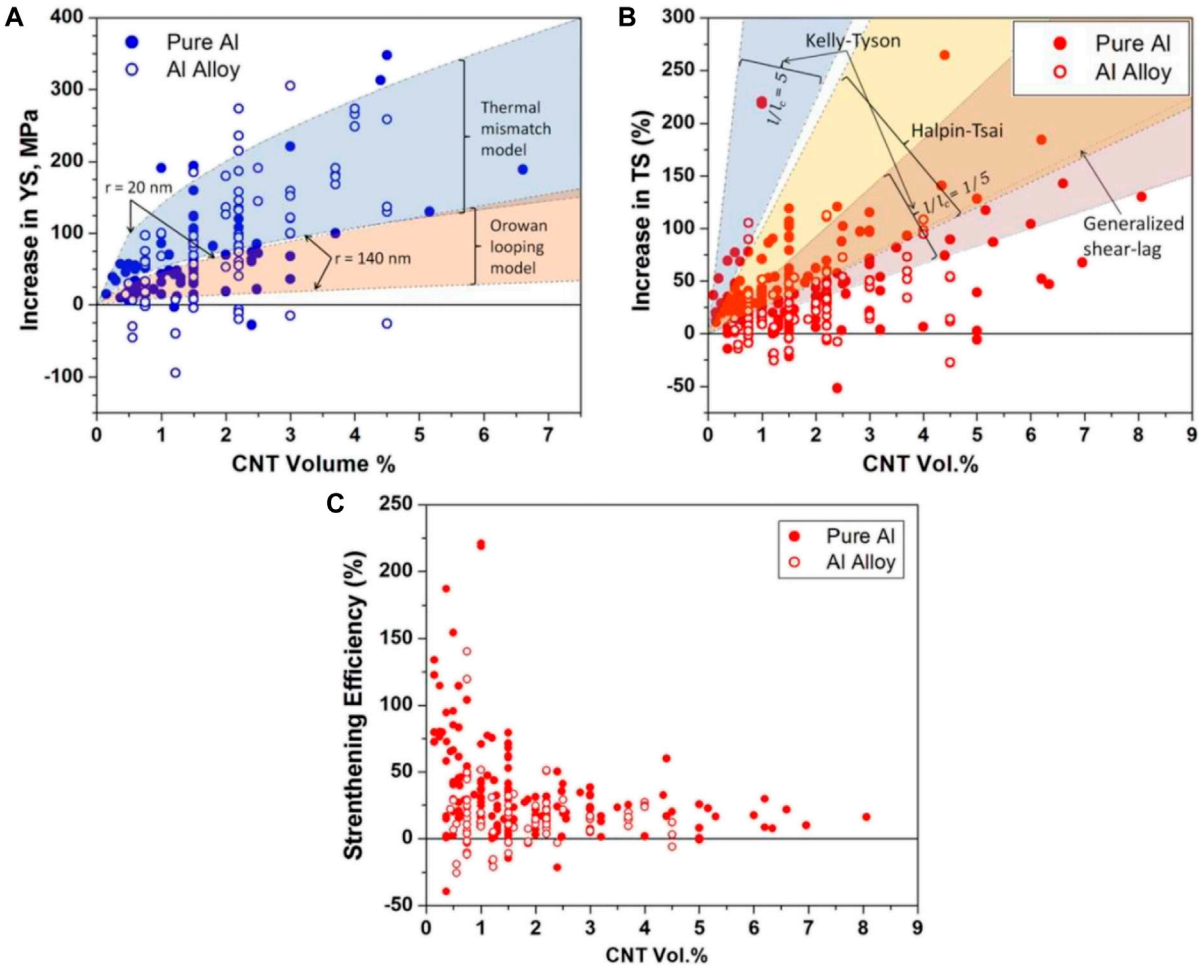

FIGURE 2 | Plots showing variation of tensile properties of Al-CNT composites as a function of CNT content. **(A)** Increase in the YS, **(B)** increase in TS and **(C)** Strengthening efficiency (Jagannatham et al., 2020) (published in Carbon 2020).

conductivity. They have been widely used in interconnections, transistors, and thermal and electrical materials. However, for some applications where metal properties are particularly important (such as interconnection) and occasions that require high device reliability and electrical performance, pure CNTs have great limitations. A large number of studies have confirmed that the addition of plated CNTs can significantly improve the mechanics and tribology of composite materials (Choudary et al., 2001; Barlian et al., 2009; Zhao et al., 2015).

Ma et al. blended acrylate resin with Ag-CNTs and Ag-GNs to synthesize a new conductive adhesive (ECA) and found that the conductivity reached 8.71 S/cm and the shear strength was 0.47 MPa when the concentration of the composite filler was 30 wt% (21 wt% of Ag-GNs and 9 wt% of Ag-CNTs) (Huan et al., 2015). Zhao et al. prepared CNTs-Ag composites by solution ball milling (SBM) of silver-plated CNTs (Ag-CNTs) obtained by plain chemical plating (CEP) and ultrasonic spray atomization (EPUSA), respectively, with Ag powder, followed by densification by spark plasma sintering (SPS). It was characterized that the composites made by EPUSA and SBM processes had better mechanical and electrical properties compared with CEP and SBM processes (Zhao et al., 2018). M. Jagannatham and Adnan Maqbool et al. prepared Cu-CNTs reinforced Al matrix composites and compared with pure Al-CNT composite materials, the yield strength and tensile strength of Al alloy-CNT composite materials has increased more. This can be attributed to the fact that most of the aluminum alloys used are precipitation hardening, and the addition of CNT improves the precipitation hardening characteristics. The percentage increase in the tensile strength is high for pure Al-CNT composites compared to Al alloy-CNT composites. Because compared with aluminum alloy-carbon nanotube composite material, pure aluminum carbon nanotube has a lower porosity. **Figure 2A** shows the increase in the Yield Strength (YS) of the composites as a function of CNT content. **Figure 2B** shows the increase in Tensile Strength (TS) of the composites with CNT content. **Figure 2C** shows the strengthening efficiency of CNT in Al-CNT composites as a function of CNT content (Jagannatham et al., 2020).

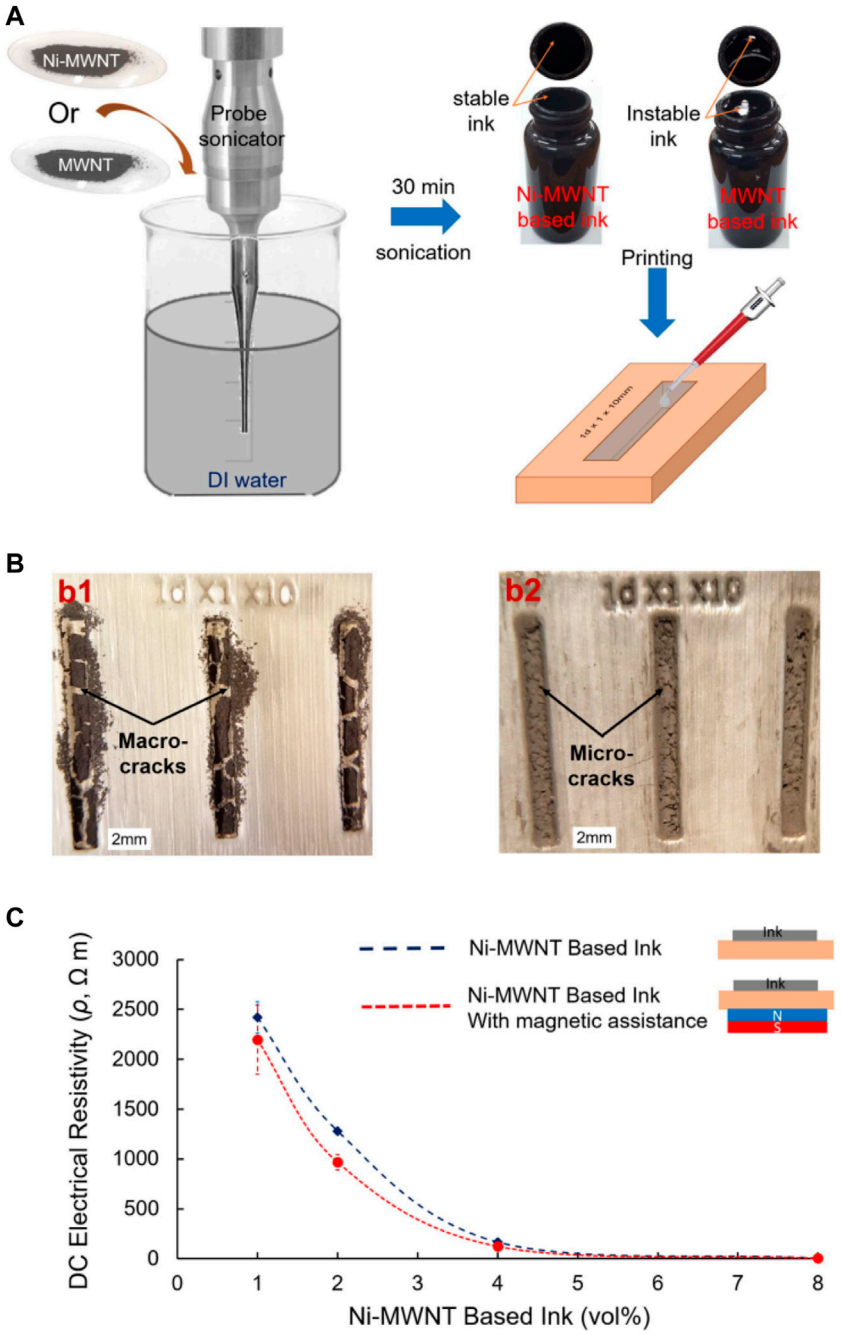

FIGURE 3 | Water-based conductive inks. **(A)** The procedure for ink preparation. Ni-MWCNTs or MWCNTs are dispersed in DI water using a probe sonicator and the ink poured into a plastic template. **(B)** Post drying, optical images show the morphology of the printed lines created by either MWCNT or Ni-MWCNT based inks (2 vol %). Macroscale cracks are clearly observed in the case of MWCNTs, while smaller microscale cracks are observed for the other case. **(C)** The measured electric resistivity of the lines printed by Ni-MWCNT based inks for different volume loadings with and without magnetic assistance (Ahmed et al., 2016) (published in Mater. Res. Express 2016).

4.3 Catalytic Material

With high surface area, porous structure and high catalytic capacity, multi-walled CNTs have been widely used in high-energy systems. MWCNTs can enhance the heat transfer during high-energy combustion reactions, and the gaseous products are easily absorbed by the catalyst active sites, so they are favorable for catalytic reactions. MWCNTs are excellent carriers for common combustion rate catalysts (Yong et al., 2018). The obtained Cu-MWCNTs were annealed at 250°C to obtain CuO-MWCNTs with good catalytic ability by Sherif Elbasuney et al. The synthesized CuO-MWCNTs were then encapsulated into ammonium perchlorate (APC) oxidant by solvent-anti-solvent

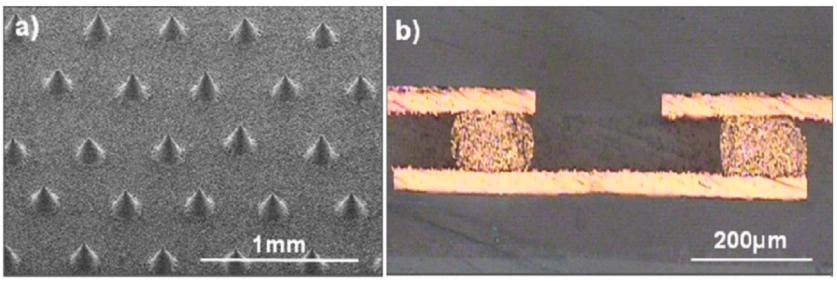

FIGURE 4 | Bump interconnects formed by the Ag-plated SWCNT–Ag paste: **(A)** Screen-printed conductive bumps and **(B)** a cross-sectional view of bumps connecting copper foils after the photolithographic patterning (Oh et al., 2008) (published in Nanotech. 2008).

technique, and differential scanning calorimetry (DSC) and thermogravimetric analysis (TGA) were used to study the catalytic performance of CuO -MWCNTs on the decomposition of APC by differential scanning calorimetry (DSC) and thermogravimetric analysis (TGA), and the results showed that 1 wt% of CuO-MWCNTs reduced the heat absorption decomposition of APC by 16.3%, and the original two exothermic decomposition stages were combined into one stage with a 100% surge in total heat release (Sherif et al., 2019). Liu et al. successfully synthesized Ni-B-coated multi-walled CNTs (MWCNTs) by a chemical deposition process. The catalytic activity of MWCNTs/Ni-B nanoparticles was evaluated and it was found that the catalytic hydrogenation by MWCNTs/Ni-B nanoparticles resulted in the selective conversion of styrene to ethylbenzene. The highest conversion of 99.8% was achieved under appropriate reaction conditions, which indicates the high catalytic activity of MWCNTs/Ni-B nanoparticles (Liu et al., 2011). Wu et al. grew CNFs on CNTs by chemically plating Ni-P alloy in order to synthesize Ni-P/CNT-CNFs composites, which were directly used as electrocatalysts in methanol-resistant redox reactions (ORR) (Wu et al., 2017). Experiments showed that this irregularly oriented hybrid material, in addition to being an ideal candidate for non-precious metal electrocatalyst carriers, exhibited satisfactory ORR activity and excellent methanol tolerance in alkaline solutions. This study provides a promising option for the synthesis of non-precious metal catalysts for fuel cells.

4.4 Electrically and Thermally Conductive Materials

In recent years, the electronics industry has developed rapidly. Electronic equipment not only tends to be miniaturized, lightweight, and highly functional, but also power and packaging density are gradually increasing. Therefore, it is becoming more and more important to obtain materials with good electrical and thermal conductivity. CNTs have a high aspect ratio and excellent electrical and thermal conductivity, and can be used as potential enhancers in electrical and thermal conductivity composite materials. However, the wettability between unmodified CNTs and metal-based materials is poor, and the interface the weak bonding is not conducive to its excellent performance. Therefore, CNTs must be modified to meet application requirements. The success of electroless plating provides an effective way to solve this problem. Zhang et al. prepared Ag surface-modified CNTs and then mixed epoxy resin and nanotubes to obtain thermal interface materials (TIM), and the conductivity of epoxy-Ag-coated CNTs was analyzed to be much higher than that of epoxy-uncoated CNTs (Zhang et al., 2012). Choi et al. investigated the effects of nickel-plated MWCNTs and uncoated MWCNTs on the thermal conductivity and fracture toughness of alumina-reinforced epoxy composites, and the experimental results showed that the Ni-MWCNTs/Al2O3/epoxy composites had better thermal conductivity and fracture toughness than the MWCNTs/Al2O3/epoxy composites (Choi et al., 2013). Chen et al. investigated the effect of copper-plated CNTs on the microstructure and thermal conductivity (TC) of copper matrix composites (Chen et al., 2017). The results showed that the CNTs modified by copper nanoparticles were uniformly dispersed and embedded in the copper matrix, and the uniform dispersion of CNTs and the reduction of interfacial thermal resistance led to the improvement of the thermal conductivity of the carbon nanotube-copper composites.

The plated CNTs are also used for the preparation of conductive pastes in the field of printed electronics due to their excellent electrical conductivity. Ahmed M Abdalla et al. chemically deposited magnetic nickel nanoparticles on multi-walled CNTs (MWCNTs) to produce Ni-MWCNT hybrids (NiCH), which are electrically conductive and have high magnetization and elastic modulus, and prepared Ni-MWCNT macrostructures with controlled morphology by applying a strong magnetic field with NiCH, and these macrostructures can be used for nanoscale and micron-scale filtration as well as printed circuits. Since the presence of nickel plating layer makes Ni-MWCNT hydrophilic, different concentrations of hydrophilic Ni-MWCNT samples and hydrophobic MWCNT samples were further dispersed in water to synthesize aqueous conductive inks as shown in **Figure 3**. The results showed that Ni-MWCNTs with 8% volume concentration had the lowest resistivity of 5.9 Ωm for printed circuits. compared with hydrophobic MWCNT inks, the degree of agglomeration of the dried hydrophilic Ni-MWCNT ink was low, and the cracks produced by the printed lines were very small. In

addition, printing the Ni-MWCNT circuit with the aid of a magnetic field further reduces the resistivity. The following figure shows the preparation of water-based conductive ink, the morphology of the printed circuit after drying, and the resistivity of the Ni-MWCNT ink at different volume concentrations (Ahmed et al., 2016).

Youngseok Oh et al. developed a new type of silver/conductive polymer composite by combining silver-plated single-walled CNTs (SWCNT-Ag) (Oh et al., 2008). A conical conductive bump with a diameter of 130 μm at the bottom and a height of 185 μm, as shown in **Figure 4A**, was printed on the composite material using screen printing to demonstrate the performance of the material as a multilayer printed circuit board electrical interconnect, and the resistance of the SWCNT-Ag bump was measured to be 3.2 mΩ, which is 83% lower than that of commercial silver pastes on the market. The resistance of this SWCNT-Ag paste is 83% lower than that of commercial silver pastes in the market. The cross-sectional view of the connected copper foil bump is shown in **Figure 4B**, and it can be seen that the electrical signal transmission of the bump is good. Thus, it is demonstrated that SWCNT-Ag paste has excellent printability as electrical interconnects.

5 CONCLUSION

In this paper, a brief classification and summary of carbon nanotube electroless plating methods was conductedm and a detailed classification and summary of carbon nanotube electroless metal/alloy nano-coating were carried out, which can be used for reference for the future research and improvement of the electroless plating of CNTs. In addition, the application progress of electroless metal/alloy nano-coating of carbon nanotubes in aspects such as electrical, mechanical, thermal, tribological, corrosion resistance and magnetic properties were discussed in detail. At present, although electroless CNTs have been widely investigated and applied, it is essential to have a good understanding of its electroless plating surface coatings firstly, so as to better take advantage of electroless plating CNTs. Therefore, it is critical to study the electroless metal/alloy nano-coating of carbon nanotubes for obtaining plated CNTs with good appearance quality and excellent comprehensive performance.

AUTHOR CONTRIBUTIONS

All authors listed have made a substantial, direct and intellectual contribution to the work, and approved it for publication.

FUNDING

This work was supported in part by NSF of the Science and Technology Department of Shaanxi Province under Grant No. 2019JM-122, Doctoral Research Initiation Fund of Xi'an University of Technology under Grant No. 108-451119007, NSF of the Key Laboratory of Shaanxi Provincial Department of Education under Grant No. 15JS075, Xi'an Science and technology plan project under Grant No. GXYD14.27, Key scientific research program of Shaanxi Provincial Department of Education under Grant No. 20JY055, Key scientific research program of Shaanxi Provincial Department of Education under Grant No. 21JY032 and Shaanxi Collaborative Innovation Center of Green Intelligent Printing and Packaging, Key scientific research program of Shaanxi Provincial Department of Education under Grant No. 21JZ010.

REFERENCES

Abdalla, A. M., Ghosh, S., Puri, I. K., and Ishwar, K. (2016). Fabrication of Nanoscale to Macroscale Nickel-Multiwall Carbon Nanotube Hybrid Materials with Tunable Material Properties. *Mater. Res. Express* 3, 125014. doi:10.1088/2053-1591/3/12/125014

Arai, S., and Endo, M. (2003). Carbon Nanofiber-Copper Composite Powder Prepared by Electrodeposition. *Electrochemistry Commun.* 5, 797–799. doi:10.1016/j.elecom.2003.08.002

Arai, S., Endo, M., and Kaneko, N. (2004). Ni-deposited Multi-Walled Carbon Nanotubes by Electrodeposition. *Carbon* 42, 641–644. doi:10.1016/j.carbon.2003.12.084

Barlian, A. A., Park, W.-T., Mallon, J. R., Rastegar, A. J., and Pruitt, B. L. (2009). Review: Semiconductor Piezoresistance for Microsystems. *Proc. IEEE* 97, 513–552. doi:10.1109/JPROC.2009.2013612

Cao, Q., Han, S.-J., Tersoff, J., Franklin, A. D., Zhu, Y., Zhang, Z., et al. (2015). End-bonded Contacts for Carbon Nanotube Transistors with Low, Size-independent Resistance. *Science* 350, 68–72. doi:10.1126/science.aac8006

Cha, S. I., Kim, K. T., Arshad, S. N., Mo, C. B., and Hong, S. H. (2005). Extraordinary Strengthening Effect of Carbon Nanotubes in Metal-Matrix Nanocomposites Processed by Molecular-Level Mixing. *Adv. Mater.* 17, 1377–1381. doi:10.1002/adma.200401933

Chaudhari, K. N., Chaudhari, S., and Yu, J.-S. (2016). Synthesis and Supercapacitor Performance of Au-Nanoparticle Decorated MWCNT. *J. Electroanalytical Chem.* 761, 98–105. doi:10.1016/j.jelechem.2015.12.020

Chen, H., Zou, Y., Li, J., Zhang, K., Xia, Y., Hui, B., et al. (2021). Wood Aerogel-Derived sandwich-like Layered Nanoelectrodes for Alkaline Overall Seawater Electrosplitting. *Appl. Catal. B: Environ.* 293, 120215. doi:10.1016/j.apcatb.2021.120215

Chen, P., Zhang, J., Shen, Q., Luo, G., Dai, Y., Wang, C., et al. (2017). Microstructure and Thermal Conductivity of Carbon Nanotube Reinforced Cu Composites. *j nanosci nanotechnol* 17 (4), 2447–2452. doi:10.1166/jnn.2017.12637

Chen, W. X., Tu, J. P., Gan, H. Y., Xu, Z. D., Wang, Q. G., Lee, J. Y., et al. (2002). Electroless Preparation and Tribological Properties of Ni-P-Carbon Nanotube Composite Coatings under Lubricated Condition. *Surf. Coat. Technol.* 160, 68–73. doi:10.1016/S0257-8972(02)00408-5

Chen, X., Xia, J., Peng, J., Li, W., and Xie, S. (2000). Carbon-nanotube Metal-Matrix Composites Prepared by Electroless Plating. *Composites Sci. Technol.* 60, 301–306. doi:10.1016/S0266-3538(99)00127-X

Choi, J.-R., Lee, Y.-S., and Park, S.-J. (2013). Influence of Electroless Ni-Plated MWCNTs on Thermal Conductivity and Fracture Toughness of MWCNTs/Al2O3/Epoxy Composites. *Polym. Korea* 37 (4), 449–454. doi:10.7317/pk.2013.37.4.449

Choi, J.-R., Lee, Y. S., and Park, S.-J. (2014). A Study on thermal Conductivity of Electroless Ni-B Plated Multi-Walled Carbon Nanotubes-Reinforced Composites. *J. Ind. Eng. Chem.* 20 (5), 3421–3424. doi:10.1016/j.jiec.2013.12.029

Choudary, B. M., Dr, M., Ateeq, R., and Venkat, R. (2001). The First Example of Activation of Molecular Oxygen by Nickel in Ni-Al Hydrotalcite: A Novel Protocol for the Selective Oxidation of Alcohols. *The cerman Chem. Soc.*

Citations 198, 763. doi:10.1002/1521-3757(20010216)113:4<785:aid-ange7850>3.0.co;2-p

Chung, D. D. L. (2012). Carbon Materials for Structural Self-Sensing, Electromagnetic Shielding and thermal Interfacing. *Carbon* 50, 3342–3353. doi:10.1016/j.carbon.2012.01.031

Daoush, W. M., Lim, B. K., Mo, C. B., Nam, D. H., and Hong, S. H. (2009). Electrical and Mechanical Properties of Carbon Nanotube Reinforced Copper Nanocomposites Fabricated by Electroless Deposition Process. *Mater. Sci. Eng. A* 513-514, 247–253. doi:10.1016/j.msea.2009.01.073

Desmaris, V., Saleem, A. M., Shafiee, S., Berg, J., Kabir, M. S., and Johansson, A. (2014). Carbon Nanofibers (CNF) for Enhanced Solder-Based Nano-Scale Integration and On-Chip Interconnect Solutions. *IEEE 64th Electron. Components Technol. Conf. IEEE.* 2014, 1071–1076. doi:10.1109/ECTC.2014.6897421

Dondoi, M. P., Bucur, B., Danet, A. F., Toader, C. N., Barthelmebs, L., and Marty, J.-L. (2006). Organophosphorus Insecticides Extraction and Heterogeneous Oxidation on Column for Analysis with an Acetylcholinesterase (AChE) Biosensor. *Analytica Chim. Acta* 578, 162–169. doi:10.1016/j.aca.2006.07.002

Duong, G. V., Sato Turtelli, R., Hanh, N., Linh, D. V., Reissner, M., Michor, H., et al. (2006). Magnetic Properties of Nanocrystalline Co1−xZnxFe2O4 Prepared by Forced Hydrolysis Method. *J. Magnetism Magn. Mater.* 307, 313–317. doi:10.1016/j.jmmm.2006.03.072

Elbasuney, S., Yehia, M., Zaky, M. G., Radwan, M., and Mostafa, R. (2019). MWNTs Coated with CuO Particles: A Novel Nano-Catalyst for Solid Propellants. *J. Inorg. Organomet. Polym.* 29 (9), 2064–2071. doi:10.1007/s10904-019-01165-5

Elbasuney, S., Yehia, M., Zaky, M. G., and Radwan, M. (2019). MWNTs Coated with CuO Particles: A Novel Nano-Catalyst for Solid Propellants: A Novel Nano-Catalyst for Solid Propellants. *J. Inorg. Organomet. Polym.* 29 (6), 2064–2071. doi:10.1007/s10904-019-01165-5

Esawi, A. M. K., Morsi, K., Sayed, A., Gawad, A. A., and Borah, P. (2009). Fabrication and Properties of Dispersed Carbon Nanotube-Aluminum Composites. *Mater. Sci. Eng. A* 508 (3), 167–173. doi:10.1016/j.msea.2009.01.002

Feng, Y. C. (2008). Preparation of Quasi-One-Dimensional Gold Nanowires by Self-Assembling. *Rare Metal Mater. Eng.* 37 (7), 1261–1263. doi:10.1016/S1875-5372(09)60033-310.1016/s1875-5372(09)60035-7

Feng, Y., and Yuan, H. (2004). Electroless Plating of Carbon Nanotubes with Silver. *J. Mater. Sci.* 39, 3241–3243. doi:10.1023/B:JMSC.0000025869.05546.94

Feng, Y., Yuan, H. L., and Zhang, M. (2005). Fabrication and Properties of Silver-Matrix Composites Reinforced by Carbon Nanotubes. *Mater. Characterization* 55, 211–218. doi:10.1016/j.matchar.2005.05.003

Gopiraman, M., Ganesh Babu, S., Khatri, Z., Kai, W., Kim, Y. A., Endo, M., et al. (2013). An Efficient, Reusable Copper-Oxide/carbon-Nanotube Catalyst for N-Arylation of Imidazole. *Carbon* 62, 135–148. doi:10.1016/j.carbon.2013.06.005

Guo, X., Zhu, G., Sun, F., Li, Z., Zhao, X., Li, X., et al. (2006). Synthesis, Structure, and Luminescent Properties of Microporous Lanthanide Metal−Organic Frameworks with Inorganic Rod-Shaped Building Units. *Inorg. Chem.* 45 (6), 2581–2587. doi:10.1021/ic0518881

Han, Y., Guo, H., Yin, F., Zhang, X., Chu, K., and Fan, Y. (2012). Microstructure and thermal Conductivity of Copper Matrix Composites Reinforced with Mixtures of diamond and SiC Particles. *Rare Met.* 31 (1), 58–63. doi:10.1007/s12598-012-0463-1

Hui, B., Li, J., Lu, Y., Zhang, K., Chen, H., Yang, D., et al. (2021). Boosting Electrocatalytic Hydrogen Generation by a Renewable Porous wood Membrane Decorated with Fe-Doped NiP Alloys. *J. Energ. Chem.* 56, 23–33. doi:10.1016/j.jechem.2020.07.037

Hui, B., Zhang, K., Xia, Y., and Zhou, C. (2020). Natural Multi-Channeled wood Frameworks for Electrocatalytic Hydrogen Evolution. *Electrochimica Acta* 330, 135274. doi:10.1016/j.electacta.2019.135274

Hyie, K. M., Resali, N. A., Abdullah, W. N. R., and Chong, W. T. (2017). Review of Nickel-Based Electrodeposited Tribo-Coatings. *Proc. Eng.* 41, 1627. doi:10.1007/s12666-017-1175-x

Jagannatham, M., Chandran, P., Sankaran, S., Haridoss, P., Nayan, N., and Bakshi, S. R. (2020). Tensile Properties of Carbon Nanotubes Reinforced Aluminum Matrix Composites: A Review. *Carbon* 160, 14–44. doi:10.1016/j.carbon.2020.01.007

Jagannatham, M., Sankaran, S., and Haridoss, P. 2015). Microstructure and Mechanical Behavior of Copper Coated Multiwall Carbon Nanotubes Reinforced Aluminum Composites. *Mater. Sci. Eng. A* 638, 197–207. doi:10.1016/j.msea.2015.04.070

Jarosz, P., Schauerman, C., Alvarenga, J., Moses, B., Mastrangelo, T., Raffaelle, R., et al. (2011). Carbon Nanotube Wires and Cables: Near-Term Applications and Future Perspectives. *Nanoscale* 3, 4542. doi:10.1039/c1nr10814j

Ju, K.-J., Feng, J.-X., Feng, J.-J., Zhang, Q.-L., Xu, T.-Q., Wei, J., et al. (2015). Biosensor for Pesticide Triazophos Based on its Inhibition of Acetylcholinesterase and Using a Glassy Carbon Electrode Modified with Coral-like Gold Nanostructures Supported on Reduced Graphene Oxide. *Microchim Acta* 182, 2427–2434. doi:10.1007/s00604-015-1584-7

Kim, K. T., Cha, S. I., Gemming, T., Eckert, J., and Hong, S. H. (2008). The Role of Interfacial Oxygen Atoms in the Enhanced Mechanical Properties of Carbon-Nanotube-Reinforced Metal Matrix Nanocomposites. *Small* 4, 1936–1940. doi:10.1002/smll.200701223

Li, H., Xu, C., Srivastava, N., and Banerjee, K. (2009). Carbon Nanomaterials for Next-Generation Interconnects and Passives: Physics, Status, and Prospects. *IEEE Trans. Electron. Devices* 56, 1799–1821. doi:10.1109/TED.2009.2026524

Liang, J., Li, H., Shi, X., Qi, L., Hu, X., and Wei, J. (2016). Continuous Co-P Coating on CNTs by Optimising Electrodeposition. *Surf. Eng.* 33, 110–115. doi:10.1080/02670844.2015.1133489

Liu, W. L., Hsieh, S. H., and Chen, W. J. (2007). Preparation of Sn Films Deposited on Carbon Nanotubes. *Appl. Surf. Sci.* 253, 8356–8359. doi:10.1016/j.apsusc.2007.03.069

Liu, Z., Li, Z., Wang, F., Liu, J., Ji, J., Park, K. C., et al. (2012). Electroless Preparation and Characterization of Ni-B Nanoparticles Supported on Multi-Walled Carbon Nanotubes and Their Catalytic Activity towards Hydrogenation of Styrene. *Mater. Res. Bull.* 47 (2), 338–343. doi:10.1016/j.materresbull.2011.11.010

Lv, R., Kang, F., Cai, D., Wang, C., Gu, J., Wang, K., et al. (2008). Long Continuous FeNi Nanowires inside Carbon Nanotubes: Synthesis, Property and Application. *J. Phys. Chem. Sol.* 69, 1213–1217. doi:10.1016/j.jpcs.2007.10.006

Ma, H., Qiu, H., and Qi, S. (2015). Electrically Conductive Adhesives Based on Acrylate Resin Filled with Silver-Plated Graphite Nanosheets and Carbon Nanotubes. *J. Adhes. Sci. Technol.* 29 (20), 2233–2244. doi:10.1080/01694243.2015.1061905

Maqbool, A., Hussain, M. A., Khalid, F. A., Bakhsh, N., Hussain, A., and Kim, M. H. (2013). Mechanical Characterization of Copper Coated Carbon Nanotubes Reinforced Aluminum Matrix Composites. *Mater. Characterization* 86, 39–48. doi:10.1016/j.matchar.2013.09.006

Martel, R., Schmidt, T., Shea, H. R., Hertel, T., and Avouris, P. (1998). Single- and Multi-wall Carbon Nanotube Field-Effect Transistors. *Appl. Phys. Lett.* 73 (17), 2447–2449. doi:10.1063/1.122477

Martin, M. N., Basham, J. I., Chando, P., and Eah, S.-K. (2010). Charged Gold Nanoparticles in Non-polar Solvents: 10-min Synthesis and 2D Self-Assembly. *Langmuir* 26, 7410–7417. doi:10.1021/la100591h

M., J., S., S., and Prathap, H. (2015). Electroless Nickel Plating of Arc Discharge Synthesized Carbon Nanotubes for Metal Matrix Composites. *Appl. Surf. Sci.* 324, 475–481. doi:10.1016/j.apsusc.2014.10.150

Nihei, M., Kawabata, A., Kondo, D., Horibe, M., Sato, S., and Awano, Y. (2005). Electrical Properties of Carbon Nanotube Bundles for Future via Interconnects. *Jpn. J. Appl. Phys.* 44, 1626–1628. doi:10.1143/JJAP.44.1626

Oh, Y., Suh, D., Kim, Y., Lee, E., Mok, J. S., Choi, J., et al. (2008). Silver-plated Carbon Nanotubes for Silver/conducting Polymer Composites. *Nanotechnology* 19, 495602. doi:10.1088/0957-4484/19/49/495602

Pal, H., and Sharma, V. (2015). Thermal Conductivity of Carbon Nanotube-Silver Composite. *Trans. Nonferrous Met. Soc. China* 25, 154–161. doi:10.1016/S1003-6326(15)63590-7

Pang, J., Li, Q., Wang, W., Xu, X., and Zhai, J. (2011). Preparation and Characterization of Electroless Ni-Co-P Ternary alloy on Fly Ash Cenospheres. *Surf. Coat. Technol.* 205, 4237–4242. doi:10.1016/j.surfcoat.2011.03.020

Peng, Y., and Chen, Q. (2009). Ultrasonic-assisted Fabrication of Highly Dispersed Copper/multi-Walled Carbon Nanotube Nanowires. *Colloids Surf. A: Physicochemical Eng. Aspects* 342, 132–135. doi:10.1016/j.colsurfa.2009.04.030

Quoc Ngo, Q., Yamada, T., Suzuki, M., Ominami, Y., Cassell, A. M., Li Jun, J., et al. (2007). Structural and Electrical Characterization of Carbon Nanofibers for

Interconnect via Applications. *IEEE Trans. Nanotechnology* 6, 688–695. doi:10.1109/TNANO.2007.907400

Sahraei, A. A., Saeed, H. N., Fathi, A., Baniassadi, M., Afrookhteh, S. S., and Besharati Givi, M. K. (2017). Formation of Homogenous Copper Film on MWCNTs by an Efficient Electroless Deposition Process. *Sci. Eng. Compos. Mater.* 24, 345–352. doi:10.1515/secm-2015-0081/html

Sudagar, J., Lian, J., and Sha, W. (2013). Electroless Nickel, alloy, Composite and Nano Coatings - A Critical Review. *J. Alloys Compd.* 571, 183–204. doi:10.1016/j.jallcom.2013.03.107

Tans, S. J., Verschueren, A. R. M., and Dekker, C. (1998). Room-temperature Transistor Based on a Single Carbon Nanotube. *Nature* 393, 49–52. doi:10.1038/29954

Tianjiao, B., Yan, Z., Xiaofeng, S., and Yuexin, D. (2011). A Study of the Electromagnetic Properties of Cobalt-Multiwalled Carbon Nanotubes (Co-MWCNTs) Composites. *Mater. Sci. Eng. B* 176, 906–912. doi:10.1016/j.mseb.2011.05.016

Wang, C., Lv, R., Kang, F., Gu, J., Gui, X., and Wu, D. (20082009). Synthesis and Application of Iron-Filled Carbon Nanotubes Coated with FeCo alloy Nanoparticles. *J. Magnetism Magn. Mater.* 321, 1924–1927. doi:10.1016/j.jmmm.2008.12.013

Wang, H., Jian, G., Egan, G. C., and Zachariah, M. R. (2014). Assembly and Reactive Properties of Al/CuO Based Nanothermite Microparticles. *Combustion and Flame* 161, 2203–2208. doi:10.1016/j.combustflame.2014.02.003

Wang, J., Hu, A., Persic, J., Wen, J. Z., and Norman Zhou, Y. (2011). Thermal Stability and Reaction Properties of Passivated Al/CuO Nano-Thermite. *J. Phys. Chem. Sol.* 72, 620–625. doi:10.1016/j.jpcs.2011.02.006

Wu, X., Liu, Z., Jiang, Y., Zeng, J., and Liao, S. (2017). Randomly Oriented Ni-P/nanofiber/nanotube Composite Prepared by Electrolessly Plated Nickel-Phosphorus Alloys for Fuel Cell Applications. *J. Mater. Sci.* 52 (14), 8432–8443. doi:10.1007/s10853-017-1094-6

Xiong, J., Zheng, Z., Qin, X., Li, M., Li, H., and Wang, X. (2006). The thermal and Mechanical Properties of a Polyurethane/multi-Walled Carbon Nanotube Composite. *Carbon* 44, 2701–2707. doi:10.1016/j.carbon.2006.04.005

Xu, M., Jiang, S., Jiang, B., and Zheng, J. (2019). Organophosphorus Pesticides Detection Using Acetylcholinesterase Biosensor Based on Gold Nanoparticles Constructed by Electroless Plating on Vertical Nitrogen-Doped Single-Walled Carbon Nanotubes. *Int. J. Environ. Anal. Chem.* 99 (10), 913–927. doi:10.1080/03067319.2019.1616714

Yamagishi, K., Yae, S., Okamoto, N., Fukumuro, N., and Matsuda, H. (2003). Adsorbates Formed on Non-conducting Substrates by Two-step Catalyzation Pretreatment for Electroless Plating. *J. Surf. Finishing Soc. Jpn.* 54, 150–154. doi:10.4139/sfj.54.150

Yang, P., You, X., Yi, J., Fang, D., Bao, R., Shen, T., et al. (2018). Simultaneous Achievement of High Strength, Excellent Ductility, and Good Electrical Conductivity in Carbon Nanotube/copper Composites. *J. Alloys Compd.* 752, 431–439. doi:10.1016/j.jallcom.2018.03.341

Yang, Y., Asiri, A. M., Du, D., and Lin, Y. (2014). Acetylcholinesterase Biosensor Based on a Gold Nanoparticle-Polypyrrole-Reduced Graphene Oxide Nanocomposite Modified Electrode for the Amperometric Detection of Organophosphorus Pesticides. *ANALYST* 139 (12), 3055–3060. doi:10.1039/c4an00068d

Yoo, S. J., Han, S. H., and Kim, W. J. (2013). A Combination of ball Milling and High-Ratio Differential Speed Rolling for Synthesizing Carbon Nanotube/copper Composites. *Carbon* 61, 487–500. doi:10.1016/j.carbon.2013.04.105

Yu, X., and Shen, Z. (2009). The Electromagnetic Shielding of Ni Films Deposited on Cenosphere Particles by Magnetron Sputtering Method. *J. Magnetism Magn. Mater.* 321, 2890–2895. doi:10.1016/j.jmmm.2009.04.040

Zhang, F., Qi, S. H., and Zhang, Y. (2012). Preparation and Characterization of Thermoplastic Acrylate Pressure-Sensitive Adhesive/nickel/multiwalled Carbon Nanotubes. *J. Thermoplastic Compos. Mater.* 26 (9), 1287–1300. doi:10.1177/0892705712445038

Zhang, Q., Qin, Z., Luo, Q., Wu, Z., Liu, L., Shen, B., et al. (2017). Microstructure and Nanoindentation Behavior of Cu Composites Reinforced with Graphene Nanoplatelets by Electroless Co-deposition Technique. *Sci. Rep.* 7, 1338. doi:10.1038/s41598-017-01439-3

Zhang, X., Jiang, W., Song, D., Liu, J., and Li, F. (2008). Preparation and Catalytic Activity of Ni/CNTs Nanocomposites Using Microwave Irradiation Heating Method. *Mater. Lett.* 62, 2343–2346. doi:10.1016/j.matlet.2007.11.091

Zhang, Y., and Liu, F. (2016). Hydrothermal Conversion of Graphite to Carbon Nanotubes (CNTs) Induced by Bubble Collapse. *J. Phys. Chem. Sol.* 98, 1–9. doi:10.1016/j.jpcs.2016.05.011

Zhang, Y., Zhang, F., Xie, Q., and Wu, G. (2015). Research on Electrically Conductive Acrylate Resin Filled with Silver Nanoparticles Plating Multiwalled Carbon Nanotubes. *J. Reinforced Plastics Composites* 34 (15), 1193–1201. doi:10.1177/0731684415587348

Zhang, Z., Ye, L.-L., Kukovecz, A., Konya, Z., Bielecki, J., and Liu, J. (2012). Characterization of CNT Enhanced Conductive Adhesives in Terms of thermal Conductivity. *ECS Trans.* 44 (1), 1011–1017. doi:10.1149/1.3694423

Zhao, J., Wang, G., Yang, R., Lu, X., Cheng, M., He, C., et al. (2015). Tunable Piezoresistivity of Nanographene Films for Strain Sensing. *ACS nano* 9, 1622–1629. doi:10.1021/nn506341u

Zhao, Q., Tan, S., Xie, M., Liu, Y., and Yi, J. (2018). A Study on the CNTs-Ag Composites Prepared Based on Spark Plasma Sintering and Improved Electroless Plating Assisted by Ultrasonic spray Atomization. *J. Alloys Compd.* 737, 31–38. doi:10.1016/j.jallcom.2017.12.066

Zhao, Q., Xie, M., Liu, Y., and Yi, J. (2017). Improved Electroless Plating Method through Ultrasonic spray Atomization for Depositing Silver Nanoparticles on Multi-Walled Carbon Nanotubes. *Appl. Surf. Sci.* 409, 164–168. doi:10.1016/j.apsusc.2017.03.032

Zhou, Y., Jin, P., Zhou, Y., Zhu, Y., and Ying, C. (2018). High-performance Symmetric Supercapacitors Based on Carbon Nanotube/graphite Nanofiber Nanocomposites. *Sci. Rep.* 8, 9005. doi:10.1038/s41598-018-27460-8

Conflict of Interest: The authors declare that the research was conducted in the absence of any commercial or financial relationships that could be construed as a potential conflict of interest.

Publisher's Note: All claims expressed in this article are solely those of the authors and do not necessarily represent those of their affiliated organizations, or those of the publisher, the editors and the reviewers. Any product that may be evaluated in this article, or claim that may be made by its manufacturer, is not guaranteed or endorsed by the publisher.

Advantages of publishing in Frontiers

OPEN ACCESS
Articles are free to read for greatest visibility and readership

FAST PUBLICATION
Around 90 days from submission to decision

HIGH QUALITY PEER-REVIEW
Rigorous, collaborative, and constructive peer-review

TRANSPARENT PEER-REVIEW
Editors and reviewers acknowledged by name on published articles

Frontiers
Avenue du Tribunal-Fédéral 34
1005 Lausanne | Switzerland

Visit us: www.frontiersin.org
Contact us: frontiersin.org/about/contact

REPRODUCIBILITY OF RESEARCH
Support open data and methods to enhance research reproducibility

DIGITAL PUBLISHING
Articles designed for optimal readership across devices

FOLLOW US
@frontiersin

IMPACT METRICS
Advanced article metrics track visibility across digital media

EXTENSIVE PROMOTION
Marketing and promotion of impactful research

LOOP RESEARCH NETWORK
Our network increases your article's readership